Target-Directed Synthesis of Protein-Protein Interaction Inhibitors

Sachi Sharma

A thesis submitted in accordance with the requirements for the degree of Doctor of Philosophy

Department of Chemistry
Imperial College London

March 2024

Statement of Originality

I, Sachi Sharma, declare that the research presented in the thesis titled “Target-Directed Synthesis of Protein-Protein Interaction Inhibitors” is my own. I confirm that information acquired from published sources is suitably referenced and any contributions from external parties is appropriately acknowledged.

Sachi Sharma

March 2024

Copyright

The copyright of this thesis rests with the author. Unless otherwise indicated, its contents are licensed under a Creative Commons Attribution Non-Commercial 4.0 International Licence (CC BY-NC). Under this licence, you may copy and redistribute the material in any medium or format. You may also create and distribute modified versions of the work. This is on the condition that: you credit the author and do not use it, or any derivative works, for a commercial purpose. When reusing or sharing this work, ensure you make the licence terms clear to others by naming the licence and linking to the licence text. Where a work has been adapted, you should indicate that the work has been changed and describe those changes. Please seek permission from the copyright holder for uses of this work that are not included in this licence or permitted under UK Copyright Law.

Abstract

Target-Directed Synthesis of Protein-Protein Interaction Inhibitors

By Sachi Sharma

Protein-protein interactions (PPIs) are prevalent across biology and play a central role in various cellular pathways. As aberrant interactions often manifest in the form of disease, the modulation of PPIs is of significant interest. A promising strategy for the development of PPI inhibitors exploits α-helical secondary structures, which are prevalent at many PPI interfaces. To date, the α-helix mimetic scaffolds reported fail to explore a diverse chemical space. This lack of diversity, in conjunction with the limited advancement of high-throughput screens in the context of PPIs, calls for the development of a novel approach for the synthesis of PPI inhibitors, whereby a large chemical space can be rapidly explored.

Herein the design and optimisation of a high-throughput target-directed screen is presented. This was designed in a manner where the natural selectivity of the native helix towards the protein of interest is exploited. For the development of this concept BCL-X_L/BAK was chosen as the model PPI. A two-pronged approach was taken, whereby in parallel both a peptidic and a hybrid mimetic route was developed. A series of BAK derived peptidic mimetics was synthesised featuring a nucleophilic thiol. This library was screened with a diverse electrophilic fragment library to generate functionalised mimetics. The binding affinity of these functionalised mimetics towards BCL-X_L was subsequently evaluated, with the hits identified serving to inform a future target-directed assay variant to be performed in the presence of the target protein. The hybrid pathway was designed where both peptidic and non-natural residues would be integrated into a single mimetic. The development of the synthetic route to produce the desired non-natural building block is detailed within this thesis. The target-directed screening approach introduced in this work has the potential to be applied to an array of PPIs, in an effort to produce potent PPI inhibitors with high selectivity.

Acknowledgements

Embarking on a journey towards completing a PhD was always going to be a challenging feat, made even more complex by starting it during a global pandemic. I would like to thank the people who helped me reach this stage and believed in me, when at times I didn't believe in myself.

First and foremost, I would like to thank my supervisors Dr Anna Barnard and Prof. Alan Armstrong for providing me with the opportunity to carry out this PhD and trusting me to explore this project and make it my own. I am immensely grateful for the support and guidance you both have shown me over the past three and a half years. Thank you for also taking the time to review this thesis and giving me excellent feedback.

I would particularly like to thank Brad for helping me navigate the qIT assay and for your continued patience, it was very much appreciated; an additional thanks to Charlie for your help in the lab when dealing with our favourite robot. Thank you also to Elena and Delia for answering my countless qIT related queries and everyone else in the lab who has supported me.

Thank you to everyone in the Barnard group, past and present, particularly those who were there when I began this journey. Gui, Dennis and Josh, thank you for creating a welcoming and friendly environment to work in, particularly during a challenging time (thank you COVID). A special thank you to Gui for believing in me from the very beginning and for taking the time to review parts of this thesis.

On a personal note, I would like to thank the friends I made along the way, without whom this journey wouldn't have been the same. So, thank you Ana, Delia, Gui, Rita, Roxani, Sarah, Sebastian, Tom and the rest of the bifunctionals for welcoming me into your circle. I look back fondly at all the good times we had, e.g. trips to Wales, Italy & Arizona, and hope to make countless more memories. I would also like to thank Ceire and Ayesha for always being there for me, I will forever cherish your friendship.

Finally, thank you to my mum and sister for their everlasting support; Luksha I could not have done this without you. A special thank you to the rest of my family, both in the UK and the US, for supporting me along this journey.

List of Collaborators

- Initial optimisation of qIT to FA assay (Section 2.6) was conducted in collaboration with Brad Hocking (Imperial College London).
- Trace metal analysis (Section 3.3.4) was performed by Fatimah Alfadel (Imperial College London).
- Fluorescein-labelled BAK peptide utilised for biochemical assays (Section 5.4) was synthesised by Dennis Worm (Imperial College London).

Presentations

Oral Presentations

Sachi Sharma *et al*. 'Target-Directed Synthesis of Protein-Protein Interaction Inhibitors', *RSC Chemical Biology and Bio-organic Group Postgraduate Symposium, Oxford, April 2023*

Sachi Sharma *et al*. 'Target-Directed Synthesis of Protein-Protein Interaction Inhibitors', *Imperial College London Department of Chemistry Postgraduate Symposium, London, July 2023*

Poster Presentations

Sachi Sharma *et al*. 'Target-Directed Synthesis of α-helix Mimetics', *RSC Chemical Biology and Bio-organic Group Postgraduate Symposium, York, April 2022*

Sachi Sharma *et al*. 'Target-Directed Synthesis of α-helix Mimetics', *Imperial College London Department of Chemistry Postgraduate Symposium, London, July 2022*

Sachi Sharma *et al*. 'Target-Directed Synthesis of α-helix Mimetics', *EMBO Workshop Chemical Biology, Heidelberg, September 2022*

Sachi Sharma *et al*. 'Target-Directed Synthesis of α-helix Mimetics', *PSL Chemical Biology Symposium, Paris, January 2023*

Sachi Sharma *et al*. 'Target-Directed Synthesis of Protein-Protein Interaction Inhibitors', *American Peptide Symposium, Arizona, June 2023*

Contents

Statement of Originality …….. ii

Copyright ……... ii

Abstract …….. iii

Acknowledgements …….. iv

List of Collaborators ……. v

Presentations …… v

List of Figures ……... xi

List of Schemes …… xv

List of Tables ……. xvi

Abbreviations ……..... xvii

1.0 Introduction ……..... 1

1.1 Protein-Protein Interactions …… 2

1.1.1 Key Characteristics of PPIs ……. 2

1.1.1.1 Classification of PPIs …… 2

1.1.1.2 Hot Spot Residues ……..... 4

1.2 α-Helix Mediated Protein-Protein Interactions ……..... 6

1.3 BCL-2 Family of Proteins …… 9

1.3.1 The Role of BCL-2 Proteins in Apoptosis …….. 9

1.3.2 BCL-X_L/BAK ……... 14

1.4 Peptidic Inhibitors Targeting Protein-Protein Interactions …….. 18

1.4.1 Cyclisations …… 20

1.4.1.1 Sidechain-to-head ……. 20

1.4.1.2 Sidechain-to-sidechain ……. 21

1.4.1.3 Head-to-tail …….. 23
1.4.2 Backbone Modifications ……..... 23
1.4.2.1 Stereochemical Variation …….. 24
1.4.2.2 Shift of Sidechain Functionality ……..... 24
1.4.2.3 Extension of the Backbone ……... 25
1.5 Proteomimetic Inhibitors Targeting Protein-Protein Interactions ……... 26
1.5.1 Mimetic Scaffolds ……... 26
1.5.1.1 Terphenyls and its Derivatives ……. 26
1.5.1.2 Oligoamides …… 30
1.6 High-Throughput Strategies …… 32
1.6.1 General Overview …….. 32
1.6.2 Activity-Directed Synthesis ……... 34
1.7 Target-Guided Synthesis ……. 37
1.8 Project Aims ……... 40
1.8.1 Perspectives and Proposed Approach …….. 40
1.8.2 Quantitative Irreversible Tethering (qIT) ……. 43
2.0 High-Throughput Assay Development ……... 45
2.1 Introduction and Objectives ……. 46
2.2 Site-Directed Mutagenesis …….. 48
2.2.1 Modifying WT BCL-X_L …… 48
2.3 Fluorescence Anisotropy Saturation Assay …….. 52
2.3.1 Principles of Assay …… 52
2.3.2 Saturation Assay …… 54
2.4 Peptide Design & Synthesis …… 56
2.4.1 Design of Peptide Library ……. 56
2.4.2 Solid-Phase Peptide Synthesis …… 57

2.5 Fluorescence Anisotropy Competition Assay …….. 59
2.5.1 Assay Design …….. 59
2.5.2 Optimisation of Assay ……... 60
2.6 Development of the qIT to FA Assay ……. 64
2.6.1 Preliminary Optimisation ……... 64
2.6.2 Acrylamide Library Screen ……... 69
2.6.2.1 Screen A - Evaluation of SS1 Under Assay Conditions 69
2.6.2.2 Screen B - Remediating Thiol Oxidation…… 71
2.6.2.3 Screen C - Preliminary Optimisation of qIT to FA…… 72
2.6.2.4 Screen D - Further Development of qIT to FA ..…… 77
2.7 SS1 High-Throughput Screen ……. 80
2.7.1 Acrylamide Library Screen …… 80
2.7.1.1 Screen E - Primary Library Screen…….. 80
2.7.1.2 Screen F - Repeat of Primary Library Screen…….. 82
2.8 SS4 High-Throughput Screen ……. 88
2.8.1 Acrylamide Library Screen …… 88
2.9 Conclusions and Future Outlook …… 91
3.0 Design and Synthesis of Hybrid Mimetics …….. 93
3.1 Introduction and Objectives ……. 94
3.2 Preliminary Design of Synthetic Route …….. 97
3.2.1 Hydrogenation …… 98
3.2.2 Fmoc Protection ……. 98
3.2.3 Radical Bromination …….. 99
3.3 Retrosynthetic Design of Revised Pathway …….. 102
3.3.1 Radical Bromination …….. 103
3.3.2 Nucleophilic Substitution …….. 104

3.3.3 Protection of the Free Thiol 106
3.3.4 Nitro Reduction 108
3.3.5 Hydrolysis of Methyl Ester 112
3.3.6 Fmoc Protection 113
3.4 Conclusions and Future Outlook 118
4.0 Conclusions and Future Outlook 122
4.1 Peptidic Pathway 123
4.2 Hybrid Pathway 124
5.0 Materials and Methods 126
5.1 Peptide Synthesis 127
5.1.1 General Information 127
5.1.2 Solid-phase Synthesis 127
5.1.3 N-Acetylation 127
5.1.4 Cleavage 128
5.1.5 Purification 128
5.2 Chemical Synthesis 133
5.2.1 General Information 133
5.2.2 Synthetic Methods 133
5.3 Protein Expression and Purification 152
5.3.1 General Protocols 152
5.3.1.1 SDS-PAGE 152
5.3.2 Site-Directed Mutagenesis 152
5.3.3 Protein Expression 153
5.3.4 Protein Purification 153
5.3.4.1 General Conditions 153
5.3.4.2 Buffers 154

5.3.4.3 Purification ……... 154

5.4 Biochemical Assays …….. 156

5.4.1 Fluorescence Anisotropy …….. 156

5.4.1.1 General Information ……... 156

5.4.1.2 Saturation Assay ……. 156

5.4.1.3 Competition Assay ……. 156

5.4.2 Quantitative Irreversible Tethering (qIT) …… 157

5.4.2.1 General Information ……... 157

5.4.2.2 Compound Preparation ……. 157

5.4.2.3 Reaction Plate ……. 157

5.4.2.4 Quench Plate …….. 158

5.4.3 qIT to FA …….. 158

5.4.3.1 General Information ……... 158

5.4.3.2 Compound Preparation ……. 158

5.4.3.3 Dilution Plates ……. 158

5.4.3.4 Reaction Plates ……... 159

References …….. 160

Appendix ……. 169

List of Figures

All figures were made through BioRender, GraphPad & ChemDraw.

Chapter 1

Figure 1: PPI classification depending on the nature of the interaction

Figure 2: PPIs between IL-2/IL-2R and BCL-X_L/BAD

Figure 3: PPI between hGH/ hGHbp

Figure 4: Structure of an α-helix

Figure 5: Examples of PPI recognition faces

Figure 6: Interactions within the BCL-2 family

Figure 7: Differences between various MOMP models

Figure 8: Caspase dependent and independent pathways leading to apoptosis

Figure 9: Crystal structure of the BCL-X_L/BAK PPI

Figure 10: Small molecules vs. biologics

Figure 11: Common peptide cyclisation strategies

Figure 12: Ring-Closing Metathesis

Figure 13: Different approaches for sidechain-to-sidechain cyclisation

Figure 14: Crystal structure of the stapled ALRN-6924 helix bound to MDMX

Figure 15: Structural difference between peptides and peptoids

Figure 16: Structural difference between α and β peptides

Figure 17: Hamilton's original terphenyl scaffold

Figure 18: Terphenyls derived scaffolds

Figure 19: Oligoamide based scaffolds

Figure 20: HTS magic triangle

Figure 21: An overview of the ADS based approach

Figure 22: Androgen receptor modulators

Figure 23: Hit scaffolds targeting the p53/hDM2 PPI identified through ADS

Figure 24: An overview of the kinetic target-guided synthesis strategy

Figure 25: Two-pronged approach for the development of inhibitors for the BCL-X_L/BAK PPI

Figure 26: An overview of the quantitative irreversible tethering (qIT) assay

Chapter 2

Figure 27: Comparing the qIT two-component system versus the revised three-component system

Figure 28: Crystal structure of BCL-X_L highlighting the native cysteine residue

Figure 29: Differences in the codons for cysteine and serine residues

Figure 30: Schematic representation detailing the PCR workflow

Figure 31:Protein expression and purification workflow

Figure 32:Principles of fluorescence anisotropy

Figure 33: Fluorescence anisotropy saturation assay

Figure 34: Sequences of peptides in the small mimetic library

Figure 35: SPPS workflow

Figure 36: DIC/Oxyma based amino acid activation pathway

Figure 37: Fluorescence anisotropy competition assay

Figure 38: Primary trial of the FA competition assay

Figure 39: FA competition assay optimisation

Figure 40: FA binding curves for mimetics SS1-SS4

Figure 41: How functionalised peptide mimetics will be evaluated

Figure 42: Titration of SS1 (10-0.04 μM) against CPM

Figure 43: Titration of SS1 (40-2.3 μM) against CPM

Figure 44: Titration of SS1 (40-1.6 μM) against CPM

Figure 45: qIT Screen A

Figure 46: qIT Screen B

Figure 47: qIT Screen C

Figure 48: FA data analysing SS1 functionalised with TAP acrylamide fragments (5-0.16 μM)

Figure 49: FA data analysing SS1 functionalised with TAP acrylamide fragments (2.5-0.16 μM)

Figure 50: FA binding curves of SS1 functionalised with TAP-4 E05, TAP-1 B04 & TAP-2 D04

Figure 51: A comparison of the qIT and FA data from library screen D and E

Figure 52: A comparison of fragment reactivity from qIT Screen E and F

Figure 53: A comparison of the FA binding curves from Screen E and F

Figure 54: FA competition binding curves of hit mimetics

Figure 55: FA competition binding curves for functionalised SS4 mimetics

Figure 56: qIT and FA binding curves of hit mimetics

Chapter 3

Figure 57: α-helix mimetic scaffolds present in the literature compared to the hybrid approach

Figure 58: An illustration depicting the three phases that make up the hybrid mimetic pathway

Figure 59: An illustration showing the replacement of a helix turn with the designed monomer

Figure 60: How the functionalised monomer will be incorporated into the BAK peptidic sequence

Figure 61: Proposed phases to produce the next generation of helix mimetics

Chapter 4

Figure 62: Flowchart detailing the peptidic and hybrid mimetic pathways

Chapter 5

Figure 63.1: SS1 sequence

Figure 63.2: SS1 HPLC trace

Figure 64.1: SS2 sequence

Figure 64.2: SS2 HPLC trace

Figure 65.1: SS3 sequence

Figure 65.2: SS3 HPLC trace

Figure 66.1: SS4 sequence

Figure 66.2: SS4 HPLC trace

Figure 67: ^{1}H NMR of **2**

Figure 68: ^{1}H NMR of **3**

Figure 69: ^{1}H and ^{13}C NMR of **8**

Figure 70: ^{1}H and ^{13}C NMR of **9**

Figure 71: ^{1}H and ^{13}C NMR of **13**

Figure 72: ^{1}H and ^{13}C NMR of **12**

Figure 73: ^{1}H and ^{13}C NMR of **14**

Figure 74: ^{1}H and ^{13}C NMR of **15**

Figure 75: ^{1}H and ^{13}C NMR of **17**

Figure 76: ^{1}H and ^{13}C NMR of **18**

List of Schemes

Chapter 3

Scheme 1: Preliminary design of the synthetic pathway to generate the protected monomer **6**

Scheme 2: Hydrogenation and Fmoc protection of **1**

Scheme 3: Goldfinger radical bromination mechanism

Scheme 4: Retrosynthetic approach for the synthesis of the functionalised monomer

Scheme 5: Radical bromination optimisation

Scheme 6: Nucleophilic substitution attempt using thiourea

Scheme 7:Sucessful route to target thiol **12**

Scheme 8: Fmoc and trityl cleavage mechanisms

Scheme 9: Thiol protection to produce **14**

Scheme 10: Hydrolysis of methyl ester to generate **17**

Scheme 11: Final synthetic route to generate the desired thiol functionalised building block

List of Tables

Chapter 3

Table 1: Reaction conditions tested for the installation of the trityl protecting group

Table 2: A comparison of the reaction conditions tested for the metal-free nitro reduction step

Table 3: A comparison of H_2O sources and how this affects the conversion of **8** to **16**

Table 4: Trace metal analysis

Table 5: A summary of the various conditions tested using H_2O source B

Table 6: A summary of the various reaction conditions trialled for the Fmoc protection of **17**

Table 7: Optimisation of the Ghosez mediated coupling of the **17** with Fmoc-Ala-OH

Appendix

Table 1-9: SS1 screen E qIT data from various timepoints

Table 10-17: SS1 screen E FA data from various dilutions

Table 18-26: SS1 screen F qIT data from various timepoints

Table 27-33: SS1 screen F FA data from various dilutions

Table 34-42: SS4 qIT data from various timepoints

Table 43-49: SS4 FA data from various dilutions

Abbreviations

δ	Chemical shift
μL	Microlitre
μM	Micromolar
°C	Degree Celsius
A_{280}	Absorbance at 280 nm
AChE	Acetylcholinesterase
ACN	Acetonitrile
ADME	Absorption, Distribution, Metabolism, and Excretion
ADS	Activity-directed synthesis
AEC	Anion exchange chromatography
AEC	Anion exchange chromatography
AIBN	Azobisisobutyronitrile
Apaf-1	Apoptotic protease activating factor 1
AR	Androgen receptor
BAD	BCL-2 associated agonist of cell death
BAK	BCL-2 homologous antagonist/killer
BAX	BCL-2 associated X protein
BCL-2	B-cell lymphoma 2
BCL-X_L	B-cell lymphoma-extra large
BH3	BCL-2 homology domain 3
BIM	BCL-2-like protein 11
BPO	Benzoyl peroxide
CaM	Calmodulin
CPM	7-Diethylamino-3-(4'-Maleimidylphenyl)-4-Methylcoumarin

CV	Column volume
DCM	Dichloromethane
DHP	3,4-Dihydropyran
DIC	N,N’-diisopropylcarbodiimide
DIPEA	N,N-Diisopropylethylamine
DMF	Dimethylformamide
DMSO	Dimethylsulfoxide
dNTP	Deoxyribonucleotide triphosphate
DODT	2,2′-(Ethylenedioxy)diethanethiol
EDT	1,2-ethanedithiol
EtOAc	Ethyl Acetate
FA	Fluorescence anisotropy
FAM	Fluorescein amidite
Fmoc	Fluorenylmethoxycarbonyl
Ghosez	1-Chloro-N,N,2-trimethyl-1-propenylamine
GSH	Glutathione
HATU	1-[Bis(dimethylamino)methylene]-1H-1,2,3-triazolo[4,5-b]pyridinium 3-oxide hexafluorophosphate
HBS	Hydrogen bond surrogate
HCMV	Human cytomegalovirus
hDM2	Human MDM2
hGH	Human growth hormone
hGHbp	Human growth hormone binding protein
His-tag	Hexa histidine-tag
HOBt	Hydroxybenzotriazole
HPLC	High-performance liquid chromatography

HRMS	High-resolution mass spectrometry
HTS	High-throughput screen
IC_{50}	Half-maximal inhibitory concentration
IL-2	Interleukin-2
IL-2R	Interleukin-2 receptor
Ile	Isoleucine
IMAC	Immobilized Metal Affinity Chromatography
IMAC	Immobilized metal affinity chromatography
IPTG	Isopropyl β-d-1-thiogalactopyranoside
K_D	Dissociation constant
KTGS	Kinetic target-guided synthesis
LB	Lysogeny broth
LCMS	Liquid chromatography–mass spectrometry
Leu	Leucine
MCL-1	Induced myeloid leukemia cell differentiation protein
MDM2	E3 ubiquitin-protein ligase
mg	Milligram
mL	Millilitre
mmol	Millimole
MOMP	Mitochondrial outer membrane permeabilization
MW	Microwave
NBS	N-Bromosuccinimide
nM	Nanomolar
NMR	Nuclear magnetic resonance
OD_{600}	Optical density at 600 nM
Omi	High-temperature requirement protein A2

O/N	Overnight
Oxyma	Ethyl cyano(hydroxyimino)acetate
PCR	Polymerase chain reaction
PDB	Protein data bank
PPI	Protein-protein interaction
*P*TSA	*p*-Toluenesulfonic acid
qIT	Quantitative irreversible tethering
SDM	Site-directed mutagenesis
SDS-Page	Sodium dodecyl-sulfate polyacrylamide gel electrophoresis
SEC	Size exclusion chromatography
SEC	Size exclusion chromatography
Smac	Second mitochondria-derived activator of caspase
S_N2	Bimolecular nucleophilic substitution
SOC	Super Optimal broth with Catabolite repression
SPPS	Solid-phase peptide synthesis
^tBU	Tert-butyl
TCEP	Tris(2-carboxyethyl)phosphine
TEA	Triethylamine
TFA	Trifluoroacetic acid
TGS	Target-guided synthesis
THF	Tetrahydrofuran
THP	Tetrahydropyranyl
TIS	Triisopropylsilane
TRIS	Tris(hydroxymethyl)aminomethane,
Trt	Trityl
Val	Valine

WT	Wild-type
XIAP	X-chromosome-linked inhibitor of apoptosis protein

Chapter 1

Introduction

1.1 Protein-Protein Interactions

Protein-protein interactions (PPIs) are prevalent in most biological processes, with these non-covalent contacts playing a central role in a variety of essential cellular pathways.[1] An intracellular network of PPIs is referred to as an interactome,[2] with the human interactome comprising of approximately 650,000 distinct PPIs.[3] PPIs within the human interactome play a central role in many pathological and physiological pathways including apoptosis, signal transduction, transcription growth and cell proliferation.[2, 4] Aberrant PPIs often manifest in the form of disease, such as cancer and HIV, as well as neurodegenerative and infectious diseases.[4]

As such, the investigation and modulation of PPIs is of significant interest, in terms of both deepening our understanding of complex cellular pathways, as well as enabling the development of novel therapeutic agents.[5] Historically, PPIs have been bestowed with the moniker of 'undruggable' or 'intractable',[6] owing to their large contact interfaces of approximately 1,500–3,000 Å^2, compared to the interface between proteins and small molecules (~300–1,000 Å^2).[7] PPI interfaces are often flat in addition to being large- a stark contrast to the well-defined binding pockets of enzyme-substrate/ receptor-substrate interactions.[6]

1.1.1 Key Characteristics of PPIs

1.1.1.1 Classification of PPIs

Taking into consideration the vast network of complex PPIs in the interactome, it is conceivable that there is a level of diversity present. PPIs are typically classified as either homo-oligomeric or hetero-oligomeric,[8] obligate or non-obligate and transient or permanent.[9] PPIs that are classified as obligate complexes refer to the fact that *in vivo* their components lack stability on their own, whereas constituents of non-obligate complexes can successfully do so. As such, obligate interactions are predominantly permanent, in contrast to non-obligate interactions which are typically transient.[9]

An alternative classification system of PPIs is centred around the structural nature of the interactions that take place. Blundell *et al.* [10] initially postulated three models by which PPIs can be classified; globular proteins that interact via a discontinuous epitope without significant conformational changes (**Figure 1a**), globular proteins that adopt a different conformation upon binding (**Figure 1b**) and interactions between a globular protein and a peptide (**Figure 1c**). Scott

et al.[11], added to this system by including interactions that take place between two peptide chains (**Figure 1d**).

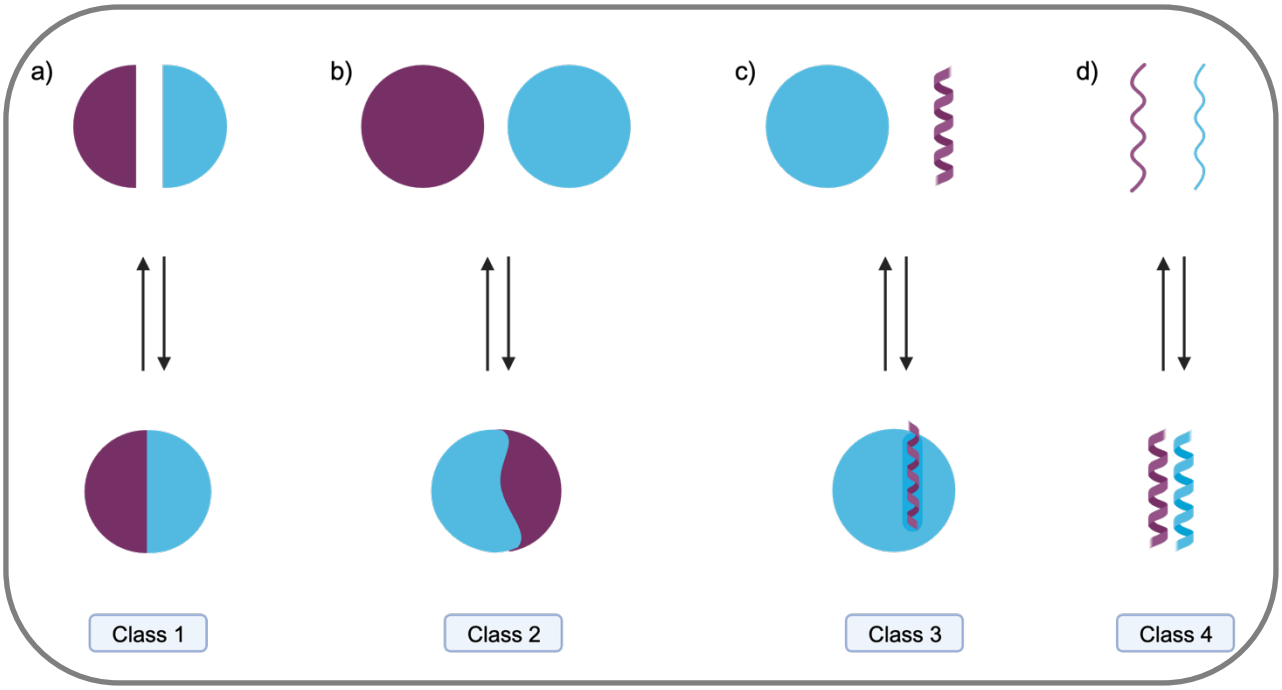


Figure 1: PPI classification depending on the nature of the interaction; **a)** Class 1- globular proteins interacting via a discontinuous epitope without conformational change, **b)** Class 2- PPIs between globular proteins that form a different conformation upon binding, **c)** Class 3- PPIs involving a globular protein and a peptide, **d)** Class 4- PPIs between two peptide chains. Figure adapted from Scott *et al*.[11]

Not all PPIs are considered challenging to target or 'undruggable' to the same extent. PPIs between globular proteins, such as IL-2 and IL-2R,[12] involve contacts between large surfaces which tend to be flatter than other PPIs, making them less susceptible to modulation by small molecules (**Figure 2a)**.[11] In comparison, PPIs between globular proteins and a single peptide chain, like BCL-X_L and BAD, are postulated to be more 'druggable' owing to their smaller contact surfaces (**Figure 2b**) .[12]

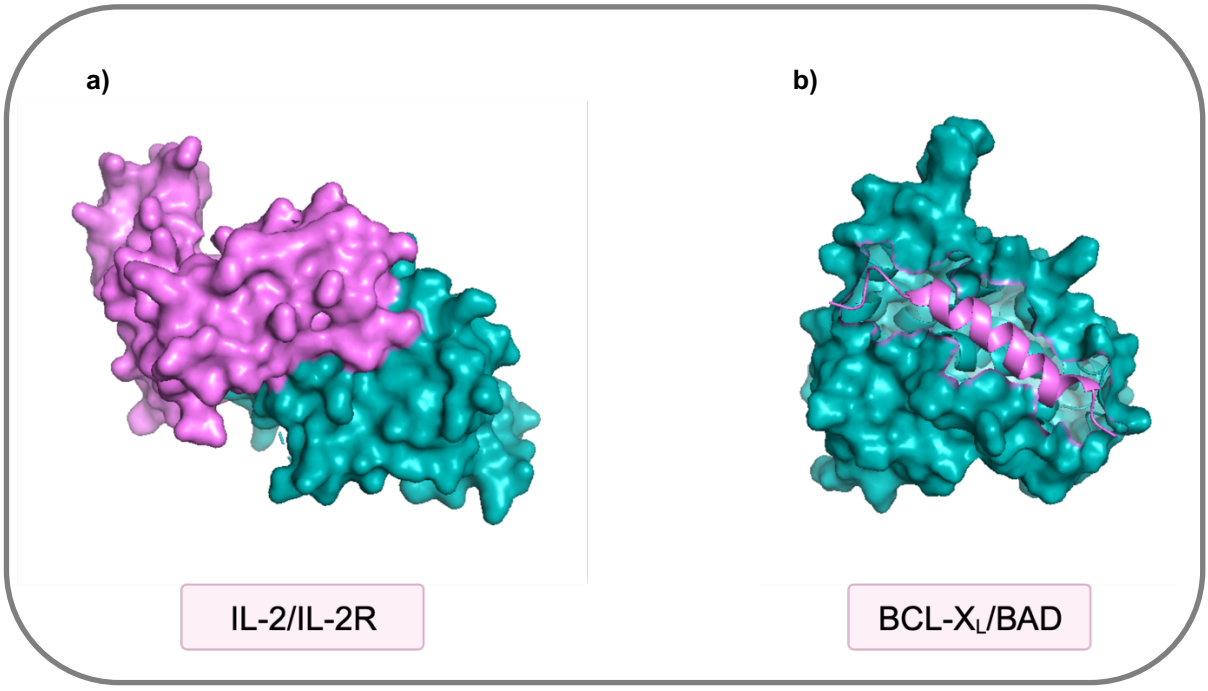


Figure 2: **a)** PPI between IL-2/IL-2R highlighting the interaction between globular proteins (PDB code 1z92). **b)** BCL-XL/BAD PPI illustrating an interaction between a globular protein and a peptide chain (PBD code 1G5J).

1.1.1.2 Hot Spot Residues

Although PPI interactions take place over large interfaces, the majority of the binding affinity is ascribed to a few key amino acid residues, as elucidated by the work of Clackson and Wells.[13] These 'hot spot' residues are hence defined as residues that upon mutation to alanine, result in a sharp rise of the absolute binding energy where the increase is greater than 2 kcal/mol.[14]

Clackson and Wells[13] demonstrated this phenomenon by mutating each of the sidechain residues of the human growth hormone binding protein (hGHbp) to alanine. They found that the functional epitope comprised of only 11 out of 33 residues, validating the hypothesis that the binding affinity across a PPI interface is not uniform. Similarly, when the human growth hormone (hGH) was subject to the same analysis, Clackson and Wells found that astonishingly 8 out of 31 residues contributed 85% towards the binding affinity.[13] The hGH and hGHbp proteins therefore interact via their complementarity functional epitopes as seen in **Figure 3**.[13, 15]

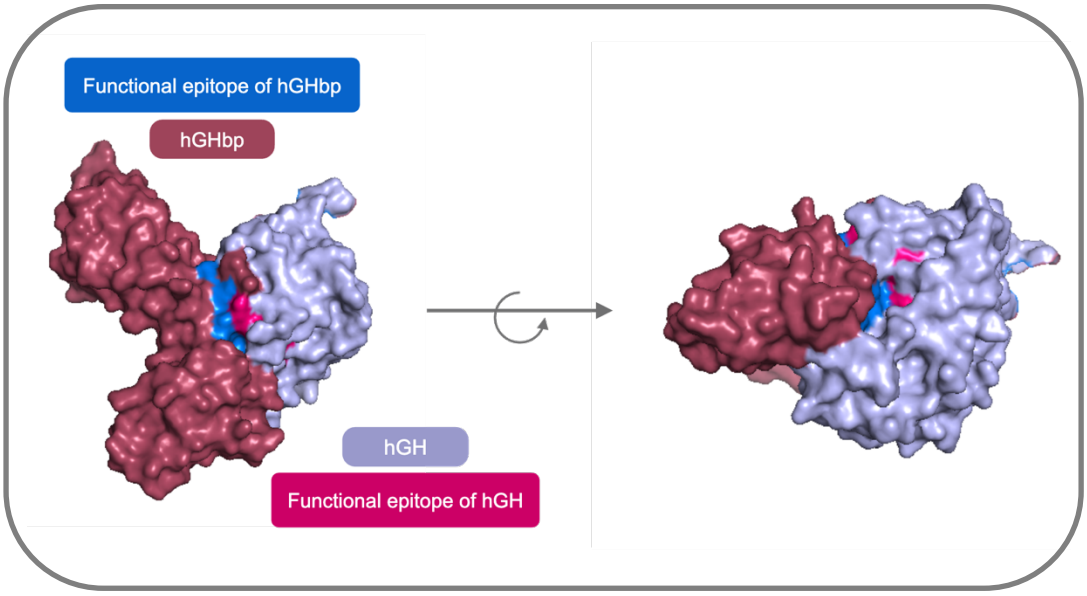


Figure 3: PPI between (human growth hormone) hGH and human growth hormone binding protein (hGHbp), with the complementary epitopes highlighted in pink for hGH and blue for hGHbp (PDB code 3HHR).

Bogan and Thorn[16] conducted an analytical study investigating the contributions of various amino acid residues involved in protein-protein binding, using alanine scanning mutagenesis. Through this investigation, they reaffirmed the seminal work of Clackson and Wells[13] by stating that the distribution of energetic contributions across PPI interfaces is highly disproportionate. Bogan and Thorn[16] added to this notion by denoting that certain residues are more likely to be found in hot spot positions than others. Tryptophan, arginine and tyrosine residues are the only residues that appear in hot spots with a frequency greater than 10%. It is postulated that tryptophan might be preferred in such a position as it can form hydrogen bonds and π-π stacking interactions, as well as providing a large hydrophobic surface. Tyrosine residues can also form such interactions, while arginine can form extensive hydrogen bonding networks and possesses pseudo-aromatic character.[16]

As highlighted in the discussion above, the interfacial energy between PPIs is non-uniform, with hot spots disproportionately contributing to the binding energy. The resulting inference is that PPIs previously envisaged as ‘intractable’ or ‘undruggable’ can undergo modulation, through the concerted investigation and manipulation of hot spot residues.

1.2 α-Helix Mediated Protein-Protein Interactions

A promising strategy for the development of PPI inhibitors involves the exploitation of the secondary structural motifs found at PPI interfaces. α-helices constitute the most prevalent class of secondary structures found at the interface of PPIs, with an analysis of the Protein Data Bank (PDB) by Arora *et al*[17] revealing that of the multiprotein complexes recorded, 62% feature an α-helix at the interface. The defining characteristics of an α-helix are the tight helical turns with around 3.4 residues per turn, resulting in sidechains pointing every 100 degrees. Consequently, side chains at *i*, *i + 3/4* and *i + 7* occupy a single face and typically form the interacting residues of a PPI[4] as illustrated in **Figure 4**.

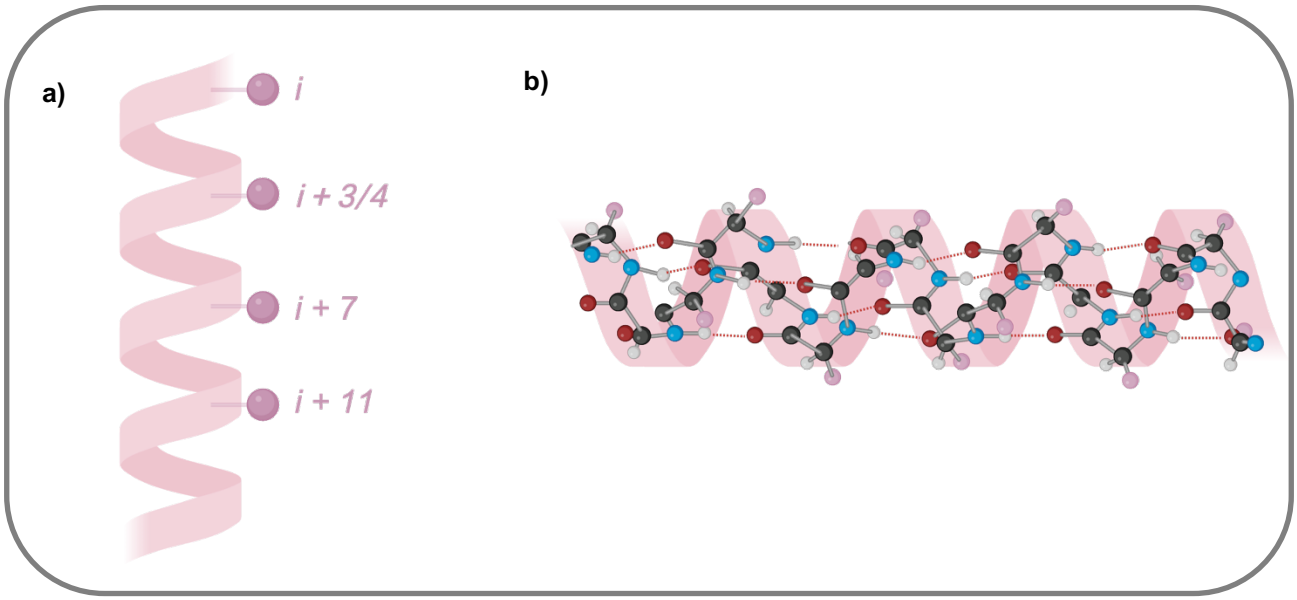


Figure 4: **a)** Structure of an α-helix highlighting the manner in which the *i*, *i + 3/4* and *i + 7* residues occupy a single face. **b)** An illustration of the intramolecular hydrogen bonding responsible for the α-helical geometry.

Arora *et al.*[17]evaluated the contribution of α-helices in multiprotein complexes using computational alanine scanning. They stated that simply the presence of an α-helix is not indicative of a role in complex formation, rather it is the energetic contributions of hot spot residues on the helices that divide the helical interfaces as either 'strongly' or 'weakly' interacting'. Analysis of hot spot residues present on 'strongly interacting' interfaces identified that approximately 60% of helical interfaces are mediated by hot spots on a single face. PPIs mediated by two helical faces account for approximately 30% of interactions, while only 10% require all three faces.[17] An example of a PPI modulated by a single face is the p53/MDM2 PPI,[18] where the crystal structure (**Figure 5a**)

highlights the presence of hot spot residues on one face. PPIs modulated by two helical faces include the MCL-1/PUMA and MCL-1/NOXAA PPIs, where PUMA and NOXAA bind as amphipathic α-helices[19] (**Figure 5b**). There are fewer examples of PPIs binding through three helical faces, such as the CaM/ αIIspec PPI[20] seen in **Figure 5c**.

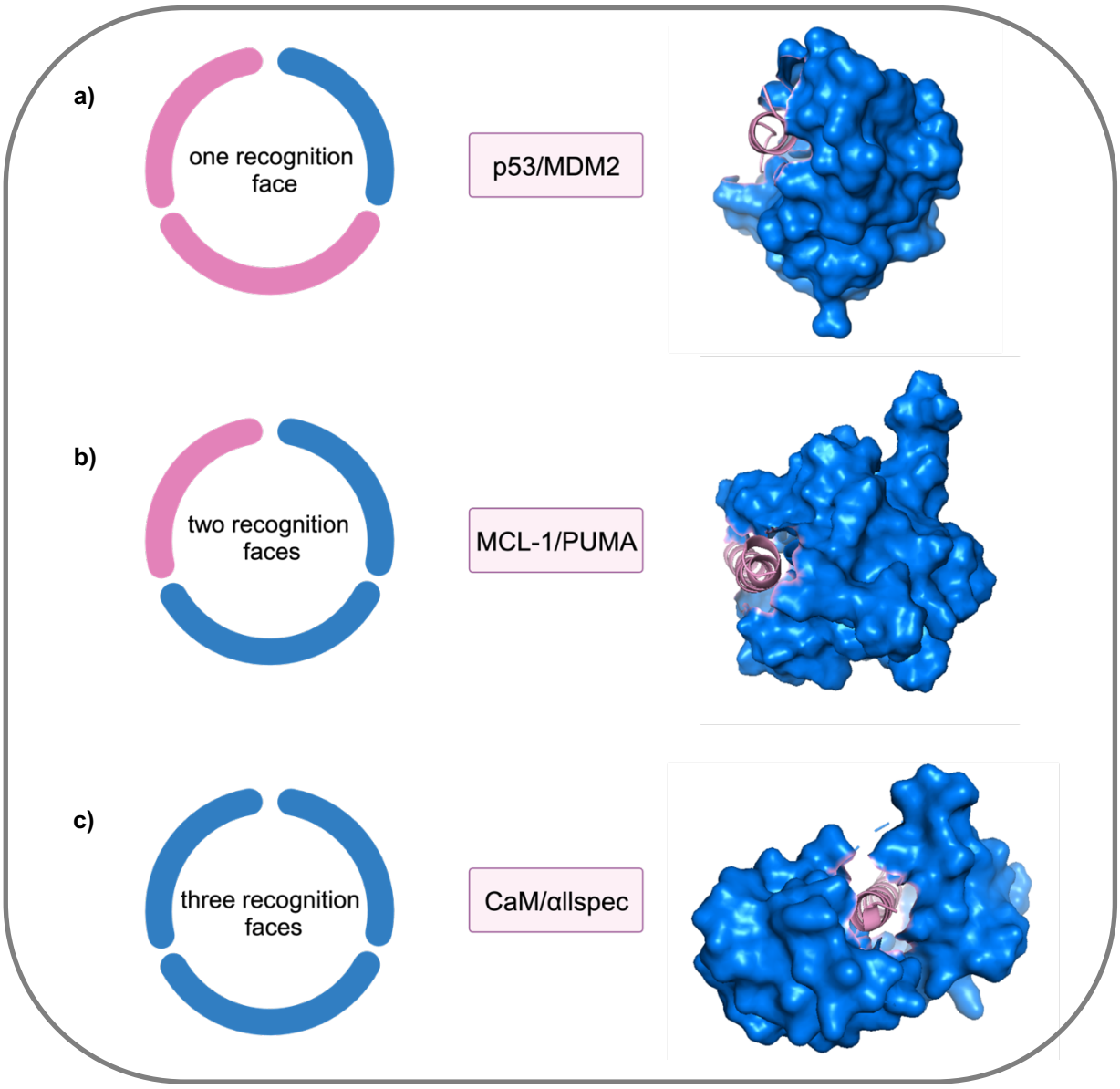


Figure 5: **a)** The p53/MDM2 PPI modulated by a single face (PDB code 1YCR). **b)** The MCL-1/PUMA PPI mediated by two helical faces (PDB code 2ROC). **c)** The CaM/ αIIspec PPI modulated by three helical faces (PDB code 2FOT).

Considering the inhibition of PPIs is of great therapeutic interest for an array of disease models, significant research efforts have been devoted to investigating interactions mediated through α-helices. As previously illustrated by Arora *et al,*[17] there is a large catalogue of interactions that could be inhibited within this category. Popular approaches for targeting helix-mediated interactions are detailed in Sections 1.4 and 1.5.

1.3 BCL-2 Family of Proteins

A frequently targeted family of interactions are those within the BCL-2 family, where significant research efforts have been devoted to identifying inhibitors of key PPIs within this family.

1.3.1 The Role of BCL-2 Proteins in Apoptosis

Apoptosis is a genetically modulated biological process by which cell death occurs.[21] The primary objective of this programmed cell death is to selectively cull cells that are mutated, damaged or that are overabundant.[22] This physiological process is vital for the regulation of general function and growth in multi-cellular organisms,[22] and is triggered in response to developmental signals, as well as cellular distress.[21] There are two distinct avenues by which apoptosis occurs: an intrinsic and extrinsic pathway.[23] The extrinsic pathway is defined as one that is activated by external stimuli, whereas the intrinsic mechanism is triggered by pro-apoptotic stimuli within the mitochondria itself.[21] Circumvention of this process may lead to disease, a notable one being cancer.[24]

A family of proteins responsible for the regulation of apoptosis is the B-cell lymphoma 2 (BCL-2) family, where the net interactions within this family determine the outcome of the cell.[25] The BCL-2 family is segregated into three distinct subfamilies, depending on the nature of the protein. The first is comprised of proteins that are anti-apoptotic in nature, including BCL-2, BCL-X_L and MCL-1. The second subfamily is made up of pro-apoptotic proteins such as BAK and BAX, which differs from the third comprising of pro-apoptotic BH3-only proteins like BAD,BID and BIM.[26]

There are four conserved BH domains that make up the proteins in this family; these are key for the BCL-2 proteins to be able to interact with each other.[27] These domains are composed of eight α-helical fragments joined together.[21] The first two groups (anti-apoptotic and pro-apoptotic) are comprised of all four BH domains, whereas the BH3-only proteins, as the name suggests, only contain the BH3 domain. As the anti-apoptotic and pro-apoptotic proteins feature multiple domains, it allows them to form a tertiary structure containing a hydrophobic cleft, which binds to the BH3 domains of other BCL-2 proteins.[27]

The way in which the BCL-2 family mediates apoptosis is through the regulation of mitochondrial outer membrane permeabilization (MOMP),[25] where the three subfamilies play distinct roles.[28] The pro-apoptotic proteins initiate MOMP directly, in comparison to the anti-apoptotic proteins that hinder this process in multiple ways. The BH3-only proteins serve as activators of the pro-apoptotic proteins through both direct and indirect pathways. A summary of these interactions is illustrated in **Figure 6** below.

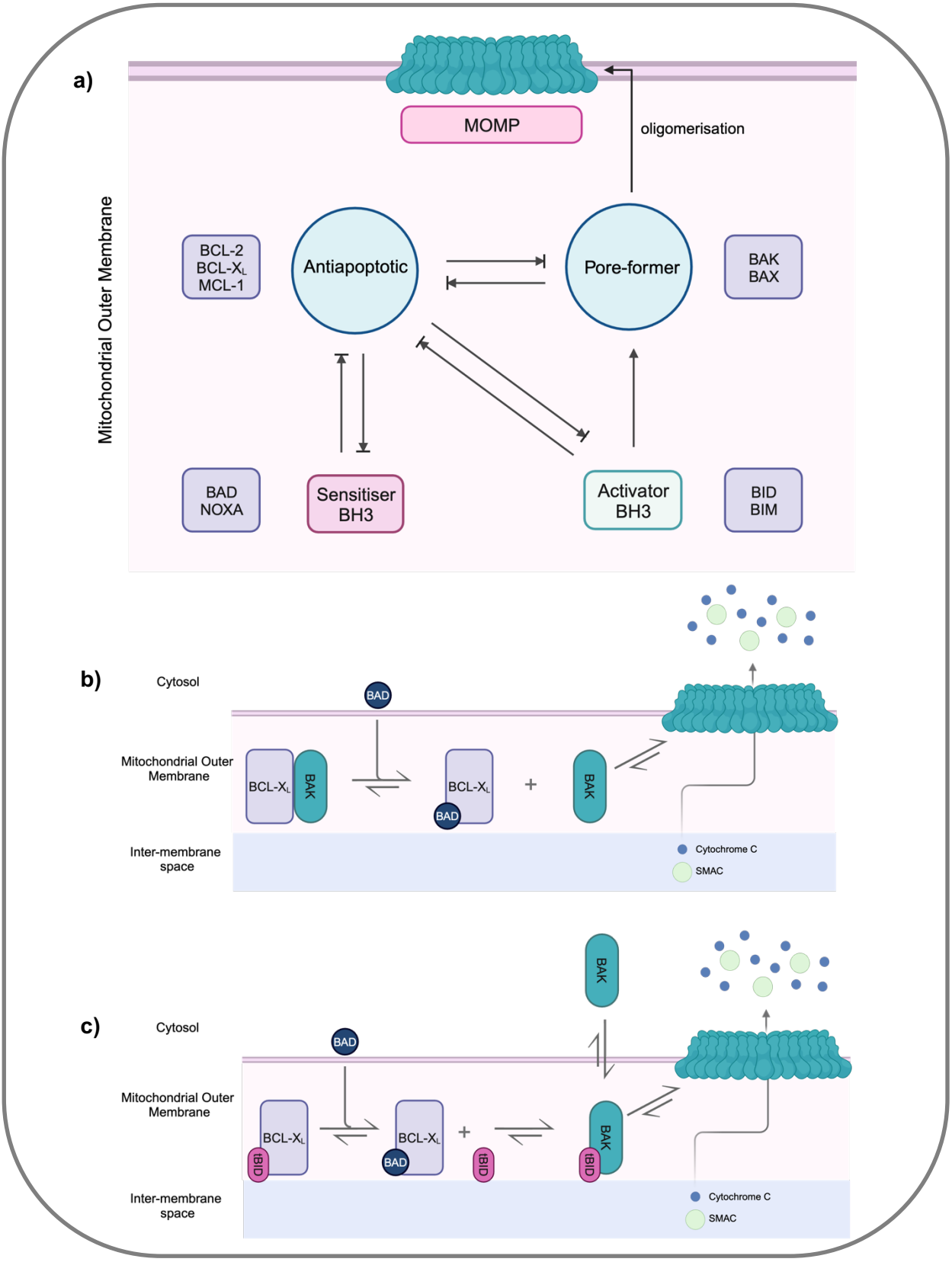


Figure 6:**a)** Schematic representation of the embedded together model. Anti-apoptotic proteins inhibit both activator and sensitiser BH3-only proteins, along with inhibiting the pro-apoptotic pore formers. Sensitiser BH3-only proteins only bind to and mutually sequester anti-apoptotic proteins, whereas activator BH3 proteins inhibit anti-apoptotic proteins via mutual sequestration whilst also being able to activate pore formers (e.g. BAK). **b)** BAD displacing BAK from BCL-X_L allowing BAK to initiate MOMP. **c)** BAD inhibits BCL-X_L allowing BID to activate BAK and initiate pore formation.

Figure adapted from Kale *et al*.[27]

As elucidated in **Figure 6**, there are a complex array of interactions that control MOMP. This figure highlights the embedded together model which states that the mitochondrial membrane is the 'locus of action' for apoptosis.[22] This model emphasises that the fate of the cell is determined by the interactions that take place between the proteins in the BCL-2 family, which in turn are dependent on the relative abundance, affinity and competing equilibria of said proteins.[22] The embedded model segregates the BH3-only proteins into two classes: activators and sensitisers. BAK and BAX are directly activated by the BH3-only activators, which allows them to oligomerise and initiate MOMP. The anti-apoptotic proteins can be inhibited by both activator and sensitiser BH3 proteins through binding. Apoptosis is repressed by pro-apoptotic and BH3 only proteins being sequestered by anti-apoptotic proteins.[28] This is in contrast to the direct activation and displacement models as indicated in **Figure 7**.[28]

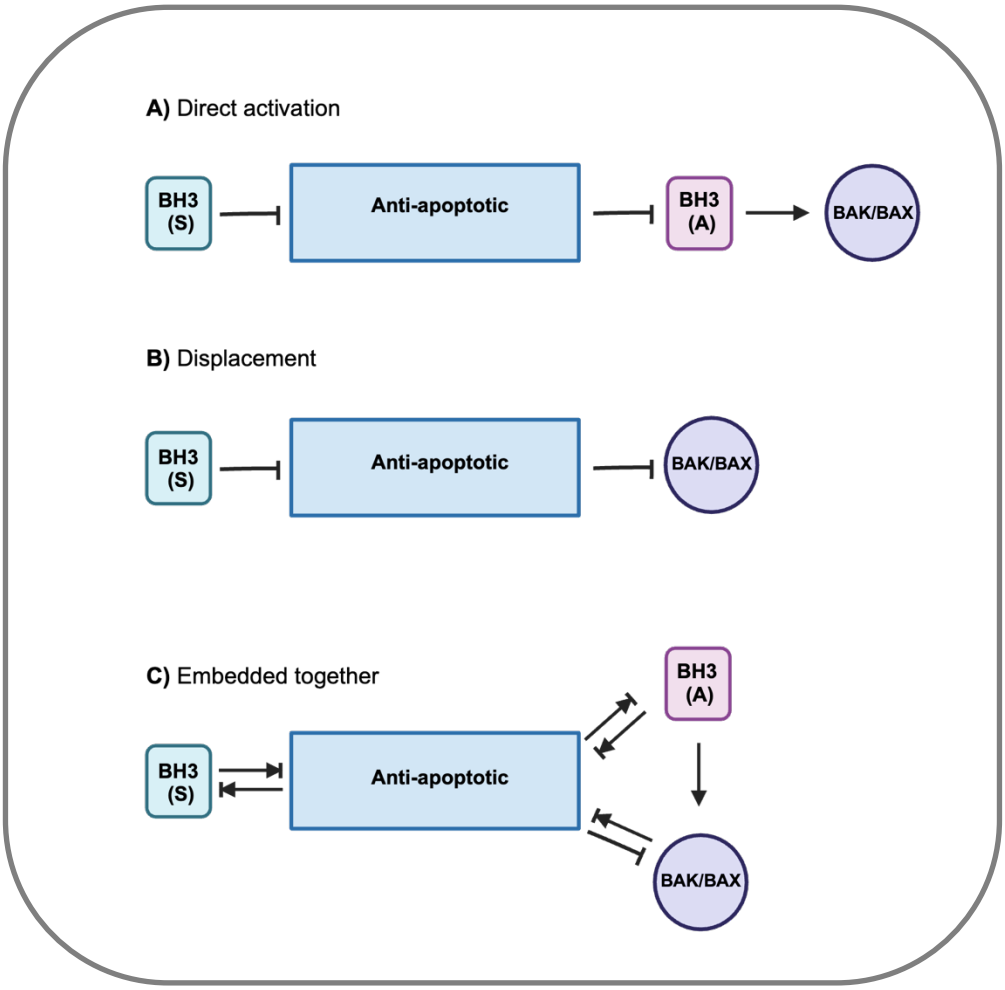


Figure 7: **a)** The direct activation model. **b)** The displacement model. **c)** The embedded together model. Figure adapted from Andrews *et al*.[28]

The direct activation model states that the BH3-only protein must bind directly to pro-apoptotic proteins BAK and BAX in order to activate them and promote MOMP.[28] Activators directly bind to and activate BAK and BAX, in contrast to sensitisers, which solely bind to the anti-apoptotic proteins. The anti-apoptotic proteins sequester the activators in order to inhibit MOMP; this can be impeded by the sensitisers binding to the anti-apoptotic proteins. The sensitisers compete with the activators, which can liberate them from the BH3 groove on the anti-apoptotic proteins, thus allowing them to initiate MOMP through BAK and BAX.[28] The displacement model stipulates that the BH3-only proteins do not bind to the pro-apoptotic BAK and BAX proteins directly. In this model BAK and BAX are constantly active leading to MOMP, and therefore must be supressed by anti-apoptotic proteins in order to preserve the cell. This occurs through the displacement of BAK and BAX from the BH3 binding groove by the BH3-only proteins.[28]

Once activated, BAK and BAX form homodimers which are symmetric in nature. They go on to oligomerise, evoking pore formation in the mitochondrial bilayer;[27] this leads to MOMP which is considered the point of no return.[29] The consequences of MOMP are the release of proteins from the intermembrane space into the cytoplasm; these proteins elicit strong caspase activity, which swiftly leads to cell death. For this rapid cell death to occur, a series of complex interactions takes place in the cell, as seen in **Figure 8**. Cytochrome *c* binds to the monomeric form of cytosolic Apaf-1, allowing it to undergo a conformational change and subsequently oligomerise.[29] Following this, the heptameric form of Apaf-1 engages Procaspase-9 in order to form an apoptosome. This results in the activation of caspase-9, which goes on to trigger the executioner caspases 3 and 7, via caspase-9-mediated cleavage. This is further facilitated by the inhibition of XIAP, a caspase inhibitor, via the activity of Smac and Omi when released through MOMP.[29] This intricate set of interactions eventually leads to the demise of the cell. Interestingly, MOMP can also result in cell death independent of caspase activity. This occurs by virtue of the slow loss of mitochondrial function and release of toxic mitochondrial proteins.[29]

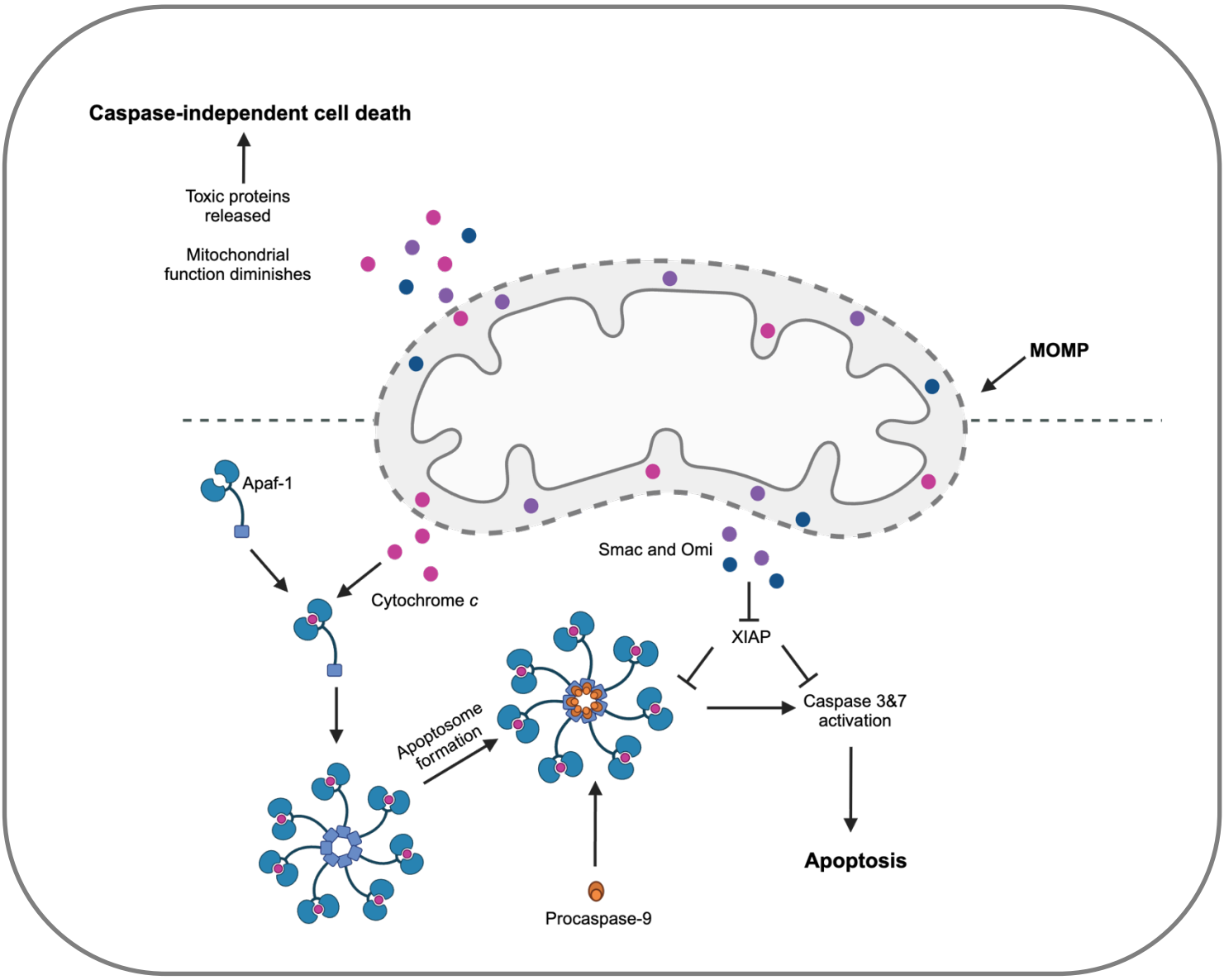


Figure 8: The caspase dependent and independent pathways leading to apoptosis. Figure adapted from Tait *et al*.[29]

1.3.2 BCL-X_L/BAK

The overexpression of anti-apoptotic proteins such as BCL-X_L is prevalent in multiple variants of cancer[30] including breast cancer,[31] glioma,[32] colorectal carcinoma[33] and chondrosarcoma.[34] BCL-X_L upregulation is linked to the maintenance and progression of tumours,[35] while also attaining resistance to apoptotic stimuli[31] and chemoresistance.[35]

The structure of human BCL-X_L was deduced through a combination of NMR and X-ray crystallography.[36, 37] BCL-X_L is comprised of eight α -helices, while also encompassing a large hydrophobic cleft generated via the BH1-3 domains. The primary helices involved in the formation of this large groove are α-3 and α-4, with α-5 forming the base.[36] This hydrophobic cleft is vital for facilitating interactions with the pro-apoptotic members of the BCL-2 family.[36]

A closer inspection of the BCL-X_L/BAK interaction reveals that a sixteen amino-acid long BAK sequence is the minimum sequence length required for binding to BCL-X_L; the residues involved are 72-87.[37] Alanine scanning mutagenesis was employed[37] in order to identify the key hot spot residues involved in the BCL-X_L/BAK PPI. The residues identified were Val^{74}, Leu^{78}, Ile^{81} and Ile^{85}.[37] These residues are orientated along one face of the BAK helix, as highlighted below in **Figure 9**.[36] The side chains of these residues are hydrophobic in nature and project into the hydrophobic groove of BCL-X_L.[37]

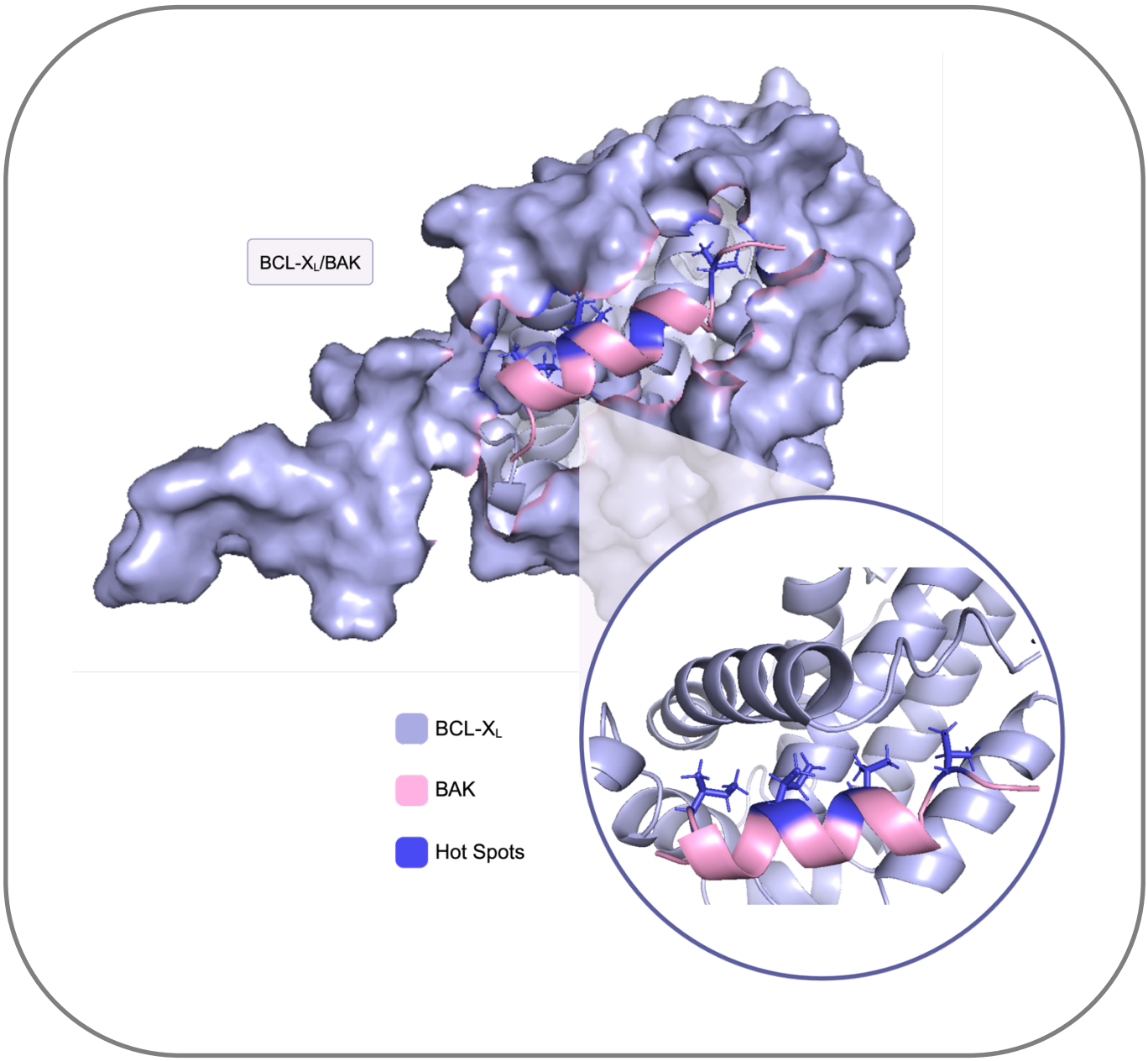


Figure 9: Crystal structure of the BCL-X_L/BAK PPI highlighting key interactions for binding. (PDB code 1BXL).

By virtue of anti-apoptotic proteins being overexpressed in cancerous cells, the identification of compounds that can inhibit their activity is a pressing need for the development of novel chemotherapeutics.[38] A prominent strategy to develop compounds that display this inhibitory activity is to target the BH3 binding site on anti-apoptotic proteins; this can be achieved by mimicking BH3-only proteins.[39]

There are several BH3 mimetics that are currently under clinical evaluation. ABT-737 was one of the primary BH3 mimetics developed;[40] this was identified via a high-throughput NMR screen,[40] combined with structure-based design.[39] This compound is a small-molecule inhibitor that targets multiple members of the BCL-2 family, including BCL-2 and BCL-X_L.[39] ABT-737 displayed efficacy in chronic lymphocytic leukaemia, as well as in small-cell lung cancer.[39] Unfortunately, the use of ABT-737 was marred by the fact that it has limited oral bioavailability and poor aqueous solubility.[35] The limiting pharmaceutical and physiochemical qualities of this compound restrict its ability to be used intravenously or in conjunction with other chemotherapeutics.[35]

The limitations of ABT-737 led to the development of ABT-263, commercially known as Navitoclax.[35] This is a potent analog of ABT-737 that is orally bioavailable and is able to trigger apoptosis within two hours after administration, by impeding the interactions between BCL-2/BCL-X_L and pro-apoptotic proteins.[35] However, the use of Navitoclax also has its caveats; it is associated with dose-dependent thrombocytopenia, due to it impeding the function of BCL-X_L.[39] As such, its clinical evaluation is primarily focused on its use in combination with other therapeutics[41] such as Ruxolitinib.[39]

A major breakthrough in the search for BCL-2 targeting mimetics came via the development of ABT-199, commercially known as Venetoclax.[42] This first-in-class potent BH3 mimetic is selective for BCL-2[42] and is able to bypass the majority of thrombocytopenia associated with Navitoclax.[39] This is the first BH3 mimetic to receive approval from the FDA and the European Commission; it is used clinically for the treatment of cancers such as chronic lymphocytic leukaemia[39] (CLL). A caveat associated with the use of Venetoclax is that resistance to its effects has emerged; this resistance mechanism is associated with the upregulation of BCL-X_L.[43] BCL-X_L can be used as a substitute for BCL-2 when the latter is sequestered by Venetoclax, which therefore circumvents the inhibition of BCL-2 and supresses the apoptosis pathway.[43]

Therefore, it is vital to develop a BCL-X_L specific inhibitor that is efficacious but doesn't lead to the thrombocytopenia associated with Navitoclax.[44] Till date there has not been a BCL-X_L specific inhibitor approved for clinical use.[39] This signifies the need to explore additional therapeutic avenues, such as peptide-based inhibitors, in addition to continuing the development of small molecule therapeutics.

1.4 Peptidic Inhibitors Targeting Protein-Protein Interactions

There are two distinct categories of drugs that have successfully received clinical approval and have been brought to market: small molecule and biologics. These two classes vary dramatically in molecular weight, with typical small molecules being below 500 Da and biologics being above 5000 Da (**Figure 10**).[45] As such, there is potential for a class of compounds to bridge this gap and advance both the scientific knowledge and therapeutic options for complex diseases. Peptides have emerged as a viable class of molecules that could be employed in this manner. Thus, a strategy extensively being explored to mediate PPIs is a peptidic approach. This approach aims to develop peptide-based inhibitors capable of targeting complex diseases including cancer and infection.[46]

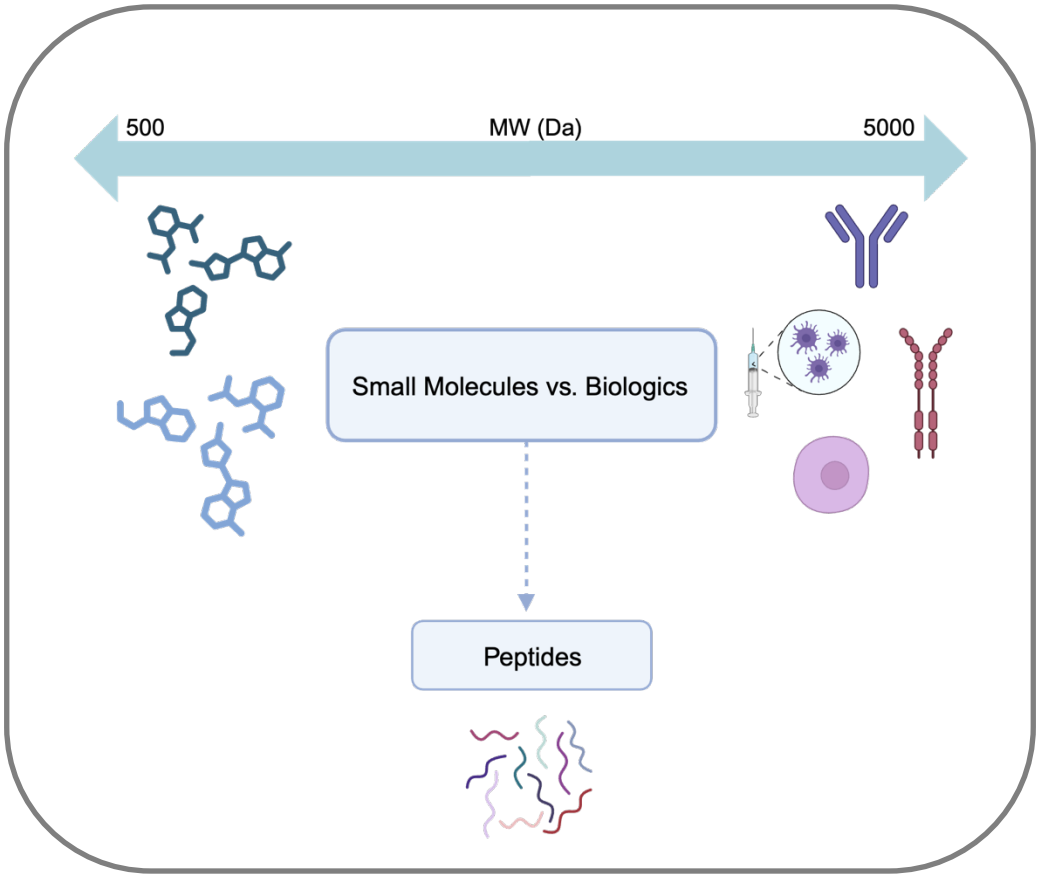


Figure 10: An illustration highlighting the potential for peptide therapeutics to bridge the gap between small molecules and biologics. Figure adapted from Craik *et al*.[45]

Peptides possess an array of qualities that make them desirable as therapeutic agents, such as exceptional target specificity,[45] well-defined mechanisms of action, low toxicity[46] and limited off target side effects.[45] They are also fairly straightforward to synthesise and allow a range of chemical diversity which can be incorporated into a native sequence.[47] However, there are a number of limitations associated with their use. Native peptides are restricted by poor oral bioavailability,[48] low cell membrane permeability[46] and a short plasma half-life due to proteolytic degradation.[48, 49] The short half-life effectively lowers the bioavailable concentration of the peptidic drug, requiring frequent dosing to maintain clinical efficacy.[49] Additionally, peptides that have a short linear structure can be plagued by a low conformational stability, which may lower binding affinity to the target.[47]

In spite of the limitations detailed above, the demand for peptide-based drugs is on the rise with global sales of over $70 billion reported in 2019 – a figure which is set to rise.[50] There are currently upwards of 170 peptides in active clinical development, with a great deal more undergoing preclinical evaluation.[50] As such, there is significant global drive associated with developing strategies towards improving the ADME properties of peptidic drugs, in order to continue the development of next generation therapeutics.[46] To decrease proteolytic susceptibility and enhance the stability of active conformations, two strategies are commonly employed; modifications of peptide backbones and cyclisations.[47]

1.4.1 Cyclisations

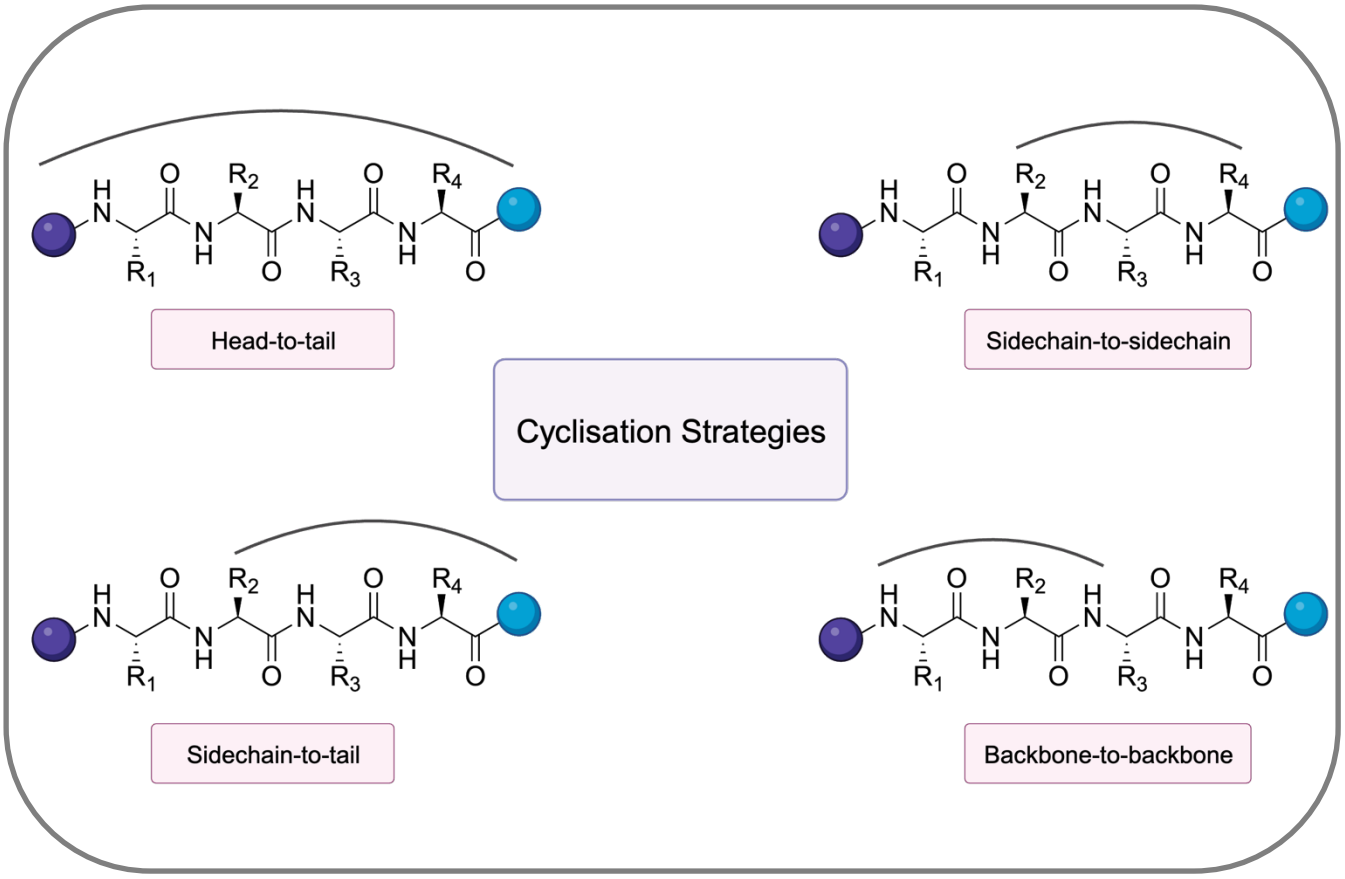


Figure 11:Common cyclisation strategies for the enhancement of peptide stability and proteolytic susceptibility. Strategies include head-to- tail cyclisation, backbone-to-backbone, sidechain-to-head/tail and sidechain-to-sidechain. Figure adapted from Wang *et al*.[56]

There are a plethora of peptide cyclisation strategies present in the literature, including head-to-tail cyclisation, sidechain-to-head/tail and sidechain-to-sidechain (**Figure 11**);[47] these approaches will be briefly discussed below.

1.4.1.1 Sidechain-to-head

Short α-helices are often susceptible to a high level of instability due to their organisation being subject to high energetic demands. A way to mitigate this is to pre-organise them, with cyclisation being a popular choice.[51] A widespread approach for sidechain-to-head cyclisation is the hydrogen bond surrogate strategy (HBS),[51] where peptides are artificially constrained in an α-helix conformation. This occurs by substituting the hydrogen bond, between the C=O and the NH of the *i* and *i* + *4* amino acid residues, with a covalent bond.[52] The covalent bond replacing the

native hydrogen bond is often of the C=X-Y-N nature where the X and Y originate from the *i* and *i + 4* residues, as demonstrated by the Arora group[51, 52] who successfully highlighted this approach through their ring-closing metathesis reaction using the Hoveyda-Grubbs catalyst[52] to form a stabilised α-helix, as shown in **Figure 12**.

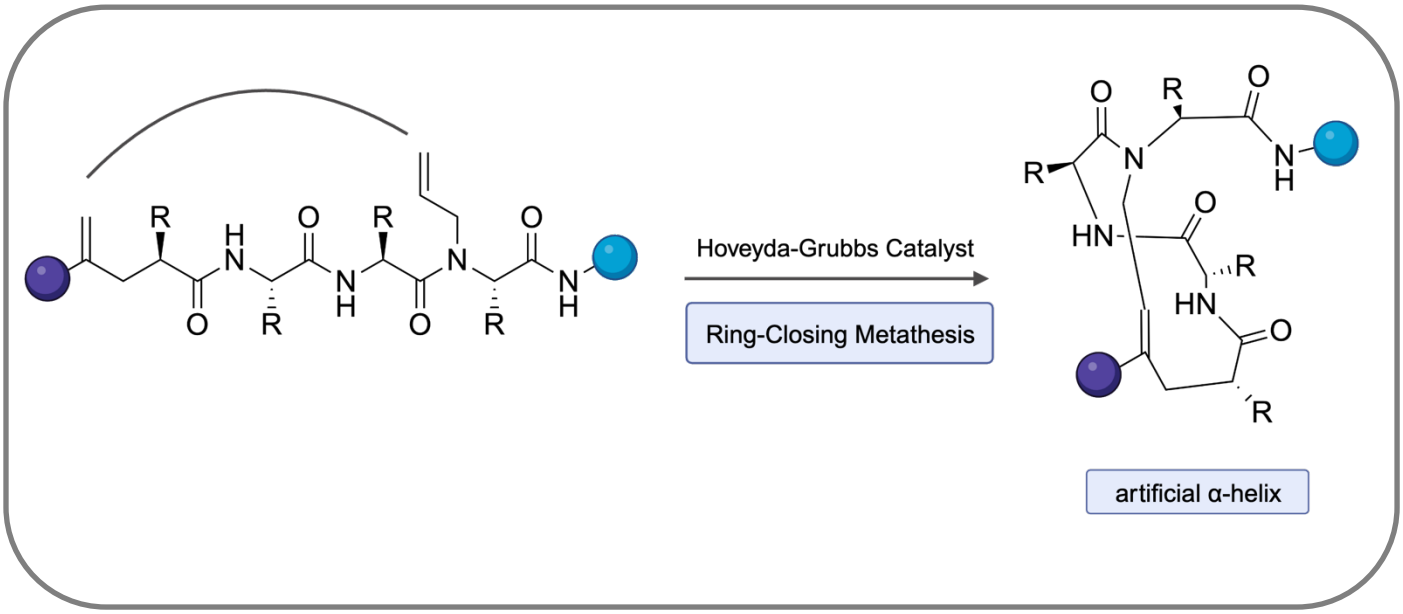


Figure 12: Ring-Closing Metathesis (RCM) cyclisation approach using the Hoveyda-Grubbs catalyst to generate a stable α-helix.[52]

1.4.1.2 Sidechain-to-sidechain

An established method for sidechain-to-sidechain cyclisation is through the stapling of amino acid residues present on the peptide.[47] This approach reinforces the α-helical nature of the peptide by linking sidechains that are orientated on the same face of the α-helix, such as residues *i, i + 4*, *i + 7* and *i + 11*.[53] These residues can include native amino acids such as Lys or Asp but are typically replaced with non-native amino acids that can be stapled together via their side chains.[53] There are various methodologies for peptide stapling including lactam formation, hydrocarbon stapling and disulfide bridges[47] as shown in **Figure 13**.

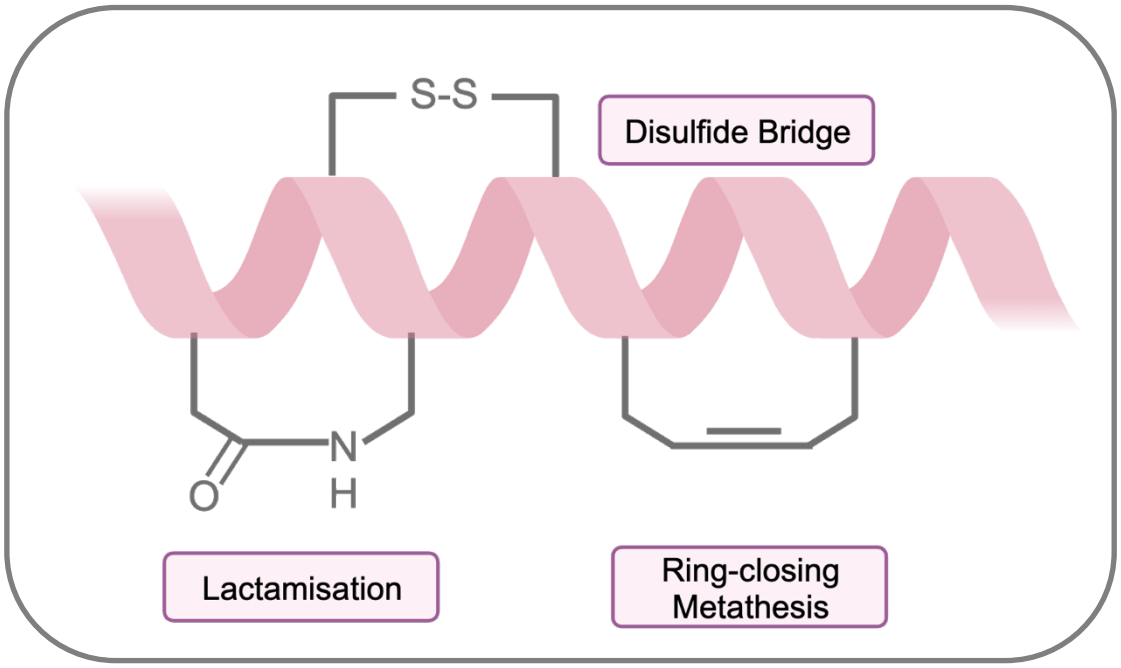


Figure 13: Different approaches for sidechain-to-sidechain cyclisation to reinforce the α-helical nature of the peptide. Figure inspired by Wang *et al*.[50]

A prominent example highlighting the advantages of the hydrocarbon stapling technique is the recent development of the cell permeating ALRN-6924 peptide.[54] This is a stapled α-helical peptide that mimics the transactivation domain of p53 in order to bind to MDM2 and MDMX with high affinity[54] (**Figure 14**).This is the first stapled α-helical peptide to undergo clinical evaluation, which showcases the potential of peptide stapling techniques to aid in the development of future therapeutics.

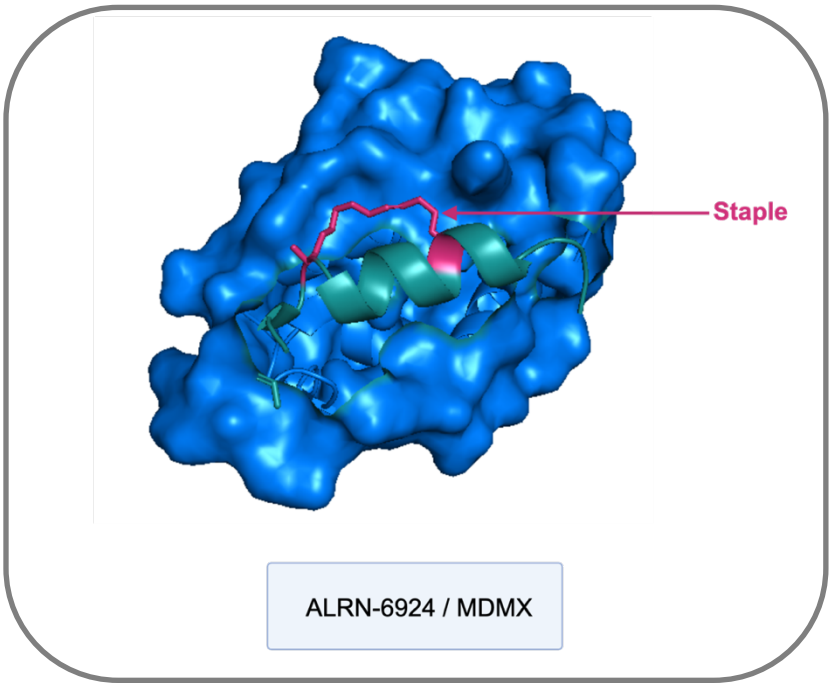


Figure 14:Crystal structure of the stapled ALRN-6924 helix bound to MDMX (PDB code 8GJS).

1.4.1.3 Head-to-tail

A cyclisation method that links the head and tail of a peptide is via the coupling of the N- and C-termini, leading to the formation of a β-hairpin.[47] The β-hairpin scaffold produced can be used to mimic epitopes of various secondary structures, including an α-helix. For example, Robinson *et al.* successfully designed a β-hairpin that was able to mimic the α-helical turn of p53 in order to inhibit the p53-HDM2 interaction.[55]

1.4.2 Backbone Modifications

Backbone modification is a strategy commonly used for the development of peptidic PPI inhibitors, where the focus predominantly lies in altering the main chain of the peptide.[56] The resulting peptides often differ to the native sequence more significantly[47] than through the use of the cyclisation techniques detailed above. Backbone modifications include extending the backbone itself, altering the stereochemistry and transferring sidechain functionality to nitrogen atoms.[47]

1.4.2.1 Stereochemical Variation

Altering the stereochemistry of a native peptide sequence is typically achieved via the insertion of D-amino acids into the sequence. D-amino acids possess higher resistance towards proteolytic degradation, as they are less likely to be cleaved by chiral proteases than their L-amino acid counterparts.[56] Pallerla *et al.* were able to successfully incorporate D-amino acids into a peptidomimetic targeting the HER2 and HER3 PPI, resulting in nanomolar IC_{50} values.[57] A caveat associated with the use of D-amino acids is that as they have the opposite stereochemistry to what is found in nature, they may not have the correct binding mode required to disrupt the PPI of interest.[47]

1.4.2.2 Shift of Sidechain Functionality

Peptoids are a class of peptidomimetics, also known as foldamers, where the sidechain traditionally attached to the α carbon, is now present on the backbone nitrogen (**Figure 15**). In essence peptoids are comprised of several repeating N-substituted glycine units.[47] They are able to successfully fold into helical conformations, thereby allowing inhibition of α-helix mediated PPIs. Peptoids are able to resist proteolytic cleavage to a high degree yet require careful design to position key residues in appropriate positions. This is due the loss of backbone derived hydrogen bonding,[47] which imparts a degree of flexibility greater than the native peptide. Appella *et al.* were able to effectively develop peptoid based inhibitors targeting the p53-HDM2 interaction, which displayed competitive binding to HDM2 in comparison with wild-type p53.[58]

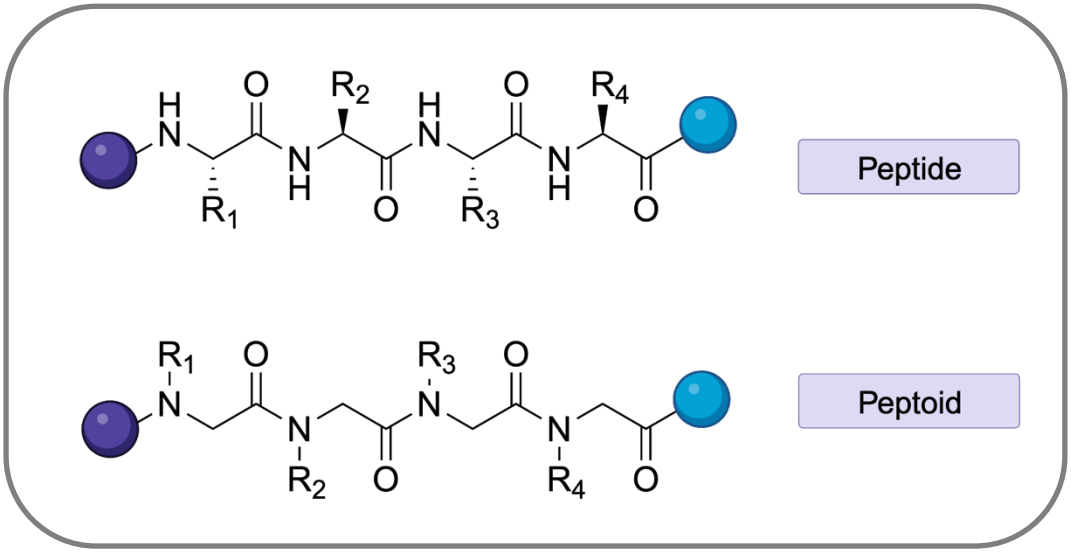


Figure 15:Structural difference between peptides and peptoids.

1.4.2.3 Extension of the Backbone

The use of β-amino acids to impart greater proteolytic stability and extend functionality of peptidic inhibitors is a popular strategy (**Figure 16**).[59] β-amino acids can either be used exclusively to build a peptide or can be used in conjunction with proteogenic α residues. β-peptides are classed as foldamers as they have a high propensity to form stable conformations when in solution.[47] Due to the presence of additional carbon atoms on the backbone and high conformational stability, peptides containing β-amino acids can be of a shorter length than the native sequence, yet attain a comparable degree of folding.[47] The Gellman group reported the development of a β-peptide that was able to successfully inhibit human cytomegalovirus (HCMV) infection, with IC_{50} value of approximately 30 μM.[60] They went on to develop a series of α/β-peptides capable of α-helix mimicry, to inhibit helix mediated PPIs.[61] These peptides were modelled on a stapled analogue of the BIM α-helix involved in apoptosis regulation. The α/β-peptides displayed the ability to bind to anti-apoptotic proteins in the BCL-2 family in a manner similar to the native BIM helix, but with increased proteolytic stability.

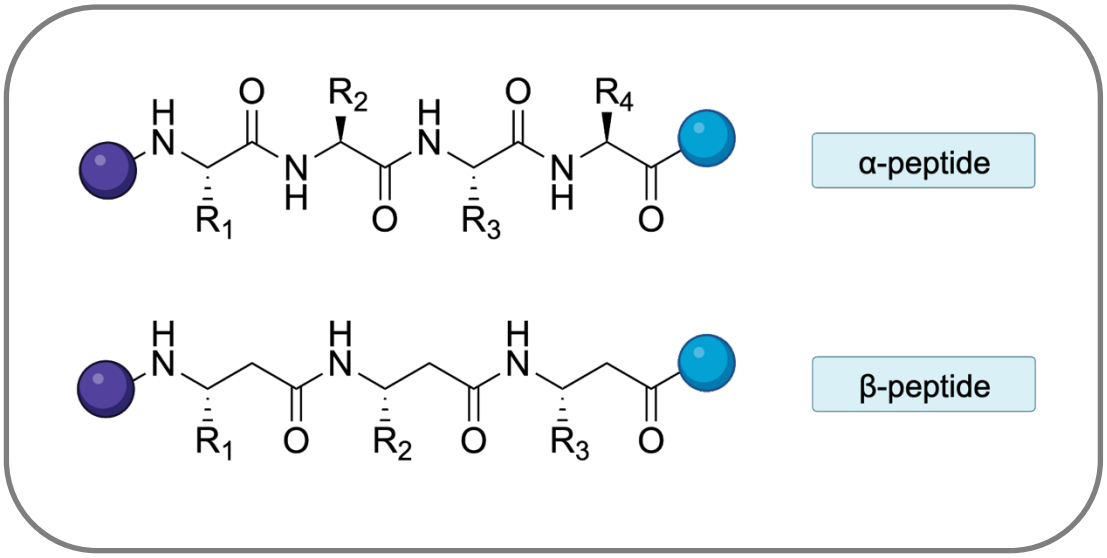


Figure 16: Structural difference between α and β peptides.

1.5 Proteomimetic Inhibitors Targeting Protein-Protein Interactions

An alternative class of PPI inhibitors that differs from the peptidic approach outlined in Section 1.4 are proteomimetics. A small-molecule based approach where a synthetic scaffold is designed, void of peptidic residues, that aims to inhibit PPIs via α-helix mimicry.[62] It is postulated that these synthetic mimetics function by replicating the spatial orientation of key recognition features belonging to the native helix; in contrast to recapitulating the conformation of the native helix itself.[5] The development of proteomimetic scaffolds has been subject to significant research efforts and scaffolds typically possess two defining features; a rigid scaffold to mimic the function and morphology of the native helical backbone, along with sidechains that project in a manner which effectively recapitulates the spatial orientation of key residues.[63]

The development of these non-natural scaffolds is particularly desirable, as in comparison to peptidic inhibitors they tend to have greater bioavailability and a higher resistance to proteolytic degradation, allowing for greater metabolic stability.[6] They also allow the possibility to incorporate a range of chemical diversity with the sidechains introduced, owing to the synthetic accessibility of several scaffold architectures. This can be exploited as a means to maximise interactions with the target of interest. A caveat associated with the proteomimetic approach is that the inhibitors developed may lack the selectivity associated with using the peptidic approach, where the inhibitor is often based on the native helix. The development of such artificial agents has led to the exploration of an array of scaffold structures, from single face helical mimicry to those mimicking multiple faces.

1.5.1 Mimetic Scaffolds

1.5.1.1 Terphenyls and its Derivatives

The development of the first scaffold capable of mimicking an α-helix was pioneered by the Hamilton group.[64] They reported on the synthesis and evaluation of trisubstituted 3,2′,2″-terphenyl derivatives (**Figure 17**) where the aryl backbone sits in a staggered conformation, as confirmed via X-ray crystallography. This allows the substituents at the 3,2',2'' positions to project in a manner that recapitulates the orientation of the *i*, *i* + *3(4)* and *i* + *7* positions on an α-helix.[64]

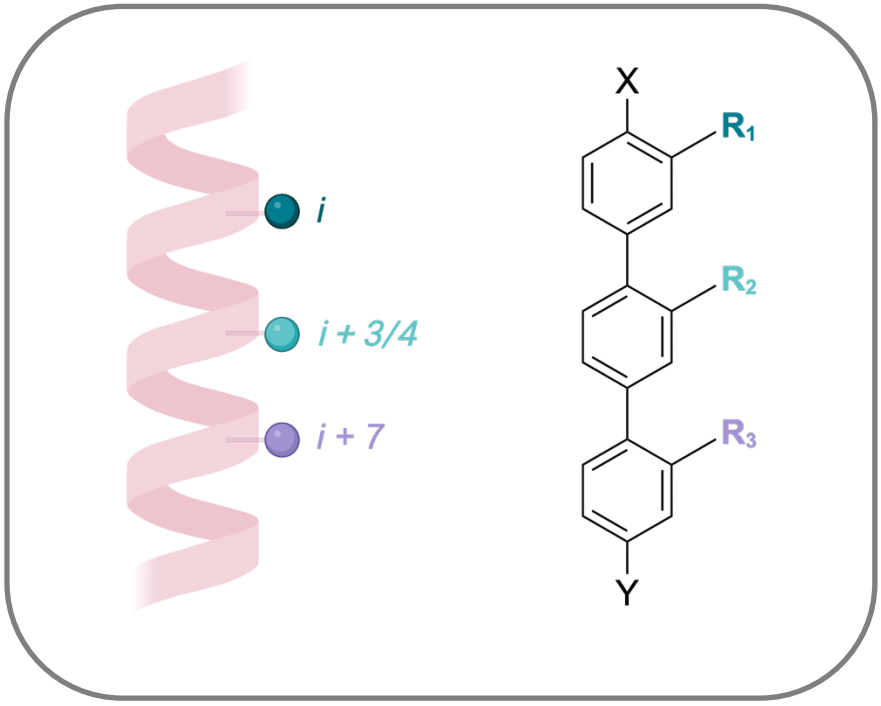


Figure 17:Left- an α-helix displaying the *i*, *i + 3(4)* and *i + 7* residues on a single face. Right – The structure of Hamilton's original terphenyl scaffold, highlighting how the sidechain residues correspond to key residues on the native α-helix.

The Hamilton group then proceeded to demonstrate how their novel terphenyl scaffold could be applied, by developing an inhibitor of the BCL-X_L/BAK PPI.[65] They developed a terphenyl based inhibitor where the substituents at the *ortho* positions contained alkyl groups to mimic the sidechains of the Val[74], Leu[78] and Ile[81] hot spots present on the native BAK α-helix[65] (**Figure 18a**). The carboxylic acid moiety on the scaffold was to mimic the ion pair interaction between the Asp[83] of BAK and a lysine residue of BCL-X_L.[65] The binding affinity of these mimetics were analysed through a fluorescence polarization competition assay, with a K_D of 114 nM observed.[65]

The use of terphenyl-based scaffolds is hindered by poor aqueous solubility, as a consequence of their extreme hydrophobic nature.[66] This, in conjunction with complex synthetic protocols, prompted the search for suitable alternative scaffolds that retain α-helix mimicry, but with improved physical properties. Once such scaffold identified by Hamilton *et al*. is the terephthalamide scaffold.[66] Within this scaffold, in place of the two phenyl rings either side of the central aryl ring, two functionalised carboxamide groups stand (**Figure 18b).** This allows the

scaffold to retain the planar geometry of the terphenyl, as a result of the restricted rotation of the amide bond, as well as the presence of an intramolecular hydrogen bond. The advantage of using this terephthalamide lies in its synthetic accessibility, void of harsh conditions, in addition to its vastly improved aqueous solubility compared to the terphenyls.[66] The terephthalamide mimetics produced by Hamilton *et al*. were able to successfully interfere with the BCL-X_L/BAK PPI, both *in vitro* and in HEK293 cell lines.[66]

The Hamilton group sought to further improve the aqueous solubility of α-helix mimetic scaffolds through the development of the 5-6-5 imidazole-phenyl- thiazole core[67] (**Figure 18c**). Within this novel scaffold, the two flanking aryl rings were replaced by five-membered heterocyclic rings, in a bid to increase the hydrophilicity of the scaffold. An inhibitor based on this scaffold displayed inhibitory activity against the Cdc42/Dbs PPI involved in cell cancer resistance, with a potency of 67 μM.[67] Scaffolds such as terphenyls and terephthalamides are aptly able to mimic interactions involving three key residues of the α-helix of interest, however many PPIs involve key contacts of more than three residues.[68] As such, a biphenyl 4,4'-dicarboxamide scaffold was developed with the ability to mimic the *i, i + 4, i+ 7,* and *i + 11* hot spot residues of an α-helix (**Figure 18d**).[68] Once again, the well-studied BCL-X_L/BAK PPI was used to test the efficacy of this scaffold, where K_i values of 1.8 μM were observed by fluorescence polarisation.[68] A diphenylindane based scaffold (**Figure 18e**) was also developed for the mimicry of the *i, i + 4, i + 7*, and *i + 11* hot spot residues of an α-helix.[69]

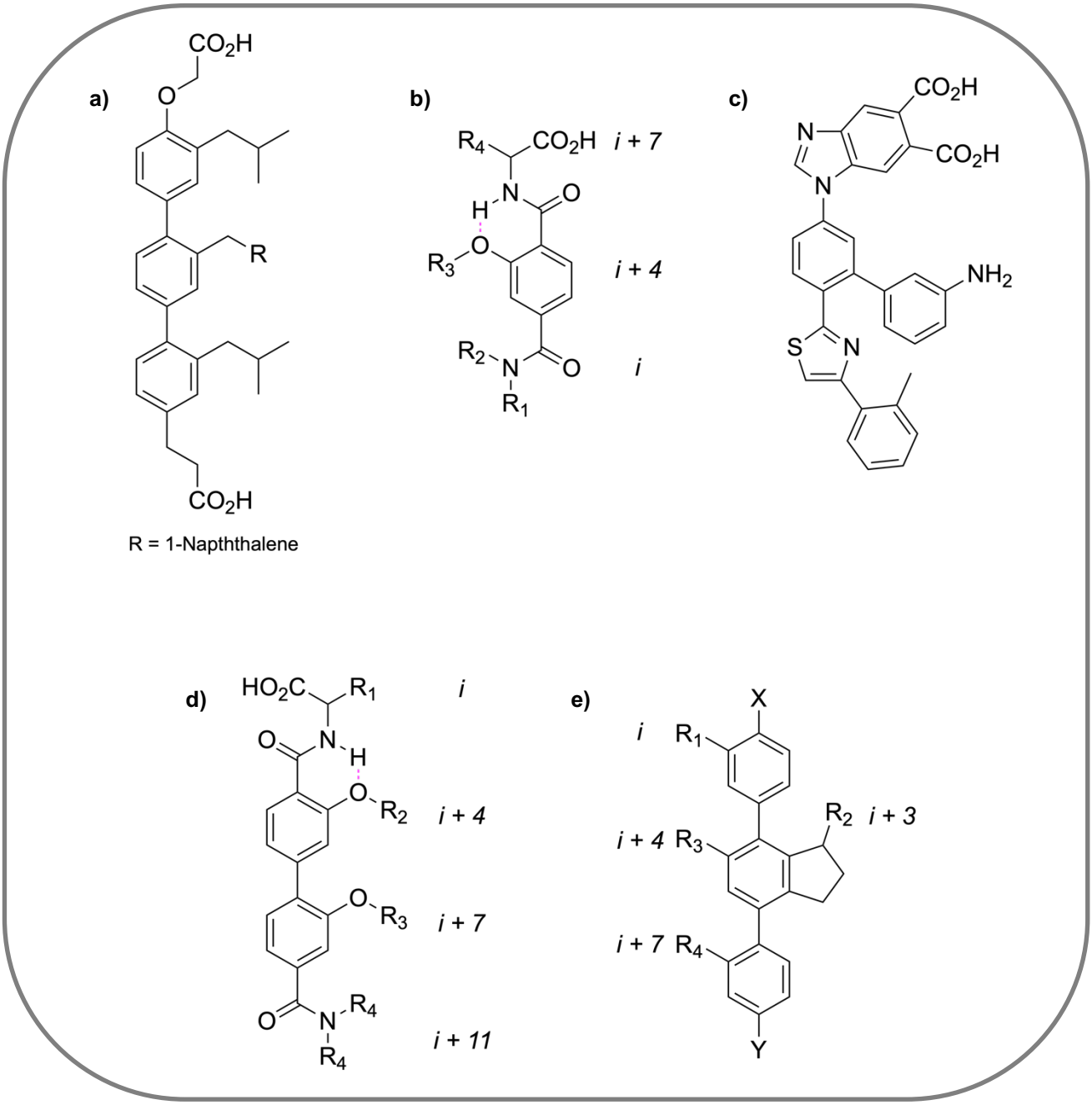


Figure 18: a) Hamilton's trisubstituted 3,2′,2″-terphenyl targeting the BCL-X_L/BAK PPI. **b)** terephthalamide scaffold. **c)** 5-6-5 imidazole-phenyl- thiazole scaffold. **d)** biphenyl 4,4'-dicarboxamide scaffold. **e)** diphenylindane scaffold.

1.5.1.2 Oligoamides

In a bid to increase the synthetic accessibility and aqueous solubility of α-helix mimetic architectures, significant research efforts have been devoted to oligoamide based scaffolds.[70] The Hamilton group were the first to report on this new class of proteomimetic scaffold, through the development of a novel oligoamide foldamer mimicking the BAK α-helix.[71] This tris-pyridylamide mimetic (**Figure 19a**) projects functionalised groups on one face of the scaffold; bifurcated intramolecular hydrogen bonds impart the required organisation to do so, through the creation of a rigid backbone. The tris-pyridylamide mimetics produced were able to bind to BCL-X_L with low micromolar affinity, effectively inhibiting the BCL-X_L/BAK PPI.

A second subclass of oligoamide-based scaffolds is the O-alkylated oligobenzamide scaffold. Ahn *et al.*[72] reported on the development of a benzamide based mimetic (**Figure 19b**), where placement of the sidechains aptly mimics the *i, i + 4* and *i + 7* residues of an α-helix. The tris-benzamide mimetic, in comparison to the tris-pyridylamide scaffold, retains a higher degree of conformational flexibility as it is void of the hydrogen bond between the nitrogen on the aryl ring and an amide proton . This lack of a bifurcated bond on the benzamide backbone allows for the possibility of the mimetic dynamically interacting with the target protein, whilst maintaining a degree of pre-organisation.[72]

The Wilson group[73] outlined a modular synthetic approach to 3-O-alkylated oligobenzamides. The synthetic route developed by this group utilises monomeric building blocks, where the key amine and carboxylate moieties are *para* to each other, allowing the eventual formation of the scaffold backbone. This is formed via the sequential coupling of said building blocks, which are pre-functionalised with the required sidechains via alkylation of the hydroxyl group *ortho* to the masked amine.[73] This class of scaffold achieves a degree of pre-organisation through the fixed rotation about the Ar-NH intramolecular hydrogen bond, while allowing free rotation about the Ar-CO bond.[74] The Wilson group further developed their use of 3-O-alkylated oligobenzamides by generating a low μM inhibitor (IC_{50} 1.0 μM) of the p53/HDM2 interaction.[74] This mimetic contains sidechain residues that suitably mimic the key Phe19, Trp23 and Leu26 residues involved in the PPI. 2-O-alkylated analogue scaffolds developed by the group[75] showed lower backbone curvature, on account of 6 membered intramolecular hydrogen bonding compared to 5-membered bonding, yet this difference had minimal impact on binding affinities to HDM2 (**Figure 19c**).

The Wilson group extended their research efforts into oligoamide-derived scaffolds through the synthesis and evaluation of N-alkylated oligoamide α-helix mimetics.[76] Their efforts led to the development of a solid-phase synthetic route to generate the desired oligoamides. This methodology was based on classical peptide-based protection strategies, as well as the corresponding solid-phase synthetic protocols. The monomers of interest were N-Fmoc protected, aligning with the standard Fmoc/^{t}Bu protection strategy used for solid-phase peptide synthesis (SPPS). These monomers were also furnished with the necessary sidechains to mimic the α-helix of interest, resulting in Fmoc protected N-alkylated monomers[76] (**Figure 19d**).

Wilson *et al.*[62, 77] employed this protocol to synthesise a library of N-alkylated oligoamide mimetics. The library generated aimed to target the p53/HDM2 PPI, with the sidechains tailored to mimic the key residues involved. Mimetics from this library were able to successfully inhibit the p53/HDM2 PPI, with low μM IC_{50} values reported. Interestingly when the same library of mimetics was trialled against the MCL-1/NOXA-B PPI, select oligoamides were also able to demonstrate binding affinity towards MCL-1. This highlights the possibility of developing a dual HDM2/MCL-1 inhibitor[62] as a potential chemotherapeutic agent.

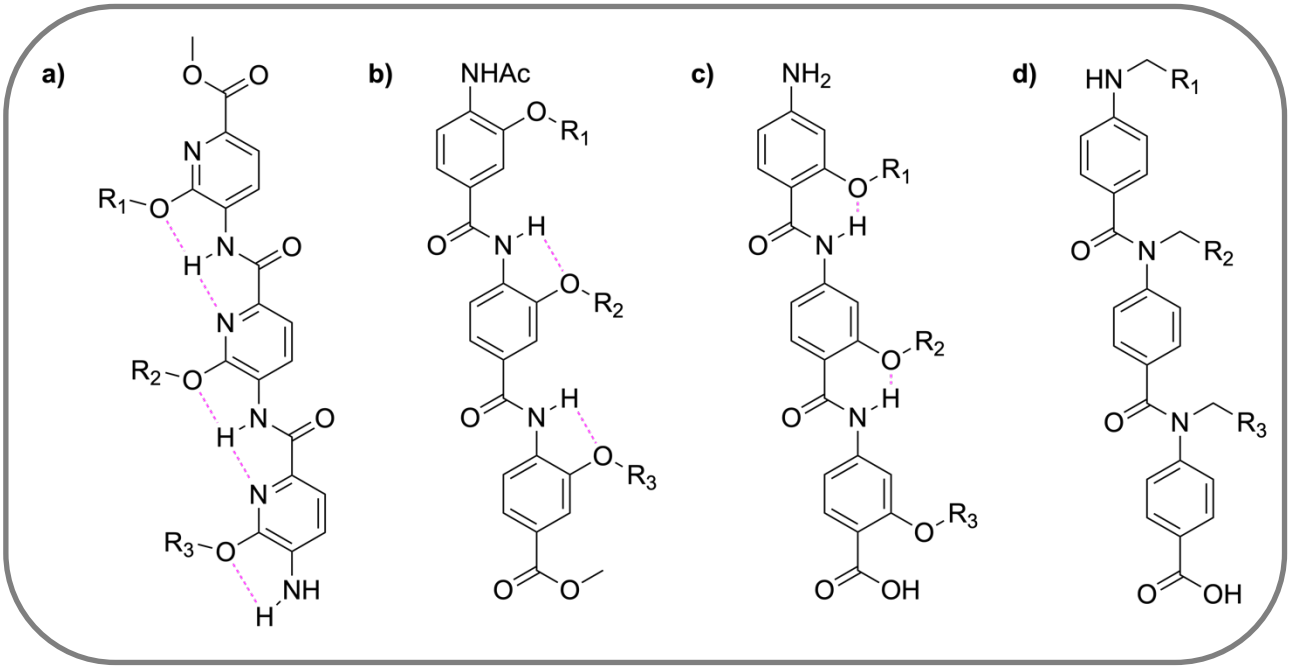


Figure 19: a) oligoamide based scaffold with a bifurcated intramolecular hydrogen bond. **b)** 3-O-alkylated oligobenzamides. **c)** 2-O-alkylated oligobenzamide scaffold. **d)** N-alkylated oligoamide.

1.6 High-Throughput Strategies

The discovery of novel therapeutics, for various drug targets, is often aided by the use of high-throughput screens. The development of PPI inhibitors, however, is one class that lags behind in the use of such screens and could therefore benefit by exploiting this technique, in order to identify potential drug candidates.

1.6.1 General Overview

High-throughput screening (HTS) is a fundamental strategy employed in drug discovery campaigns, providing starting points for the development of therapeutic agents,[78] in an effort to aid the typically lengthy and arduous drug development process. This approach entails screening a vast fragment library against a biological target with the goal of identifying bioactive compounds; techniques such as automation and assay miniaturisation are harnessed during this process.[79]

Compound libraries utilised are of a substantial size, often ranging from 10^4-10^6 fragments;[78] this is in stark contrast to helix mimetic libraries which are significantly smaller. These libraries are comprised of fragments that adhere to general principles associated with 'drug-likeness', whereby factors such as hydrophobicity, toxicity and molecular mass are taken into consideration.[78] Screening these sizable compound libraries necessitates extensive data analysis, in order to identify hit fragments displaying activity against the target of interest. Upon completion of a primary screen resultant hits are confirmed and validated, prior to lead optimisation. With the widespread integration of HTS approaches, it remains crucial that an acceptable balance between quality and quantity is retained. Key parameters to be considered are time, cost and quality – the so called 'magic triangle' [79] (**Figure 20**).

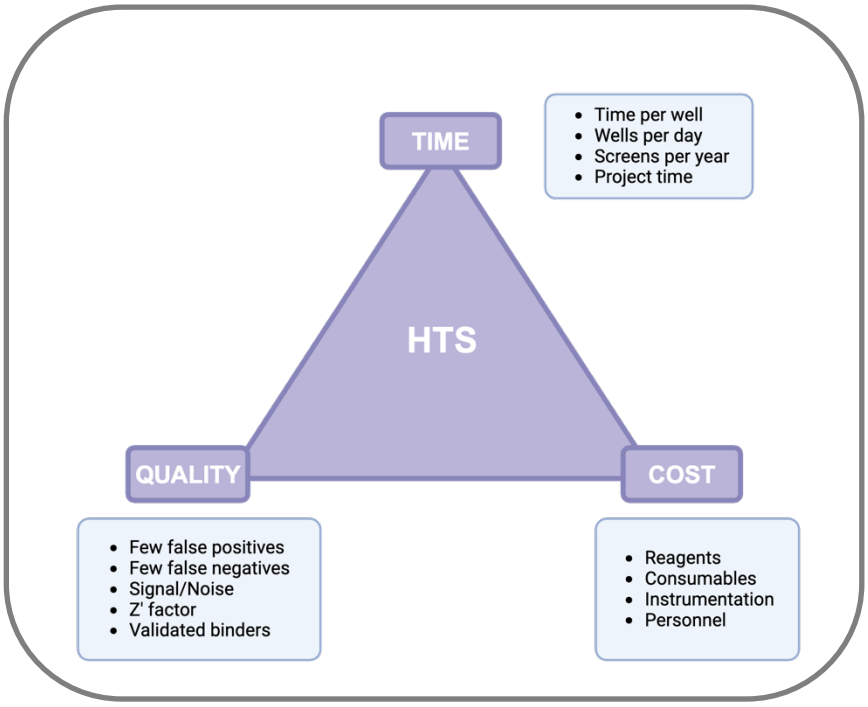


Figure 20: The 'magic triangle' highlighting key parameters for a successful HTS campaign.

This triangle encapsulates the link between key screening parameters, which when balanced results in successful lead discovery.[79] It serves as a reminder that in the pursuit of increased assay throughput, the effect on the entire HTS campaign must be taken into consideration. In modern day HTS campaigns the initial screen represents a fraction of the overall timeframe, with respect to lead generation. The development of assays, data analysis and subsequent hit validation constitute the majority of the overall HTS project. Thus, factors such as time taken to run and process screens, the cost of running the campaign and the quality of data produced must be continually evaluated. This in turn results in an increased likelihood of developing promising clinical candidates.[79]

Although the employment of HTS campaigns in the field of PPI drug discovery has lagged behind in comparison to its use in classical drug discovery approaches,[2] it has had some success with respect to the discovery of small molecule PPI inhibitors. Vassilev *et al.*[80] successfully employed a HTS approach to identify a series of compounds, termed Nutlins, that displayed inhibitory activity against the p53/MDM2 PPI. These small molecule inhibitors functioned by mimicking the p53 helix, through which they were able to bind to MDM2 and inhibit the native p53/MDM2 interaction. This discovery is an example of the potential that HTS campaigns have when exploited in the context of PPIs. Subjecting this HTS approach to extensive development is required in order to develop efficacious PPI inhibitors. Specifically, for PPIs it is imperative that

this development includes screening campaigns comprised of diverse compounds, such as peptidic candidates, in addition to small molecules, with the potential to inhibit various classes of PPIs.

1.6.2 Activity-Directed Synthesis

Activity-directed synthesis (ADS) is a screening approach where biological activity takes precedence over structural identity;[81] an approach that has been harnessed for the development of PPI inhibitors. This unique approach exploits the use of reactive fragments which rapidly generate a diverse library of compounds, covering a large chemical space. The reactive fragments employed in this approach are selected such that multiple products may be formed, the structures of which are not further elucidated unless biological activity is observed (**Figure 21**).

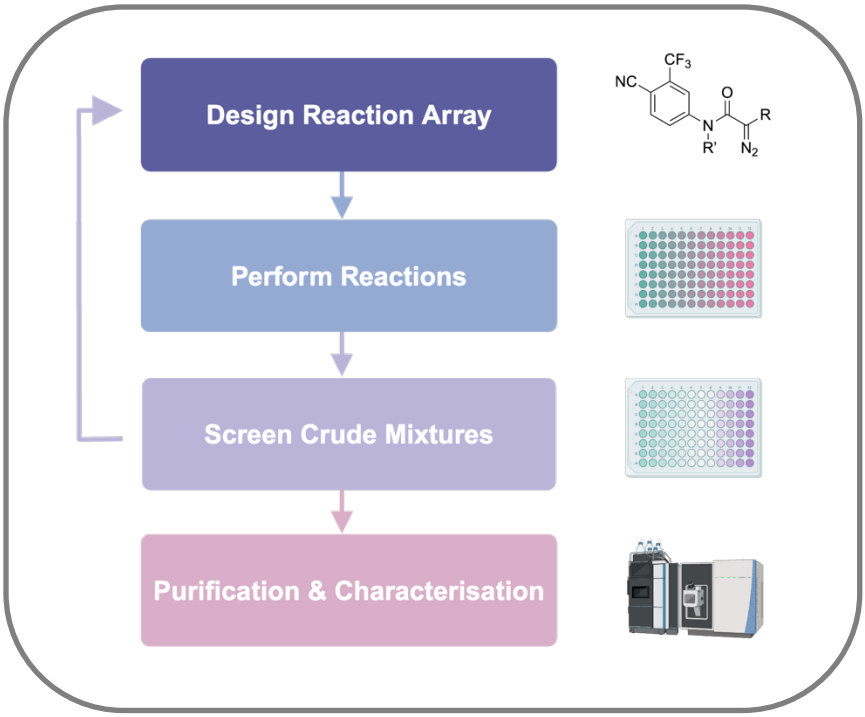


Figure 21: An overview of the ADS based approach.

As highlighted in **Figure 21**, ADS is designed in a manner by which multiple reaction products are formed in parallel, with the resultant crude mixtures subsequently evaluated in a biological setting. Hit reactions comprising of bioactive products are scaled up prior to further characterisation and structural identification.[82] Harnessing the ability of reactive fragments to simultaneously form a

diverse array of products allows a large chemical space to be rapidly explored. The activity-driven foundation upon which ADS was developed, allows it to circumvent the restrictions placed on conventional HTS approaches, where large libraries of compounds are equally investigated regardless of biological functionality.

This ADS based approach was developed by Nelson *et al* [81] and employed in the discovery of androgen receptor (AR) modulators. Promising bioactive ligands were derived from scaffolds void of pre-existing activity against androgen receptors, highlighting the merits of exploring a diverse chemical space. The reagents utilised in primary screen comprised of various diazo amides in conjunction with rhodium-based catalysts, to generate a mixture of crude products. The hit product mixtures went on to inform the secondary screen, which in turn informed the final screen. The hit mixtures were subsequently purified, allowing the structure of the bioactive ligands to be deduced. This led to the identification of three ligands displaying sub-micromolar activity modulation of AR (**Figure 22**).[81]

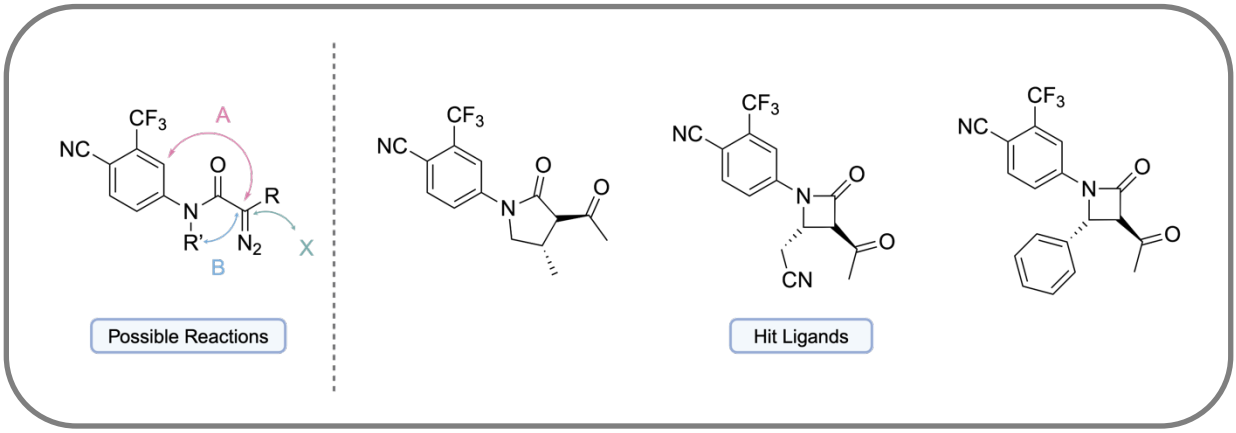


Figure 22: Left) Possible intramolecular/intermolecular reactions. Right) Hit ligands identified through ADS.

Nelson *et al* also employed the ADS approach to generate inhibitors of the p53/hDM2 PPI.[83] The reactive fragment library was comprised of various diazo substrates and co-substrates; these contained functional groups that either previously displayed mimicry of p53 hot spots or had the potential to. Upon reaction, in the presence of rhodium-based catalysts, a large library of crude product mixtures was generated. These were subsequently evaluated through fluorescence anisotropy against a fluorogenic p53 tracer, in the presence of hDM2. The resultant hit mixtures informed the secondary screen, where ultimately four novel scaffolds were identified in parallel, displaying inhibitory activity against the p53/hDM2 PPI (**Figure 23**).

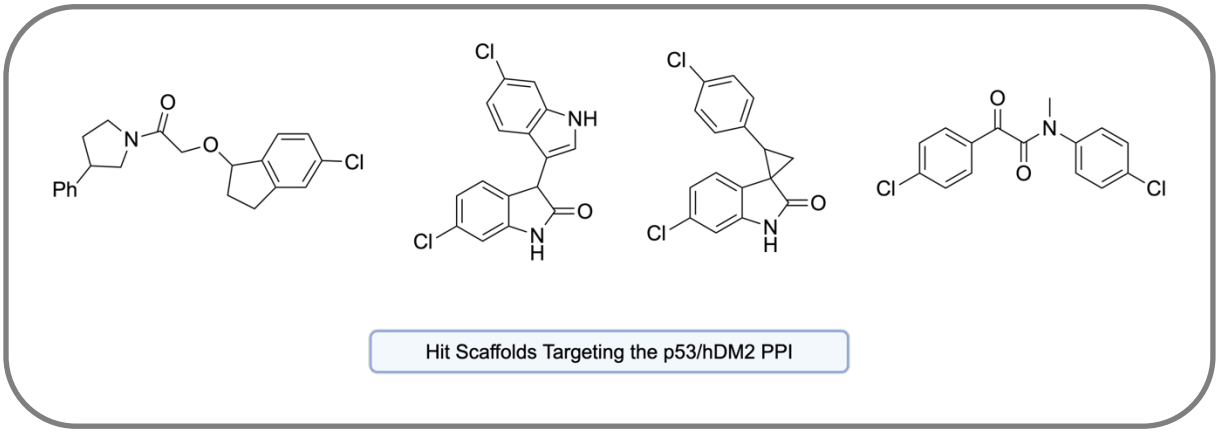


Figure 23:Hit scaffolds targeting the p53/hDM2 PPI identified through ADS.

Ultimately, compared to conventional high-throughput approaches, an ADS based strategy allows an extended chemical space to be rapidly explored, whilst remaining less resource intensive.

1.7 Target-Guided Synthesis

The developmental process behind the production of novel therapeutic agents is often expensive, lengthy and arduous. Consequently, over the past 20 years there has been a paradigm shift in drug discovery campaigns, where novel strategies are being developed to generate clinical candidates with greater relevancy to the biological target, whilst streamlining the process such that it is less time and financially intensive.[84]

One such strategy is referred to as target-guided synthesis (TGS), in which the target itself assembles bioactive ligands when complexed with a pool of reactive fragments.[85] This strategy is broken down into two concepts that are distinguishable by the factor in which the process is governed by. The strategy under thermodynamic control, also referred to as a dynamic combinatorial process, takes places whereby ligands are assembled reversibly favouring the thermodynamically preferred ligand; a prominent reaction employed for this purpose is the reversible formation of hydrazones.[86] The often preferred approach however is referred to as kinetic TGS (KTGS), where the biological target accelerates an irreversible covalent bond formation between the best reactive fragments for each respective binding site, as depicted in **Figure 24**.[84]

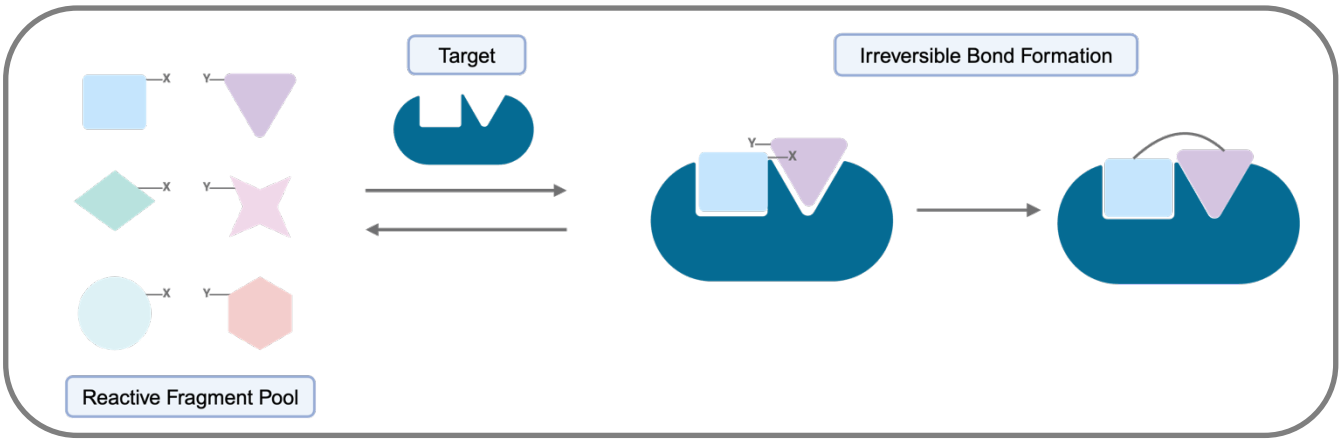


Figure 24: An overview of the kinetic target-guided synthesis (KTGS) strategy, where the formation of an irreversible covalent bond is accelerated by the target of interest.

The irreversible bond formation between complementary reactive fragments occurs when said fragments are in close proximity and the resultant product has a clear affinity for the target. As such this bond formation is considered to be a biologically accelerated process, where the target behaves as a catalyst;[87] the difference in the rate of reaction, between when the target is present

or absent, should clearly demonstrate this.[84] Ultimately, employing this KTGS strategy results in the formation of a potent bioactive ligand with high target selectivity. As fragments are combined *in situ*, the KTGS strategy bypasses the need for an extensive compound library comprised of purified ligands,[85] with hit dimeric ligands analysed directly via analytical methods such as LCMS.[87, 88]

Enzymes are the biological target class which KTGS strategies have primarily been applied to,[85] with one of the most notable examples highlighted by Sharpless *et al* .[89] Sharpless *et al* exploited the azide-alkyne cycloaddition, pioneered by Huisgen,[90] to develop a triazole-linked dimeric ligand against acetylcholinesterase (AChE) – a known drug target for the treatment of Alzheimer's disease.[84] AChE was employed as a biological target in an effort to validate the use of azide-alkyne *in situ* click chemistry, in the context of KTGS based strategies.[84] This 1,3-dipolar cycloaddition produced a 1,2,3-triazole linker, connecting the large peripheral active site to the deeper catalytic site on AChE.[89] The biorthogonality of the azide/alkyne functional groups allowed them to be employed for the development of AChE inhibitors under physiological conditions.[89]

Sharpless *et al* also sought to develop an inhibitor of HIV-1 protease – a prominent target involved in viral replication.[91] The role of the enzyme in the assembly of its own inhibitors was elucidated through the evaluation of triazole formation in the presence of a known HIV-1 protease ligand. The addition of this known active site ligand, in the presence HIV-1 protease, supressed the previously accelerated product formation. This clearly demonstrated that the enzyme itself was vital for ligand self-assembly, through biological acceleration.[91]

A recent example highlighting the merits of enzymes templating was reported by Soellner *et al*.[92] In place of traditional *in situ* azide-alkyne click chemistry, a thiol-acrylamide Michael addition was exploited to identify a bivalent kinase inhibitor targeting c-Src - a kinase implicated in cancer metastasis. A known inhibitor was furnished with a thiol and incubated with a library of acrylamide fragments, with the use of acrylamides particularly attractive owing to their low intrinsic reactivity. From this screen four hit fragments were identified that displayed a significant increase in enzyme inhibition when the thiol functionalised ligand was present. This screen thus identified bivalent ligands displaying activity against c-Src, by harnessing the reactivity between thiols and acrylamides.[92]

KTGS is a powerful tool by which bioactive ligands are generated using the biological target itself. Although this strategy has primarily been applied to various enzymes, recent examples have

demonstrated how it could be employed to target PPIs. Manetsch *et al* [93] reported on a KTGS approach, via sulfo-click chemistry, whereby they were able to successfully identify PPI modulators targeting both BCL-X_L and MCL-1. This example showcases the merits of applying KTGS based strategies in the context of PPIs and how it could lead to the identification of potent inhibitors with high target selectivity. This would in turn aid the drug discovery process, in the pursuit of generating strong clinical candidates. Diversifying KTGS strategies by expanding the repertoire of tools used to link fragments, as well as exploring alternative methods to detect biological acceleration will also aid in this search.

1.8 Project Aims

1.8.1 Perspectives and Proposed Approach

Although a sizeable array of α-helix mimetic scaffolds have been reported in the literature,[5] there is often an absence of chemical diversity found in relation to the groups mimicking key hot spot residues. For proteomimetic scaffolds, this is through the use of groups at each helical turn which often closely mimic the side chains of the hot spots found in the native helix. This is in contrast to expanding the functionality of said groups, to potentially exploit further interactions with the target protein. Moreover, these side chains are often introduced early on in the synthetic pathway, typically requiring a different monomer to be generated for each side chain as illustrated by Wilson *et al*.[76] This thereby limits the ability of such helix mimetic libraries to cover a large chemical space. Similarly, for peptidomimetic mimetics, often the focus lies on increasing the ADME properties of the mimetic verses diversifying the peptidic sequence by substituting proteogenic amino acids for non-natural residues. Additionally, high-throughput approaches typically used in drug discovery campaigns have not been extensively developed in the context of PPIs. As such, the exploitation of a high-throughput based approach for PPIs would accelerate the development of diverse inhibitors, covering a large chemical space.

Thus, the primary objective of this thesis is to report on the development of a novel target-directed route for the synthesis of a diverse α-helix mimetic library. A two-pronged approach to this objective was taken, whereby in parallel both a peptidic and a hybrid mimetic route was developed as illustrated in **Figure 25**.

The peptidic pathway discussed in Chapter 2, was designed in a manner that would allow the tunability of the scaffold towards a variety of α-helix mediated PPIs, whilst exploiting the natural selectivity of the native helix towards the protein of interest. For the development of this concept the model PPI chosen was the BCL-X_L/BAK PPI, whereby retaining segments of the BAK sequence, only those fragments within an electrophilic library which associate with BCL-X_L, will be preferentially incorporated into the mimetic. The hot spot residues on the WT BAK sequence would be substituted with cysteine residues, which when screened with an electrophilic library in the presence of BCL-X_L, would generate potent inhibitors with high target specificity. This peptidic pathway would then serve to inform the parallel hybrid pathway.

The hybrid approach follows suit to the peptidic approach, with respect to the retention of the BAK sequence. The primary difference, however, is that the hot spot residues are replaced with a synthetic monomer, as opposed to a cysteine residue. Thus, this hybrid scaffold would contain both peptidic and non-peptidic elements and would be achieved through the systematic replacement of peptide segments with a non-natural monomer, functionalised with a 'clickable' handle. This hybrid mimetic approach was inspired by the work of Burslem *et al.*,[94] where they successfully presented the first known example of a functional peptide-helix hybrid mimetic, by replacing sequences of a peptide with a suitable topographical mimic. Recently Wilson *et al* [95] applied a hybrid-based strategy towards the development of inhibitors against β-sheet mediated PPIs, using GKAP/SHANK1 PDZ as the model PPI. Peptide-fragment hybrid ligands were successfully identified that displayed inhibitory activity against the GKAP/SHANK1 PDZ, through competitive binding with SHANK1 PDZ. Chapter 3 details the approach to the hybrid mimetic pathway, as well as the way in which it could be further explored.

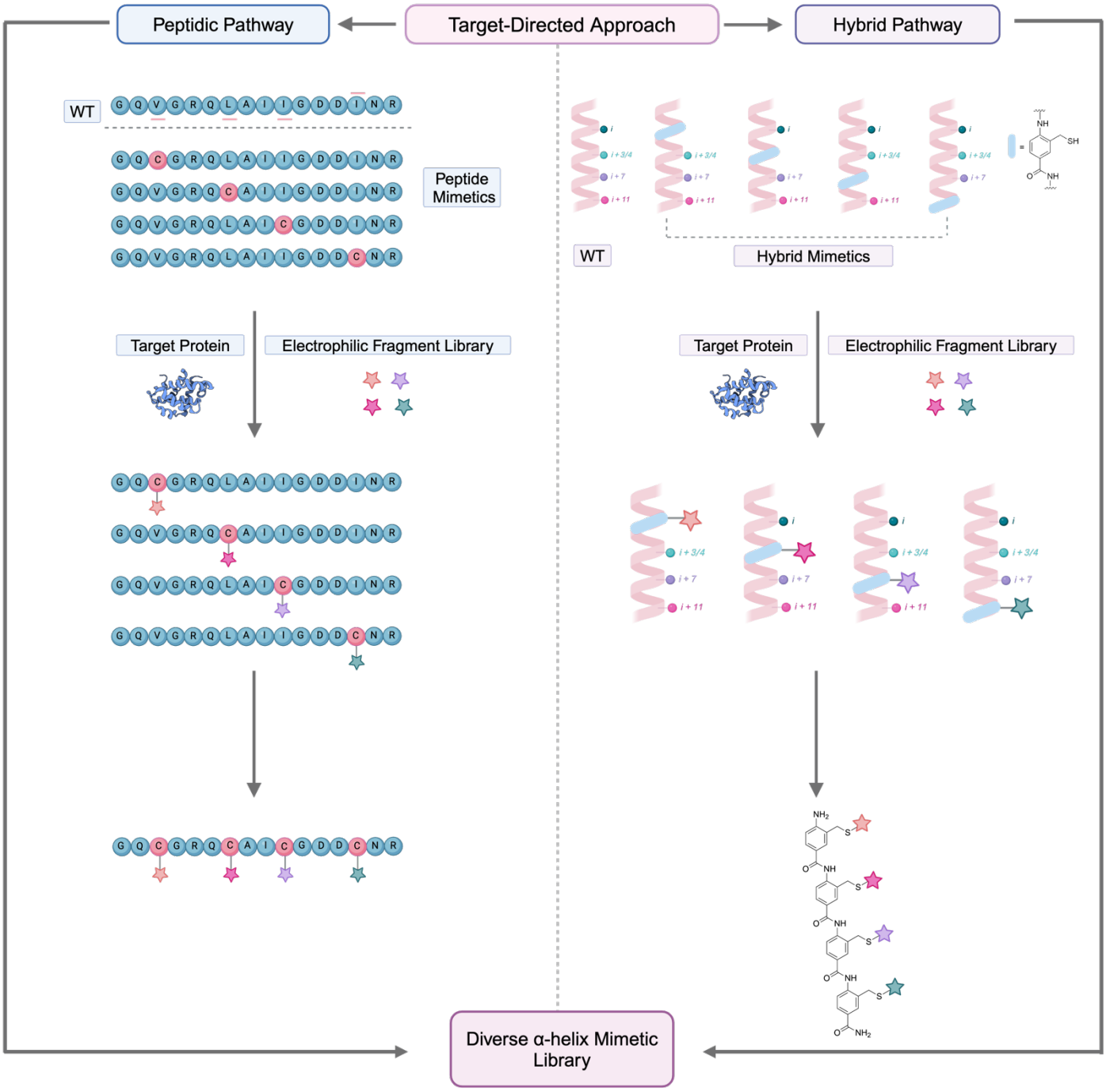


Figure 25: Two-pronged approach for the development of inhibitors for the BCL-X_L/BAK PPI.

1.8.2 Quantitative Irreversible Tethering (qIT)

In order to successfully monitor the target-directed approach within the BCL-X_L/BAK PPI, the use of a thiol quantification method is fundamental. Quantitative irreversible tethering (qIT) is a screening method established by Craven *et al* [96] founded on the principles of fluorogenic thiol quantification. This assay enables the progress of a reaction to be monitored, through the detection of residual thiol concentration at various timepoints, as highlighted below in **Figure 26**.

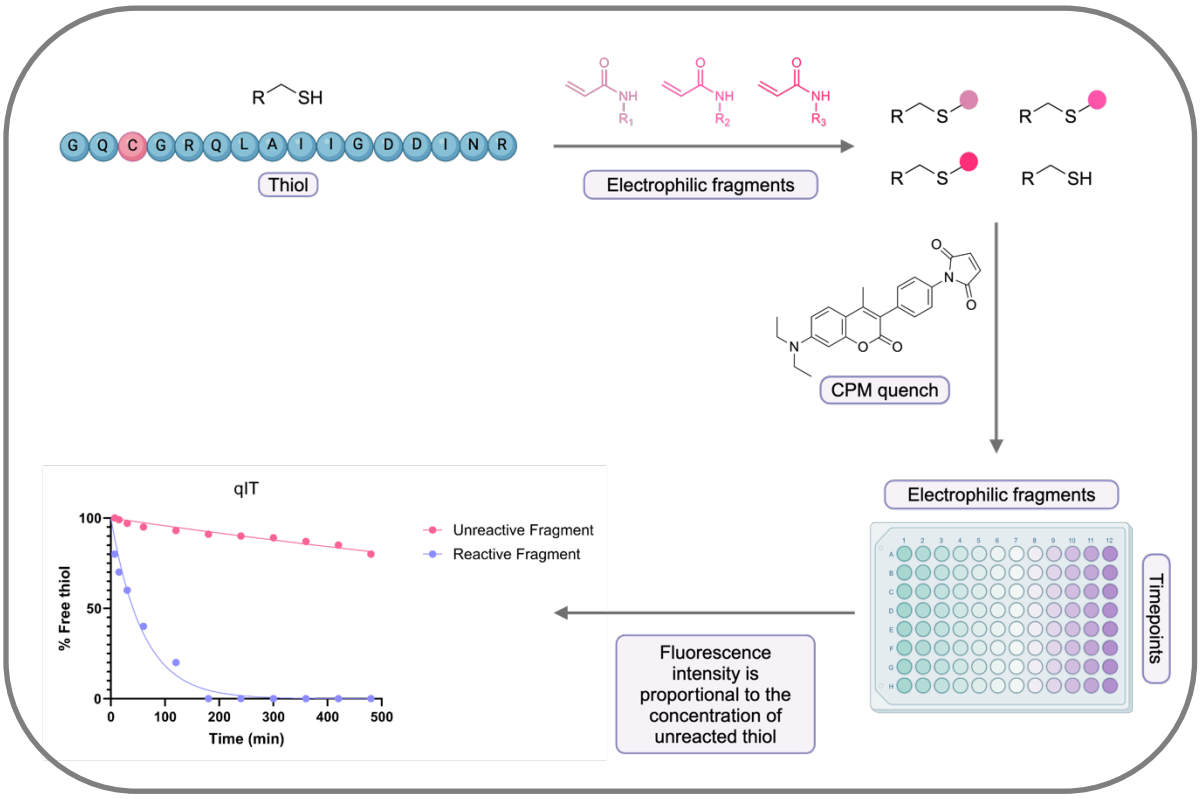


Figure 26: An overview of the quantitative irreversible tethering (qIT) assay. The target thiol reacts with an electrophilic library, with the reaction progress monitored through intermittent quenches using the fluorogenic probe CPM.

As depicted in **Figure 26**, the assay begins when the thiol of interest is screened with an appropriate electrophilic fragment library, under pseudo-first-order conditions. The progress of the reaction is subsequently monitored through recurring measurements of residual thiol concentration at various timepoints. This is facilitated through the use of 7-diethylamino-3-(4′-maleimidylphenyl)-4-methylcoumarin (CPM), where the maleimide moiety reacts with the target thiol to form a fluorescent adduct.[97] Fluorescence intensity is proportional to the concentration of

unreacted thiol. Rate constants can thereafter be derived from these time-dependant measurements, allowing the reactivity of the fragment library to be evaluated.

Electrophilic libraries comprising of fragments with acrylamide warheads are frequently employed in cysteine-targeting high-throughput screens,[98] owing to their selectivity and irreversible reactivity.[99] A library is typically chosen such that it is either void of known promiscuous compounds,[100] or is evaluated prior to screening using glutathione (GSH) as the model thiol;[101] this is to mitigate potential false positive/negative hits.[102] The use of GSH in parallel to the target thiol also allows identification of hit fragments that display accelerated reactivity in the presence of the target.[96]

Craven *et al* [96] employed this technique in the discovery of covalent fragments capable of successfully inhibiting Cdk2- a key oncological drug target. Craven *et al* screened an electrophilic compound library against Cdk2, facilitating covalent bond formation between the reactive fragments and the surface exposed cysteine residue on Cdk2. Hit fragments were subsequently identified that displayed accelerated reactivity in the presence of Cdk2.

Integrating the qIT assay with the target-directed approach outlined in section 1.8.1 would facilitate the discovery of potent inhibitors of the BCL-X_L/BAK PPI. These inhibitors would be derived from electrophilic fragments that display a notable increase in reactivity when incubated in the presence of BCL-X_L.

Chapter 2

High-Throughput Assay Development

2.1 Introduction and Objectives

High-throughput assays are often the origin source from which clinically relevant therapeutics are developed.[103] These campaigns are responsible for expediting the development of novel drugs and span a multitude of disease areas. Targeted PPI mediation is one category that has particularly benefitted from advances in high-throughput screenings.[104] These assays must be developed in a manner such that they not only maintain relevancy towards the target of interest, but also are robust and economically sound.[78] This is to ensure that compounds of interest identified in a primary screen, which is typically conducted once, can be classed as hits with confidence. These hit compounds are then further evaluated and validated following the primary screen.[78] This chapter details the development of a high-throughput screen, with the end goal of establishing a target-directed assay.

This target-directed approach was designed based on the principles of the qIT assay. As previously described (Chapter 1), the foundation of this assay is built upon fluorogenic thiol quantification, whereby thiol consumption is evaluated in a high-throughput format.[96] The target-directed approach, although centred around this core principle, has been modified with respect to the nucleophilic species that the electrophilic library interacts with, as seen in **Figure 27**.

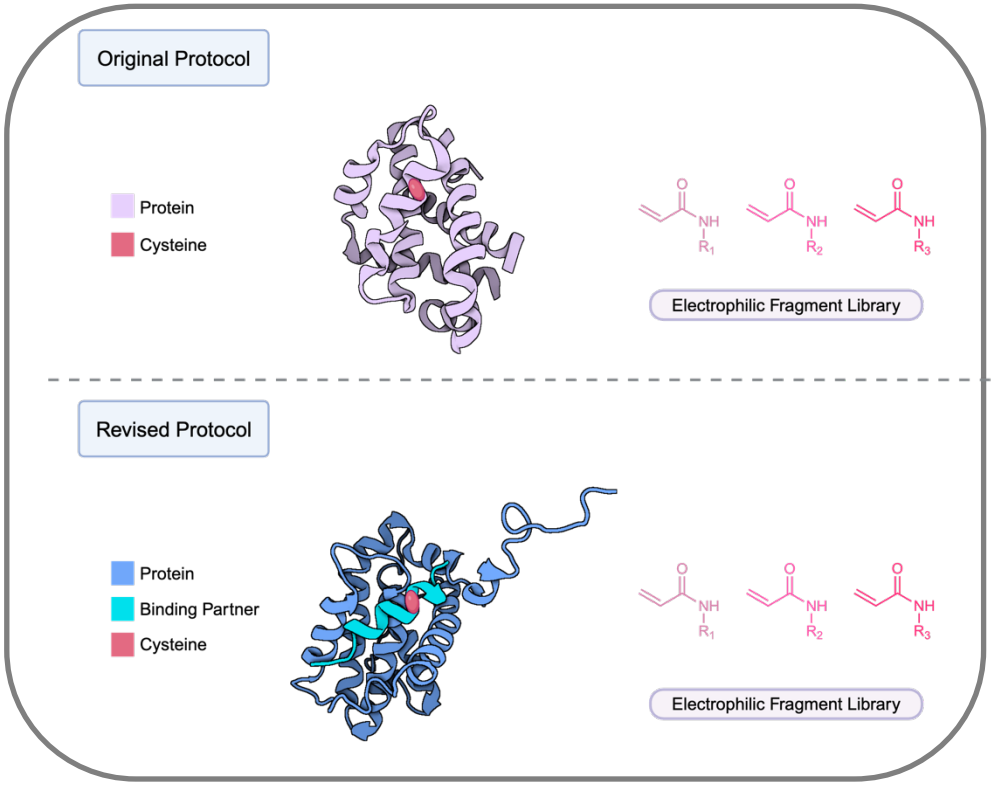


Figure 27: A comparison of the original qIT two-component system versus the revised three-component system, containing the reactive thiol on the binding partner as opposed to the target protein.

As illustrated in **Figure 27**, the revised target-directed assay features the nucleophilic thiol on the binding partner to the protein of interest. This is in stark contrast to the protein itself being the covalent anchor to which electrophilic fragments react with, as per the original design.

Although the protein of interest does not covalently bind to a reactive library, employing a modified binding partner allows protein dependent selectivity to be maintained. In the case of the BCL-X_L/ BAK PPI, when the assay is conducted in the presence of BCL-X_L with a BAK derived mimetic, the natural selectivity of BCL-X_L is exploited. Harnessing the inherent selectivity that BAK has for BCL-X_L, allows fragments that have an affinity for BCL-X_L to be preferentially incorporated into the BAK mimetic.

In order to initiate the development of this target directed approach, appropriate controls must be established such that they aptly inform future hit selection. These assay parameters would guide optimisation of the target-directed approach, as transitioning from a two to three component system increases the assay complexity. A more complex dynamic is introduced between the three components (protein, binding partner, fragment library) and thus results in a uniquely challenging optimisation process.

Therefore, a protocol was designed whereby BAK derived mimetics, each containing a reactive cysteine, would be screened against a diverse acrylamide library. This screen would be conducted using the qIT assay, allowing the percentage of free thiol i.e. percentage of functionalised peptide, to be determined at various timepoints. This screen would in essence generate a new library of peptide mimetics, which would subsequently be evaluated in a fluorescence anisotropy (FA) competition assay. This qIT to FA assay would enable the binding affinity of the newly functionalised mimetics towards BCL-X_L, to be determined.

The results generated would go on to inform the target-directed approach, whereby the hits would be employed as positive controls. Fragments that decrease binding affinity would also be used to inform optimisation by acting as a reference point, to which subsequent reductions in affinity could be compared against. Predetermining the identity of fragments that strongly affect binding affinity will validate the results obtained from the target-directed approach and reduce the overall complexity of its optimisation. The key to this lies with the effective translation of results from the qIT to FA screen, across to the target-directed screen.

This chapter therefore details the development of said qIT to FA assay and how the results obtained serve to inform a future target-directed screen.

2.2 Site-Directed Mutagenesis

2.2.1 Modifying WT BCL-X_L

As outlined in Section **2.1**, development of the target-directed qIT assay hinges on the BAK binding partner being the source of a nucleophilic thiol, in contrast to the target protein as per the original protocol.[96] Upon inspection of the residues that make up BCL-X_L, it was revealed that it does indeed contain a native cysteine residue (**CYS 151**) as highlighted in **Figure 28**.

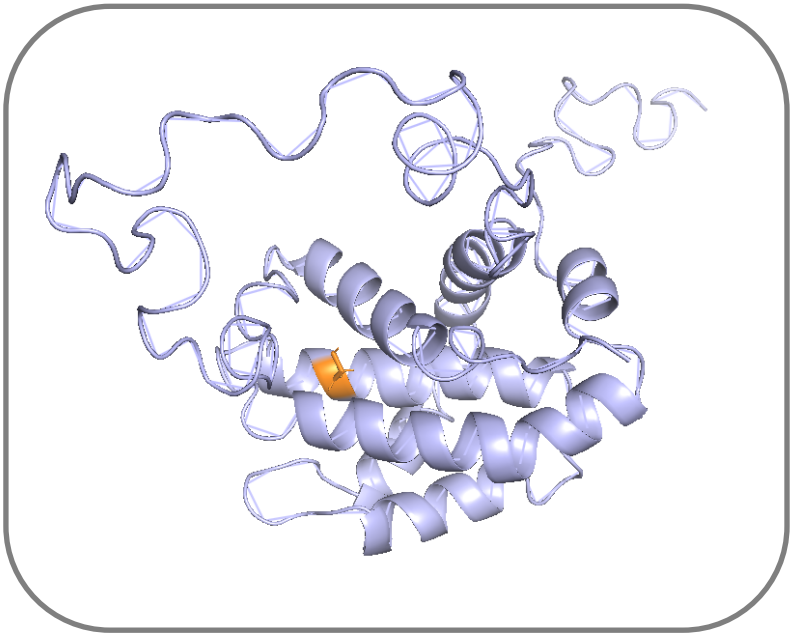


Figure 28: Crystal structure of BCL-X_L highlighting the native cysteine residue (PDB code 1BXL).

Therefore, in order to proceed with the development of this novel qIT assay, it became pertinent to eliminate any possible competition with the target thiol on the BAK mimetics. This elimination came in the form of substituting the native cysteine to a serine residue (**Figure 29**), via Site-directed mutagenesis (SDM).

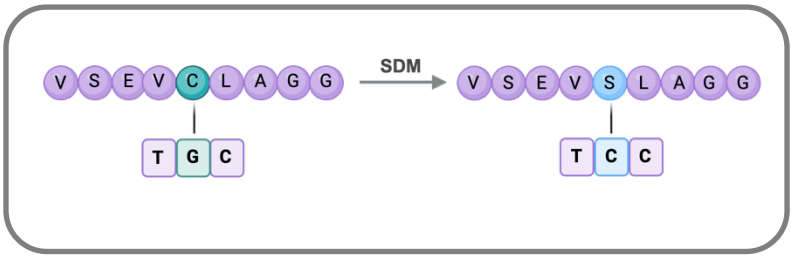


Figure 29: Differences in the codons for cysteine and serine residues.

SDM is an indispensable technique in the field of molecular biology[105] where mutant DNA can be generated *in vitro*,[106] as a way to probe the importance of specific residues in proteins with regards to their function[105]. SDM is predominantly meditated through polymerase chain reaction (PCR) based methods, where mutations are introduced by way of oligonucleotide primers carrying the desired mutation.[106] These complementary primers carry the desired mutation through misaligned nucleotides at the core of their sequence.[106] This PCR based process makes use of the oligonucleotide primer pairs in conjunction with a template DNA plasmid, to generate a plasmid containing the desired mutation.[105] This plasmid is subsequently transformed in *E.coli*, prior to being isolated as depicted in **Figure 30**.

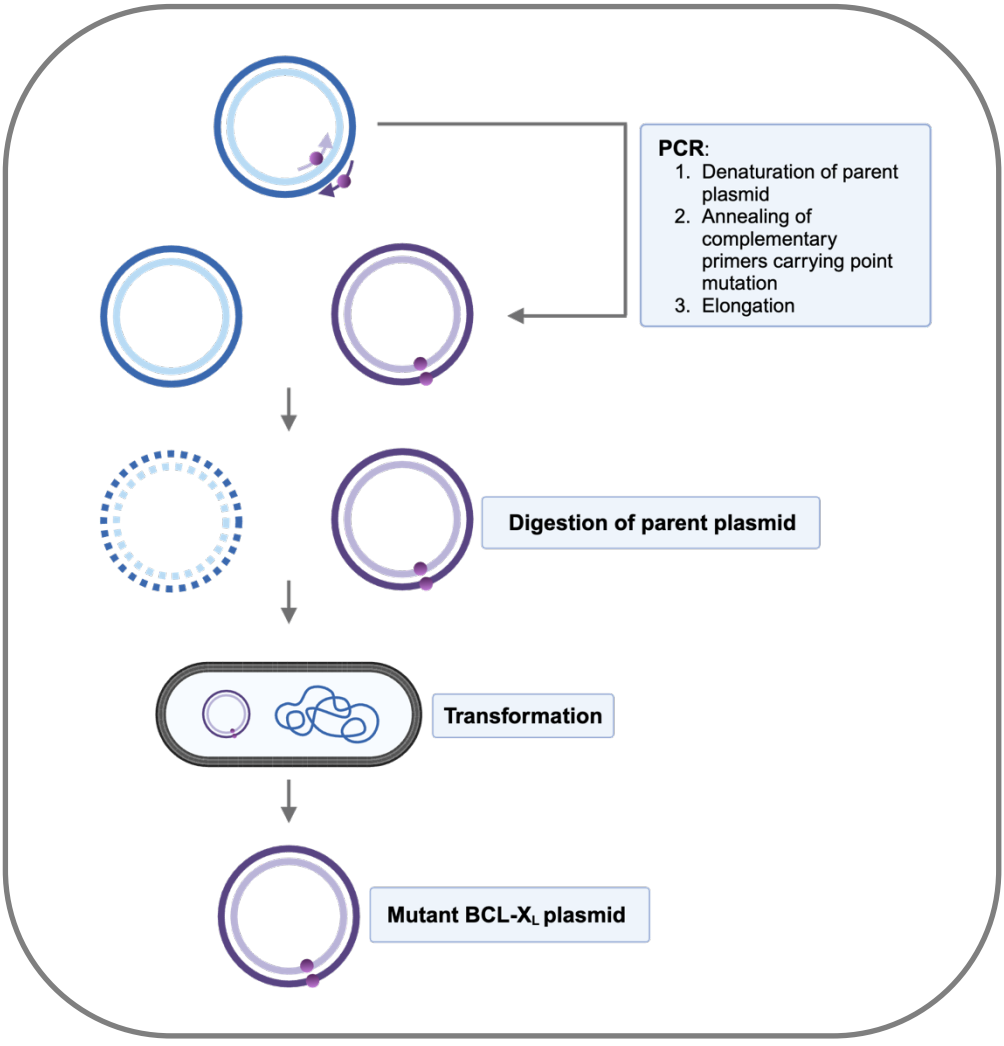


Figure 30: Schematic representation detailing the PCR workflow employed.

Through the aforementioned SDM protocol, a mutant BCL-X_L plasmid was generated where the native cysteine was successfully substituted with a serine residue. This was confirmed through Sanger sequencing, verifying that the desired BCL-X_L construct (Δ45-84, domain 1-209, C111S) was generated.

Once the target plasmid was acquired, it was used to transform chemically competent *E.coli* cells - a common host for recombinant protein production.[107] The transformed colonies were used to inoculate Lysogeny broth (LB) media, propagating the growth of the transformed bacterial cells. Once sufficient optical density was reached (OD_{600} – 0.6), protein expression was induced through the addition of isopropyl β-d-1-thiogalactopyranoside (IPTG). The bacterial cells were then lysed and subsequently purified using the ÄKTA pure™ chromatography system. The BCL-X_L protein contained a His-tag allowing it to be initially purified through immobilized metal affinity chromatography (IMAC), a cobalt-based method for the purification of His-tagged proteins. This was subsequently followed by purification through anion exchange chromatography (AEC) and size exclusion chromatography (SEC) in accordance with standard protocols, to produce the desired BCL-X_L construct (**Figure 31).**

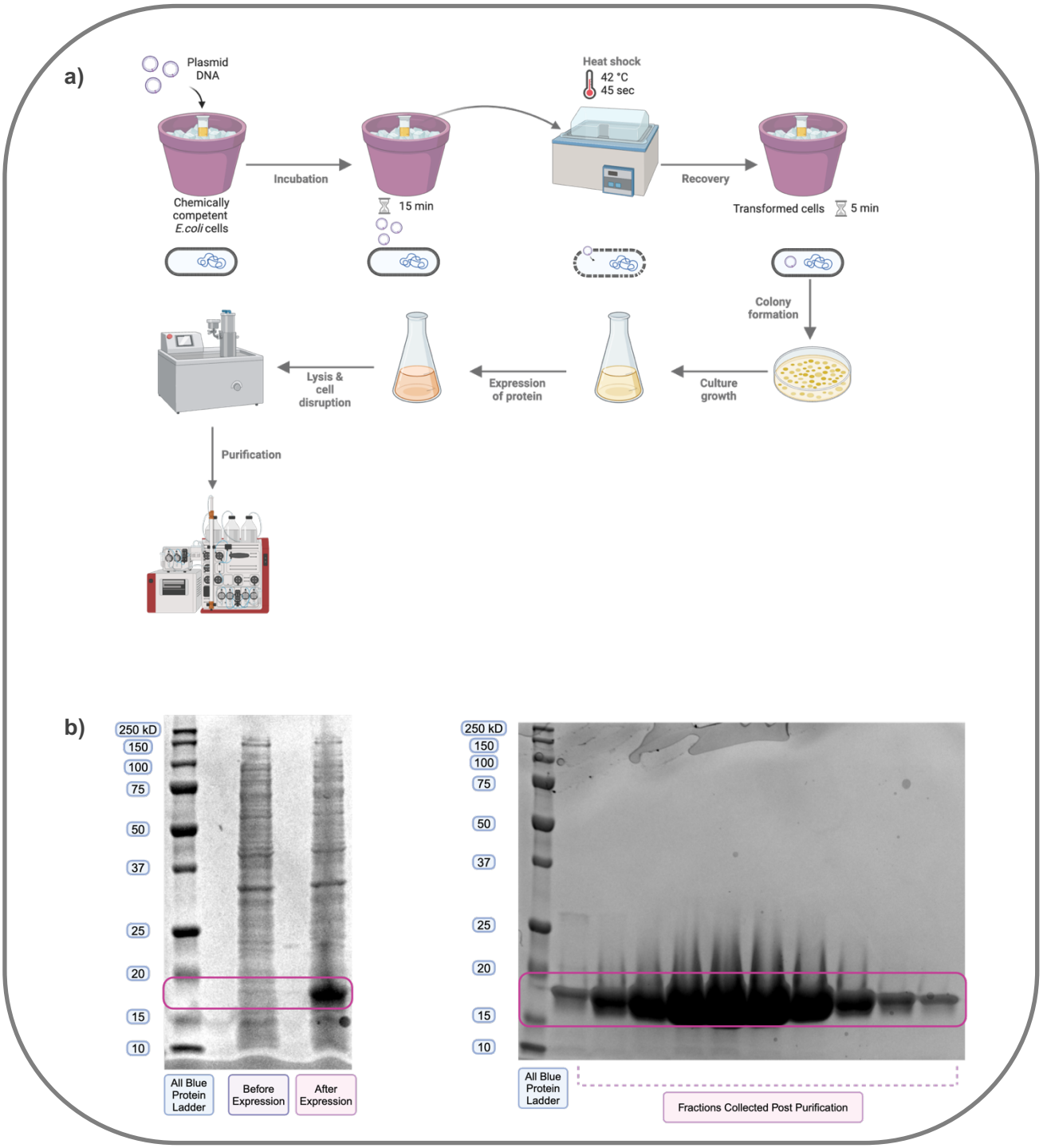


Figure 31: **a)** Workflow of the protein expression and purification protocol used to isolate the modified BCL-X_L construct. **b) Left:** SDS-PAGE highlighting the BCL-X_L protein band post IPTG expression (MW 20.3 kD). **Right:** SDS-PAGE highlighting the BCL-X_L protein fractions collected post purification through size exclusion chromatography .

2.3 Fluorescence Anisotropy Saturation Assay

With the modified protein in hand, the following phase of assay development entailed establishing conditions for a fluorescence anisotropy assay. This was in order to employ the newly acquired protein in a high-throughput assay, where binding affinity of potential mimetics would be measured via fluorescence anisotropy.

2.3.1 Principles of Assay

The principle of a fluorescence anisotropy assay, first described by Perrin,[108] is founded on the sensitivity of a fluorophore, specifically with regards to the effect molecular weight has on its rate of molecular rotation and the resultant differences in polarised light emission. When a small fluorescently labelled ligand (<1500 Da) is excited by polarised light, the light emitted will be depolarised to a large degree. This is a consequence of rapid Brownian molecular rotation, which in turn reorients the fluorophore during the lifetime of its excited state.[109] However, when complexed with a higher molecular weight protein (> 10 kDa), this reorientation occurs to a significantly smaller degree. This is a direct consequence of the high molecular weight protein reducing the rotational speed of the overall complex. Consequently, the light emitted by the fluorophore will retain a substantial degree of polarisation, as highlighted in **Figure 32**. This overall signifies that the degree of emitted light polarisation is inversely proportional to the rate of molecular rotation.[109]

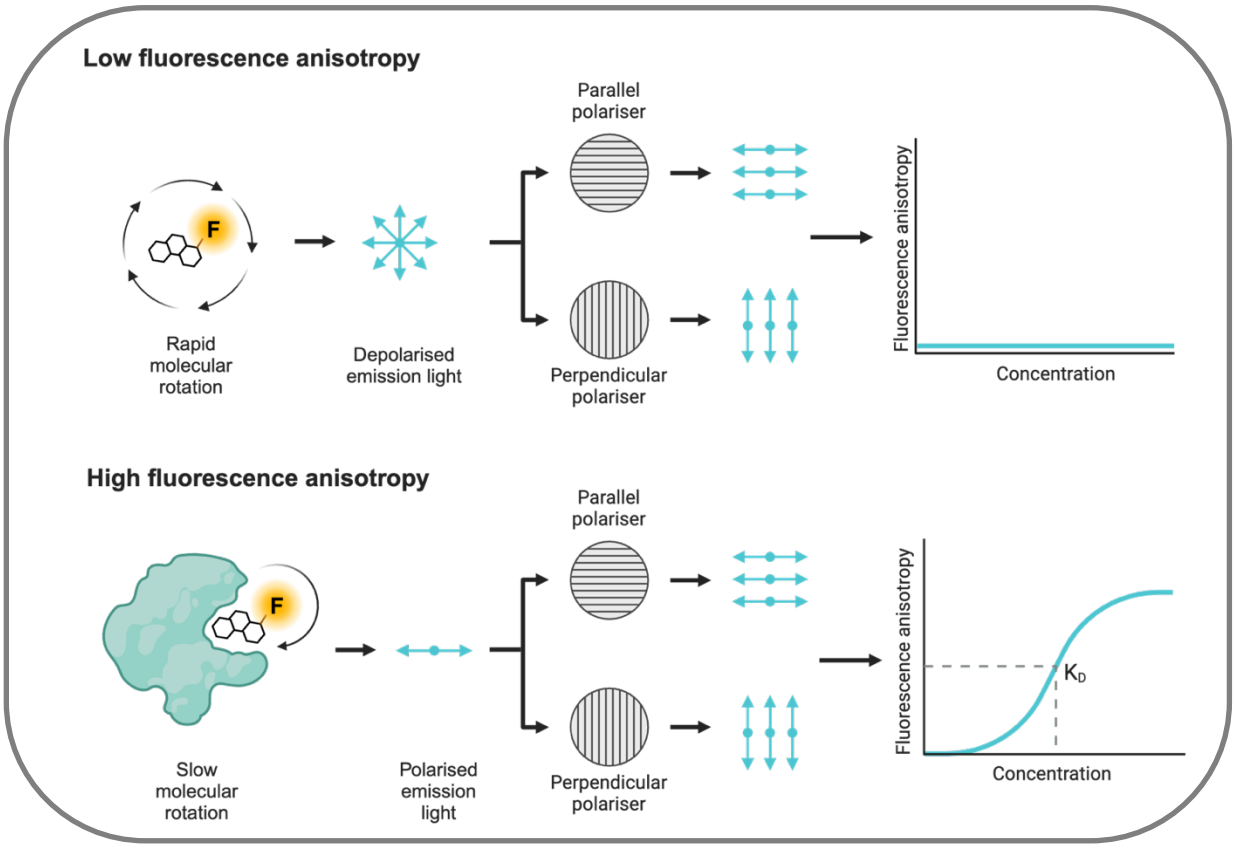


Figure 32: An illustration of how molecular rotation impacts the fluorescence anisotropy detected.

The principle behind this assay makes it a popular technique to measure degree of ligand binding, a feature which the drug discovery community is heavily reliant on. This assay can be applied to an array of biological processes, whilst being amenable towards high-throughput formats.

To conduct this assay, the fluorophore of interest is excited by polarised light and the resultant emissions are collected through two channels, one parallel ($I_{\parallel}$) and one perpendicular ($I_{\perp}$) to the plane of the excitation light.[110] These values are subsequently used to calculate fluorescence anisotropy via the equation shown in **Equation 1**.

$$FA = \frac{I_{\parallel} - I_{\perp}}{I_{\parallel} + 2I_{\perp}}$$

Equation 1: Fluorescence anisotropy equation, where $I_{\parallel}$ and $I_{\perp}$ are the fluorescence intensities of emissions from the parallel and perpendicular channels, respectively.

2.3.2 Saturation Assay

In order to use this new construct of BCL-X_L for assay development, its ability to interact with BAK in the same manner as the WT construct had to be investigated. Using the principles of fluorescence anisotropy discussed above, the BCL-X_L construct (Δ45-84, domain 1-209, C111S) generated through SDM was evaluated in comparison to WT BCL-X_L.

Thus, a FA saturation assay was conducted where serial two-fold dilutions provided a BCL-X_L concentration range of 1 μM to 0.015 nM for both constructs. This was titrated against a fixed concentration of fluorescein (FAM) labelled WT BAK (FAM-Bak$^{72-87}$ - 1 nM), as shown below in **Figure 33**.

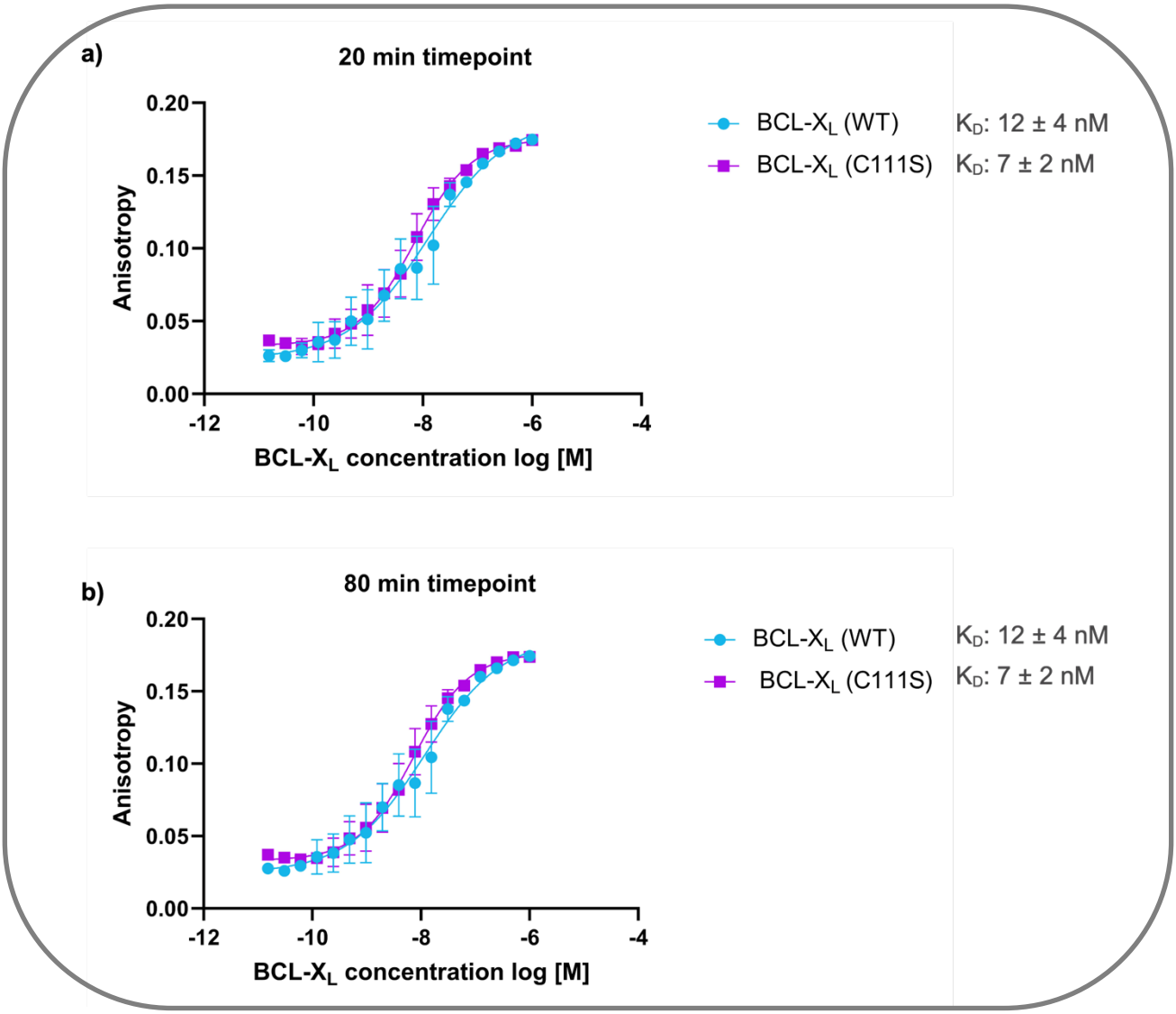


Figure 33: Fluorescence anisotropy saturation assay. BCL-X_L (1 μM to 0.015 nM) titrated against FAM-Bak$^{72-87}$ (1 nM). Binding curve at **a)** 20-minute and **b)** 80-minute and timepoints with WT BCL-X_L construct in blue and mutated (C11S) construct in purple. K_D values are reported in nM and include the standard error of the mean.

Anisotropy was measured at two timepoints in an effort to ensure complete binding to of the BCL-X_L constructs. As indicted in **Figure 33**, there was minimal difference between the K_D values obtained from the 20- and 80-minute timepoints, signifying that 20 minutes is sufficient for complete binding. Upon further inspection of the K_D values extracted from the saturation curves, it became evident that there was virtually no difference between the mutated and WT constructs of BCL-X_L. This confirmed that mutating the cysteine residue on WT BCL-X_L to serine did not affect BAK's ability to bind in the BH3 binding cleft, allowing the mutated construct to be employed in future assay development.

2.4 Peptide Design & Synthesis

2.4.1 Design of Peptide Library

The peptidic pathway of the two-pronged target-directed approach was inspired by the replicable functionality of a proteogenic cysteine residue in comparison to a synthetic thiol. Retaining the thiol functionality was of paramount importance, considering the peptides were designed to be employed in the thiol dependent qIT assay as previously detailed in **Chapter 1**.

Thus, the peptidic mimetics were designed in a manner whereby the majority of the native BAK sequence was retained, with the primary alteration being the substitution of the relevant hot spot with a cysteine residue. As the native BAK sequence contains four hot spot residues (Val^{74}, Leu^{78}, Ile^{81} and Ile^{85}),[37] a small library of 'naked' peptide mimetics was designed containing cysteine residues in place of hot spots, as illustrated in **Figure 34**.

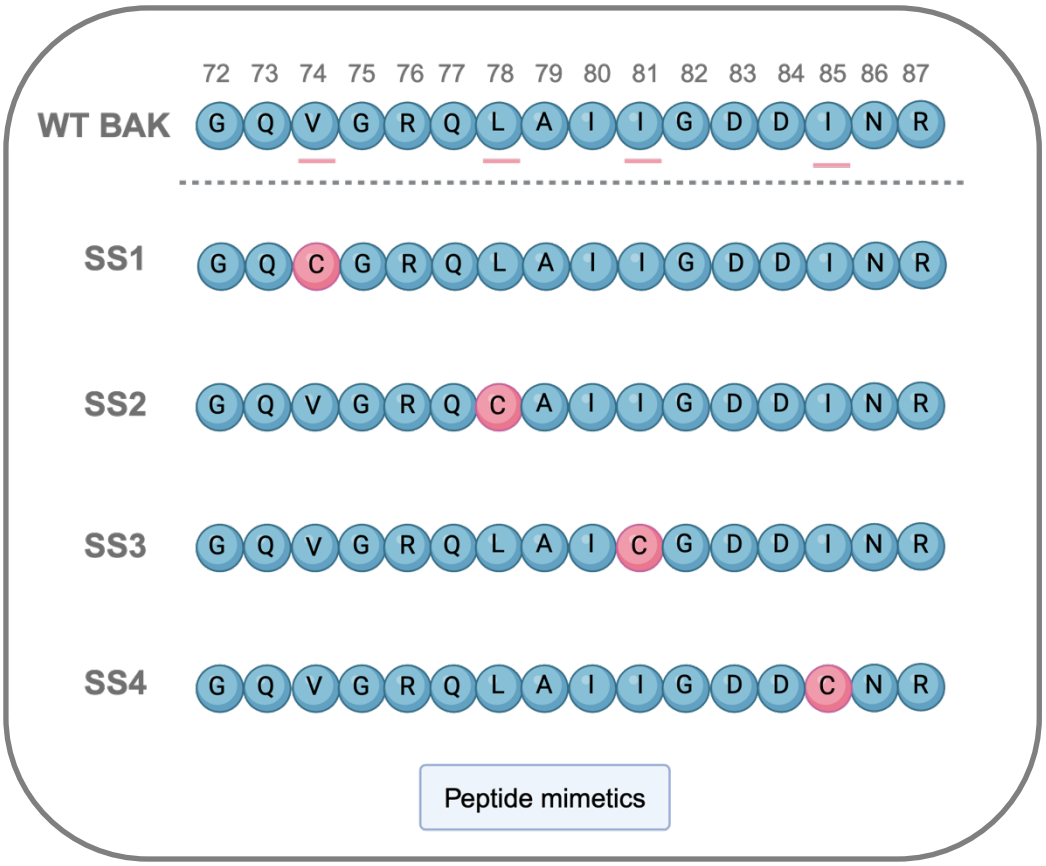


Figure 34: Sequences of peptides in the small mimetic library, highlighting hot-spot replacement with a cysteine residue. Hot-spots are underlined in the WT BAK sequence (Val^{74}, Leu^{78}, Ile^{81} and Ile^{85}).

2.4.2 Solid-Phase Peptide Synthesis

The peptide library highlighted in **Figure 34** was synthesised via the solid-phase peptide synthesis (SPPS) approach pioneered by Merrifield.[111] This was conducted on an automated microwave peptide synthesiser, where the industry standard Fmoc/^{t}Bu protection strategy[112] was employed as depicted in **Figure 35.**

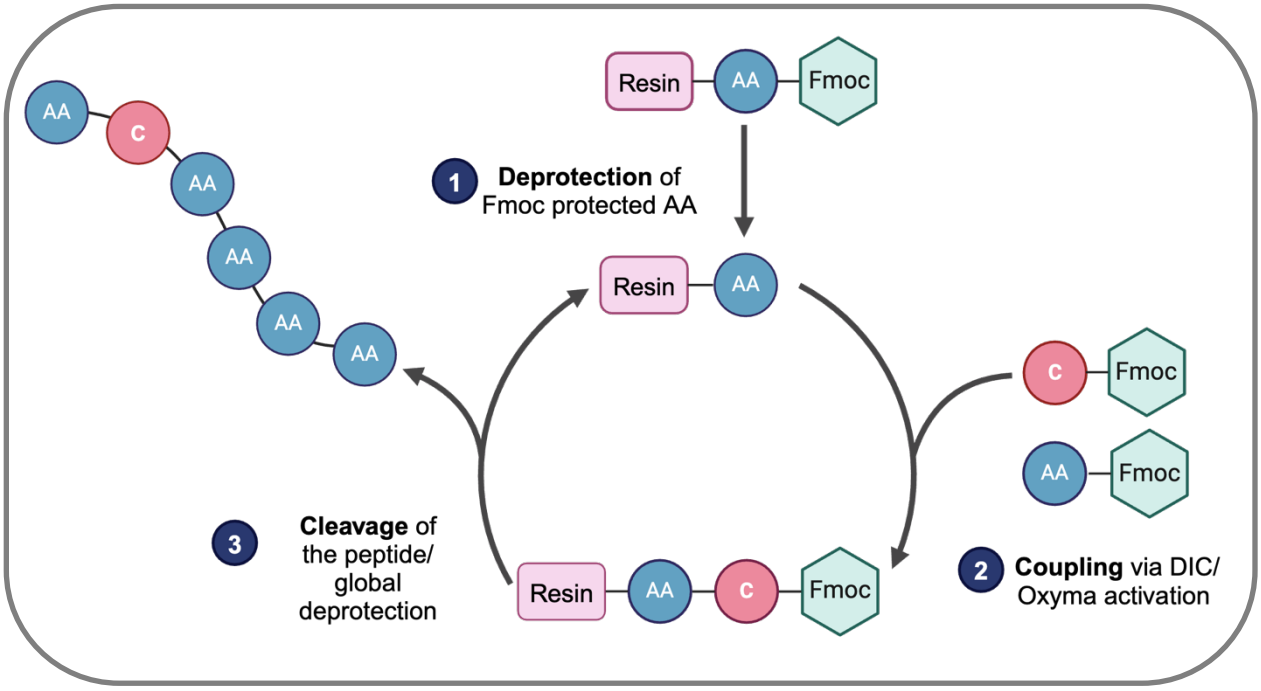


Figure 35: Schematic illustration of the solid-phase peptide synthesis (SPPS) approach. AA refers to an amino acid residue, with C specifically referring to a cysteine residue.

Activation of the Fmoc-protected amino acid residues was carried out using diisopropylcarbodiimide (DIC), a carbodiimide-based activator, with ethyl (hydroxyimino)cyanoacetate (Oxyma) as an additive. This activator combination is a popular choice for SPPS due to its superior coupling efficiency and inhibition of racemisation,[113] in comparison to benzo-triazole-based additives such as hydroxybenzotriazole (HOBt).[114] Oxyma is also a lower thermal risk and safer to handle than reagents such as HOBt.[115]

Activation occurs when the amino acid of interest reacts with DIC; this forms an *O*-acylisourea intermediate. The intermediate generated goes on to react with Oxyma forming an active ester.[113]

This oxime-based ester is the species that reacts with the target amino acid residue to form a peptide bond as seen in **Figure 36**.

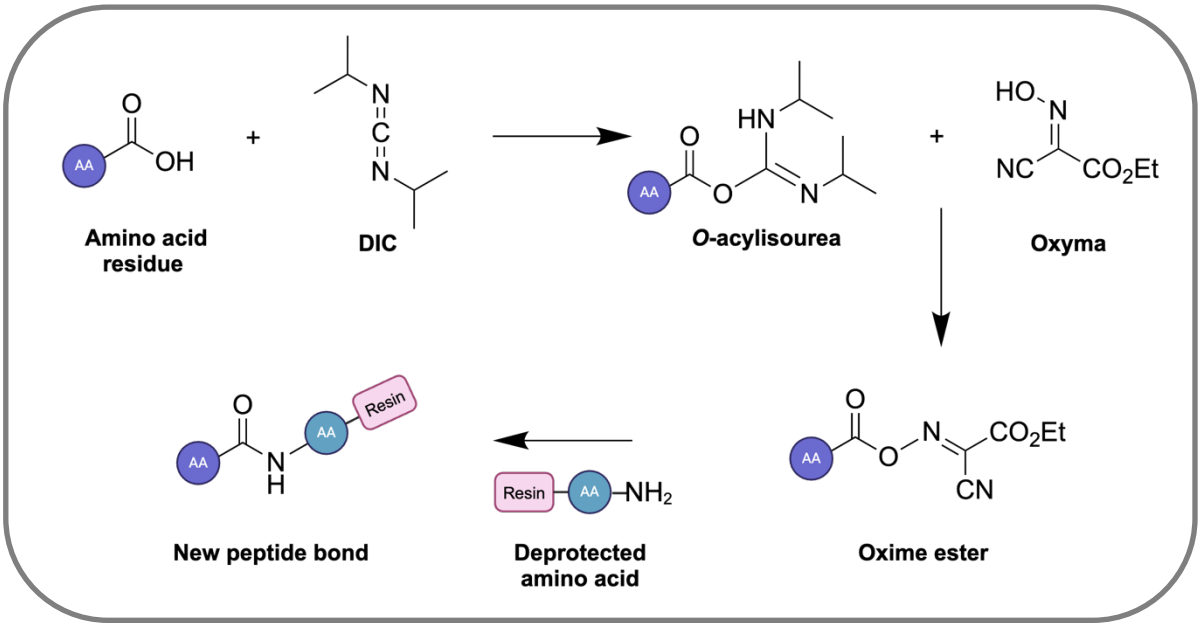


Figure 36: DIC/Oxyma based amino acid activation pathway.

The conditions that paired with this activation system to synthesise **SS1-4** were 2-minute coupling cycles (2 x 2 mins for double coupling) at 90 °C. Following a final N-terminal Fmoc cleavage using piperidine, the newly generated peptides were removed from the automated peptide synthesiser to allow for post synthetic modifications. Peptides **SS1-4** were manually acetylated at the N-terminus under standard conditions, in order to remove the positive charge, to mimic a natural protein backbone and increase stability.[116] Finally, the peptides were cleaved off the solid support and as the resin of choice was a Rink amide based resin (TentaGel™ S RAM), the peptides were afforded as C-terminal amides. All respective sidechain protecting groups were also cleaved during this final deprotection stage. The crude peptides generated were subsequently purified via high-performance liquid chromatography (HPLC) to provide the target peptides (**Figure 34**). The peptides were characterised via liquid chromatography–mass spectrometry (LCMS) and HPLC, where the molecular mass and purity of each peptide was determined (**Figures 63-66**).

It is worth noting that the ease of synthesis in comparison to the functionalised monomer detailed in **Chapter 3**, propagated the use of ‘naked’ peptides **SS1-SS4** for the optimisation and development of the novel target-directed qIT assay. The term ‘naked’ in this instance is defined as a thiol functionalised peptide, by virtue of including a cysteine residue, without a fragment attached to the thiol.

2.5 Fluorescence Anisotropy Competition Assay

2.5.1 Assay Design

For the newly generated 'naked' peptides (**SS1- 4**) to be employed in the development of the novel target-directed qIT assay, their inherent binding affinities towards BCL-X_L must be determined, in order to establish the baseline affinity. For this purpose, a fluorescence anisotropy (FA) assay was designed in a competition format, as showcased below in **Figure 37**.

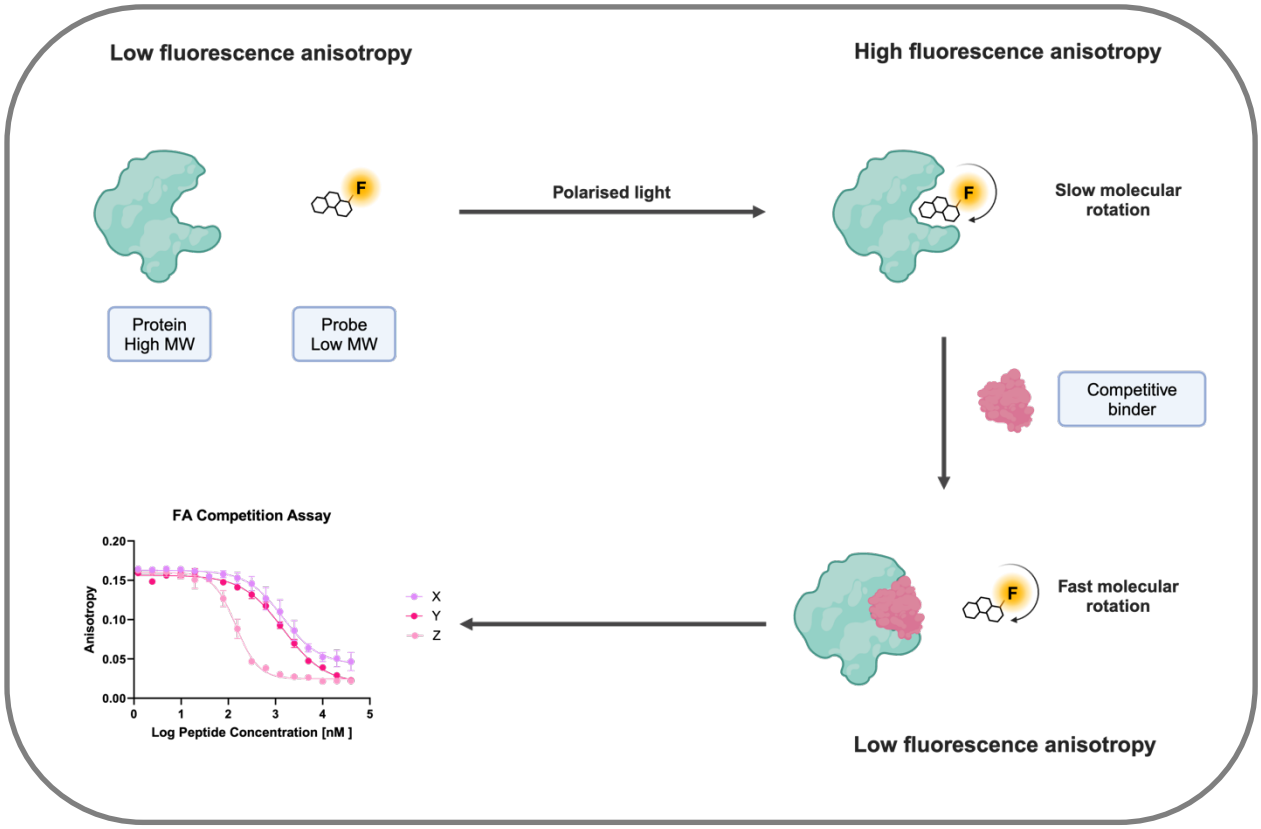


Figure 37: An illustration detailing the design of a fluorescence anisotropy competition assay, as a way to evaluate potential competitive binders.

As illustrated in **Figure 37**, this assay variation introduces a competitive binder, in contrast to the saturation format previously discussed in Section 2.3.2. The competitor displaces the fluorescent probe from the protein-probe complex, resulting in the newly liberated probe being subject to an increase in rotational mobility.[117] Consequently, a low fluorescence anisotropy signal is detected – a shift from the high anisotropy value detected whilst complexed with a high molecular weight

protein. This assay format exploits the dependence that the fluorescent probe has on its molecular weight and the resultant differences in emission of polarised light.[110]

2.5.2 Optimisation of Assay

The FA competition assay was designed using a FAM labelled WT BAK peptide as the probe, in conjunction with the BCL-X_L construct (Δ45-84, domain 1-209, C111S) generated through SDM. The primary attempt of this competition assay was trialled using **SS1** and **SS3**, in an effort to establish baseline affinity towards BCL-X_L. The peptide concentration range initially selected was from 5 μM to 0.15 nM, produced via serial two-fold dilutions. This was then titrated against a fixed concentration of BCL-X_L (100 nM) and FAM-Bak$^{72-87}$ (1 nM). The titration curves were plotted in a manner where the anisotropy values detected were compared to the concentration of the peptide, as seen in **Figure 38**.

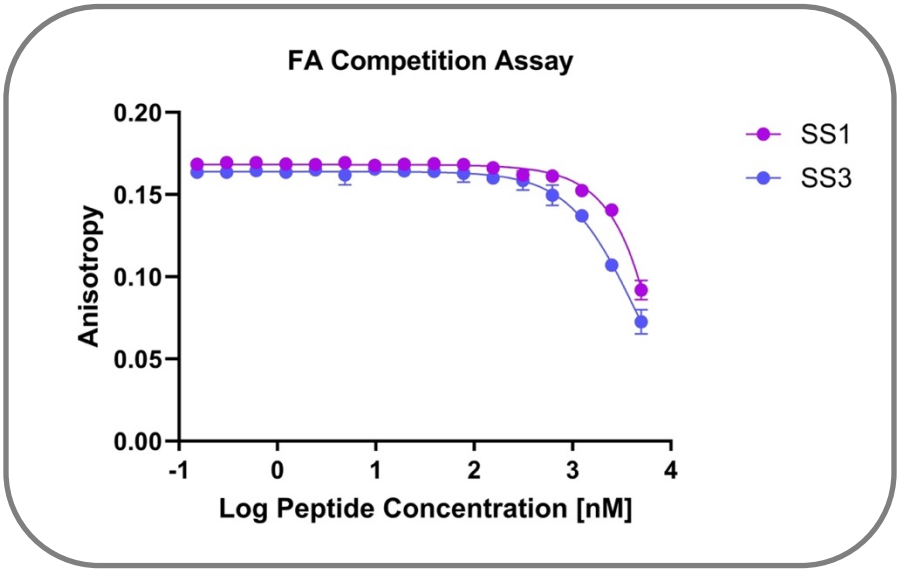


Figure 38: Primary trial of the FA competition assay. SS1 and SS3 (5 μM to 0.15 nM) titrated against BCL-X_L (100 nM) and FAM-Bak$^{72-87}$ (1 nM).

As seen in **Figure 38**, the titration curves produced were not sufficient to allow extrapolation of plausible IC_{50} values. The 5 μM to 0.15 nM concentration range did not elicit a significant difference in the corresponding anisotropy values detected. Furthermore, this concentration range did not allow a baseline plateau to be established to signify total displacement of the tracer. The lack of baseline plateau indicated that the maximal peptide concentration must be increased.

Thus, a second attempt at this FA competition assay was conducted with a modified peptide concentration range of 40 μM to 1.2 nM, prepared once again through serial two-fold dilutions. This was then titrated against the same fixed concentrations of BCL-X_L (100 nM) and FAM-Bak$^{72-87}$ (1 nM) as the previous attempt (**Figure 39).**

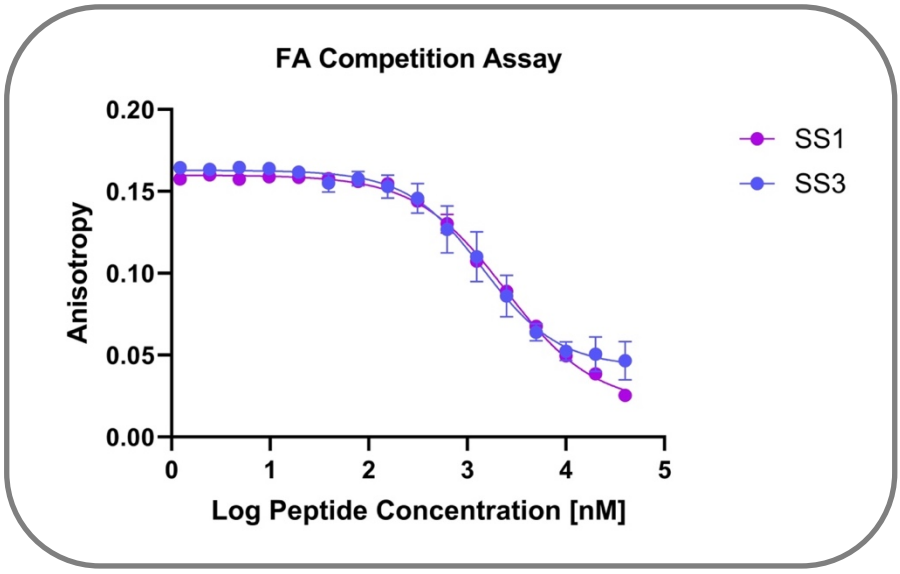


Figure 39: FA competition assay. SS1 and SS3 (40 μM to 1.2 nM) titrated against BCL-X_L (100 nM) and FAM-Bak$^{72-87}$ (1 nM).

As depicted in **Figure 39**, the modified concentration range allowed sufficient binding of peptides **SS1** and **SS3**, to the point where virtually all of the tracer was displaced. This enabled rational IC_{50} values to be extracted, with **SS1** having an IC_{50} value of 2.4 μM and **SS3** having an IC_{50} of 1.4 μM.

Having optimised the ideal peptide concentration range for this FA assay format, the binding affinity of the remaining peptides (**SS2 & SS4**) was analysed, alongside WT BAK which served as a control. **Figure 40** displays the competition binding curves for all peptides.

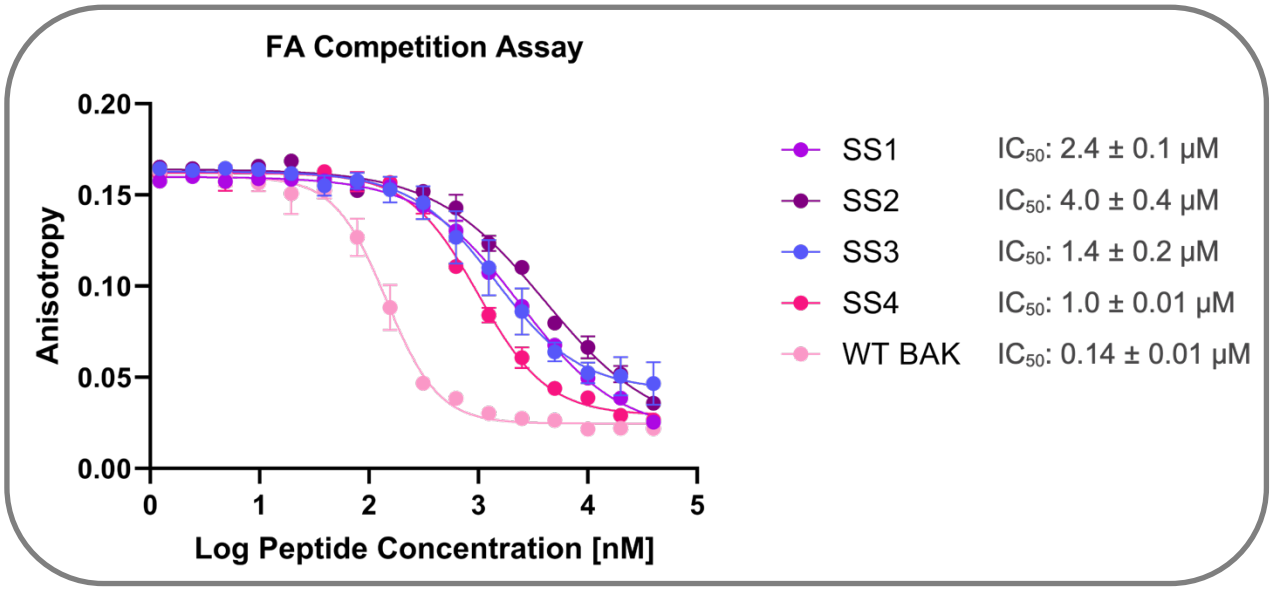


Figure 40: FA binding curves for mimetics SS1-SS4, plotted against the curve for WT BAK. IC_{50} values are reported in μM and include the standard error of the mean.

On closer inspection of the IC_{50} values generated from competition binding curves, it is evident that even the substitution of a sole hot spot on the native BAK sequence translates to a significant decrease in binding affinity towards BCL-X_L. When comparing the IC_{50} values of **SS1-4** to that of WT BAK, there is approximately a 10-fold reduction in binding affinity. This notable reduction in affinity results in a greater assay window, as opposed to if the affinities of WT BAK and **SS1-4** were closer, allowing hit compounds to be effectively evaluated.

Analysis of the baseline affinity for 'naked' peptides **SS1-4** allows them to be employed in the development of the novel target-directed qIT assay. The premise of this concept is that once 'hit' fragments are identified, the peptide + fragment complex can be subsequently evaluated in a FA competition assay. The IC_{50} values produced from those binding curves will be compared to the IC_{50} values of the 'naked' peptides, as elucidated in **Figure 41**.

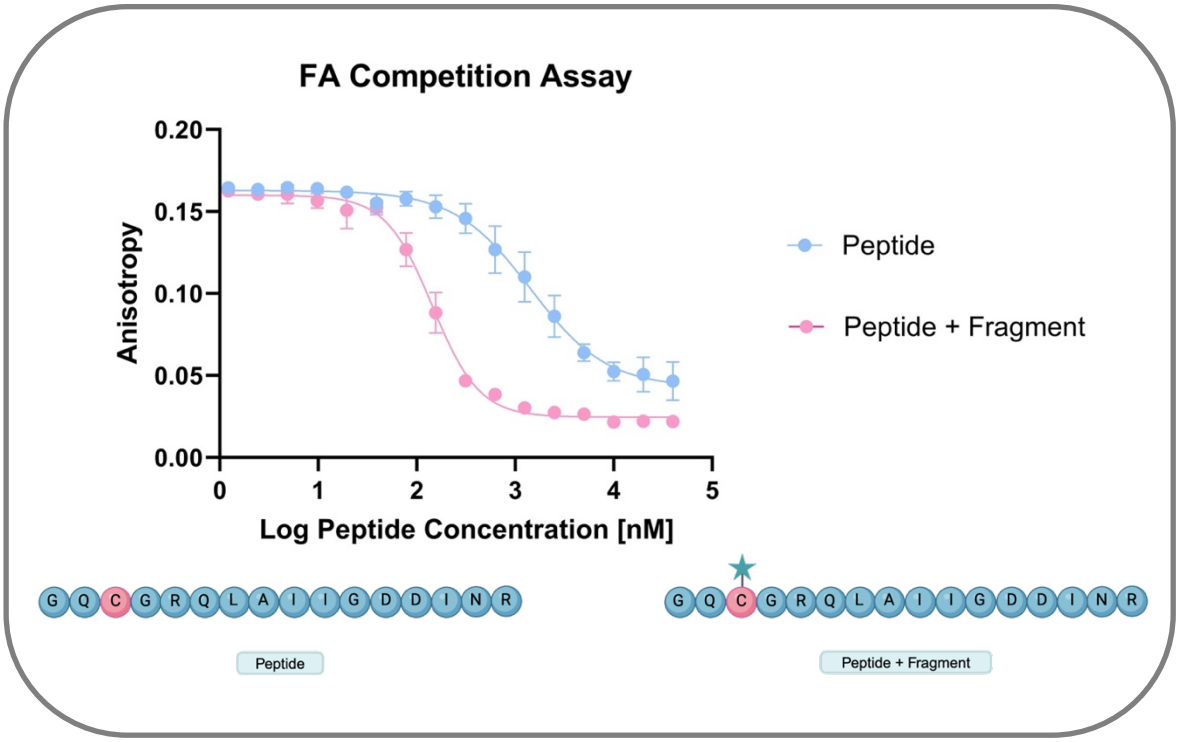


Figure 41: An illustration of how functionalised peptide mimetics will be evaluated in a fluorescence anisotropy competition assay against the unfunctionalized peptide.

2.6 Development of the qIT to FA Assay

2.6.1 Preliminary Optimisation

The preliminary requirement to aid development of the qIT to FA high-throughput assay was to establish the optimal concentrations of the peptide of interest. Moreover, the appropriate assay concentration of the fluorogenic probe (CPM) had to be determined, such that the fluorescent intensity was proportional to the concentration of free thiol.

A primary factor under consideration when establishing the optimal peptide concentration was to evaluate the signal-to-noise ratio, to the effect of maintaining an appropriate difference in comparison to the background 'signal'.

To assess the aforementioned reagent concentrations **SS1** was employed as the model thiol, where an initial concentration range of 10 μM to 0.04 μM was titrated against a fixed concentration of CPM (1.25 μM) at various timepoints, as shown in **Figure 42**. At the desired timepoint, aliquots of **SS1** from the reaction plate were taken and quenched with CPM. The quench plate produced was subsequently covered and incubated for 1 h at r.t prior to reading.

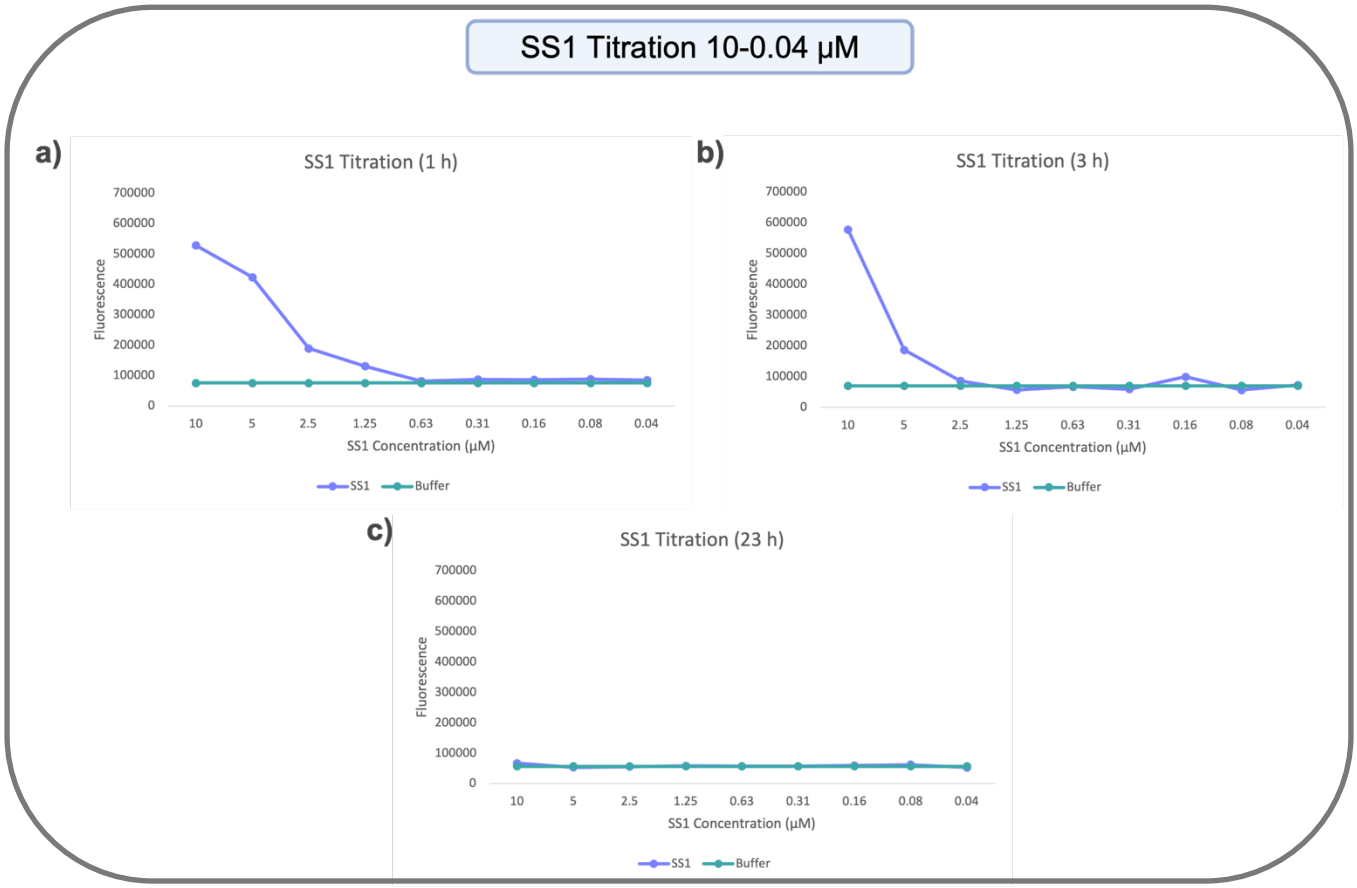


Figure 42: Titration of SS1 (10-0.04 µM - reaction plate concentration) against CPM (1.25 µM – quench plate concentration) comparing the signal-to-noise ratio against the assay buffer. **a)** 1 h CPM quench. **b)** 3 h CPM quench. **c)** 23 h CPM quench.

As illustrated in **Figure 42**, the difference in fluorescent intensity between **SS1** and the 'background' assay buffer was minimal, with the signal-to-noise ratio faring worse at lower concentrations of peptide. Suspected oxidation of **SS1** was also observed at the overnight timepoint (**Figure 42c**). This initial attempt clearly indicated that a larger concentration range of **SS1** was required, in order to improve the signal-to-noise ratio.

The following attempt implemented a revised peptide concentration range of 40 µM to 2.3 µM, initially titrated against 1.25 µM CPM and increasing to 5.4 µM CPM (**Figure 43**).

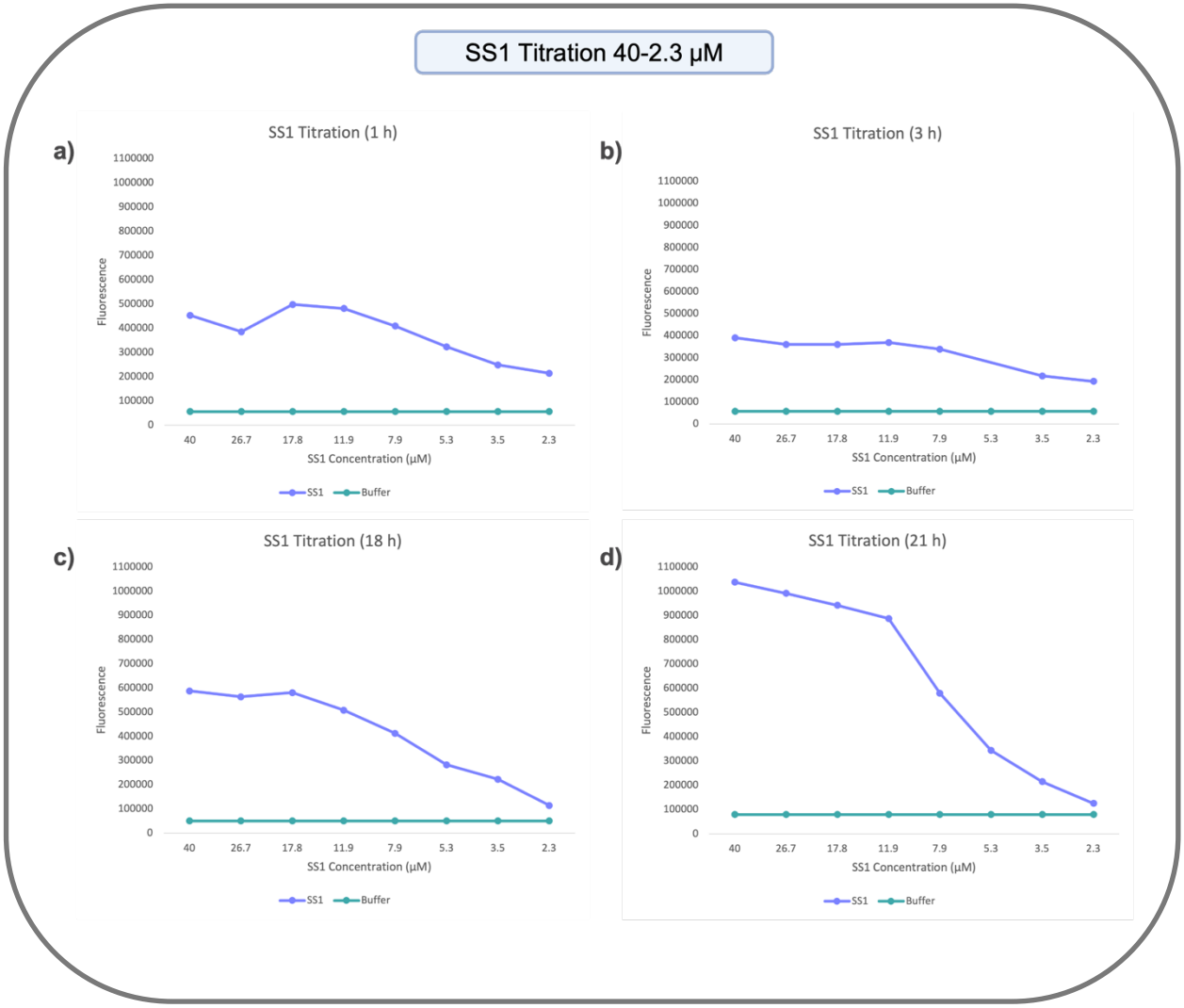


Figure 43: Titration of SS1 (40-2.3 µM - reaction plate concentration) against CPM (quench plate concentration) comparing the signal-to-noise ratio against the assay buffer. **a)** 1 h CPM quench (1.25 µM). **b)** 3 h CPM quench (1.25 µM). **c)** 18 h CPM quench (1.25 µM). **d)** 21 h CPM quench (5.4 µM).

Figure 43 highlights the results of the second optimisation test, illustrating that indeed a higher concentration of **SS1** was required in order to obtain a sufficient signal-to-noise ratio, with approximately a 10-fold difference in fluorescent signal observed. However, despite this improvement, at 1.25 µM CPM the fluorescence intensity observed for higher concentrations of **SS1** did not increase in alignment with the increase in peptide concentration. This was particularly notable at high peptide concentrations, such as 40 µM. A potential explanation for this phenomenon could simply be that at high peptide concentrations using 1.25 µM CPM is

insufficient, with the fluorescent probe being oversaturated with **SS1**. If the amount of unreacted **SS1** is significantly larger than the quantity of CPM available, a proportional increase in fluorescence signal will not be detected. Thus, to evaluate this hypothesis, at the overnight timepoint the quantity of CPM used for the quench step was increased approximately 4-fold, to a final assay concentration of 5.4 μM. The results of this endeavour are highlighted in **Figure 43d** where it was evident that this increase in CPM had a notable impact on the fluorescence intensity observed.

As the CPM concentration used for the initial three timepoints (**Figure 43**) failed to represent an accurate fluorescence intensity for higher peptide concentrations, a third set of conditions was trialled. In this instance the higher CPM concentration (5.4 μM) was used for all timepoints, with a peptide concentration range of 40 μM to 1.6 μM. Additionally, **SS1** was reduced with TCEP prior to the start of the test, in order to address the oxidation seen at overnight timepoints and to simulate conventional qIT assay conditions (**Figure 44**).

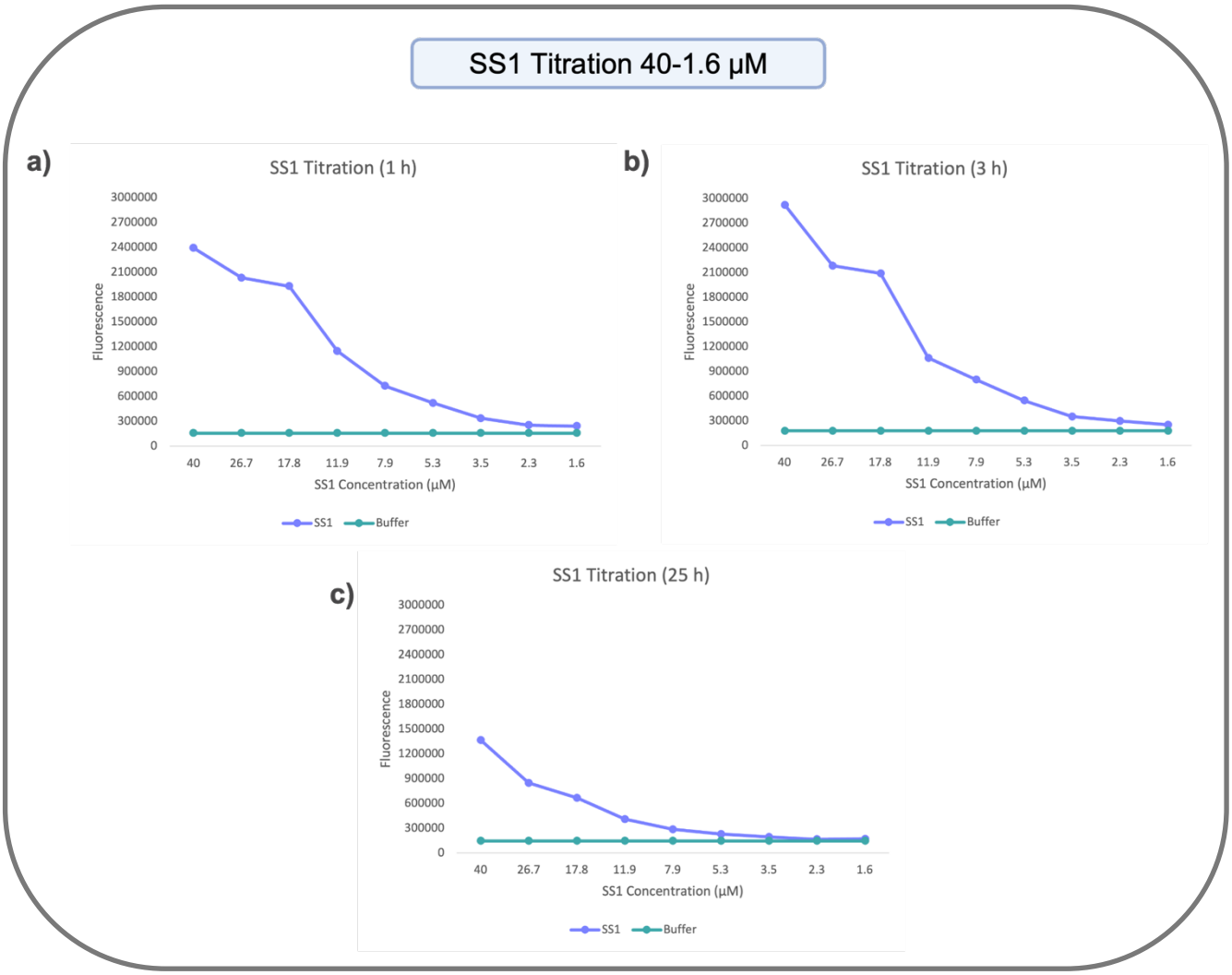


Figure 44: Titration of SS1 (40-1.6 µM - reaction plate concentration) against CPM (5.4 µM- quench plate concentration) comparing the signal-to-noise ratio against the assay buffer. **a)** 1 h CPM quench. **b)** 3 h CPM quench. **c)** 25 h CPM quench.

Figure 44 in essence is a summation of the two previous optimisation attempts. The data confirm not only that high peptide concentrations are required for sufficient signal-to-noise ratios, but that this reflects the need to employ higher CPM concentrations. This is in order to paint an accurate picture of fluorescence intensity and hence reactivity. Reduction of **SS1** with TCEP must also be included in future assays, in order to mitigate thiol oxidation.

2.6.2 Acrylamide Library Screen

2.6.2.1 Screen A - Evaluation of SS1 Under Assay Conditions

The next phase of assay optimisation called for the evaluation of **SS1** concentrations under conventional qIT assay conditions. Previous optimisation attempts (Section 2.6.1) provided a baseline assessment regarding optimal reagent conditions, which in turn informed the selection of peptide concentrations to be evaluated. The two peptide concentrations chosen were 15 μM and 5 μM. The rationale behind this selection was that 15 μM was between the 17.8 and 11.9 μM concentrations that displayed a sufficient signal-to-noise ratio (**Figure 44**), with 5 μM being evaluated to solidify the notion that higher concentrations of peptide were required. The acrylamide library chosen for this screen was commercially purchased from Enamine and featured 320 acrylamide fragments functionalised with various moieties, including a range of aromatics, heteroaromatics and aliphatics. These fragments were considered to be minimally promiscuous, allowing the reactivity of meaningful hits to be followed. Thus, the two concentrations of **SS1** were simultaneously screened in the presence of this library with selected examples shown in **Figure 45**.

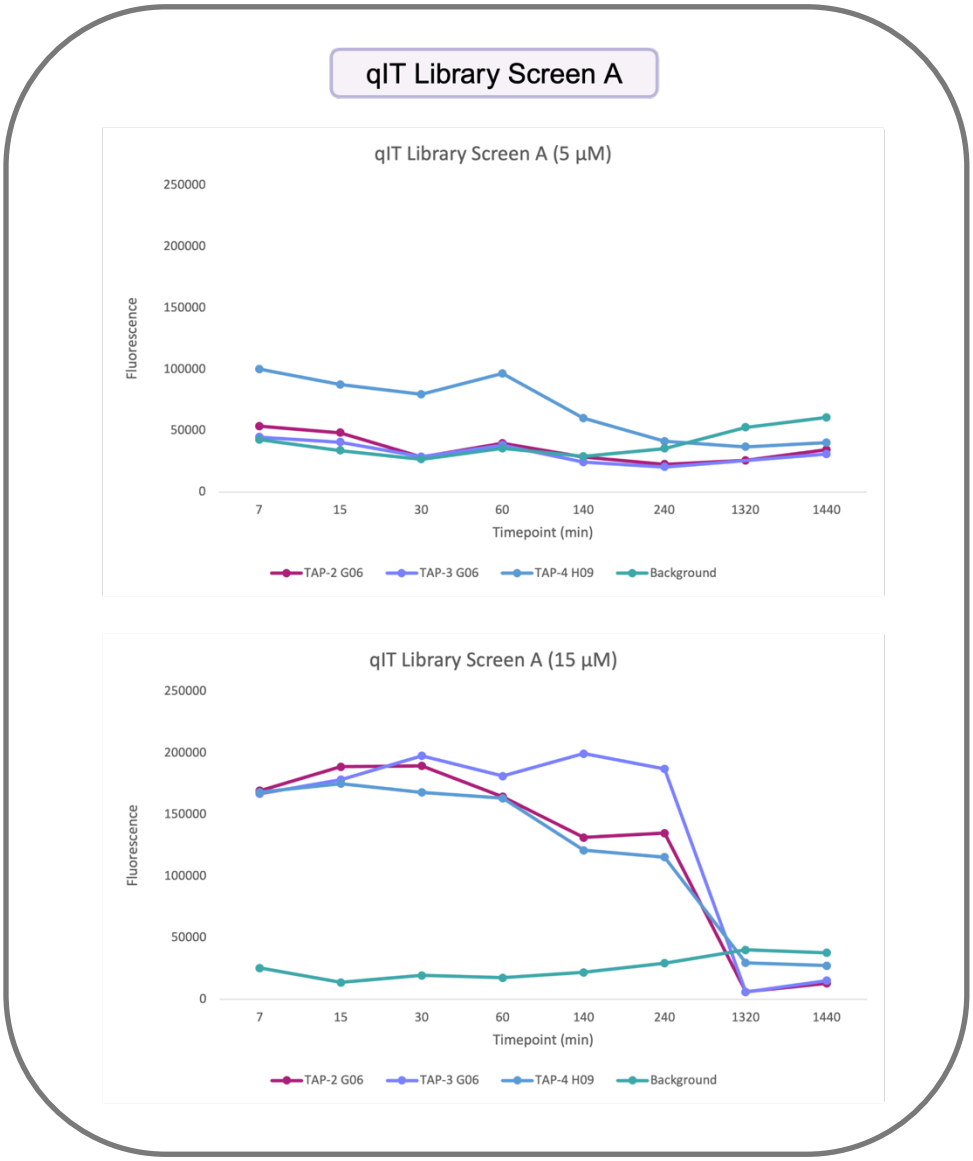


Figure 45: qIT Screen A, displaying the fluorescence values detected in comparison to the background (assay buffer) at both **a)** 5 µM and **b)** 15 µM concentrations.

Figure 45 compares the raw fluorescence readings at 15 µM and 5 µM, derived from the reaction between the respective acrylamide and **SS1**. Readings from the fragments highlighted signify an overarching trend that at a peptide concentration of 5 µM, the difference in fragment signal in comparison to the background noise is insignificant. At a 5 µM **SS1**, CPM produces a weak fluorescence signal upon quenching of the reaction. This close similarity between reaction fluorescence and the background noise gives rise to a false portrayal of reactivity, whereby fragments appear to react with **SS1** at a faster rate than in actuality.

This was validated by the direct comparison of fragment readings from the 15 μM screen, where the fluorescence reading was on average an order of magnitude greater than at 5 μM. Employing a 15 μM peptide concentration allows a greater difference to be observed against the background noise, in turn generating a more reliable data set upon background correction.

Despite the improved fluorescence readings at 15 μM, the overnight timepoints generated seemingly abnormal readings. The raw fluorescence values at the 1320- and 1440-minute timepoints were in a similar range to the background noise signal. A likely explanation was the suspected oxidation of **SS1** during overnight incubation of the assay plate. This indicated that perhaps conventional qIT assay conditions of using 0.5% TCEP as the reducing agent was not sufficient in this instance. Thus, moving forward, further optimisation of this assay was designed retaining the use of 15 μM **SS1**, with increased TCEP to rectify any possible oxidation.

The qIT to FA assay variant was initially trialled where an aliquot from the qIT reaction plate was taken at the 1440-minute timepoint and screened with BCL-X_L and FAM-Bak$^{72\text{-}87}$ in a competition format. However, as the qIT reaction plate appeared prone to thiol oxidation at the overnight timepoints, any readings derived from this may not be a true representation of binding affinity towards BCL-X_L and hence must be additionally verified. Further optimisation of this FA assay was not pursued until the qIT assay conditions were further developed.

2.6.2.2 Screen B - Remediating Thiol Oxidation

The next stage of assay development aimed to remediate the suspected thiol oxidation occurring at extended reaction timepoints. For this purpose, it was deemed unnecessary to screen all 320 fragments, but rather more efficient to continue optimisation with a modest fragment library. As such, out of the 320 fragments previously screened, 10 were selected for further development (Screen B). These fragments either displayed potential affinity in the previously trialled FA assay or complete lack thereof; it is worth noting that as previously discussed these readings may not have been a true representation of binding affinity. Nevertheless, these fragments were screened in a qIT assay where 15 μM **SS1** was used in conjunction with 1% TCEP- increased from the 0.5% employed in the previous screen (**Figure 46**).

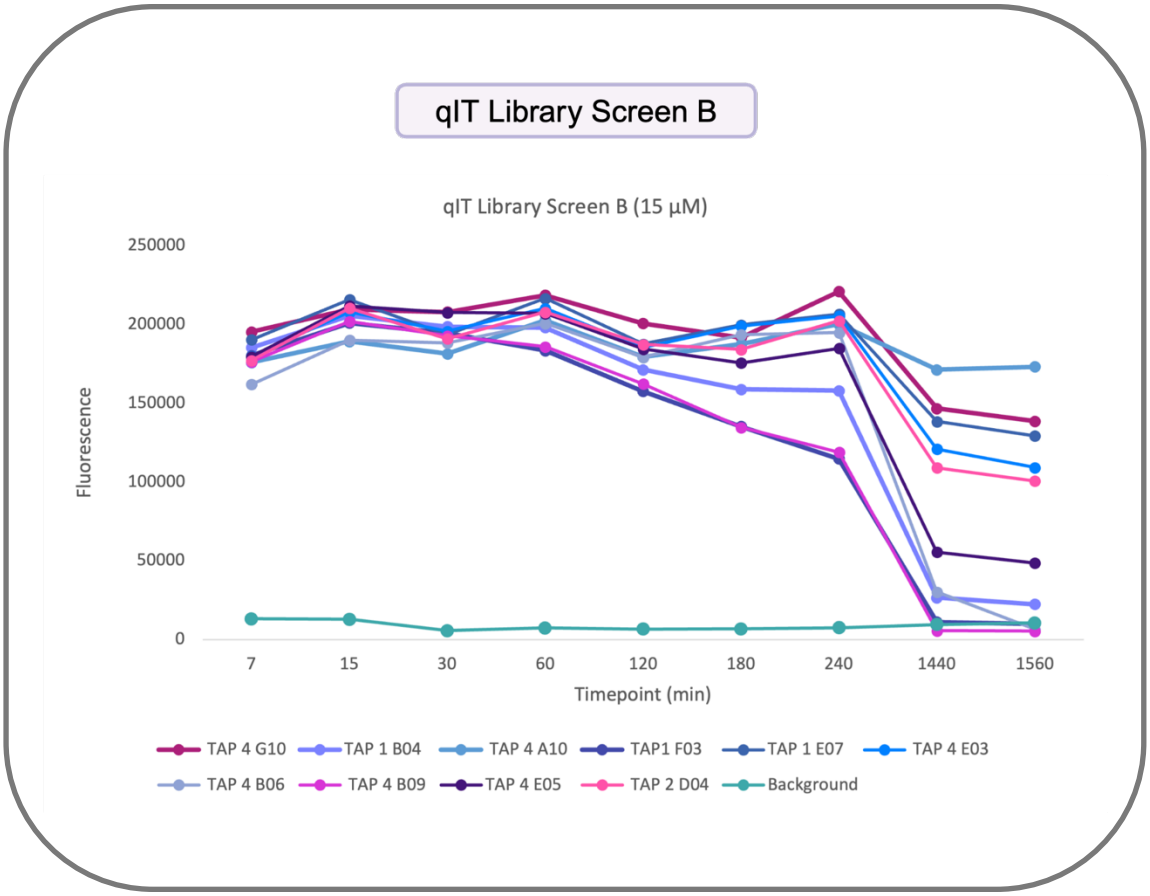


Figure 46: qIT Screen B employing 15 µM SS1 and 1.0 % TCEP.

Figure 46 displays the results of this endeavour, comparing the raw fluorescence readings to the background noise. This dataset demonstrates that by using a higher quantity of TCEP to mitigate thiol oxidation, the readings at overnight timepoints (t = 1440, 1560 min) have a much better signal-to-noise ratio than the previous screen. These results provide confidence that low fluorescence readings can be attributed to fragment reactivity, as opposed to thiol oxidation.

2.6.2.3 Screen C - Preliminary Optimisation of qIT to FA

The assay development efforts detailed above successfully established optimal reaction conditions, whereby the ideal concentrations of **SS1**, CPM and TCEP were determined. As such, the ensuing optimisation attempts were primarily targeted towards cultivating the qIT to FA assay format. The premise behind this would be that the 'new' peptide library generated from the reaction between the **SS1** and the acrylamide fragments, could successfully be evaluated in a FA competition format. Aliquots taken from the qIT reaction plate at the final assay timepoint would be screened with BCL-X_L and FAM-Bak$^{72\text{-}87}$, in an attempt to generate an inhibitor with greater affinity towards BCL-X_L than the 'naked' peptide mimetic.

Development of this assay format entailed repeating the previous qIT screen (Screen C), with the addition of transitioning into an FA competition assay upon completion of the final quench step. An aliquot from the qIT reaction plate was taken at t = 1500 min and used to prepare a series of dilution plates, with a final assay concentration range of 5 μM to 0.16 μM. This was then mixed with BCL-X_L (100 nM) and FAM-Bak^{72-87} (1 nM), prior to a 20-minute covered incubation. Finally, the anisotropy values were measured, with the results of this endeavour highlighted in **Figure 47** and **Figure 48.**

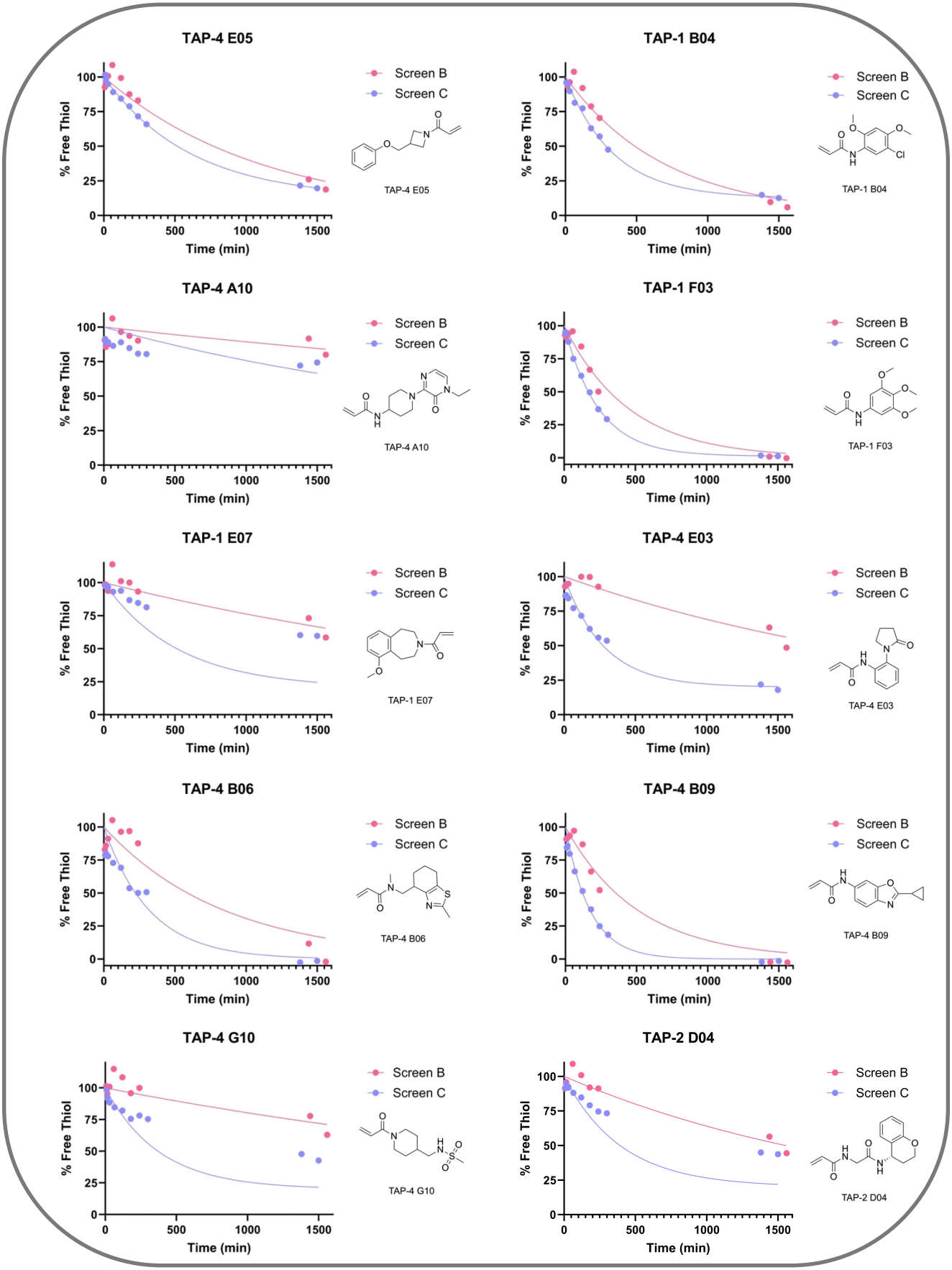


Figure 47: qIT Screen C employing 15 μM SS1 and 500 μM acrylamide. The variation in reactivity of acrylamide fragments between Screen B and C are highlighted.

Figure 47 highlights the comparison between the qIT data from the previously run screen (Screen B) to the current screen (Screen C). The featured graphs emphasise that whilst the majority of the results are reproducible to a reasonable degree (e.g. TAP-1 B04, TAP-1 F03, TAP-4 B09 etc), there still seems to be a degree of variation (e.g. TAP-4 E03, TAP-1 E07) that requires further investigation.

Figure 48 below however, displays the more pressing issue – the poor data quality stemming from the FA competition assay.

FA Screen

Concentration (μM)	5	2.5	1.25	0.63	0.31	0.16
TAP- 4 G10	49	75	73	95	133	143
TAP- 1 B04	-26	6	1	21	54	63
TAP- 4 A10	47	77	70	98	134	143
TAP- 1 F03	35	60	47	79	111	120
TAP- 1 E07	53	43	41	72	102	124
TAP- 4 E03	32	74	76	98	132	133
TAP- 4 B06	36	62	63	94	127	152
TAP- 4 B09	32	67	66	88	119	142
TAP- 4 E05	4	19	19	32	90	89
TAP- 2 D04	38	75	71	93	132	155
Negative control	-12	8	22	9	41	18
Positive control	36	63	75	100	138	142
Z'	-0.95	0.04	-0.05	0.47	0.47	0.65

Figure 48: FA results analysing SS1 functionalised with TAP acrylamide fragments (5 - 0.16 μM), using FAM-Bak$^{72-87}$ (1 nM) and BCL-X_L (100 nM). The negative control (blue) is comprised of FAM tracer, reaction buffer and DMSO (DMSO is an aliquot from qIT reaction plate). The positive control (green) is comprised of FAM tracer, BCL-X_L and naked SS1 (SS1 is an aliquot from qIT reaction plate). The Z' values for each dilution plate are highlighted in red.

This dataset features negative anisotropy values, as well as a poor assay window. This poor assay window is a direct result of the insufficient gap between the positive and negative controls, particularly at higher concentrations. This gives rise to subpar Z prime (Z') values, as calculated through the following equation (**Equation 2**)

$$Z' = 1 - \frac{3\sigma_p + 3\sigma_n}{(\mu_p - \mu_n)}$$

Equation 2: Z' equation. σ_p and σ_n refer to the standard deviations of the positive and negative controls, respectively. μ_p and μ_n represent the means of the positive and negative controls, respectively.

The Z' factor, introduced by Zhang *et al* [118] is a statistical tool often used for assay optimisation and validation. The Z' score allows the quality of an assay to be assessed, which can inform further assay development. Typically, an assay is deemed ideal if it produces a Z' score of 1; the closer the value is to 1 generally indicates that the assay is of a higher quality. Assays with Z' values between 0.5 and 1 are also considered as good quality, with values between 0.5 and 0 considered sub-optimal to poor. Assays with negative Z' values cannot be used.

As the majority of Z' values for the FA assay were either close to 0 or below 0.5, the quality of the assay was categorised as poor and hence unacceptable. Analysing the subpar dataset clearly indicated that the upper limit of the assay was insufficient and required improvement. Thus, the FA assay conditions required further investigation, in order to generate an optimal assay window, where the anisotropy values produced could be used with confidence.

A potential reason for the poor anisotropy values was that perhaps the concentration of tracer employed was not sufficient enough to produce a strong fluorescence signal. Increasing this concentration may lead to an increase in anisotropy values, especially with respect to the positive control, and hence could increase the overall assay window.

2.6.2.4 Screen D - Further Development of qIT to FA

The ensuing qIT to FA assay was designed with the purpose of trying to increase the FA assay window and hence the Z' factor. The condition trialled for this purpose was to increase the final assay concentration of FAM-Bak$^{72-87}$ from 1 nM to 3 nM, whilst retaining the formerly established concentrations of all other reagents. The acrylamide library in this instance was comprised of 3 fragments, selected from the previous library of 10 fragments, in an effort to increase efficiency. An aliquot from the qIT reaction plate (t = 1500 min) was used to prepare two-fold serial dilution plates, with a final assay concentration range of 2.5 μM to 0.16 μM. This was then mixed with BCL-X_L (100 nM) and FAM-Bak$^{72-87}$ (3 nM), with the results this endeavour highlighted below in **Figure 49**.

FA Screen

Concentration (μM)	2.5	1.25	0.63	0.31	0.16
TAP- 1 B04	43	49	63	89	125
TAP- 4 E05	58	74	93	127	155
TAP- 2 D04	175	177	190	196	195
Negative control	26	27	24	27	28
Positive control	112	133	157	179	186
Z'	0.69	0.91	0.86	0.90	0.93

Figure 49: FA results analysing SS1 functionalised with TAP acrylamide fragments (2.5-0.16 μM), using FAM-Bak$^{72-87}$ (3 nM) and BCL-X_L (100 nM). The negative control (blue) is comprised of FAM tracer, reaction buffer and DMSO (DMSO is an aliquot from qIT reaction plate). The positive control (green) is comprised of FAM tracer, BCL-X_L and naked SS1 (SS1 is an aliquot from qIT reaction plate). The Z' values for each dilution plate are highlighted in red.

The anisotropy values in this dataset clearly demonstrate that the increase in tracer concentration was able to successfully open the assay window, with a Z' score above 0.5 for each assay plate.

Figure 50 below displays these results in a graphical format, where the raw anisotropy values have been background corrected (**Figure 50a**) and normalised (**Figure 50b**) against the positive control ('naked' **SS1**).

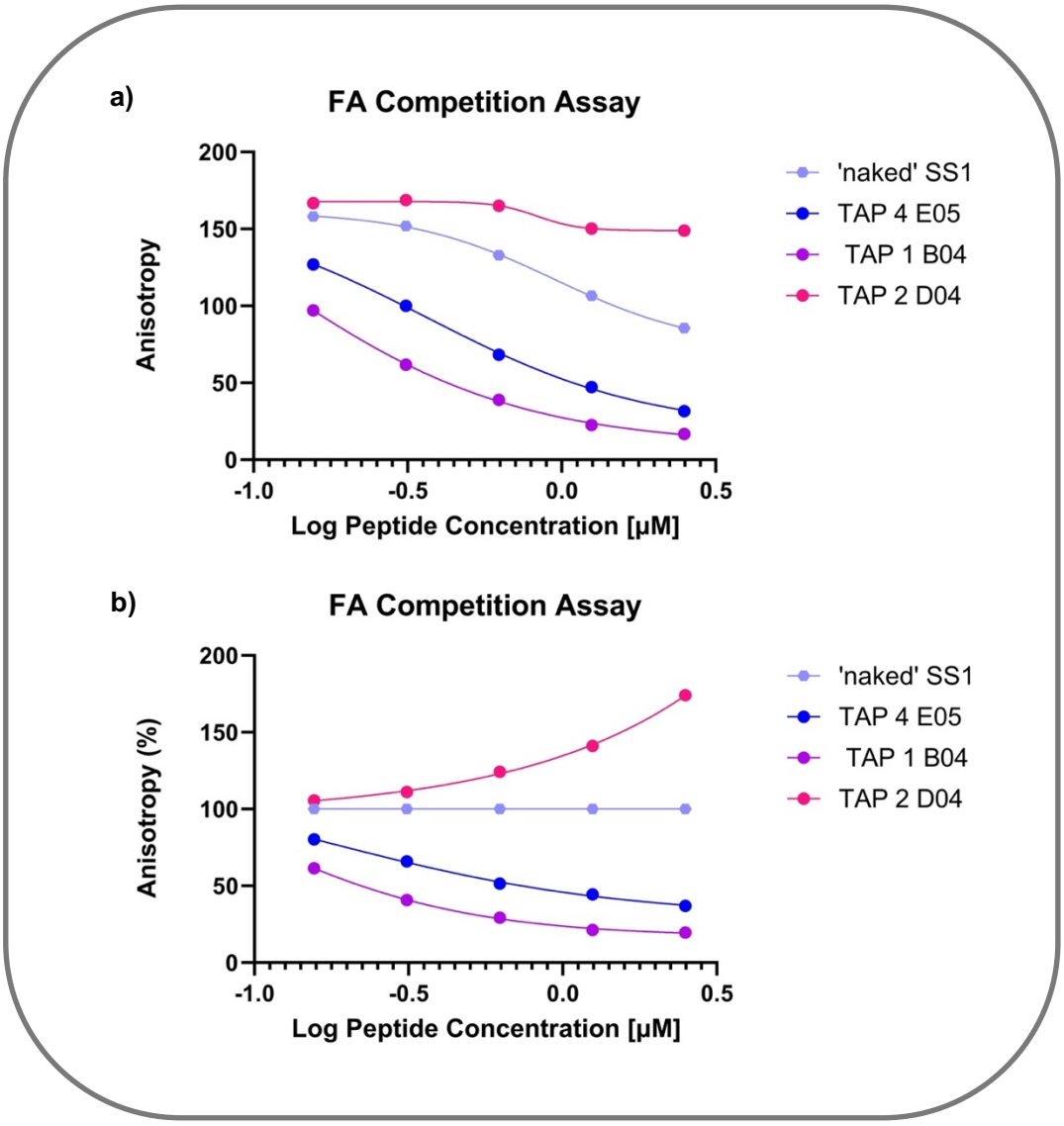


Figure 50: FA competition binding curves. (A) Raw anisotropy values (background corrected) of SS1 functionalised with TAP-4 E05, TAP-1 B04 & TAP-2 D04, plotted against 'naked' SS1. (B) Normalised anisotropy in the context of 'naked' SS1.

The background corrected anisotropy values (**Figure 50a**), when graphically plotted, allows the comparison between functionalised peptides and the positive control, with respect to the binding affinity towards BCL-X_L. Yet it is the normalisation (**Figure 50b**) that allows a more straightforward comparison.

The normalisation allows the anisotropy values of the functionalised mimetic to be put into context with respect to the affinity of the 'naked' peptide mimetic (**SS1**). A value near 100% indicates that the binding affinity towards BCL-X_L has not been improved over the 'naked' peptide. On the other hand, if the value is closer to 0 it indicates an improvement in binding affinity. Values over 100% indicate that the binding affinity is worse than the 'naked' peptide.

For a functionalised mimetic to be classified as a hit, it would be expected that at higher concentrations, the normalised anisotropy value would be low (i.e. closer to 0 than 100). This would steadily rise as the concentration of the functionalised peptide mimetic decreased. This increase in anisotropy with decreasing concentrations of functionalised SS1 is a consequence of displacement by the tracer (FAM-$Bak^{72\text{-}87}$). The tracer is now able to retain a higher degree of polarisation owing to a decrease in Brownian molecular rotation.[109] The assay curves seen in **Figure 50** indicate that functionalised peptides with TAP-1 B04 & TAP-4 E05 fragments, have an increased binding affinity towards BCL-X_L compared to the unfunctionalized SS1 peptide. The opposite trend is seen with a TAP-2 D04 functionalised peptide.

As the conditions for the qIT to FA assay have been established to a reasonable standard, the following phase was to employ these conditions in a high-throughput screen using peptides **SS1** and **SS4**, in an effort to identify potent inhibitors of the BCL-X_L / Bak PPI.

2.7 SS1 High-Throughput Screen

2.7.1 Acrylamide Library Screen

2.7.1.1 Screen E - Primary Library Screen

SS1 was screened with the acrylamide library previously used in Section 2.6.2 featuring 320 diverse fragments, in order to generate a new library of functionalised peptide mimetics (Screen E). This new library was subsequently evaluated in a FA competition assay, with an extended peptide concentration range (2.5 μM – 0.02 μM), in an effort to generate BCL-X_L binding curves. Despite the seemingly positive results, upon comparison of the previously screened TAP-1 B04, TAP- 4 E05 & TAP-2 D04 functionalised peptides, variation in both the qIT and FA data was observed (**Figure 51**). The extent of this variation was unanticipated as the reagent conditions and assay protocol from the previous screen (Screen D) remained the same.

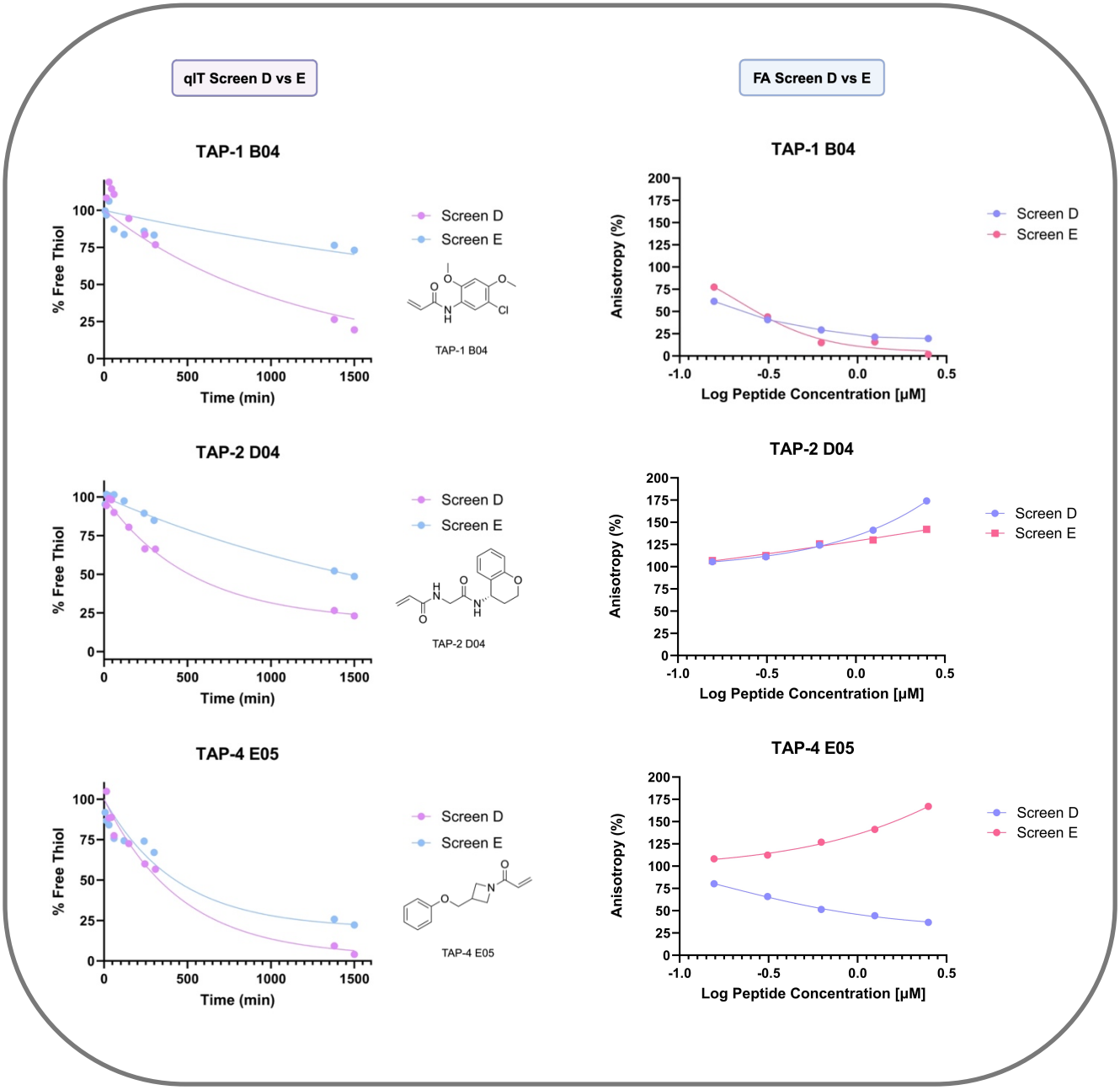


Figure 51: A comparison of the qIT and FA data from library screen D and E.

The variation between the qIT screens D & E is most prominent for TAP-1 B04, yet this does not translate into a corresponding variation in the FA Screen, as it is TAP-4 E05 that displays a significant difference between FA screens D & E. However, a caveat worth consideration was that only 3 fragments/functionalised peptides were comparable; this doesn't allow a full comparison between the two screens. Therefore, the contrasting data observed may not be an accurate representation of overall assay reproducibility.

It was imperative to discern whether the inconsistency was due to an inherent variability associated with this high-throughput screen, or a result of a deeper root cause.

2.7.1.2 Screen F - Repeat of Primary Library Screen

The full screen was thus repeated (Screen F), with a few key results from the qIT screen highlighted below (**Figure 52**).

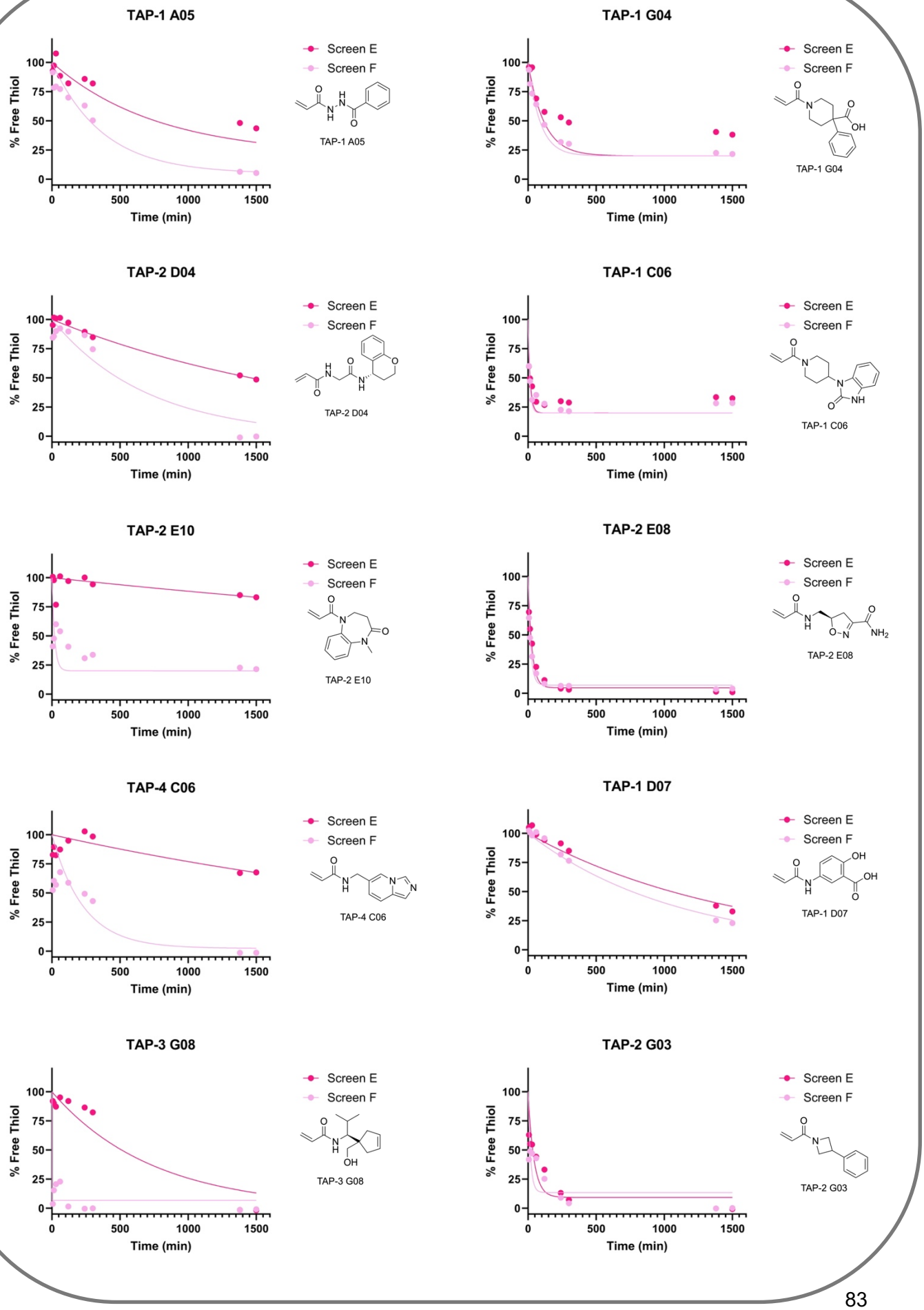


Figure 52: A comparison of fragment reactivity from qIT Screen E and F.

The data graphically displayed in **Figure 52** clearly emphasises the irregularity detected between the two qIT datasets (Screen E & F). Interestingly, the irregularity between the datasets does not extend to all functionalised peptides in the library. The qIT results for **SS1** functionalised with fragments such as TAP-1 G04, TAP-2 E08 & TAP-2 G03, seem to display excellent reproducibility between the two screens. This is in stark contrast to peptides functionalised with fragments such as TAP-2 E10, TAP-4 C06 & TAP-3 G08, which display severe variation from one dataset to another.

Upon further analysis of the two datasets, it appears as though fragments in Screen F display greater reactivity with **SS1**, in comparison to Screen E. The lower percentage of free thiol upon completion of the assay (t = 1380, 1500 min) is indicative of greater reactivity, determined by the low fluorescence upon CPM quench. This implies that in Screen F there is less 'free thiol' in each respective fragment well for CPM to react with, in comparison to Screen E.

This notable discrepancy in reactivity also appears to be independent of the assay quality associated with each screen. The Z' scores for each timepoint, in both Screen E & F, were approximately 0.8 and above. This gives rise to the belief that the root cause of the fluctuation may lie with an uncontrolled variable, as opposed to the assay setup.

The lower fluorescence of CPM at various timepoints in Screen F, particular at the t= 1380 &1500 min, is indicative of a lack of 'free' **SS1** for it to react with. A potential reason why this could be greater in Screen F, compared to Screen E, is the temperature at which the assay was conducted at. The standard protocol for the qIT assay is for it to be conducted at 'room temperature'. However, it is the fluctuation in said 'room temperature' that seems to be an uncontrolled variable. If the temperature at which Screen F was conducted at was lower than Screen E, it could lead to a decrease in solubility of **SS1** in the reaction solution. This decrease in solubility would in turn affect the amount of **SS1** present in solution, available for CPM to react with. Therefore, perhaps this assay has an increased sensitivity to deviations in temperature than initially anticipated. A way to test this hypothesis and potentially remediate this issue, would be to store the qIT reaction and quench plates in a temperature-controlled environment, providing a fixed 'room temperature'. This would ensure consistency across all screens and eliminate any temperature variability.

Surprisingly, the irregularity observed in the qIT screens does not directly correlate to variation in the FA assay, as shown below in **Figure 53**.

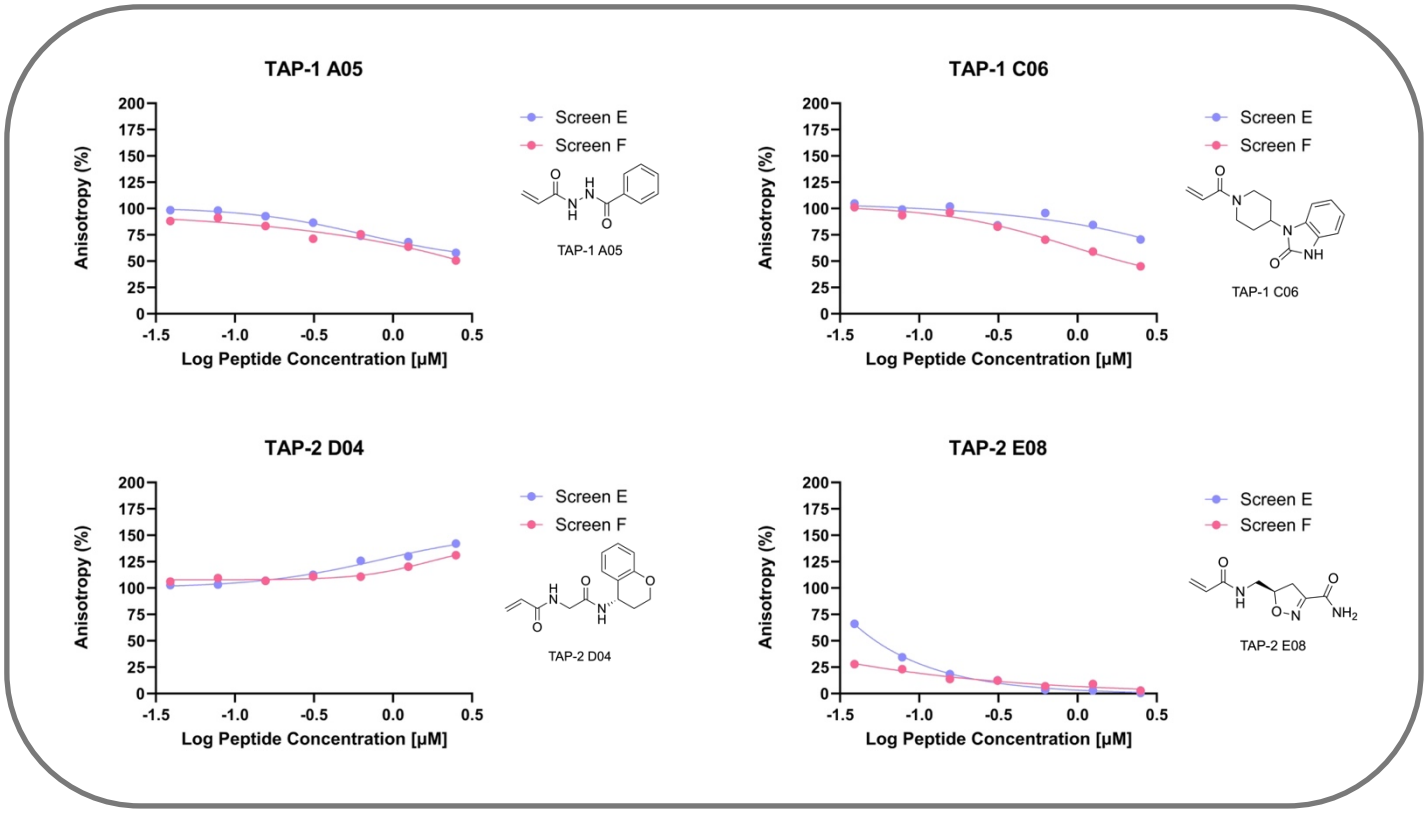


Figure 53: A comparison of the FA binding curves from Screen E and F (peptide dilution range 2.5-0.04 μM).

As seen in **Figure 53**, fragments such as TAP-1 A05 & TAP-2 D04, which produced variable qIT results, seem to maintain a good degree of reproducibility when the FA assays from Screen E & F were compared. Interestingly, a few fragments that displayed minimal fluctuation between qIT datasets had a more pronounced variation in the FA assays, e.g. TAP-1 C06 & TAP-2 E08. However, considering that a qIT aliquot (t=1500 min) is used for the FA assay, the disparity in the FA datasets cannot be clearly elucidated until the qIT variability is resolved.

Despite this array of variable data, a few examples were found where the functionalised peptides not only displayed greater binding affinity towards BCL-X_L than the naked peptide, but also predominantly displayed comparable anisotropy values between the two FA screens. Additionally, the qIT data from the 1500 min timepoint, representing the percentage of free thiol remaining, was reasonably similar (**Figure 54**).

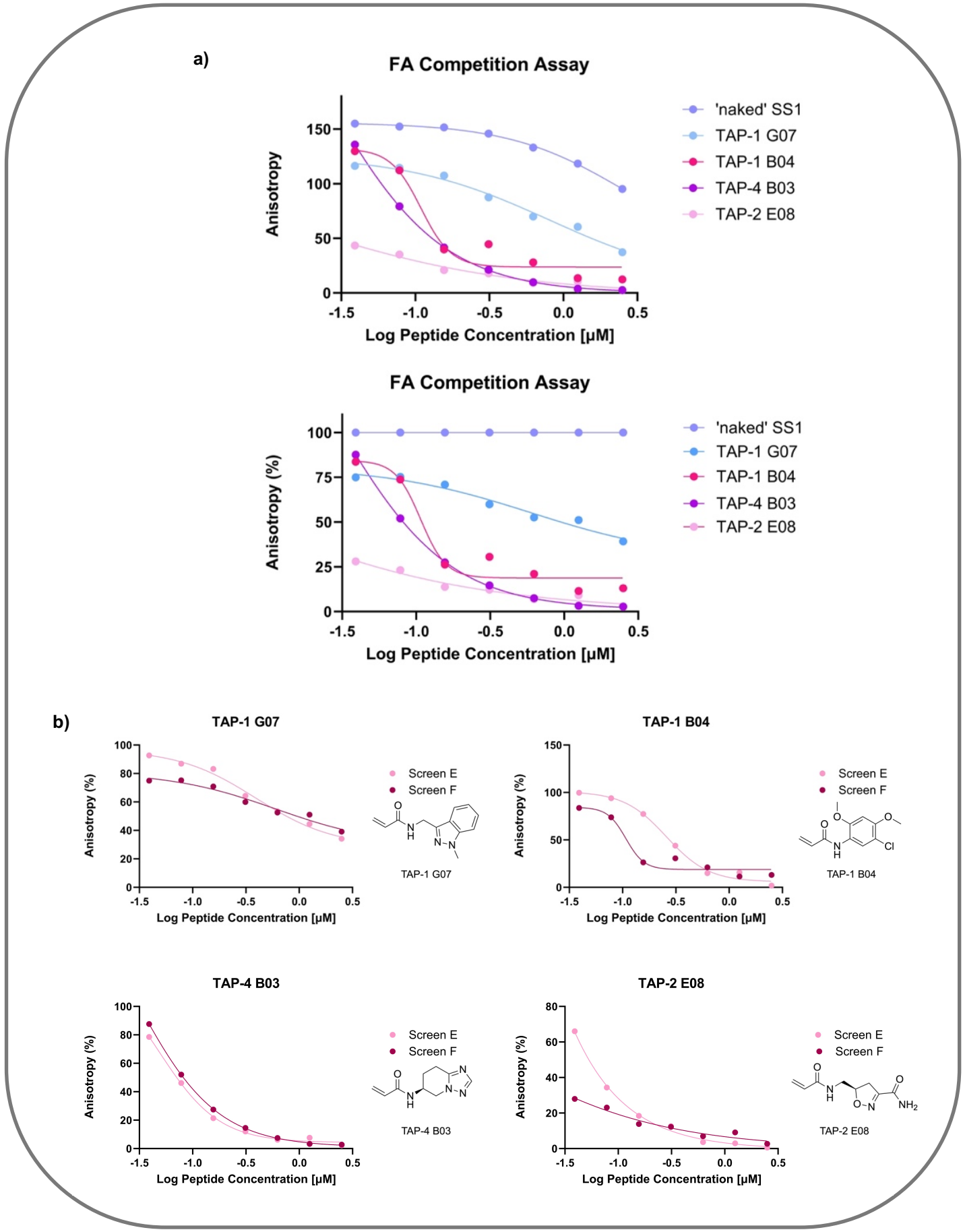


Figure 54: a) FA competition binding curves of hit mimetics both background corrected (**top**) and normalised (**bottom**). **b)** Comparison of anisotropy values of hit mimetics from Screen E and F.

Figure 54a highlights the increase in binding affinity towards BCL-X_L, in comparison to the 'naked' peptide, for **SS1** functionalised with TAP-1 G07,TAP-1 B04, TAP-4 B03 & TAP-2 E08. This is also displayed in a format where this affinity is normalised in the context of the 'naked' peptide.

This normalisation is what allows a straightforward comparison of anisotropy between different screens (Screen E & F), independent of the control values within each assay. Using this method, the anisotropy values (compared to the 'naked' peptide) of the 4 'hit' compounds were compared between the two screens (**Figure 54b**). The hit fragments identified are all of a comparable size, with molecular weights ranging between 192-242 Da. All fragments possess a cyclic moiety, with the majority of fragments also containing aromatic/heteroaromatic functionality. At this stage the reproducibility between the screens, particularly at high peptide concentrations, is sufficient to where the hits can be further investigated with confidence.

These functionalised peptides will thus be utilised to further optimise the qIT and FA screens, in order to reduce such prominent variability in data. The hit acrylamide fragments, functionalising **SS1**, will also be employed in the development of the target-directed qIT screen, and serve as positive controls.

2.8 SS4 High-Throughput Screen

2.8.1 Acrylamide Library Screen

Following the aforementioned evaluation of **SS1** in a high-throughput screen (Section 2.7), **SS4** was subsequently evaluated through the same qIT to FA format; the reagent concentrations were also kept consistent. The objective of this screen was to identify 'hit' fragments that when covalently bound to **SS4**, result in an increased binding affinity towards BCL-X_L, compared to the 'naked' **SS4** mimetic. The ultimate goal, as stated in the introduction to this chapter (Section 2.1), would be to employ these hits as controls in the target-directed variant of the qIT assay.

Hence, **SS4** was initially screened in a qIT assay with the same library **SS1** was screened against; this acrylamide library featured 320 fragments with a large chemical diversity. This screen formed a new library of functionalised **SS4** mimetics, which were subsequently evaluated in a FA competition assay, to produce a series of BCL-X_L binding curves. A few key examples are highlighted below in **Figure 55**.

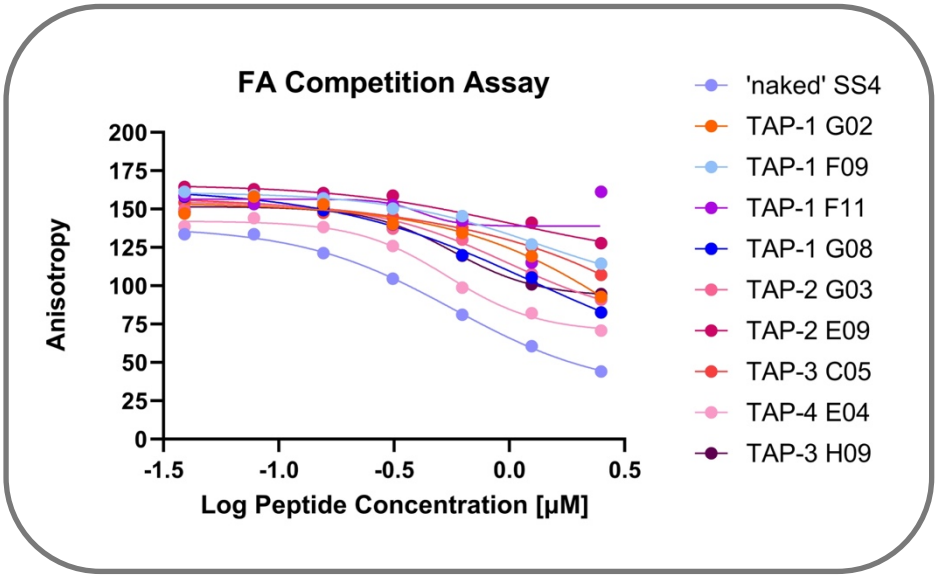


Figure 55: FA competition binding curves for functionalised SS4 mimetics.

The anisotropy results highlighted in **Figure 55** represents a trend with respect to the affinities of functionalised **SS4** mimetics towards BCL-X_L. The vast majority of this newly generated peptide library displays a decreased affinity towards BCL-X_L, in comparison to the unfunctionalized 'naked' **SS4** mimetic. The binding curves displayed in **Figure 55** are comprised of functionalised

mimetics with the greatest decreases in binding affinity. Peptides functionalised with TAP-1 F11,TAP-2 E09 & TAP-1 F09 exhibit the most notable decrease in binding affinity when compared to the 'naked' **SS4** mimetic.

These results elucidate that predominantly substitutions at the Ile^{85} hot spot position, with fragments in this acrylamide library, are not well tolerated. This is in contrast to substitutions at the Val^{74} position (**SS1**), where an increase in binding affinity was clearly observed.

A select few examples were found that displayed a slight improvement over the unfunctionalized 'naked' **SS4** mimetic (**Figure 56**).

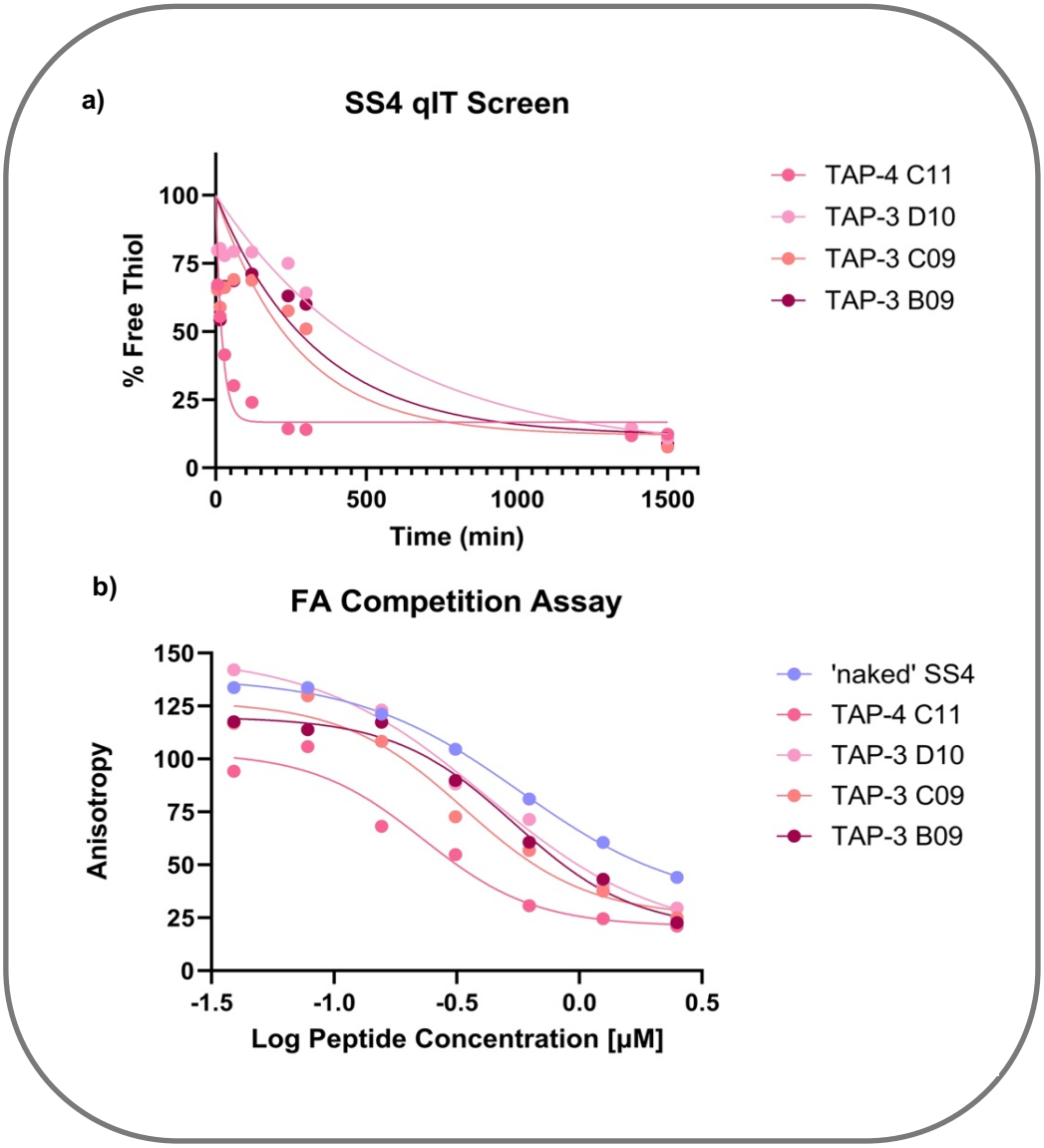


Figure 56: **a)** Reactivity of hit acrylamide fragments. **b)** FA binding curves results of hit mimetics.

The reactivity of acrylamide fragments TAP-4 C11, TAP-3 D10, TAP-3 C09 & TAP-3 B09 is shown in **Figure 56a**, with the binding curves of **SS4** furnished with these fragments displayed in **Figure 56b**. From these binding curves it is evident that substitutions at the Ile^{85} hot spot position yield only a slight increase in binding affinity, with a TAP-4 C11 functionalised peptide possessing the greatest increase.

To determine whether the lack of a significant increase in affinity towards BCL-X_L is related to the nature of fragments present in the acrylamide library, or if is a universal effect of substitution at the Ile^{85} hot spot, additional testing is required. Thus, a future goal would be to repeat this **SS4** screen with additional electrophilic libraries, in an effort to deduce the effect that modifications to this hot spot position have on binding affinity towards BCL-X_L.

Nevertheless, the positive and negative results obtained will serve to inform the target-directed screen, where examples of increased and decreased binding affinity will be known.

2.9 Conclusions and Future Outlook

This chapter reported on the development of a qIT to FA assay format, the ultimate aim of which was to identify potent inhibitors of the BCL-X_L/BAK PPI. The inhibitors identified would serve to inform the target-directed variant of this assay, as detailed in the introduction to this chapter.

To ensure compatibility with the qIT assay, WT BCL-X_L was successfully mutated to a cysteine free construct (Δ45-84, domain 1-209, C111S) via SDM. This allowed the 'naked' peptide mimetics **SS1** and **SS4** to remain the only sources of nucleophilic thiol.

These peptides constituted a small library of peptide mimetics where hot spot positions on BAK (Val^{74}, Leu^{78}, Ile^{81} and Ile^{85}) were substituted with a cysteine residue. The baseline binding affinity of mimetics **SS1**, **SS2**, **SS3** & **SS4** was subsequently determined through FA competition studies, confirming that replacement of hot spots leads to a reduction in binding affinity.

The qIT to FA assay was subjected to extensive development, where the optimal reagent concentrations were established, using **SS1** as the model mimetic. Having determined these conditions, **SS1** was screened with an electrophilic library, featuring 320 acrylamides with a large chemical diversity. Despite previously establishing the optimal assay conditions, significant variably was observed upon repetition of this high-throughput screen. It was hypothesised that the assay's sensitivity to fluctuations in temperature may be more pronounced than initially envisioned- a variable that had not been previously controlled. Thus, to investigate this further the screen would be repeated, with the qIT plates stored in a temperature-controlled environment, in an effort to eliminate any temperature variability.

Nevertheless, a few hits were found where a significant improvement in binding affinity towards BCL-X_L was observed. These hits will be further investigated and employed for the continued optimisation of both qIT and FA screens. In order to draw further conclusions on key structural features required for binding, the screen must be repeated once reproducibility is no longer a concern, following which the composition of resultant hits can be analysed. The identity of said hit compounds would be further validated through mass spectrometry, in order to confirm the desired peptide-fragment conjugation has taken place and is indeed the reactive species. Once validated, the hit fragments will function as controls for the development of the target-directed qIT screen.

SS4 was also evaluated in a high-throughput screen, under the same assay format as **SS1**, where it was ascertained that substitution at the Ile^{85} position was not well tolerated. The vast majority of functionalised peptide mimetics led to a decrease in binding affinity, when compared to the unfunctionalized **SS4** mimetic. In spite of this, a few mimetics were identified where the functionalisation of **SS4** led to a slight improvement in binding affinity. Ultimately, both the positive and negative hits will be used inform the development of target-directed qIT screen.

The next phase of assay development entails the evaluation of mimetics **SS2** and **SS3** in a high-throughput screen, as previously executed for **SS1** and **SS4**, in order to identify inhibitors of the BCL-X_L/BAK PPI.

Once each hot-spot position is screened in this manner, the mimetics identified which exhibit increased binding affinity will serve as positive controls for the target-directed assay variant. The hit compounds will inform the development of this novel assay, where they will serve as a tool by which the results generated will be compared against. This allows appropriate fragments screened in the target-directed assay to be aptly classified as hit compounds, facilitating future lead generation.

Chapter 3

Design and Synthesis of Hybrid Mimetics

3.1 Introduction and Objectives

PPI mediation through α-helix mimicry is a prominent strategy, by which synthetic building blocks are combined in a manner that aptly imitates the spatial arrangement of key residues found in the native interaction.[119] Despite this widely adopted strategy, there is a lack of chemical diversity in relation to the groups used to mimic key hot-spot residues. These groups often functionally or structurally resemble the side chains found on said hot-spot residues,[62] as opposed to potentially exploring alternate interactions with the target protein. Additionally, these groups are frequently introduced early on in the synthetic pathway, which combined with arduous synthetic protocols, makes developing novel building blocks a challenging feat.[63] Furthermore, these mimetics often lack selectivity for the target protein without covalently trapping the helix mimetic to the protein of interest. This therefore hinders the ability of these mimetics to exploit alternative interactions with the target protein.

The current array of α-helix mimetic scaffolds in the literature includes terphenyl derivatives,[64] aromatic oligoamides,[120] terpyridines[121] and benzoylureas[122] among others. These scaffolds either involve complex synthetic methodologies, such as for terphenyls, or require the synthesis of multiple monomeric building blocks, as in the case of aromatic oligoamides.[63] These features place limitations on the use of these scaffolds as global tools for the inhibition of diverse PPIs, as well as on their compatibility with high-throughput strategies.

The hybrid α-helix mimetic detailed in this chapter was designed to address the limitations of scaffolds present in the literature. This chapter therefore reports on the approach for the design and synthesis of the proposed α-helix mimetic, furnished with a thiol serving as a ‘clickable handle’, to allow for late-stage functionalisation. The foundation of this approach was based on a rationally designed monomeric building block, where the primary focus lay in the development of the clickable handle, as seen in **Figure 57**. The strategy behind the development of a multi-step synthetic route to said monomer is described in great detail, particularly with respect to compatibility with SPPS techniques.

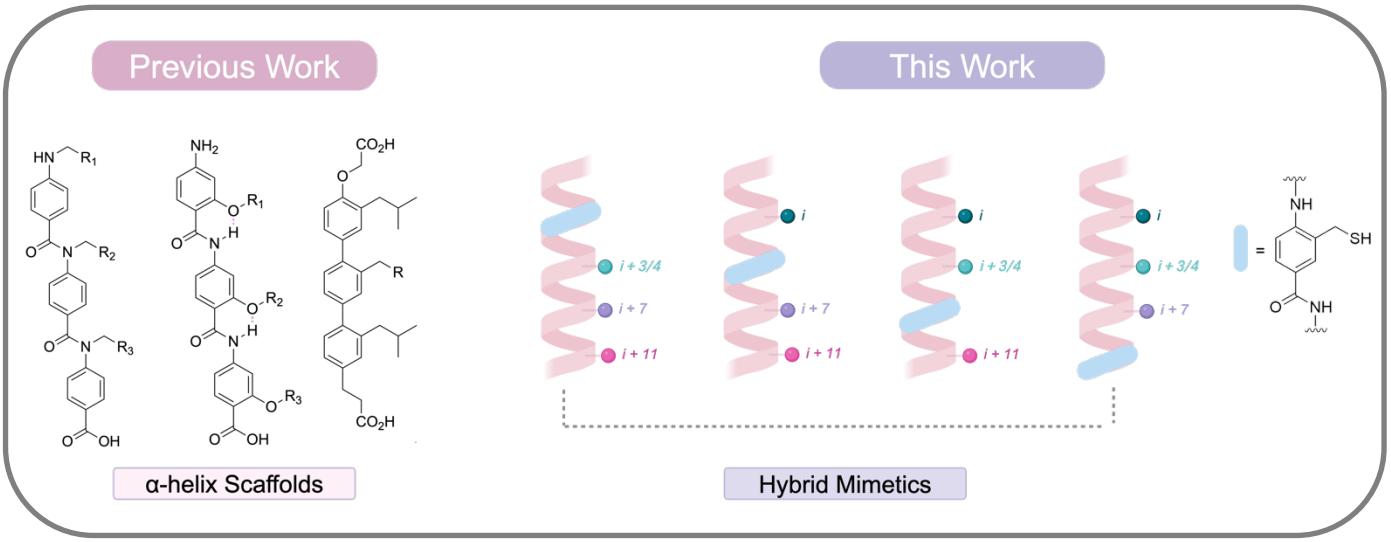


Figure 57: α-helix mimetic scaffolds present in the literature, in comparison to the novel hybrid approach detailed in this chapter where a functionalised monomer replaces a turn in the native BAK helix.

The hybrid feature of the mimetic is what allows it to harness the natural selectivity of the target protein. By conserving the majority of the native targeting peptide sequence and replacing one turn of the α-helix with the functionalised monomer, a degree of selectivity can be retained. Harnessing the natural selectivity of the native peptide ligand towards the target protein allows the clickable handle to come into close proximity towards the binding cleft, allowing it to react preferentially with fragments that have an affinity for said interface. This paves the way for a novel target-directed approach to be developed, as highlighted in the previous chapter.

The monomeric building block, highlighted in **Figure 58**, was designed in a manner such that it is possessed compatibility with traditional peptide synthesis techniques. Exploiting an orthogonal protection strategy, by way of using Fmoc and Trityl groups, enables the target monomer to be easily incorporated into a peptide ligand, generating the desired hybrid mimetic.

The clickable thiol handle on the proposed hybrid mimetic makes it amenable to high-throughput strategies. This would entail screening the mimetic with large electrophilic compound libraries using the qIT assay detailed in previous chapters. This essentially allows an extensive α-helix mimetic library to be rapidly generated upon the reaction of the clickable handle with an array of electrophilic fragments, covering a large chemical space. The inhibitory activity of these mimetics would then be investigated through fluorescence anisotropy, as shown in **Figure 58**, where ligands identified in the primary screen would inform fragment selection for further screens, guiding the optimisation of ligands capable of efficiently disrupting the PPI of interest.

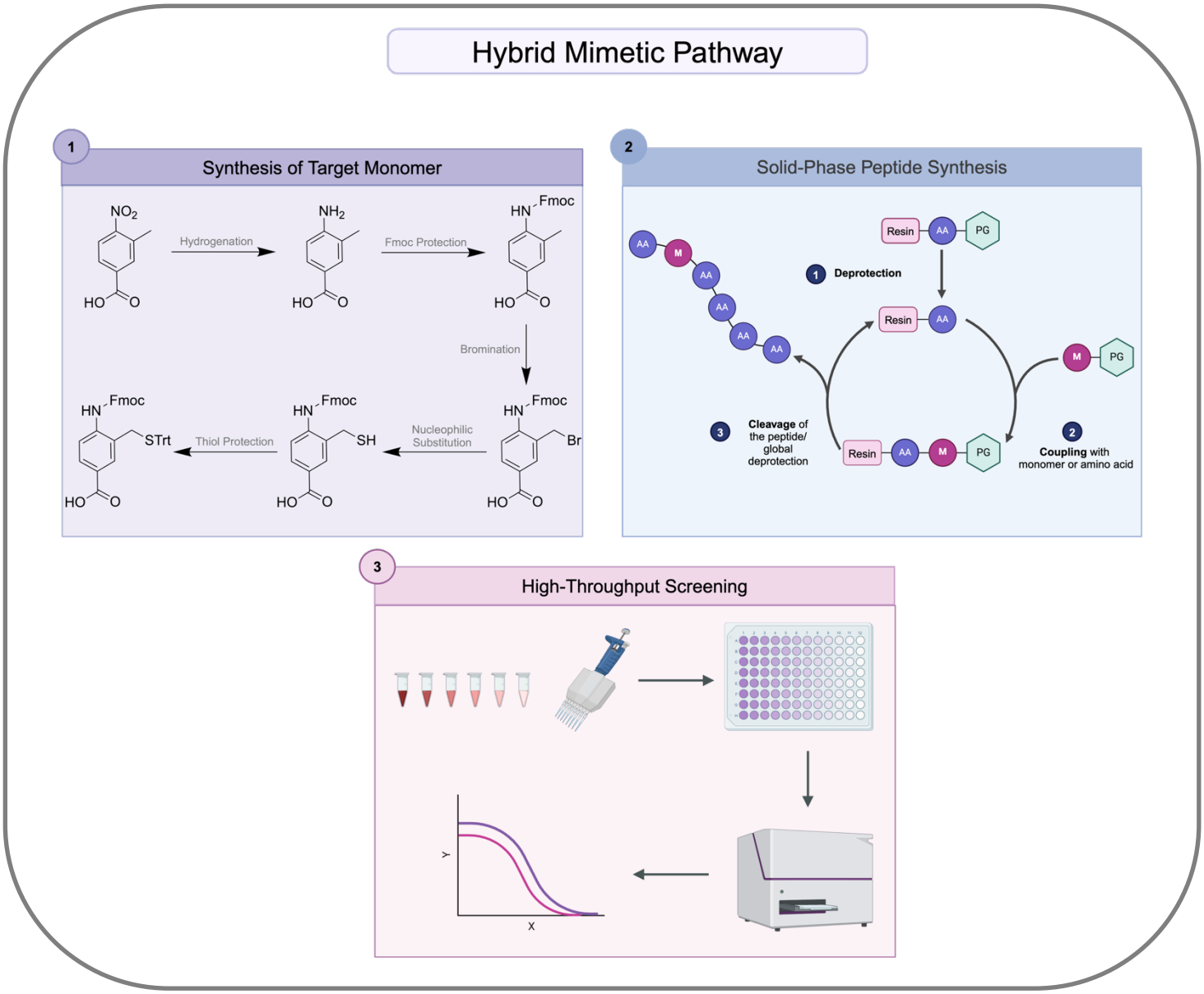
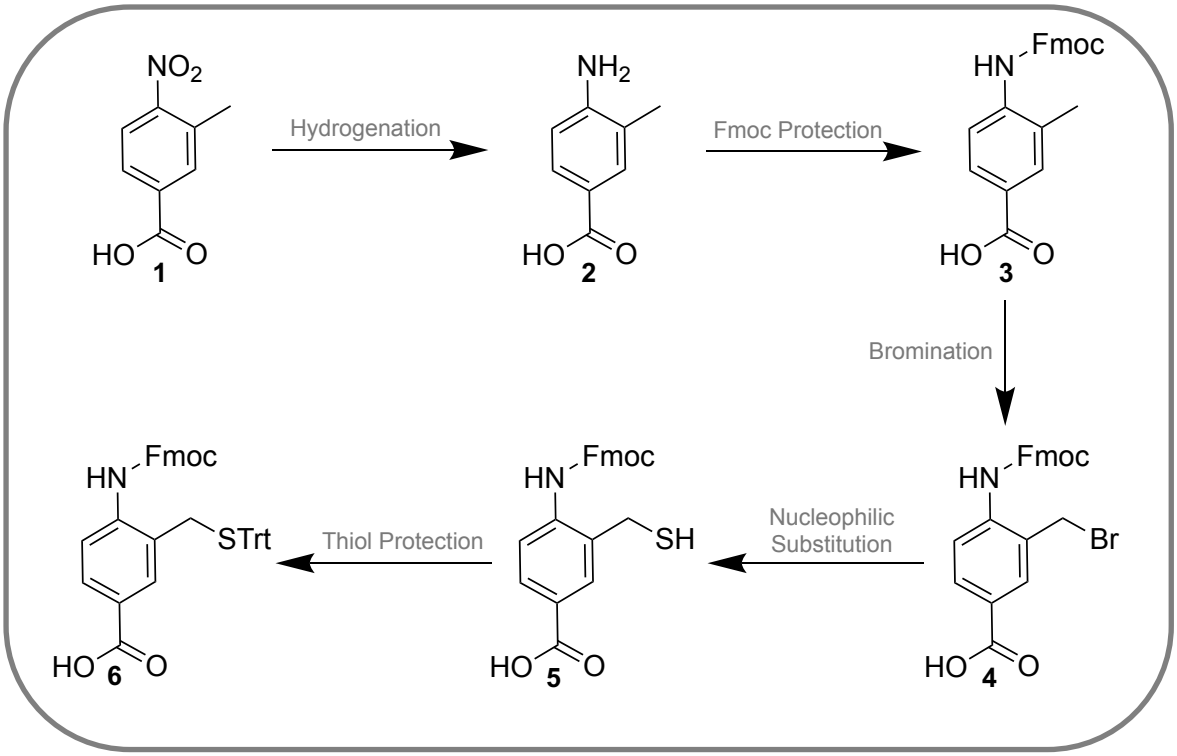


Figure 58: A schematic illustration depicting the three fundamental phases that make up the hybrid mimetic pathway.1) Synthesis of the target monomeric building block. 2) Solid-phase synthesis workflow. 3) High-throughput electrophilic screen.

3.2 Preliminary Design of Synthetic Route

The preliminary design of the pathway to produce the desired monomeric building block is detailed below in **Scheme 1**. This pathway involves the transformation of the commercially available building block 3-Methyl-4-nitrobenzoic acid. A classical hydrogenation constitutes the first step, whereby the nitro group would be reduced to form an aniline prior to being Fmoc protected. The benzylic bromination of the methyl group would then follow. The presence of this halide leaving group would allow the nucleophilic substitution reaction to occur, forming the desired thiol. Lastly the free thiol would be protected with an acid labile protecting group, such as the trityl (Trt) group, to allow for orthogonal protection to the previously installed Fmoc group; a requirement for compatibility with an Fmoc/^{t}Bu solid-phase peptide synthesis (SPPS) strategy.



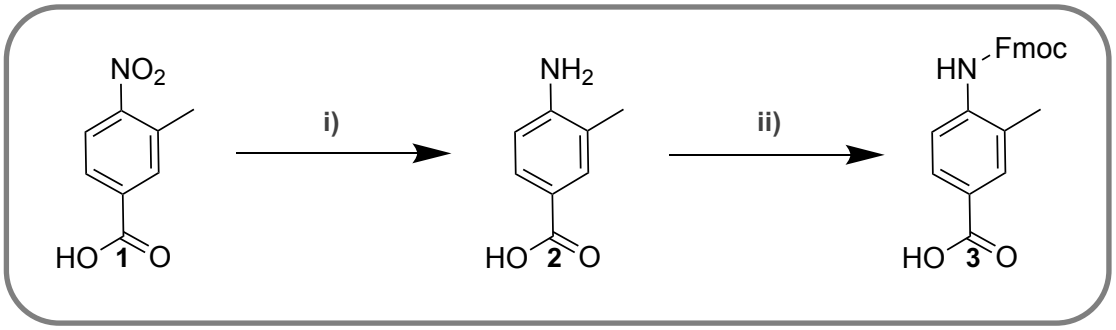
Scheme 1: Preliminary design of the synthetic pathway to generate the orthogonally protected monomer **6**.

3.2.1 Hydrogenation

The synthetic route began with the use of 3-Methyl-4-nitrobenzoic acid (**1**), a commercially available functionalised building block. This building block was catalytically hydrogenated using 10% Pd/C in line with standard literature protocols[123] to afford the desired aniline in quantitative yields (**2**). To verify the reaction had occurred as planned, a ^{1}H NMR spectra was taken and subsequently compared to the spectra present in the literature.

3.2.2 Fmoc Protection

In order to synthesise a functionalised building block capable of being incorporated into a peptidic sequence, it must be compatible with commonly used reagents and protecting groups. A prominent strategy for the synthesis of peptide sequences using SPPS involves the Fmoc/^{t}Bu approach. This orthogonal protection system allows the N-terminal protecting group and the side chain protecting group to be removed independently of each other.[124] Therefore, the logical choice for the protection of the newly synthesised aniline (**2**) was the Fmoc group. The Fmoc protection of the aniline was initially attempted using Fmoc chloride as the source of Fmoc and $CHCl_3$ as the solvent of choice,[125] however this attempt was unsuccessful owing to the poor solubility of the aniline in $CHCl_3$. A second attempt to protect the aniline was made, with THF replacing $CHCl_3$ as the solvent of choice,[126] leading to the Fmoc protected aniline (**3**) in good yields as shown in **Scheme 2**.



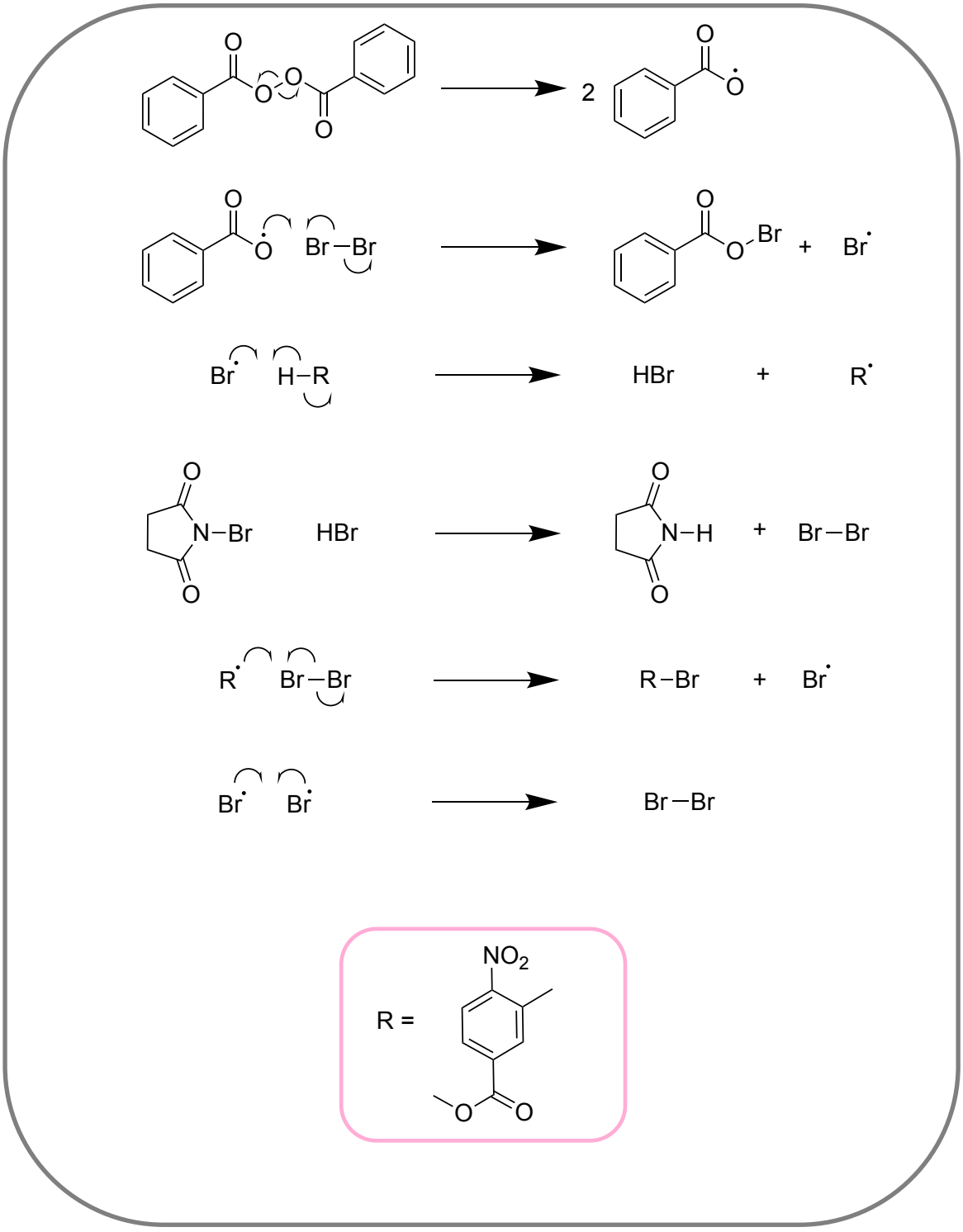
Scheme 2: **i)** Pd/C, H_2, MeOH, r.t., 18 h, 99%. **ii)** Fmoc-Cl, THF, reflux, o/n, 76%.

3.2.3 Radical Bromination

The next step in the synthetic route involved the radical bromination of the methyl group *meta* to the carboxylic acid moiety. The protocol chosen[127] followed the Wohl–Ziegler reaction conditions, employing N-Bromosuccinimide (NBS) in conjunction with a radical initiator to produce the desired bromide.

The mechanism by which radical bromination occurs is widely considered to be the one proposed by Goldfinger.[128] This view states that the function of NBS is to generate and maintain a low concentration of bromine, which goes on to function as the species that reacts with the radical initiator[129] as detailed in **Scheme 3**. This mechanism is in contrast to the one put forward by Bloomfield,[130] which suggests that the initial radical is generated from NBS itself.

Scheme 3 details the way in which a radical initiator, such as benzoyl peroxide (BPO), initiates the radical mechanism, which goes on to interact with the bromine generated from NBS. This propagates the reaction, allowing a benzylic radical to form by breaking the C-H bond via the bromine radical. This benzylic radical ultimately reacts with a bromine radical to form the desired brominated monomer.

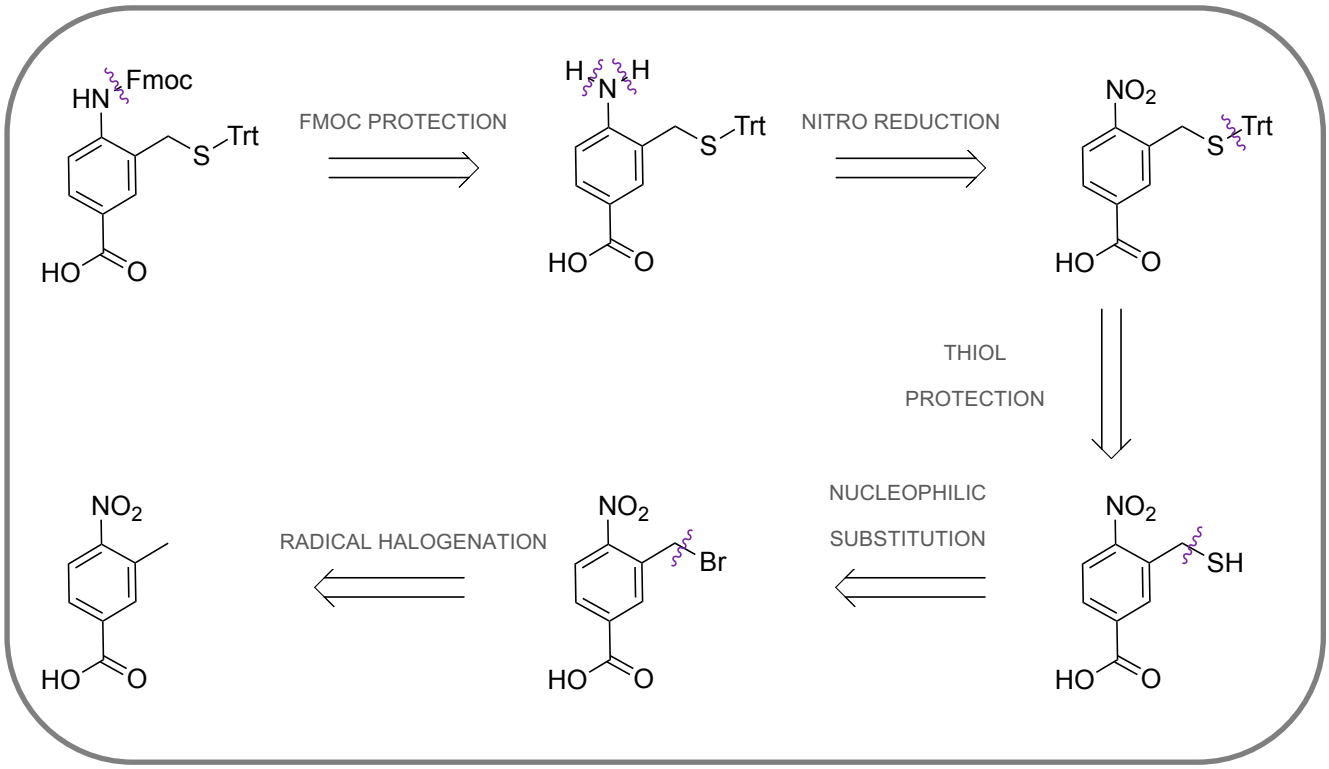


Scheme 3: Goldfinger radical bromination mechanism.

This reaction was first trialled using NBS as the bromination reagent, with Azobisisobutyronitrile (AIBN) acting as the radical initiator. Unfortunately, this reaction was unsuccessful as the

presence of the target product was not detected by ^{1}H NMR spectroscopy, with Fmoc degradation observed instead. As such, continuing with the initial route was no longer feasible and a revised synthetic pathway had to be designed in order to produce the desired building block.

3.3 Retrosynthetic Design of Revised Pathway



Scheme 4: Retrosynthetic approach for the synthesis of the functionalised monomer.

As the route previously envisioned was unsuccessful, an alternative approach to design a revised pathway was taken, as shown in **Scheme 4**. A retrosynthetic method was thus used, where the target building block was broken down into its precursor components. A path was then designed where the reaction conditions for each successive step were compatible with the functional groups present on the monomer.

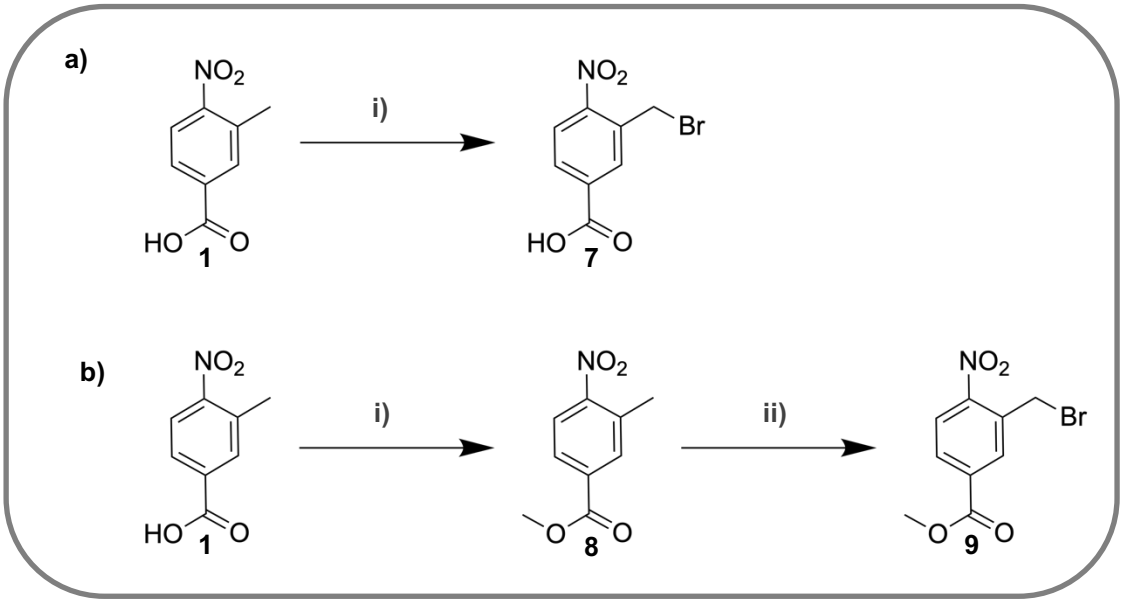
To ensure said compatibility, the nitro group present on the monomer was used as a *de facto* protecting group and was preserved throughout the majority of the synthetic pathway. This therefore allows the monomer to be subject to harsh reaction conditions in the multi-step route, without the interference of any potential amine reactivity.[131]

Therefore, the primary step in the revised route would be the radical bromination, which would be proceeded by the formation of the thiol; the thiol would be protected with the same protecting group as the previous strategy. The penultimate step proposed would be the nitro reduction to generate the free amine, which would subsequently be Fmoc protected.

3.3.1 Radical Bromination

The revised route began with the free radial bromination of 3-Methyl-4-nitrobenzoic acid. This was attempted several times trialling either AIBN[127] or BPO[132] as the radical initiator, with NBS present as the bromination reagent. All attempts made resulted in negligible yields of the target product (**Scheme 5**); it was hypothesised that this may be due to the solvent of choice. Carbon tetrachloride (CCl_4) was used as the solvent for all attempts, as it is the standard solvent for free radical bromination reactions. The starting material, 3-Methyl-4-nitrobenzoic acid, had extremely poor solubility in CCl_4 owing to its polar nature. Hence, in order to successfully brominate the methyl group, the polarity of the starting material had to be reduced.

A way in which to do so, was to transform the carboxylic acid moiety through methyl ester formation. The carboxylic acid was esterified using standard conditions[133] **(Scheme 5**) which successfully reduced the polarity of the scaffold and greatly improved its solubility in CCl_4. This in turn facilitated the bromination of the methyl group present on the scaffold.



Scheme 5: **Route a)** Initial approach to the brominated monomer producing negligible yields, **i)** NBS, BPO, CCl_4, reflux, 4%. **Route b)** Revised route via the methyl ester formation of the starting material, **i)** H_2SO_4, MeOH, reflux, 26 h, 88%. **ii)** NBS, BPO, CCl_4, reflux, 25 h, 49%.

A limitation of this step was the conversion factor from the starting material (**8**) to the brominated product (**9**). A conversion of approximately 50% was observed by ^1H NMR spectroscopy, with 33% remaining as staring material. Additionally, the presence of bis-halogenated monomer was

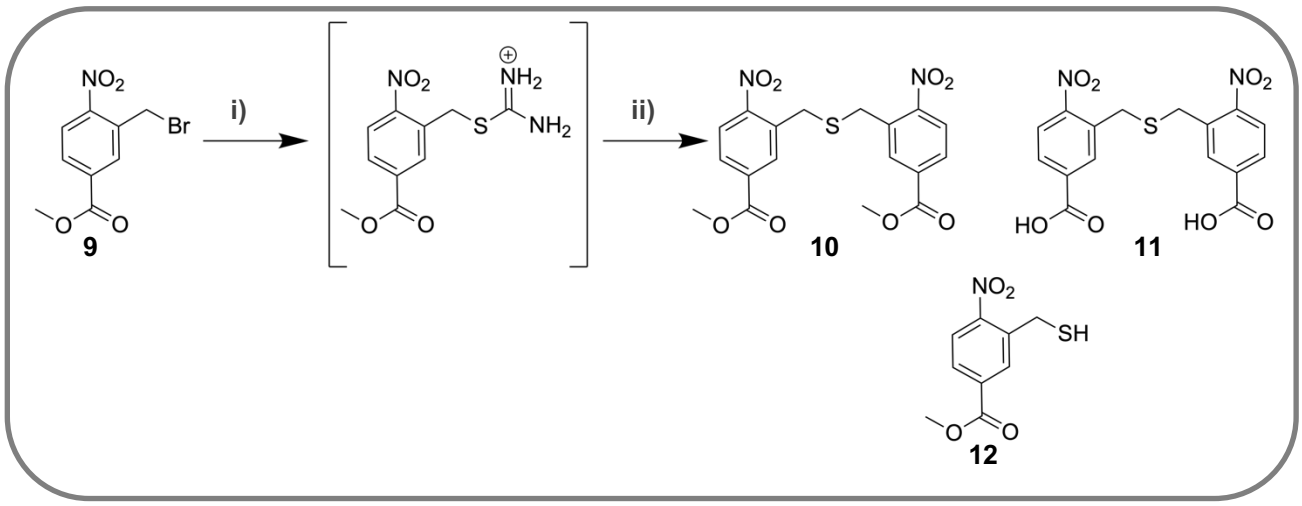
also observed (17%). This step presented a significant bottleneck in the synthetic route, establishing the need for the reaction to be conducted on a larger scale than necessarily required.

Furthermore, purification of the crude mixture was particularly difficult as the retention factor values for both the methyl ester (**8**) and product (**9**) were incredibly similar, with a difference of approximately 0.1. After considerable optimisation for purification by flash chromatography, the ideal conditions were found to be an elution gradient of 1-25% EtOAc in Hexane over 30 column volumes, resulting in an isolated yield of 49%. Whilst the conversion of starting material to pure product was lower than ideal, when conducted on a larger scale a sufficient quantity of product was able to be isolated. For example, in a single run where 1.40 g of **8** was utilised, 0.97 g of **9** was isolated post purification; a quantity that enabled further development of the synthetic route.

3.3.2 Nucleophilic Substitution

The following step in the synthetic route was a nucleophilic substitution reaction. In this step the bromine leaving group previously installed would be substituted to generate a free thiol using thiourea as the nucleophile of choice; thiourea was selected due to its widespread usage in thiol formation, as per the literature. Thiourea would attack the monomer (**9**) via an S_N2 reaction forming an isothiouronium salt intermediate, which would subsequently undergo hydrolysis to release the free thiol (**12**).[134]

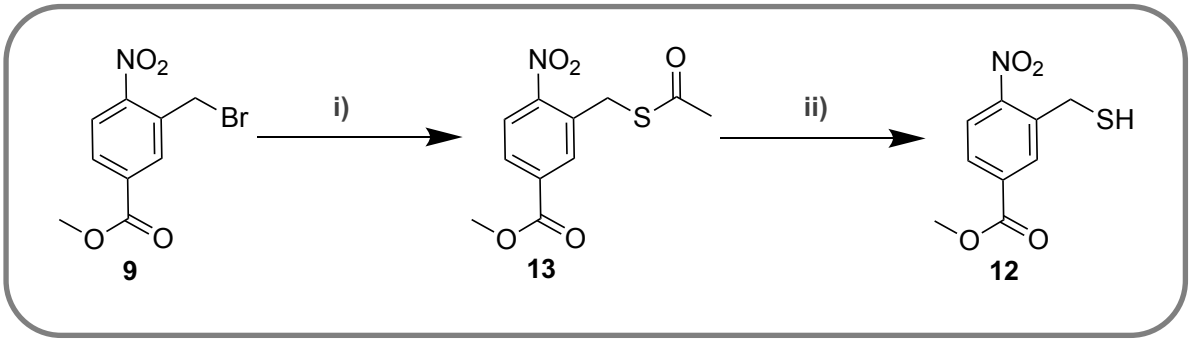
However, when attempted this route proved to be more challenging than initially anticipated. The formation of the isothiouronium salt intermediate was observed via LCMS indicating that the nucleophilic substitution step was successful; the difficulty laid in the hydrolysis of the intermediate. When said hydrolysis was attempted using NaOH, a mixture of components was observed in place of the target thiol. Certain components identified through LCMS included the thioether formed from the reaction between the free thiol and unreacted bromide, in both the esterified form as well as the carboxylic acid form (**Scheme 6**). This indicated that one of the side reactions occurring was the hydrolysis of the methyl ester *para* to the nitro group on the scaffold. A trace amount of the desired thiol was also observed; this was not successfully isolated from the crude mixture. Ultimately it was determined that due to the complexity of the resulting crude mixture post hydrolysis, pursuing a route using thiourea was not a viable option.



Scheme 6: i) $SC(NH_2)_2$, EtOH, reflux, 23 h. **ii)** NaOH, reflux, 24 h.

A second attempt to install the thiol handle was made using sodium hydrosulfide as the nucleophilic source of sulphur.[135] This reaction followed a similar pattern as with thiourea, where both ester and acid analogues of the thioether were detected; the desired product was not observed.

A third attempt at the nucleophilic substitution reaction aimed to use potassium thioacetate as the reagent of choice to form a thioester, which would then undergo deacetylation to release the free thiol.[136] Potassium thioacetate successfully reacted with the brominated monomer via an S_N2 reaction forming the thioester (**13**). Deacetylation was unsuccessfully attempted under basic conditions using potassium carbonate[137], prompting a change to acidic reaction conditions.[136] Successful deacetylation was conducted using HCl, resulting in the isolation of the free thiol (**12**) in excellent yields (**Scheme 7**).

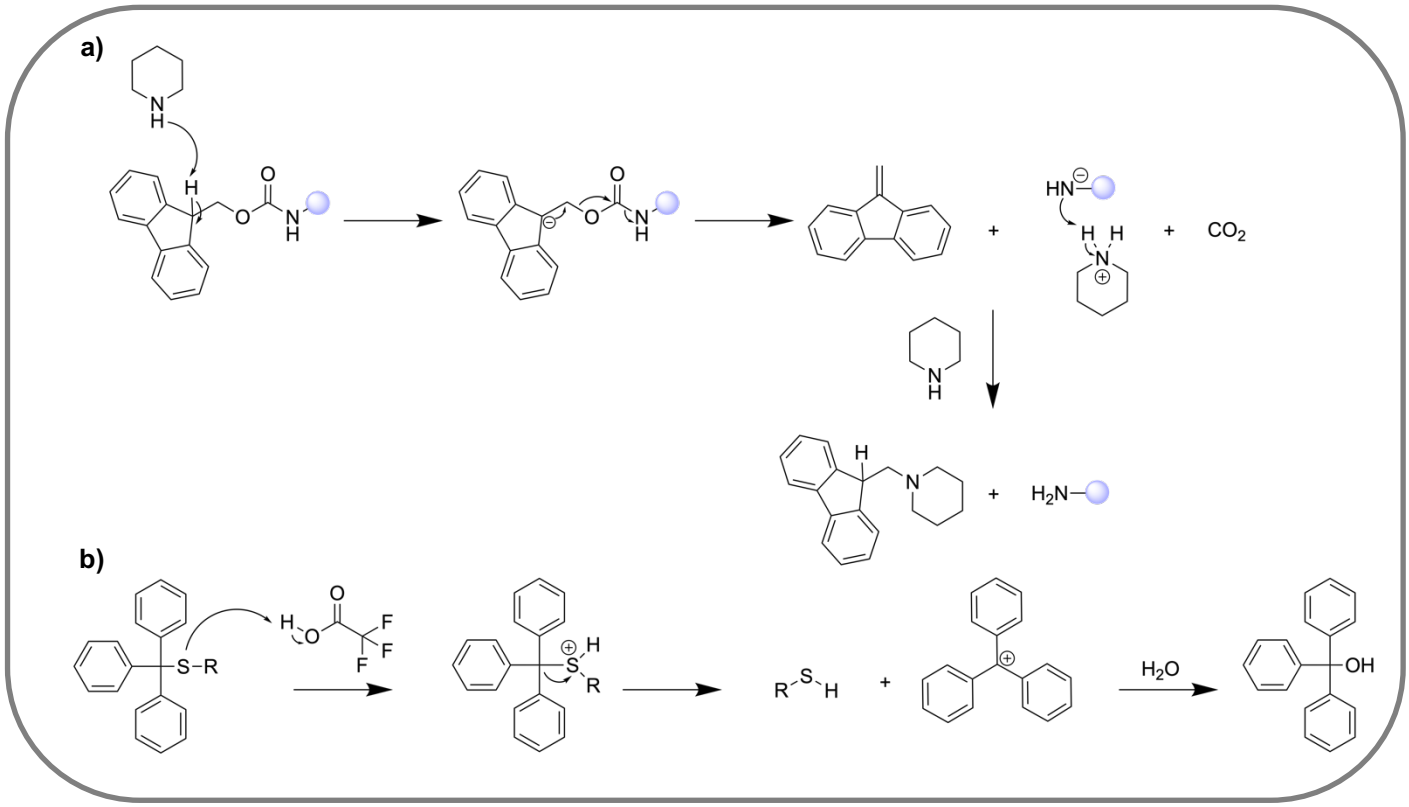


Scheme 7: **i)** CH_3COSK, MeOH, r.t., 25 h, 89%. **ii)** HCl, MeOH, reflux, 23 h, 92%.

3.3.3 Protection of the Free Thiol

The monomer was designed to ensure compatibility with SPPS protocols, where it was vital that the thiol remained protected when under conditions required to deprotect the Fmoc group present on the monomer, as well as on the other amino acids in the BAK sequence. This is to ensure that the thiol handle remained active at the end of the synthetic processes, which following a final global deprotection step, is ready to react with an electrophilic library.

As such, an acid labile protecting group was required considering Fmoc is cleaved under basic conditions. A standard protecting group used for this purpose in SPPS is the triphenylmethyl (trityl) group, as shown in **Scheme 8**.[138]



Scheme 8: **a)** Base mediated cleavage of the Fmoc protecting group. **b)** Acid mediated deprotection of the trityl protecting group.

To install a trityl protecting group mild reaction conditions are typically sufficient, along with the presence of a base.[139] **Table 1** highlights the conditions trialled for this step.

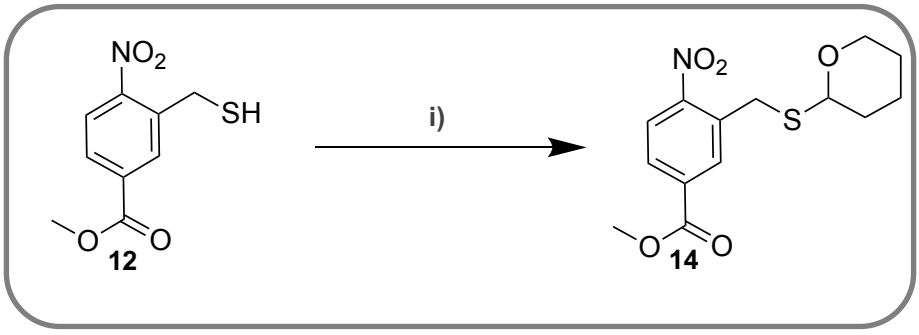
Reagent	Solvent	Temperature	Base	Product isolated
Trityl chloride	DCM	r.t	Pyridine	-
Trityl chloride	DCM	r.t	DIPEA	-
Trityl chloride	DCM	r.t	TEA	-

Table 1:Reaction conditions tested for the installation of the trityl protecting group.

As shown in **Table 1**, several reaction conditions were tested where the base of choice was modified, whilst keeping all other reaction conditions consistent. The bases trialled were selected from literature examples where the trityl group was successfully installed on the compound of interest.[140] In each case, the target product was never isolated from the crude reaction mixture. Purification of this mixture was attempted numerous times via flash chromatography, however no product could be isolated.

It became apparent that the protection strategy using the trityl group was not feasible, considering several attempts had been made. In order to move forward with the synthetic route, an alternative protecting group had to be found that retained the acid lability required. The tetrahydropyranyl (THP) group was proposed as a suitable alternative.[141]. There are numerous advantages of using this ether group for protection, including its stability under different reaction conditions, ease of insertion and removal, as well as the cost effectiveness of its precursor dihydropyran (DHP). A notable advantage of the THP group over traditional benzyl-based protecting groups, is the improved solubility of the compound synthesised due to the lack of aromaticity present;[142] a feature that is preferred in a complex multi-step synthetic route.

This reaction was carried out using 3,4-dihydropyran (DHP) and *p*-toluenesulfonic acid (*P*TSA), whereby the free thiol was successfully protected with the THP group and isolated in good yields (**14**), as shown in **Scheme 9**.

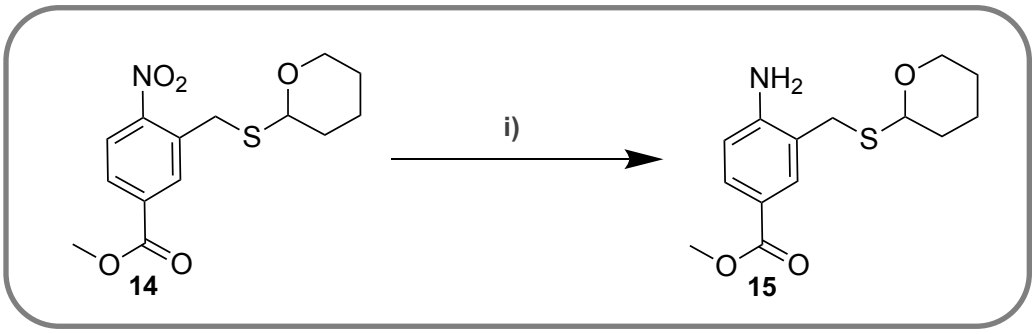


Scheme 9: **i)** *P*TSA, DHP, DCM, r.t., 26 h, 75%.

3.3.4 Nitro Reduction

Following the successful protection of the free thiol, the next step in the synthetic route involved the reduction of the nitro group present to release the reactive amine. The first condition trialled was a classical hydrogenation reaction, using palladium on carbon (Pd/C) with a hydrogen balloon;[123] ; this condition was initially trialled owing to its prevalent use in the literature, including in the synthesis of aromatic monomeric building blocks.[63] Unfortunately, this endeavour was ineffective as only the starting material was observed through ^{1}H NMR spectroscopy. A second classical condition was tested, in this instance using iron powder (Fe) and ammonium chloride (NH_4Cl),[143] which was chosen in a similar manner to Pd/C and H_2 , where this condition is commonly employed in aromatic nitro reduction protocols. As with the previous attempt, under these conditions the desired product was not obtained; only the starting material was observed via ^{1}H NMR spectroscopy.

After two failed attempts at the nitro reduction using standard conditions, it was hypothesised that the thiol moiety on the monomer may not be compatible with the use of metal catalysis. The literature indicates that sulphur can be acutely poisonous to metal catalysts, owing to its chemical adsorption on the surface of the metal.[144] This adsorption therefore renders the catalyst ineffective through either a partial or complete loss of activity.[145] Therefore, to effectively reduce the nitro group on the monomer, metal-free reaction conditions were required. Whilst researching the literature available, two possible conditions were found that seemed viable.[146] The first condition utilises trichlorosilane ($HSiCl_3$) with a Lewis base[147] under mild reaction conditions, while the second condition employs sodium dithionite ($Na_2S_2O_4$)[148] as the reducing agent. **Table 2** highlights the results of this endeavour.



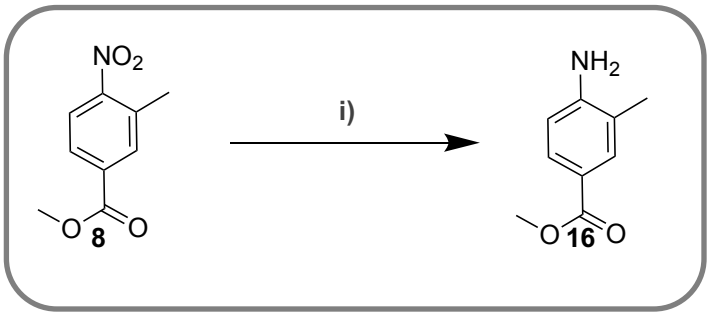
Reagents	Solvent	Temperature	Time	Isolated Yield
$HSiCl_3$, DIPEA	DCM	0 °C - r.t	18 h	38%
$Na_2S_2O_4$	THF/H_2O	50 °C	25 h	94%

Table 2: A comparison of the reaction conditions tested for the metal-free nitro reduction step.

As seen in **Table 2**, both conditions led to the formation of the desired amine (**15**). However, as the yield produced using $Na_2S_2O_4$ was far superior compared to using $HSiCl_3$, this was determined as the optimal reagent for this step. Additionally, the reaction using $Na_2S_2O_4$ is milder and easier to handle than the metal catalysis originally envisioned, while successfully producing the target amine (**15**) in an excellent yield.

Interestingly, upon repetition of this step, a difference in the yield of the amine was observed when the source of H_2O for the solvent differed. Source A was initially used resulting in a yield of 94% however, when source B was used a reduction in yield of approximately 24% was noted, due to an incomplete conversion of the starting material.

In order to investigate this further, a model substrate **8** was used to mimic the nitro group on the previous monomer. The rationale behind this was simply the fact that the previous monomer **14** was obtained via an extended synthetic route, compared to the readily available model substrate **8**. The nitro reduction using $Na_2S_2O_4$ was carried out under the same reaction conditions as previously stated, however this time the source of H_2O was varied.



Reagent	Solvent	H_2O Source	Time	Temperature	Conversion
$Na_2S_2O_4$	THF/H_2O	A	25 h	50 °C	100%
$Na_2S_2O_4$	THF/H_2O	B	25 h	50 °C	79%
$Na_2S_2O_4$	THF/H_2O	C	25 h	50 °C	49%

Table 3: A comparison of three H_2O sources and how this affects the conversion of starting material to product.

As seen in **Table 3**, the conversion (by ^1H NMR spectroscopy) of starting material **8** to product **16** greatly differed depending on the H_2O source. The pH of these H_2O sources was measured, as a possible means to explain the differences observed, yet all measured at pH 5.

In an attempt to examine this further, H_2O sources A and B were sent for trace metal analysis conducted by Fatimah Alfadel, through mass spectroscopy (**Table 4**).

	Element
Greater in H_2O Source A	Mo (x 13)
	Zn (x 6)
Greater in H_2O Source B	Hg (x 1.3)
	Tl (x 2)
	Pb (x 3)
	Ba (x 1.5)
	Sr (x 20)
	Cu (x 1.4)
	Na (> x 2)

Table 4: Trace metal analysis with the difference between the sources displayed in brackets. Elements greater in source A are highlighted in green.

As highlighted in **Table 4**, the quantity of trace metals detected in H_2O sources A and B differed to varying degrees. As source A had demonstrated to be the superior source of H_2O, on account of obtaining full conversion from **8** to **16** when used, the ensuing analysis focused on the elements that were present in increased quantities over source B. Source A had six times the amount of Zn and thirteen times the amount of Mo as source B; these quantities were present in a parts per billion (ppb) scale.

To probe this further, various reaction conditions for the nitro reduction were tested as summarized in **Table 5**:

Reagents	Solvent	H_2O Source	Conversion
Zn	THF/H_2O	B	0%
$Na_2S_2O_4$ + MoO_2Cl_2	THF/H_2O	B	38%
$Na_2S_2O_4$ + $ZnCl_2$	THF/H_2O	B	53%
$Na_2S_2O_4$ + Mo	THF/H_2O	B	65%
$Na_2S_2O_4$	THF/H_2O	B	79%
$Na_2S_2O_4$ + Zn	THF/H_2O	B	100%

Table 5: A summary of the various conditions tested using H_2O source B and its impact on conversion of starting material **8** to product **16**.

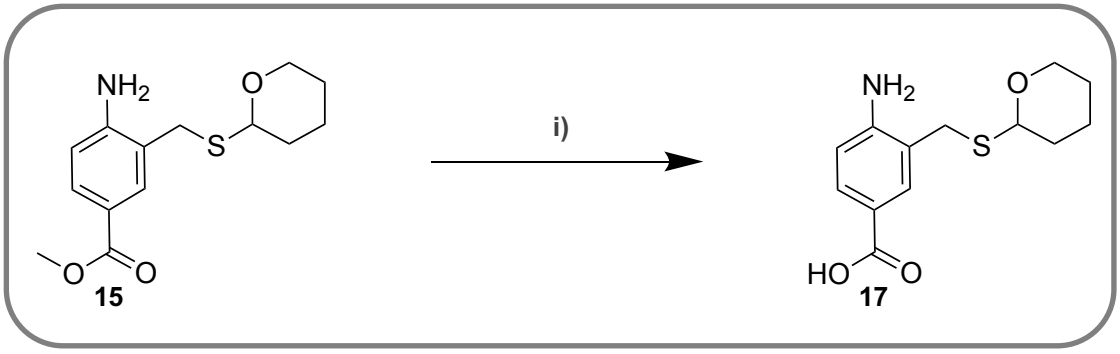
The regents initially chosen as sources of Zn and Mo were $ZnCl_2$ and MoO_2Cl_2.This was in an effort to create a homogenous reaction mixture that would emulate the conditions found in H_2O source A, to a greater degree than through solid-phase catalysis. Unfortunately, when either $ZnCl_2$ or MoO_2Cl_2 was added to H_2O source B (in addition to $Na_2S_2O_4$), the conversion factor from **8** to **16** was inferior to the sole use of source B and $Na_2S_2O_4$, void of any additives. These results prompted a deviation in reagent choice to elemental Zn and Mo, with the aim of driving the reaction towards completion via solid-phase catalysis. As shown in **Table 5**, the use of Mo as a catalytic additive resulted in an increased conversion compared to when MoO_2Cl_2. was employed, however this once again remained lower than the use of source B and $Na_2S_2O_4$. Interestingly, as highlighted in **Table 5**, the sole condition that emulated the results from using source A was the use of source B with the addition of Zn. However, the quantity of Zn required to obtain this result was approximately 3 equivalents, signifying that Zn was not catalytic as expected.

An alternate avenue was briefly explored where the organic solvent was varied, whilst the source of H_2O was kept consistent. Inspired by Hay *et al*[149] EtOH was employed in place of THF, in conjunction with H_2O source B. Surprisingly, this substitution resulted in the complete conversion of starting material **8** to product **16,** with a notable increase in the rate of reaction. Substituting EtOH for THF resulted in the nitro reduction reaching completion in approximately 2 h, in comparison to an incomplete conversion at 25 h when THF was utilised. This signifies that the choice of organic solvent also plays an important role in the conversion /rate of this reaction and is another avenue that requires further investigation.

Given that a condition was not found that could replicate the results produced from source A, using metals in trace amounts, the best course of action was to continue using source A where possible with source B as a satisfactory alternative. In order to gain a deeper understanding of factors that affect this reaction, additional investigation is required. The influence of factors such as solvents, trace metals and even particle size of said metals, requires further evaluation.

3.3.5 Hydrolysis of Methyl Ester

Following on from the nitro reduction detailed above, hydrolysis of the methyl ester was carried out under standard conditions[150] to release the free carboxylic acid (**17**) in excellent yields (**Scheme 10**), confirmed through both ^{1}H and ^{13}C NMR spectroscopy.



Scheme 10: **i)** NaOH, MeOH, THF, r.t., 46 h, 95%.

3.3.6 Fmoc Protection

The final step in the synthetic route was the protection of the free amine using Fmoc, to allow for compatibility with SPPS. Multiple attempts at this protection were made including the use of two different sources of Fmoc - Fmoc-Cl[151] and Fmoc-OSu,[152] with attempts showcased below in **Table 6**.

Fmoc Source	Fmoc Equivalence	Base	Solvent	Temperature	Product isolated
Fmoc-Cl	1.5	$NaHCO_3$	THF	reflux	-
Fmoc-Cl	3.0	$NaHCO_3$	THF	reflux	-
Fmoc-Cl	1.5	-	THF	reflux	-
Fmoc-Cl	1.5	-	DMF/$CHCl_3$	M.W 60 ^oC	-
Fmoc-Cl	2.0	-	DMF/$CHCl_3$	M.W 60 ^oC	-
Fmoc-Cl	2.9	-	DMF/$CHCl_3$	M.W 60 ^oC	-
Fmoc-Osu	0.90	Na_2CO_3	dioxane	r.t	-
Fmoc-Osu	0.96	Na_2CO_3	dioxane/H_2O	r.t	-
Fmoc-Osu	0.96	DIPEA	THF	r.t	-
Fmoc-Osu	1.1	DIPEA	DMF	r.t	-

Table 6: A summary of the various reaction conditions trialled for the Fmoc protection of aniline **17**.

As shown in **Table 6**, despite varying the reaction conditions the desired product was never isolated. Attempts made using Fmoc-OSu did not display traces of product. In some cases where Fmoc-Cl was employed, the presence of the target product was observed but could not be isolated. As the Fmoc protection of similar aniline building blocks is considered standard practice, where Fmoc protected analogs have been successfully produced,[63] the challenging protection of **17** was unexpected. The root cause of this difficulty was not further explored at this stage; however, it was suspected that perhaps the presence of the THP protected thiol *ortho* to the aniline may have had an influence on its reactivity with Fmoc-Cl/Fmoc-OSu.

Nevertheless, an alternative solution had to be found which retained compatibility with SPPS, whilst being amenable to a high-throughput strategy. As such, the strategy chosen to synthesise the desired hybrid mimetics, was to pre-couple the monomer to the next amino acid in the target peptide sequence. The target monomer replaces a turn in the peptide sequence (3.4 amino acids)[4] therefore the next amino acid in the sequence would be one further in the sequence as opposed to the amino acid beside the hot spot residue.

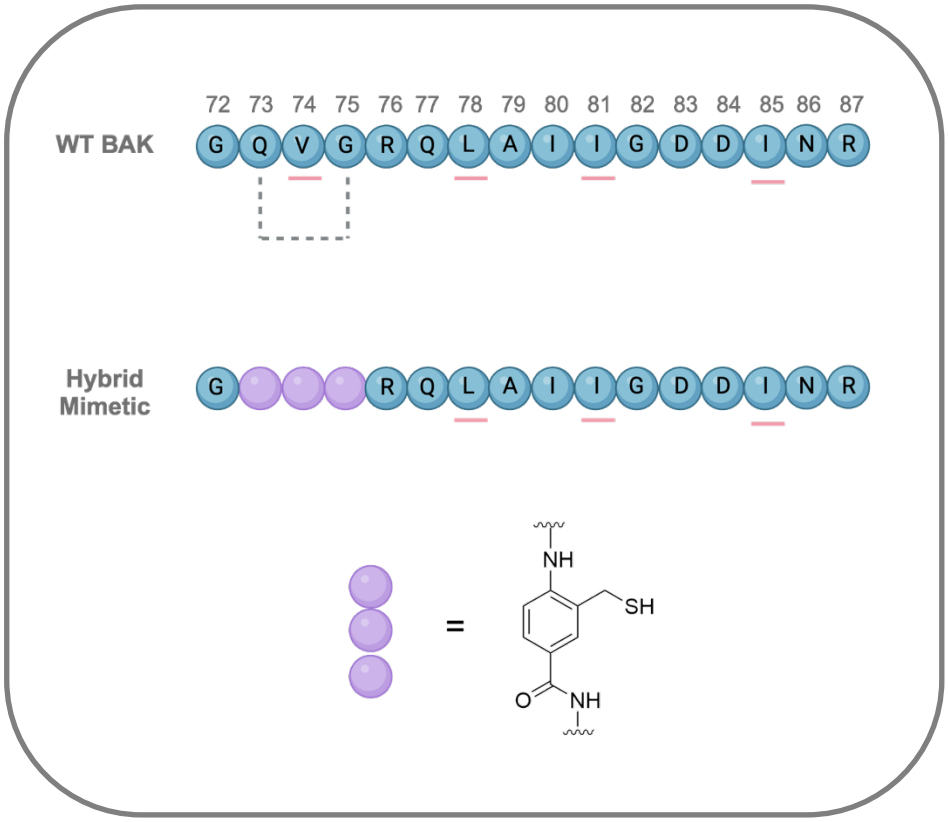
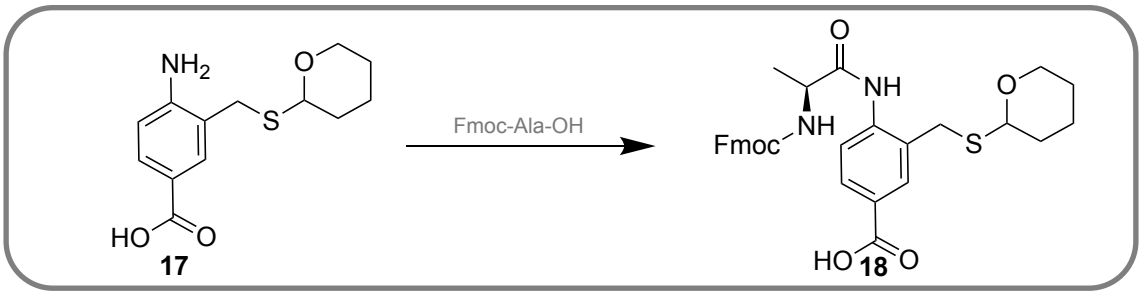


Figure 59: A schematic illustration depicting the replacement of 3 amino acid residues with the designed monomer.

For the targeting of BCL-X_L/BAK this strategy requires the synthesis of four monomers, as each turn containing a hot spot differs in which amino acid it is adjacent to, as seen in **Figure 59**. This is a departure from the initial strategy where the synthesis of only one monomer was required. This is due to the original monomer maintaining compatibility with the synthesis of all hybrid mimetics, as it did not retain specificity in terms of where it could be inserted into the peptide sequence. Despite the final step requiring variation for all hot spot positions, the strategy remains compliant with a high-throughput approach, as once synthesised the hybrid mimetics can be rapidly screened with large compound libraries.

The first condition tested was the replacement of isoleucine (Ile^{81}), therefore the amino acid next in the sequence was alanine. Various reaction conditions were trialled for this step as showcased in **Table 7**.



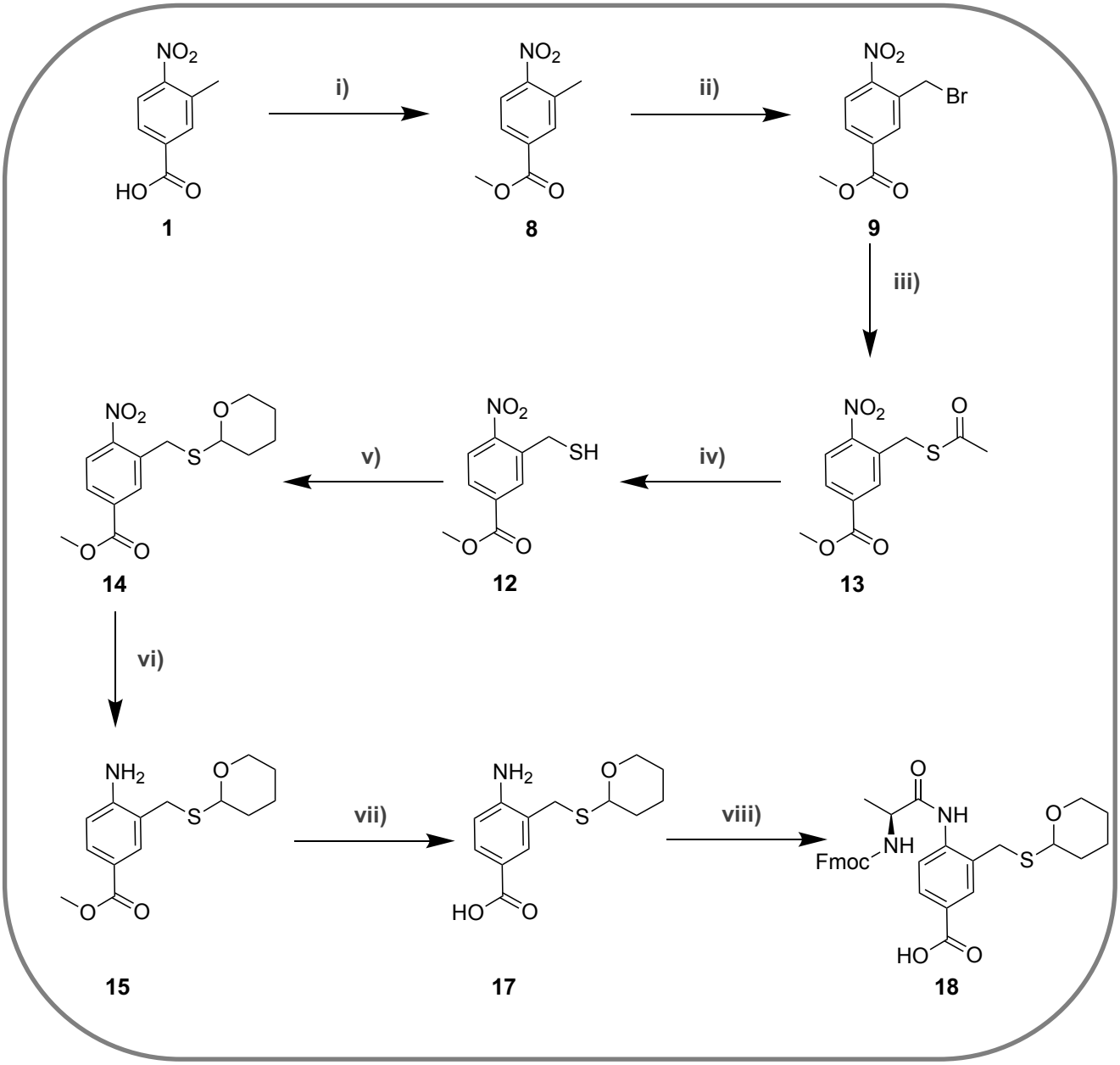
Coupling Reagent	Solvents	Temperature (MW)	Time	Conversion
Ghosez	**$CHCl_3$:DMF (5:1)**	**60 °C**	**30 min**	**Incomplete**
Ghosez	$CHCl_3$:DMF (5:1)	70 °C	25 min	Incomplete
Ghosez	$CHCl_3$:DMF (7:1)	80 °C	90 min	Incomplete
Ghosez	$CHCl_3$:DMF (7:1)	90 °C	60 min	Incomplete
Ghosez	$CHCl_3$:DMF (7:1)	100 °C	30 min	-
Ghosez	$CHCl_3$	60 °C	60 min	Incomplete
Ghosez	DMF	95 °C	30 min	-
HATU	DMF	r.t	o/n	-

Table 7: Optimisation of the reaction conditions for the Ghosez mediated coupling of the aniline **17** with Fmoc-Ala-OH to generate the desired pre-coupled monomer. Incomplete conversion was monitored via LCMS, where the presence of both starting materials was observed alongside the product **18**.

As depicted in **Table 7**, despite several attempts to optimise this step the conversion from starting material to product remained incomplete resulting in poor yields. It was determined that $CHCl_3$ was required for the reaction, as solely using DMF did not result in product formation, unlike in SPPS where DMF is the solvent of choice. Similarly, the use of Ghosez's reagent[153] was important as other coupling agents such as HATU[154] did not work. Ultimately the condition used to isolate the target product **18** was first condition highlighted in **Table 7**, resulting in an isolated yield of 15%. As this reaction was conducted on a small scale, 16 mg of **18** was isolated post purification from 51 mg of **17**, signifying the need to conduct this reaction on a larger scale in order to produce a sufficient quantity of **18** to incorporate into a peptide ligand.

3.4 Conclusions and Future Outlook

This chapter reported on the successful development and optimisation of a multi-step pathway for the synthesis of the target monomer displayed in **Scheme 11**.



Scheme 11: Final synthetic route to generate the desired thiol functionalised building block. **i)** H_2SO_4, MeOH, reflux, 26 h, 88%. **ii)** NBS, BPO, CCl_4, reflux, 25 h, 49%. **iii)** CH_3COSK, MeOH, r.t., 25 h, 89%. **iv)** HCl, MeOH, reflux, 23 h, 92%. **v)** *P*TSA, DHP, DCM, r.t., 26 h, 75%.**vi)** $Na_2S_2O_4$, THF, H_2O, 50 °C, 25 h, 94%.**vii)** NaOH, MeOH, THF, r.t., 46 h, 95%. **viii)** Fmoc-Ala-OH, Ghosez, $CHCl_3$, DMF, MW 60 °C, 30 min,15%.

The final route to the monomeric building block differed to the pathway initially envisioned. The functionalisation of the aromatic monomer with a thiol handle proved to be a greater synthetic challenge than anticipated. These hurdles included difficulties installing the bromine leaving group on **9**, isolating the free thiol and the reduction and subsequent protection of the nitro group. The initial synthetic pathway had to be extended to esterify the carboxylic acid moiety, in an effort to increase the solubility of **1**, which facilitated the radical bromination step. Although this bromination reaction was a bottleneck in terms of yield, it was satisfactory enough to continue with the route planned. The protecting group on the thiol **12** had to be altered to allow for synthetic accessibility, yet it retained compatibility with SPPS techniques. Finally, metal-free conditions had to be investigated in a bid to successfully reduce the nitro group, which proved challenging to Fmoc protect. This challenge led to a deviation of the primary objective, where in place of one monomeric building block for all four hybrid mimetics, each requires coupling to a different amino acid prior to SPPS. Nevertheless, the final monomers designed remain compatible with the high-throughput strategies initially envisaged.

The next phase of the hybrid mimetic route would be the incorporation of monomer **18** into the BAK peptide sequence using SPPS. This would occur using an automated peptide synthesiser, where the monomer **18** would be treated as an external amino acid and incorporated into the sequence in place of residues Ile^{80}, Ile^{81} and Gly^{82} to obtain hybrid mimetic **1** (**Figure 60**), thereby replacing a turn in the native helix. Following this, the three other hybrid mimetics can be produced in a similar fashion, where the relevant amino acid is pre-loaded on to the monomer before being inserted into the BAK sequence. Once this small library of hybrid mimetics is synthesised, they can be screened with a library of electrophilic fragments in the presence of BCL-X_L in order to identify potential inhibitors of the BCL-X_L/BAK PPI.

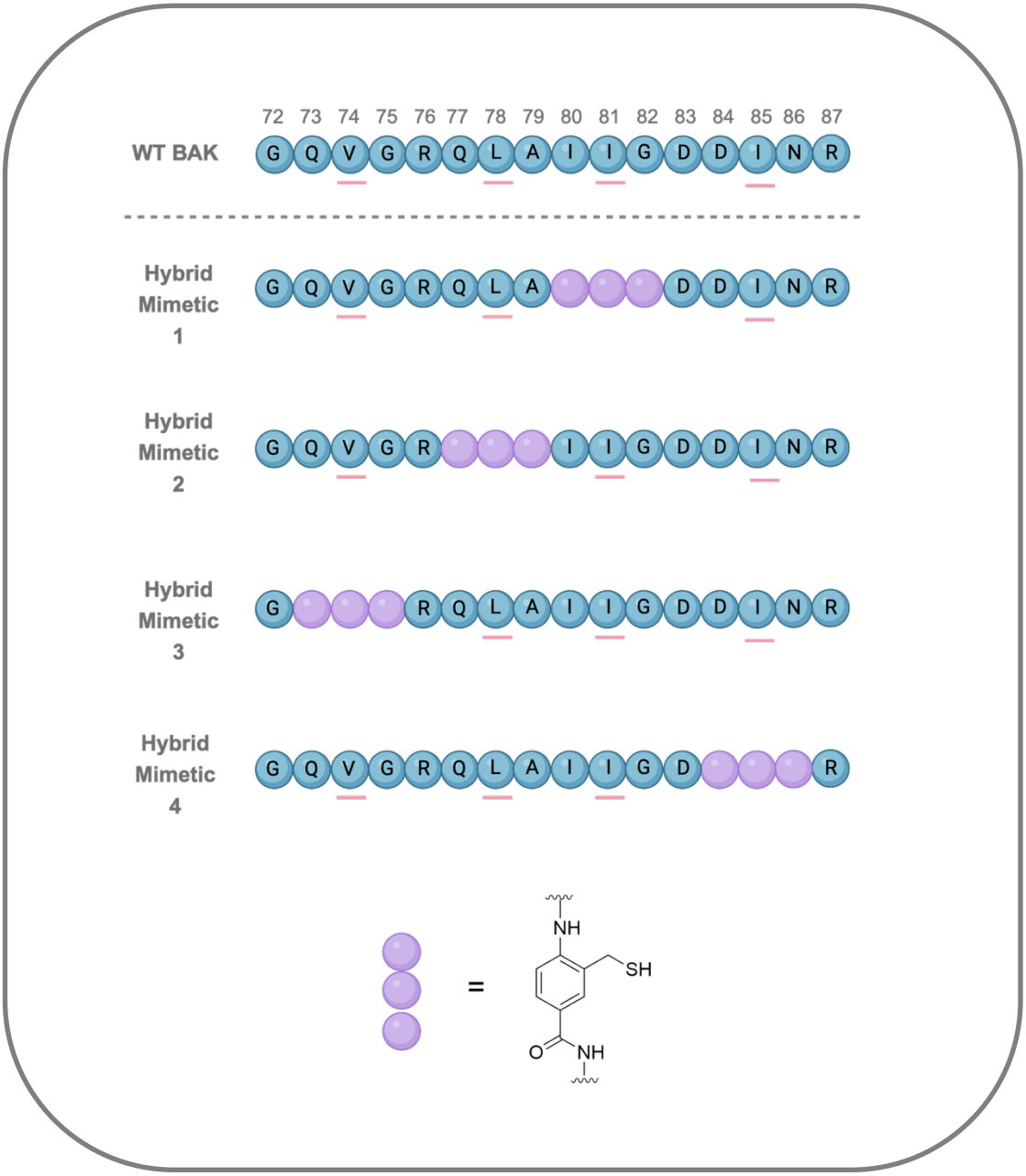


Figure 60: An illustration depicting how the thiol functionalised monomeric block will be incorporated into the BAK peptidic sequence. This replaces a hot spot each time to generate 4 hybrid mimetics. Hot spots on the native BAK sequence are underlined.

Once each hot spot position has been systematically screened, the next phase would involve replacing multiple hot spot residues on a single mimetic with non-natural residues. These residues would contain the 'hit' sidechains identified in the initial electrophilic screen, in the hopes of developing a more potent inhibitor. Finally, the peptide could be removed all together to produce

a completely synthetic a-helix mimetic containing key fragments required for binding to BCL-X_L (**Figure 61**).

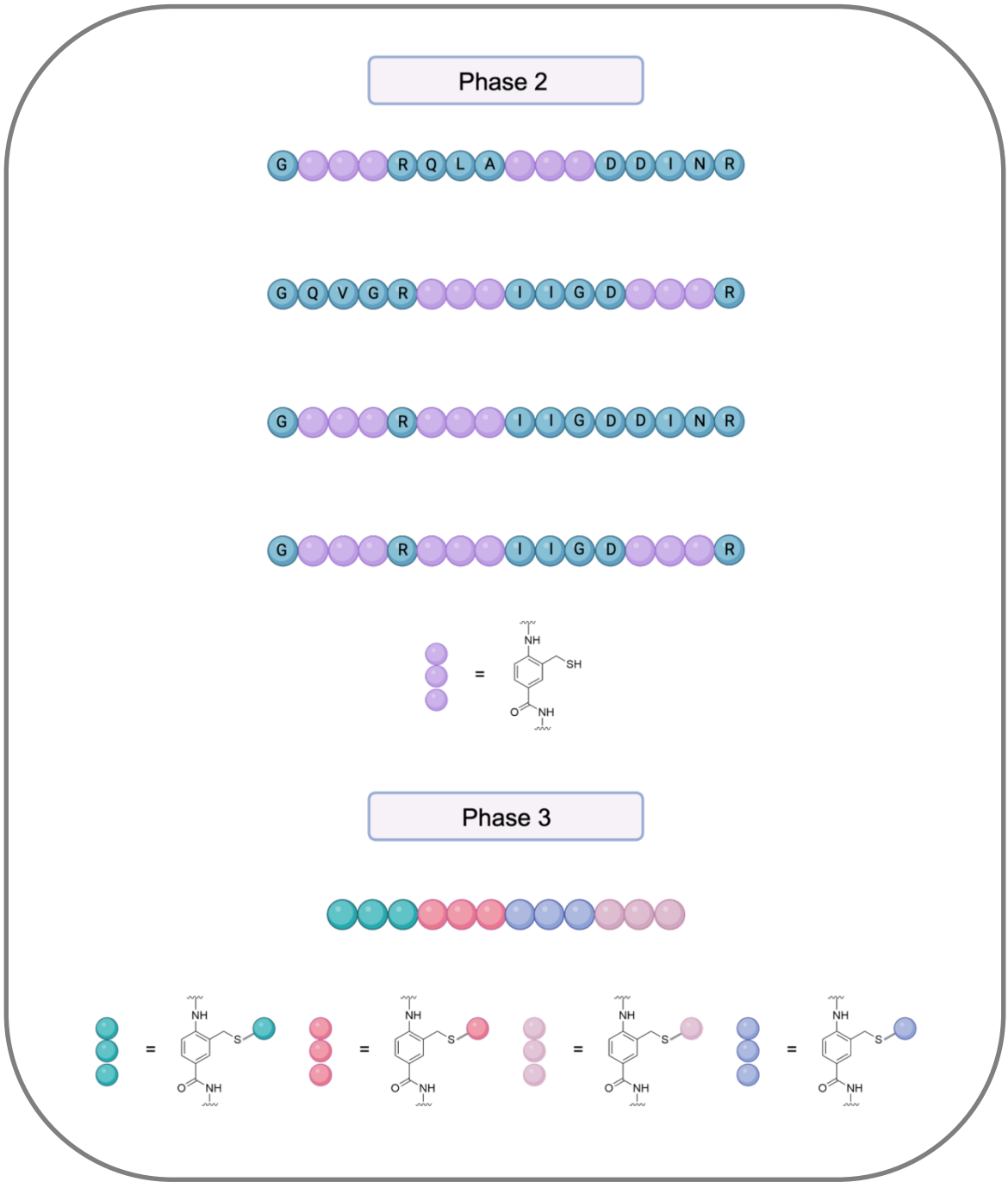


Figure 61: Proposed phases to produce the next generation of helix mimetics. Phase 2 involves replacing multiple hot spot residues on a single mimetic, while Phase 3 aims to remove all peptidic elements to produce a completely synthetic a-helix mimetic.

Chapter 4

Conclusions and Future Outlook

The following chapter recounts the conclusions surmised for each pathway in the two-progged target-directed approach, and details the future endeavours required for its continued development.

4.1 Peptidic Pathway

The peptidic pathway was designed in a manner such that it served a dual purpose. This two-fold objective entailed synthesising a library of BAK derived mimetics and subsequently employing them in the development of the high-throughput target-directed assay. This target-directed assay was designed to feature the nucleophilic thiol on the binding partner to the protein of interest, as opposed to the protein itself. As such, a library of BAK derived mimetics was designed, where hot spot positions were systematically substituted with cysteine residues. These mimetics would subsequently be screened against a diverse acrylamide library, in the presence of BCL-X_L, to retain target-directed selectivity.

In order to aid the development of the target-directed approach and reduce the overall complexity of its optimisation, a qIT to FA assay protocol was developed. This protocol entailed employing the peptidic mimetics in a qIT screen to generate a new library of functionalised mimetics, which would subsequently be evaluated in a FA competition assay to determine binding affinity towards BCL-X_L. This act of predetermining the identity of fragments that strongly affect binding affinity will provide validation for the results obtained from the target-directed approach.

The qIT to FA assay was subject to extensive development, where the optimal reagent concentrations were established, using **SS1** as the model mimetic. **SS1** was subsequently screened with a large acrylamide library and the resultant mimetics evaluated in a FA screen. Variability in both the qIT and FA screens was observed, with suspected temperature sensitivity as a potential cause, requiring further optimisation. However, a few reliable hits were found where a significant improvement in binding affinity towards BCL-X_L was observed. These hits require further validation before being employed as controls for the development of the target-directed qIT screen.

SS4 was also evaluated in the qIT to FA screen, where it was ascertained that hot spot (Ile^{85}) substitution was not well tolerated. The vast majority of functionalised mimetics led to a decrease in binding affinity when compared to the unfunctionalized mimetic. Nevertheless, a few mimetics

were identified where the functionalisation of **SS4** led to a slight improvement in binding affinity; these will also inform the target-directed screen.

In order to establish said target directed screen, mimetics **SS2** and **SS3** must be evaluated in the qIT to FA assay, as previously executed for **SS1** and **SS4.** Once each hot spot has been screened in this manner, the mimetics identified which exhibit increased binding affinity will serve as positive controls for the target-directed assay variant.

4.2 Hybrid Pathway

As elucidated in Chapter 1, the hybrid branch of the parallel pathway was devised in order to integrate both peptidic and non-natural residues into a single mimetic, with the non-natural residue replacing a hot spot position in the native BAK sequence. The resultant mimetic would thus possess the ability to undergo late-stage functionalisation, whilst retaining selectivity for the protein of interest. Functionalisation would occur through a Michael addition between the non-natural monomer (thiol) and a chemically diverse fragment library. This was designed in an effort to address the limitations of scaffolds present in the literature, by increasing the diversity of functional groups used to mimic PPI hot spots.

The synthetic protocol developed to produce the thiol functionalised monomer was more arduous than initially anticipated. The primary difficulties were associated with the installation of said thiol, along with suitably protecting both the thiol and amine in an orthogonal manner; this was required for compatibility with SPPS protocols. The challenges presented in developing this synthetic route led to a deviation in the design of the non-natural monomer. In place of generating a single monomeric building block applicable for all hybrid mimetics, each mimetic now requires the synthesis of a separate monomer. However, the synthetic route only varies in the last step, where each monomer requires pre-coupling to the appropriate amino acid adjacent to the respective hot spot position. This pre-loading bypasses the requirement of the free amine to be subject to Fmoc protection- a feat that remained unsuccessful. In spite of such challenges a monomeric building block was produced, retaining compatibility with the envisioned high-throughput strategy.

Further development of the hybrid pathway would begin with the successful incorporation of the thiol functionalised monomer into the native BAK sequence. Once the library of hybrid mimetics was synthesised, through the systematic replacement of Val^{74}, Leu^{78}, Ile^{81} and Ile^{85} residues, the target-directed screen would be conducted. This screen would be primarily developed through

the aforenoted peptidic pathway (**Figure 62**). Once established, the hybrid mimetics would be screened with an electrophilic library, in a similar manner to the peptide-based mimetics.

Once each hot spot position has been systematically screened, the following phases would entail the replacement of multiple hot spot residues on a single mimetic, with the non-natural monomer. The monomer would contain the 'hit' sidechain fragments identified in the primary screens, with the goal of identifying a more potent inhibitor of the BCL-X_L/BAK PPI. Ultimately, the peptide would be completely removed to produce an entirely synthetic α-helix mimetic, containing key fragments required for binding to BCL-X_L.

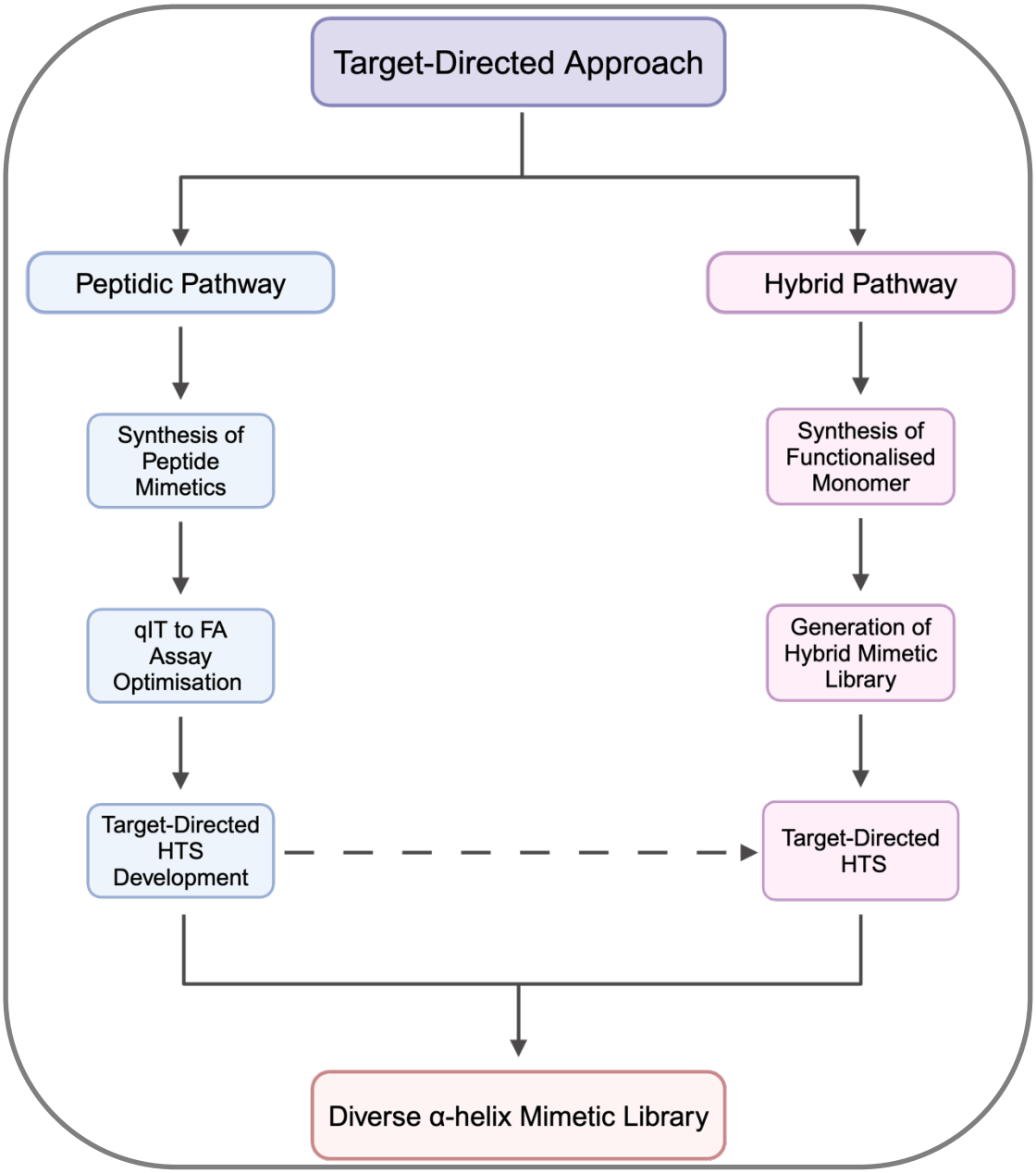


Figure 62: Flowchart detailing the progression of the two-pronged approach for the synthesis of a diverse α-helix mimetic library, via a target-directed screen.

Chapter 5
Materials and Methods

5.1 Peptide Synthesis

5.1.1 General Information

All 9-fluorenylmethoxycarbonyl (Fmoc)-protected amino acids were obtained from CEM and Fluorochem. N,N'-diisopropylcarbodiimide (DIC) was purchased from Fluorochem while Ethyl cyano(hydroxyimino)acetate (Oxyma Pure) was acquired from CEM. Triisopropylsilane (TIS), 2,2′-(Ethylenedioxy)diethanethiol (DODT), 1,2-ethanedithiol (EDT), Piperidine, Acetic anhydride, Formic acid, Acetonitrile (ACN) , and Dimethylformamide (DMF) were purchased from Sigma-Aldrich. Dichloromethane (DCM), Diethyl ether and Dimethylsulfoxide (DMSO) were from VWR Chemicals. Trifluoroacetic acid (TFA) was acquired from Fisher scientific, while the Tentagel S RAM resin was from Sigma-Aldrich.

5.1.2 Solid-phase Synthesis

All peptides (**SS1- 4**) were synthesised via solid-phase peptide synthesis (SPPS). This was conducted using the CEM Liberty Blue microwave peptide synthesiser in conjunction with the industry standard 9- fluorenylmethoxycarbonyl/tert-Butyl (Fmoc/tBu) strategy. TentaGel S RAM resin (0.24 mmol/g loading, 50 µmol scale) was used for synthesis allowing the peptides to be synthesised as C-terminal amides. The Fmoc protected amino acids (250 µmol, 5 eq., 0.2 M in DMF), DIC (500 µmol, 10 eq., 0.5 M in DMF) and Oxyma Pure (250 µmol, 5 eq., 0.5 M in DMF) were coupled at 90 ^{o}C for 2 mins (single coupling) or 2 x 2 mins (double coupling) in DMF. All Arg residues underwent double coupling by default, as well as residues QL for **SS1,3,4** and QC for **SS2**. The N-terminal Fmoc group was cleaved using 10% piperidine and 0.1 M Oxyma Pure in DMF at 90 ^{o}C for 60 seconds.

5.1.3 N-Acetylation

The resin was submerged in DMF (6 mL) to allow for swelling and was shaken for 15 minutes. The DMF was then drained prior to the addition of the N-Acetylation mixture (6 mL - 5 % DIPEA, 5 % Ac_2O in DMF). The resin was shaken for 10 minutes before the N-Acetylation mixture was drained and was subsequently washed with DMF. This process was repeated two further times before the resin was washed with DMF (5x) and DCM (5x).

5.1.4 Cleavage

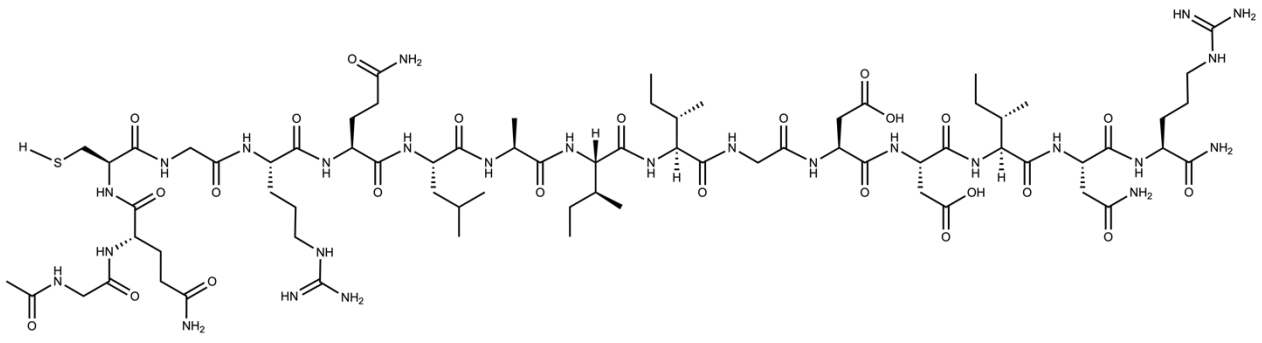
The resin was immersed in the cleavage mixture (4 mL – TFA: 92.5%, H_2O: 2.5%, TIS: 2.5%, DODT: 2.5%) and was shaken for 3 hours. The mixture was drained, and the crude peptide was precipitated with ice-cold diethyl ether before being isolated via centrifugation. The crude peptide was dissolved in ACN (1 mL) and H_2O (4 mL) and was subsequently lyophilised to produce a white solid.

5.1.5 Purification

The crude peptide was dissolved in ACN/ H_2O (6 mL, 20% ACN) and purified via HPLC (20-50-95 ACN gradient). For purification the Shimadzu preparative HPLC system was used (LC-20AR) with a reversed-phase Phenomenex Aeris PEPTIDE XB-C18 column (150 mm x 21 mm, 5 µm, 100 Å). The purity of the final product was determined using the Shimadzu analytical HPLC system (LC-2030C). The identity of the product was confirmed using the Waters LC-MS system with the reversed-phase C18 column (100 mm × 4.6 mm, 5 µm, 130 Å). *m/z* values are reported in Daltons.

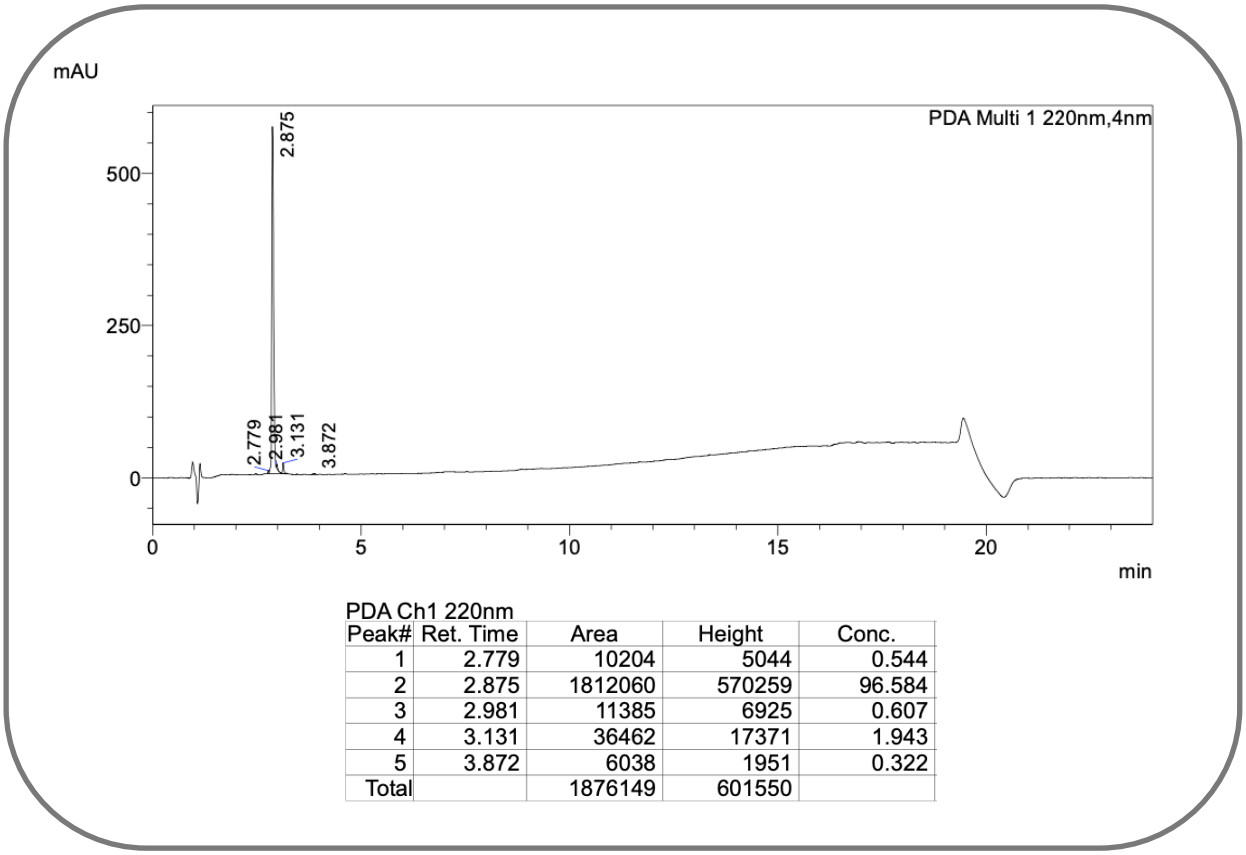
SS1

SS1 was synthesised via general methods **5.1.2 – 5.1.5**. LCMS (*m/z*): Calculated for $[M+H]^+$ = 1771.00, Found = 1771.16 (Δ = +0.16). Purity 97% by HPLC.



$H_3COC\text{-}GQ\underline{C}GRQLAIIGDDINR\text{-}NH_2$

Figure 63.1: SS1 Sequence



PDA Ch1 220nm

Peak#	Ret. Time	Area	Height	Conc.
1	2.779	10204	5044	0.544
2	2.875	1812060	570259	96.584
3	2.981	11385	6925	0.607
4	3.131	36462	17371	1.943
5	3.872	6038	1951	0.322
Total		1876149	601550	

Figure 63.2 :HPLC trace of SS1 highlighting the purity of the peptide isolated.

SS2

SS2 was synthesised via general methods **5.1.2 – 5.1.5**. LCMS (*m/z*): Calculated for $[M+2H]^{2+}$ = 878.99, Found = 878.96 (Δ = -0.03). Purity 96% by HPLC.

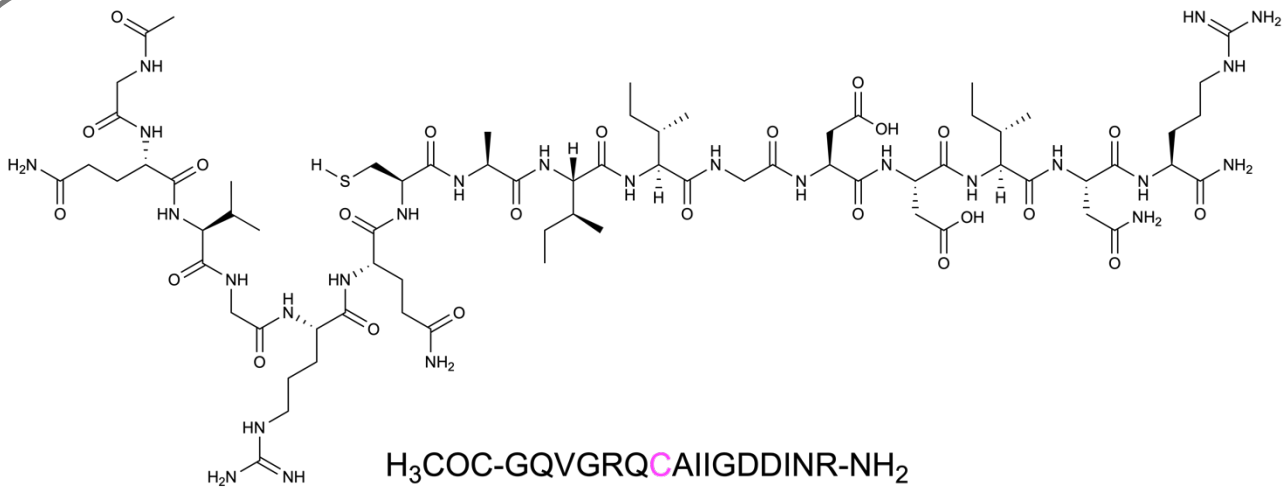
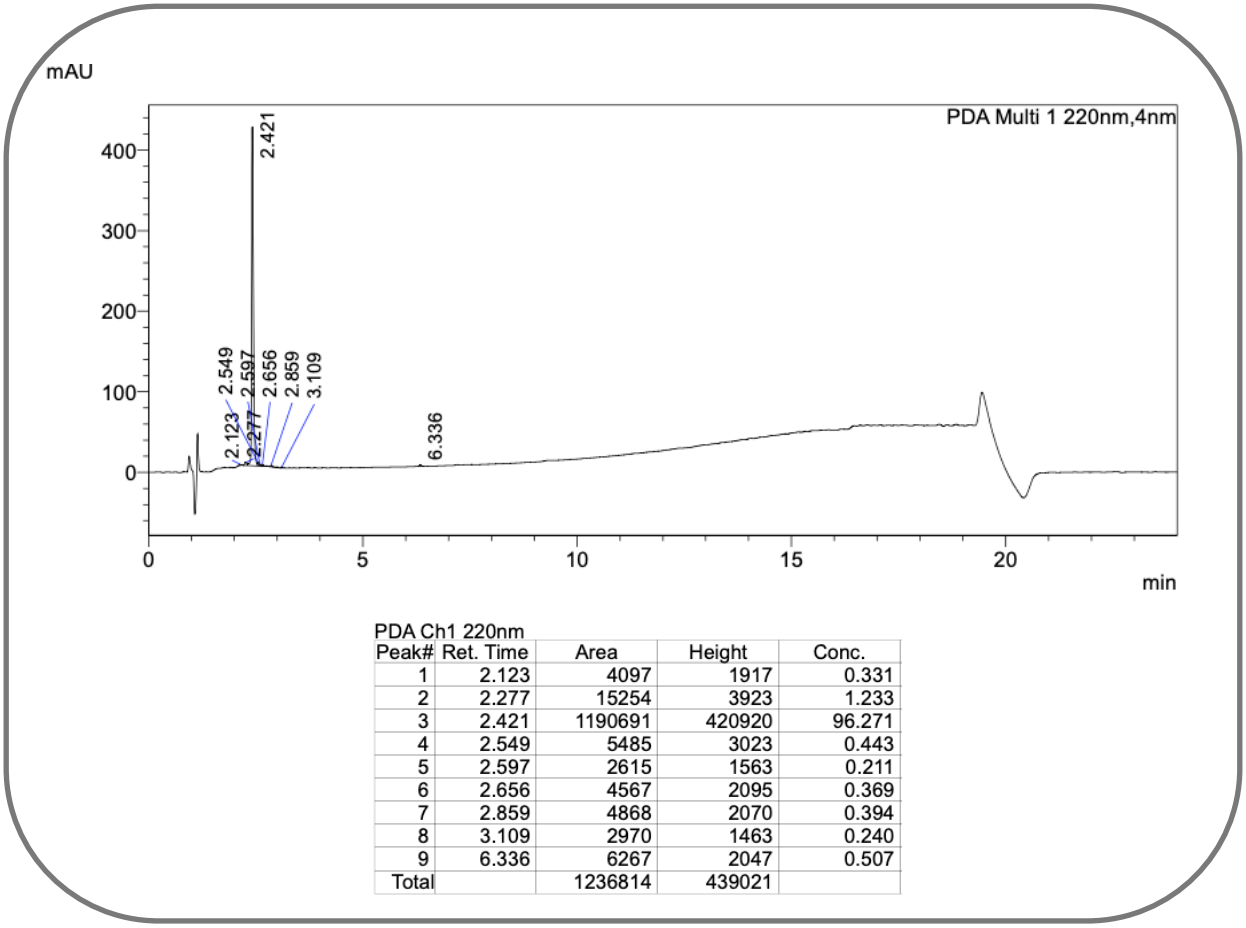


Figure 64.1: SS2 Sequence



PDA Ch1 220nm

Peak#	Ret. Time	Area	Height	Conc.
1	2.123	4097	1917	0.331
2	2.277	15254	3923	1.233
3	2.421	1190691	420920	96.271
4	2.549	5485	3023	0.443
5	2.597	2615	1563	0.211
6	2.656	4567	2095	0.369
7	2.859	4868	2070	0.394
8	3.109	2970	1463	0.240
9	6.336	6267	2047	0.507
Total		1236814	439021	

Figure 64.2: HPLC trace of SS2 highlighting the purity of the peptide isolated.

SS3

SS3 was synthesised via general methods **5.1.2 – 5.1.5**. LCMS (*m/z*): Calculated for $[M+2H]^{2+}$ = 878.99, Found = 878.80 (Δ = -0.19). Purity 92% by HPLC.

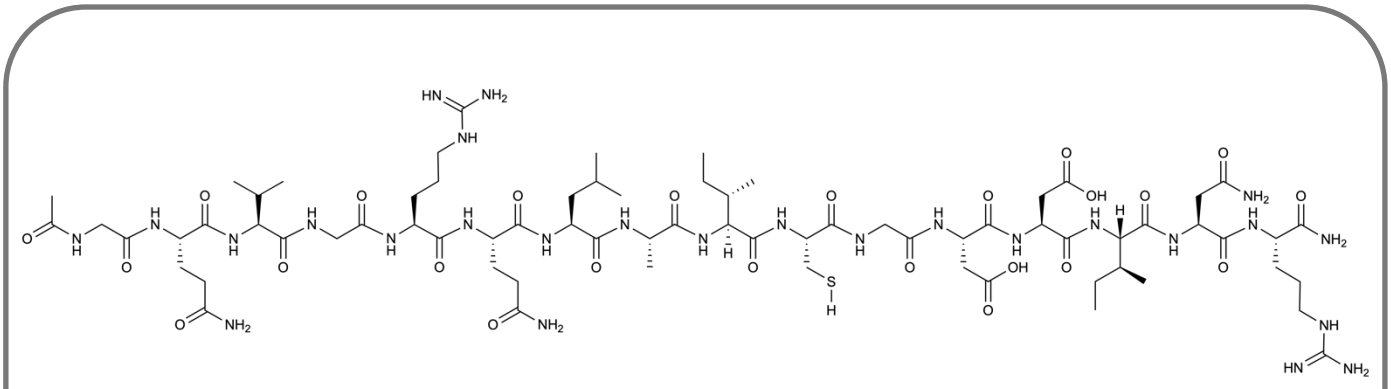
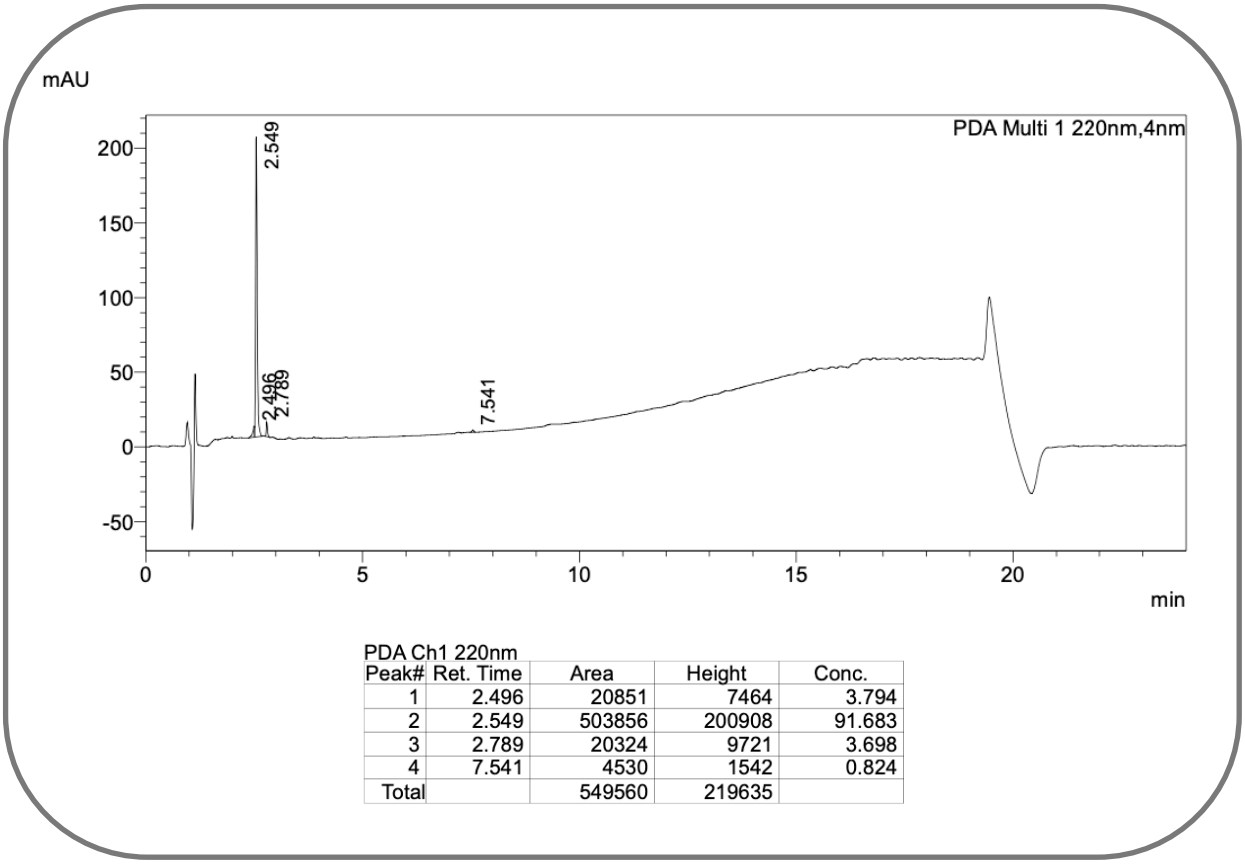


Figure 65.1: SS3 Sequence



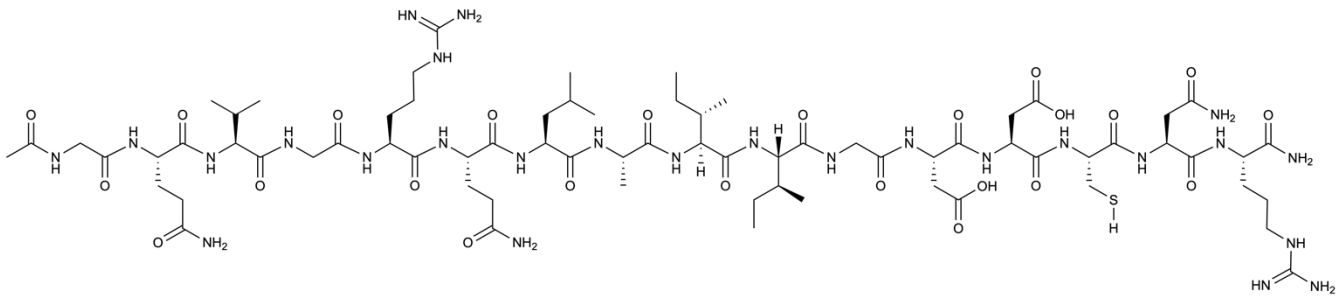
PDA Ch1 220nm

Peak#	Ret. Time	Area	Height	Conc.
1	2.496	20851	7464	3.794
2	2.549	503856	200908	91.683
3	2.789	20324	9721	3.698
4	7.541	4530	1542	0.824
Total		549560	219635	

Figure 65.2: HPLC trace of SS3 highlighting the purity of the peptide isolated.

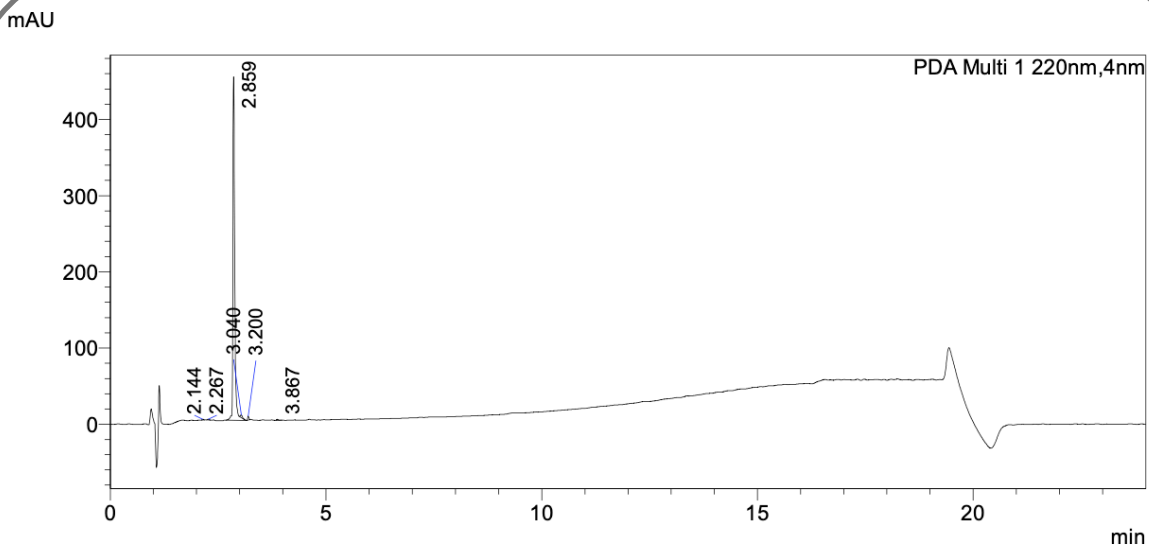
SS4

SS4 was synthesised via general methods **5.1.2 – 5.1.5**.LCMS (*m/z*): Calculated for $[M+2H]^{2+}$ = 878.99, Found = 878.80 (Δ = -0.19). Purity 98% by HPLC.



H_3COC-GQVGRQLAIIGDDCNR-NH_2

Figure 66.1: SS4 Sequence



PDA Ch1 220nm

Peak#	Ret. Time	Area	Height	Conc.
1	2.144	2300	1150	0.169
2	2.267	2468	1121	0.182
3	2.859	1327785	450690	97.834
4	3.040	11244	3406	0.829
5	3.200	9937	5114	0.732
6	3.867	3450	1225	0.254
Total		1357185	462707	

Figure 66.2: HPLC trace of SS4 highlighting the purity of the peptide isolated.

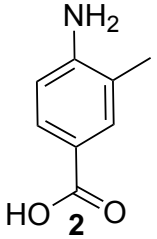
5.2 Chemical Synthesis

5.2.1 General Information

All starting materials, reagents and solvents used were purchased as high-grade commercial products from Sigma-Aldrich, Acros Organics, Fluorochem, Alfa-Aesar, or VWR. Anhydrous solvents were either purchased in sealed bottles from the suppliers mentioned above or were dispensed using a Pure SolvTM solvent purification system under inert conditions. For analytical thin-layer chromatography, Merck silica gel plates (60 F254) were used in conjunction with a UV light (λ 254 nM and 365 nM) for detection. The analytical thin-layer chromatography plates were stained with either vanillin, ninhydrin, bromocresol green or potassium permanganate solutions where appropriate. All products were purified either by normal or reverse phase flash chromatography using a glass column with silica gel (type 60) or using a Biotage Isolera One system. When purified via the Biotage Isolera one system, Sfär Silica Standard Duo cartridges of various sizes were used for normal phase, while the RediSep C18 columns were used for reverse phase. Nuclear magnetic resonance (NMR) spectra were recorded on a Bruker Avance III 400 MHz spectrometer (^{1}H, 400 MHz; ^{13}C, 101 MHz). Chemical shifts (d) are expressed in parts per million and coupling constants (*J*) are expressed in hertz (Hz). The following abbreviations are used to describe the peak patterns observed: s (singlet), d (doublet), t (triplet), m (multiplet). High resolution mass spectrometry (HRMS) was performed by the Imperial Mass Spectrometry service, using an electrospray ionization (ESI) mode.; m/z values are reported in Daltons. Liquid chromatography–mass spectrometry (LC-MS) was conducted on the Waters LC-MS system using the analytical reversed-phase XBridge C18 column.

5.2.2 Synthetic Methods

4-amino-3-methylbenzoic acid (2)



2

To a solution of 3-methyl-4-nitrobenzoic acid (2.05 g, 11.3 mmol, 1 eq.) in MeOH (40 mL) under an inert environment, Pd/C (206 mg, 10% wt.) was added. The flask was carefully evacuated and backfilled with hydrogen. The reaction mixture was gently stirred for 18 hours at r.t and upon completion, was filtered using a celite plug. The filtrate was subsequently concentrated *in vacuo* to afford the target compound **2** (1.70 g, 99%) as a beige solid. ^{1}H NMR (400 MHz, Methanol-d4) δ 7.66 – 7.61 (m, 2H), 6.65 (d, *J* = 8.2 Hz, 1H), 2.15 (s, 3H) ppm. Analytical data are consistent with the literature.[155]

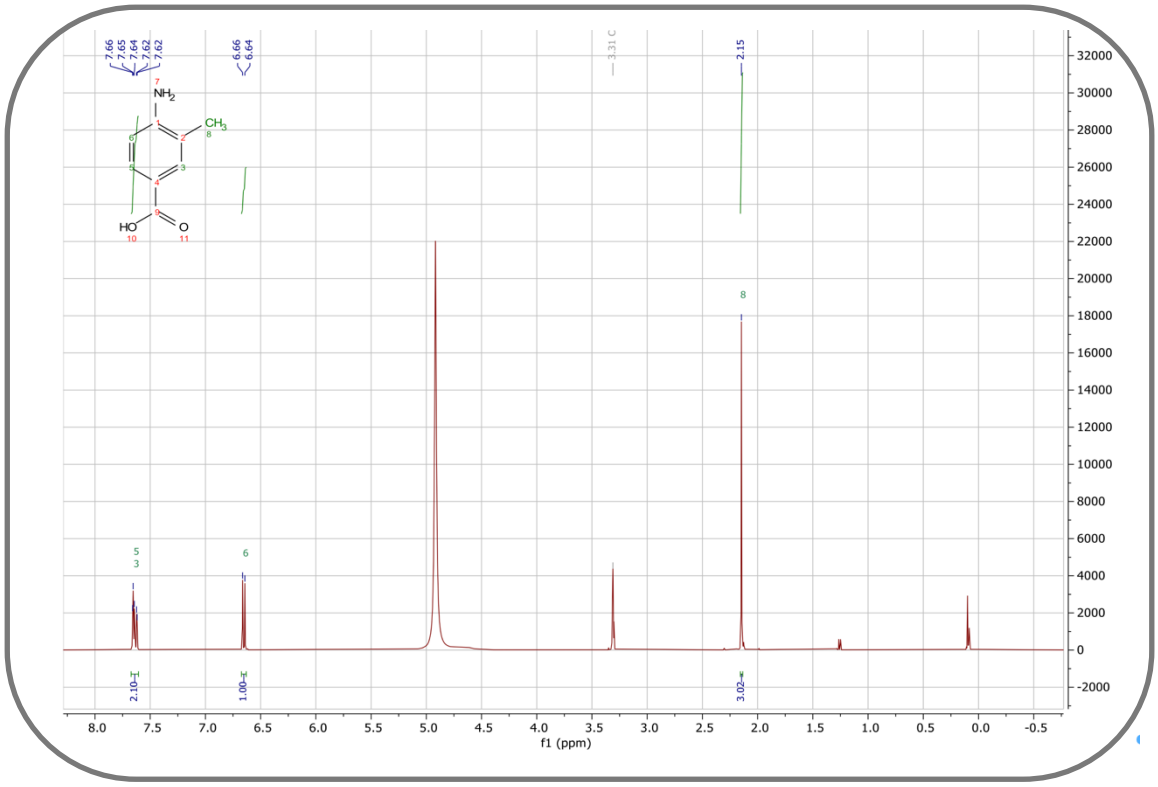
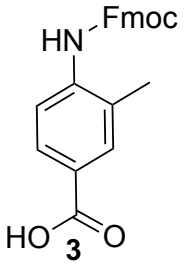


Figure 67: ^{1}H NMR of **2**.

4-((((9*H*-fluoren-9-yl)methoxy)carbonyl)amino)-3-methylbenzoic acid (3)



3

4-amino-3-methylbenzoic acid (153 mg, 1.01 mmol, 1 eq.) was dissolved in anhydrous THF (3 mL) and heated at reflux under N_2. To the reaction mixture, a solution of Fmoc-Cl (386 mg, 1.49 mmol, 1.5 eq.) in anhydrous THF (4 mL) was added dropwise. The reaction mixture was subsequently heated at reflux overnight, upon completion it was then cooled to r.t and concentrated *in vacuo*. Purification by column chromatography (30-100% EtOAc/hexane gradient) produced the target product **3** (288 mg, 76%) as a pale yellow solid. ^{1}H NMR (400 MHz, DMSO-d6) δ 12.75 (s, 1H), 9.19 (s, 1H), 7.91 (d, *J* = 7.6 Hz, 2H), 7.78 – 7.68 (m, 4H), 7.48 – 7.39 (m, 3H), 7.38 – 7.32 (m, 2H), 4.47 (d, *J* = 6.9 Hz, 2H), 4.32 (t, *J* = 6.8 Hz, 1H), 2.26 (s, 3H) ppm. Analytical data are consistent with the literature.[126]

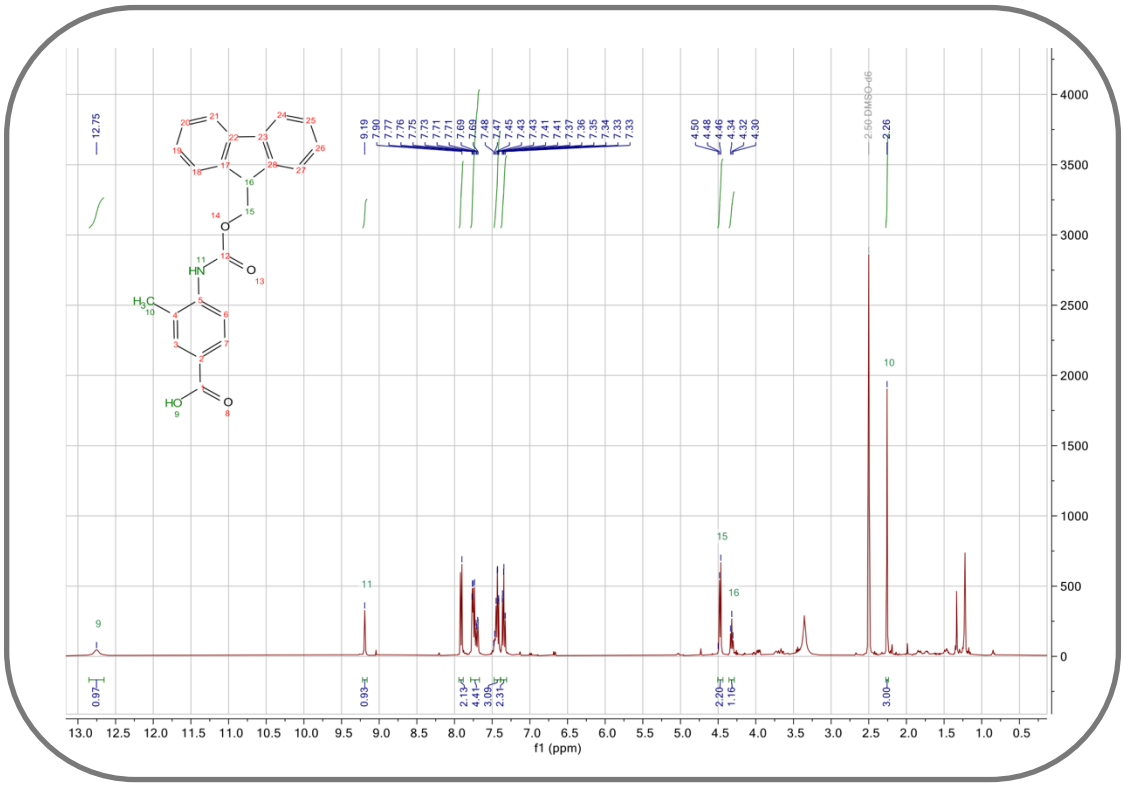
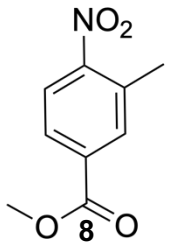


Figure 68: ^{1}H NMR of **3**.

Methyl 3-methyl-4-nitrobenzoate (8)



3-Methyl-4-nitrobenzoic acid (5.00 g, 27.6 mmol, 1 eq.) was dissolved in MeOH (50 mL). Concentrated H_2SO_4 (0.84 mL, 15.8 mmol, 0.57 eq.) was added and the reaction mixture was heated at reflux for 26 h. The reaction mixture was then cooled to r.t and the solvent was removed *in vacuo*. The residue was subsequently diluted with DCM, washed with sat. sodium bicarbonate and brine, before being dried over anhydrous M_gSO_4. The organic layer was then concentrated *in vacuo* to produce the target compound **8** (4.72 g, 88%) as a white solid, which was used without further purification. ^{1}H NMR (400 MHz, Chloroform-d) δ 8.03 – 8.02 (m, 1H), 8.00 – 7.95 (m, 2H), 3.96 (s, 3H), 2.62 (s, 3H) ppm. ^{13}C NMR (101 MHz, Chloroform-d) δ 165.5, 152.0, 134.1, 133.9, 133.6, 128.2, 124.7, 52.9, 20.2 ppm. Analytical data are consistent with the literature.[156]

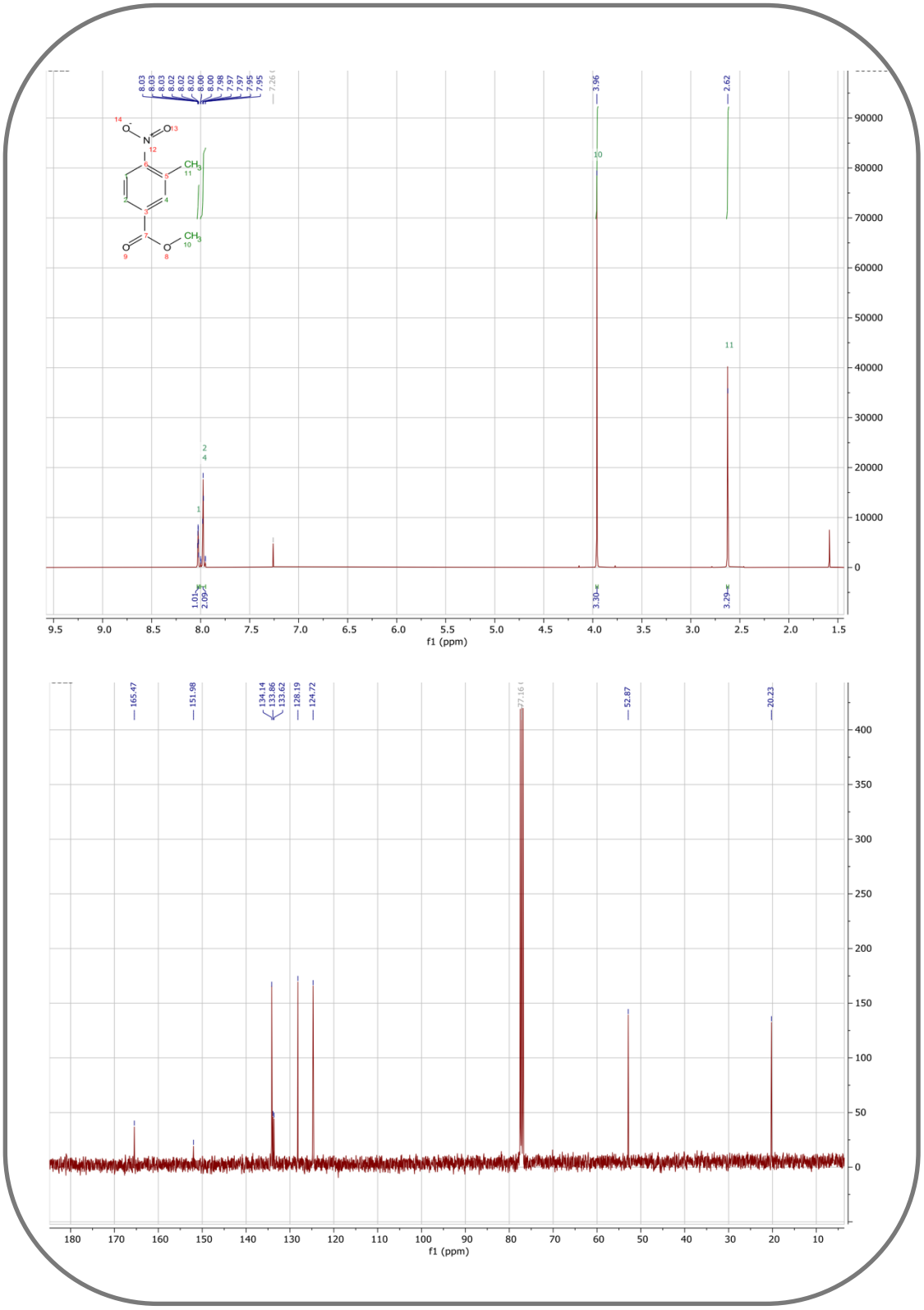
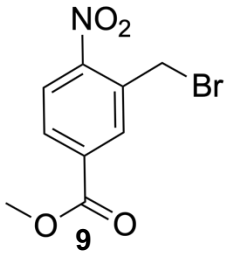


Figure 69: ^{1}H (top) and ^{13}C (bottom) NMR of **8**.

Methyl 3-(bromomethyl)-4-nitrobenzoate (9)



Methyl 3-methyl-4-nitrobenzoate (1.40 g, 7.17 mmol, 1 eq.) was dissolved in CCl_4 (15 mL). NBS (1.28 g, 7.19 mmol, 1 eq.) and benzoyl peroxide (109 mg, 0.45 mmol, 0.06 eq.) were added, and the reaction mixture was heated at reflux for 25 h under N_2. The reaction mixture was cooled to r.t, filtered and concentrated *in vacuo* to give the crude bromide. The crude compound was then purified by column chromatography (1-25% EtOAc/hexane gradient) to afford the target product **9** (969 mg, 49%) as a white solid. ^{1}H NMR (400 MHz, Chloroform-d) δ 8.24 (d, *J* = 1.8 Hz, 1H), 8.13 (dd, *J* = 8.5, 1.8 Hz, 1H), 8.07 (d, *J* = 8.4 Hz, 1H), 4.83 (s, 2H), 3.99 (s, 3H) ppm. ^{13}C NMR (101 MHz, Chloroform-d) δ 164.8, 150.6, 134.7, 133.9, 133.2, 130.8, 125.7, 53.1, 28.1 ppm. HRMS-ESI (*m/z*): Calculated for $[C_9H_9NO_4{}^{79}Br]^+$ = 273.9709. Found = 273.9706 (Δ = -0.0003). Analytical data are consistent with the literature.[157]

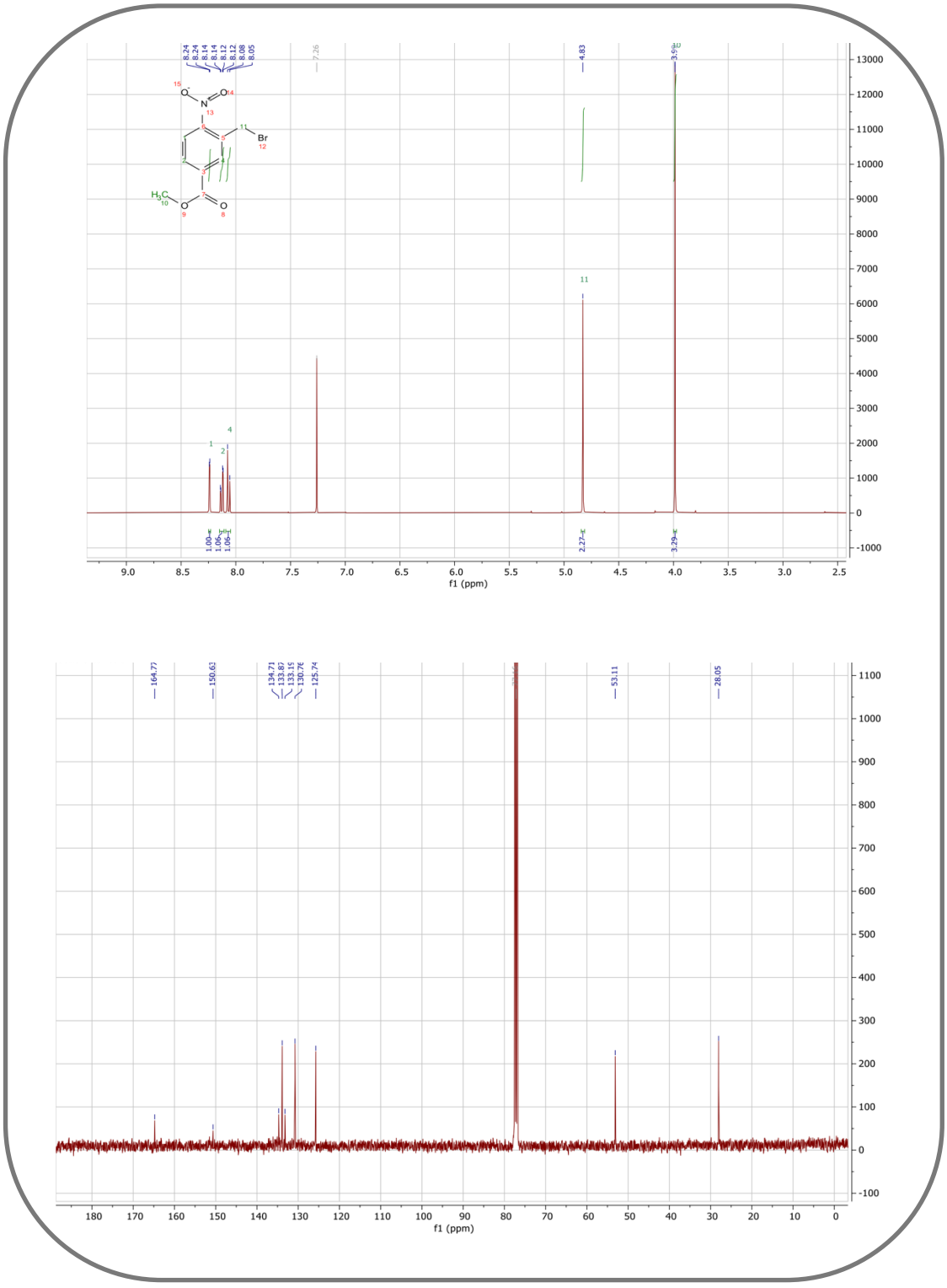
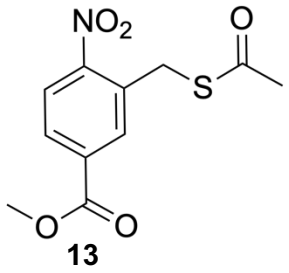


Figure 70: ^{1}H (top) and ^{13}C (bottom) NMR of **9**.

Methyl 3-((acetylthio)methyl)-4-nitrobenzoate (13)



13

To a solution of methyl 3-(bromomethyl)-4-nitrobenzoate (2.01 g, 7.35 mmol, 1 eq.) in MeOH (25 mL), potassium thioacetate (1.26 g, 11.03 mmol, 1.5 eq.) was added and the reaction mixture was stirred at r.t for 25 h. Upon completion, MeOH was removed *in vacuo* and the residue was dissolved in DCM. The solution was then washed with H_2O, dried over anhydrous $MgSO_4$, filtered and concentrated *in vacuo* to afford the target product **13** (1.75 g, 89%) as a pale yellow solid. The purity of the product was sufficient at this stage to take forward without requiring additional purification. ^{1}H NMR (400 MHz, Chloroform-d) δ 8.27 (d, *J* = 1.7 Hz, 1H), 8.09 – 8.02 (m, 2H), 4.43 (s, 2H), 3.97 (s, 3H), 2.33 (s, 3H) ppm.^{13}C NMR (101 MHz, Chloroform-d) δ 194.9, 165.1, 134.6, 134.0, 129.8, 125.3, 53.0, 30.9, 30.3 ppm (two quaternary carbons not observed).

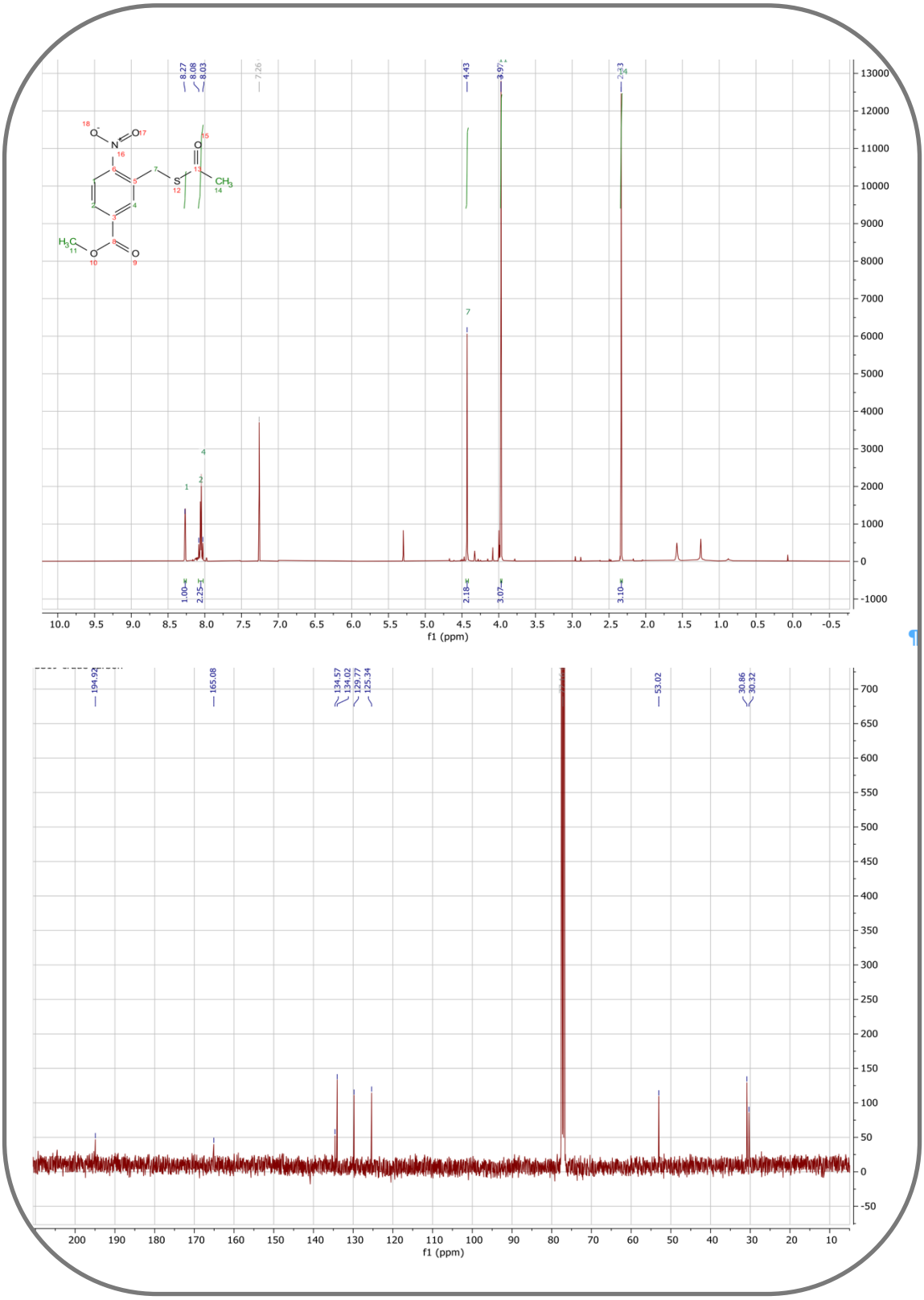
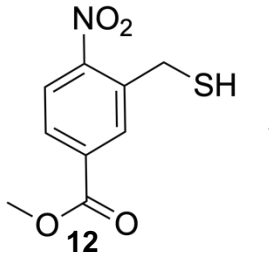


Figure 71: ^{1}H (top) and ^{13}C (bottom) NMR of **13**.

Methyl 3-(mercaptomethyl)-4-nitrobenzoate (12)



12

To a solution of methyl 3-((acetylthio)methyl)-4-nitrobenzoate (1.18 g, 4.38 mmol, 1 eq.) in MeOH (32 mL), conc. HCl (8.0 mL) was added and the reaction mixture was heated at reflux for 23 h. Upon completion, MeOH was removed *in vacuo* and the residue was dissolved in DCM. It was washed with H_2O, dried over anhydrous $MgSO_4$, filtered and concentrated *in vacuo* to afford the target product **12** (917 mg, 92 %) as a yellow solid, which was used without further purification. ^{1}H NMR (400 MHz, Chloroform-d) δ 8.16 (d, *J* = 1.4 Hz, 1H), 8.08 – 8.00 (m, 2H), 4.03 (d, *J* = 8.6 Hz, 2H), 3.98 (s, 3H), 2.16 (t, *J* = 8.6 Hz, 1H) ppm. ^{13}C NMR (101 MHz, Chloroform-d) δ 165.0, 150.5, 137.2, 134.6, 133.0, 129.4, 125.5, 53.0, 26.3 ppm. HRMS-ESI (*m/z*): Calculated for $[C_9H_8NO_4S]^-$ = 226.0180. Found = 226.0178 (Δ = -0.0002).

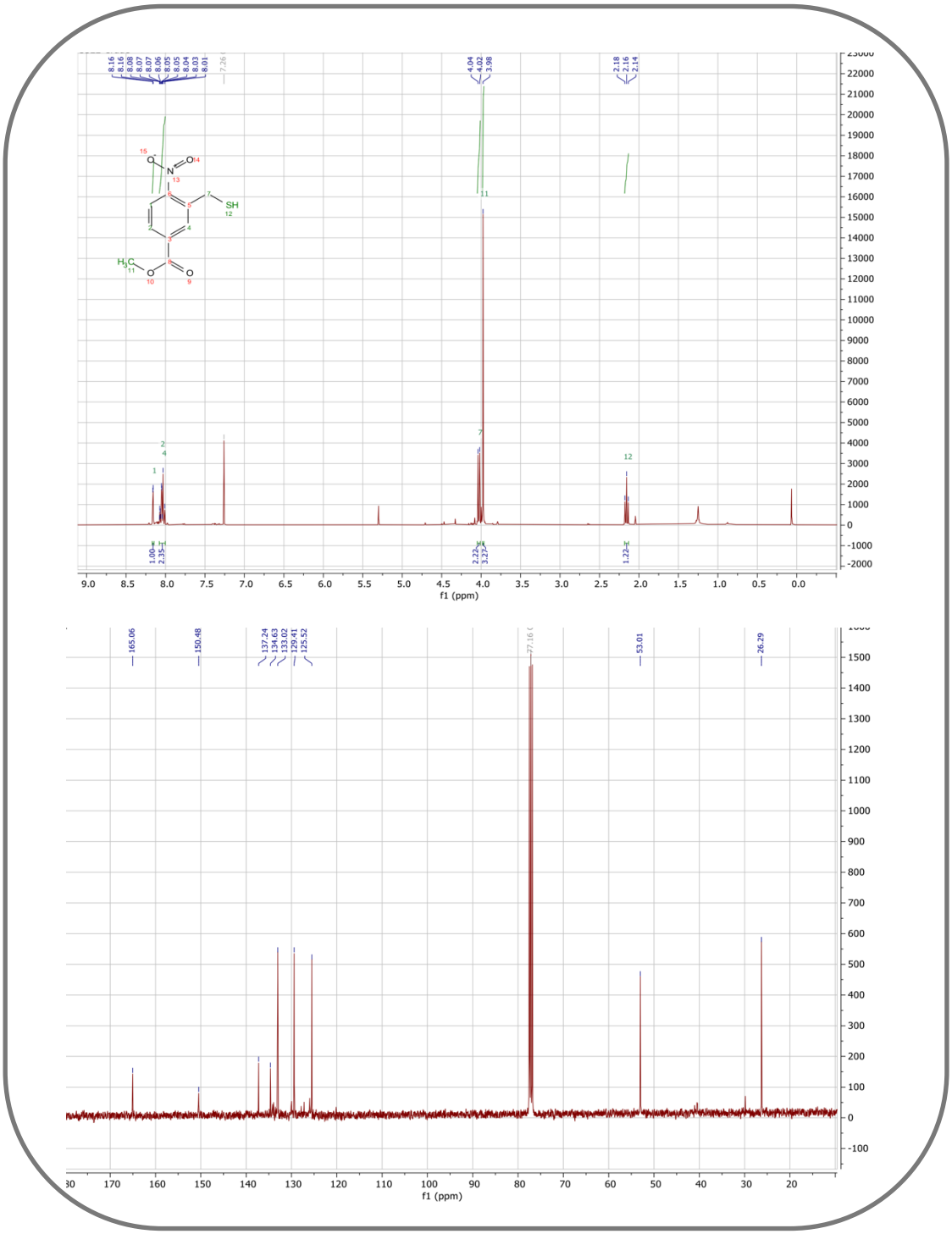
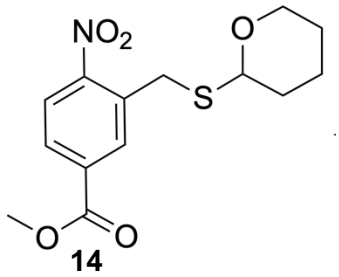


Figure 72: ^{1}H (top) and ^{13}C (bottom) NMR of **12**.

Methyl 4-nitro-3-(((tetrahydro-2H-pyran-2-yl)thio)methyl)benzoate (14)



14

To a solution of methyl 3-(mercaptomethyl)-4-nitrobenzoate (582 mg, 2.56 mmol, 1 eq.) and DHP (420 µL, 4.60 mmol, 1,8 eq.) in anhydrous DCM (23 mL), *P*TSA (113 mg, 0.59 mmol, 0.23 eq.) was added. The reaction mixture was stirred at r.t under N_2 for 26 h. The reaction mixture was then washed with brine, dried over anhydrous $MgSO_4$, filtered and concentrated *in vacuo* to afford the crude residue. The residue was subsequently purified via column chromatography (5-30% EtOAc/hexane gradient) to produce the target product **14** (600 mg, 75%) as a white solid. ^{1}H NMR (400 MHz, $CDCl_3$) δ 8.13 (d, *J* = 1.9 Hz, 1H), 8.03 (dd, *J* = 8.4, 1.8 Hz, 1H), 7.98 (d, *J* = 8.5 Hz, 1H), 4.74 – 4.70 (m, 1H), 4.18 (d, *J* = 13.8 Hz, 1H), 4.11 (d, *J* = 13.8 Hz, 1H), 4.03 – 3.97 (m, 1H), 3.96 (s, 3H), 3.48 – 3.41 (m, 1H), 1.89 – 1.80 (m, 1H), 1.79 – 1.70 (m, 1H), 1.65 – 1.48 (m, 4H) ppm. ^{13}C NMR (101 MHz, $CDCl_3$) δ 165.2, 151.2, 135.2, 133.9, 133.7, 129.2, 125.4, 81.4, 64.1, 52.9, 31.1, 30.6, 25.6, 21.4 ppm.

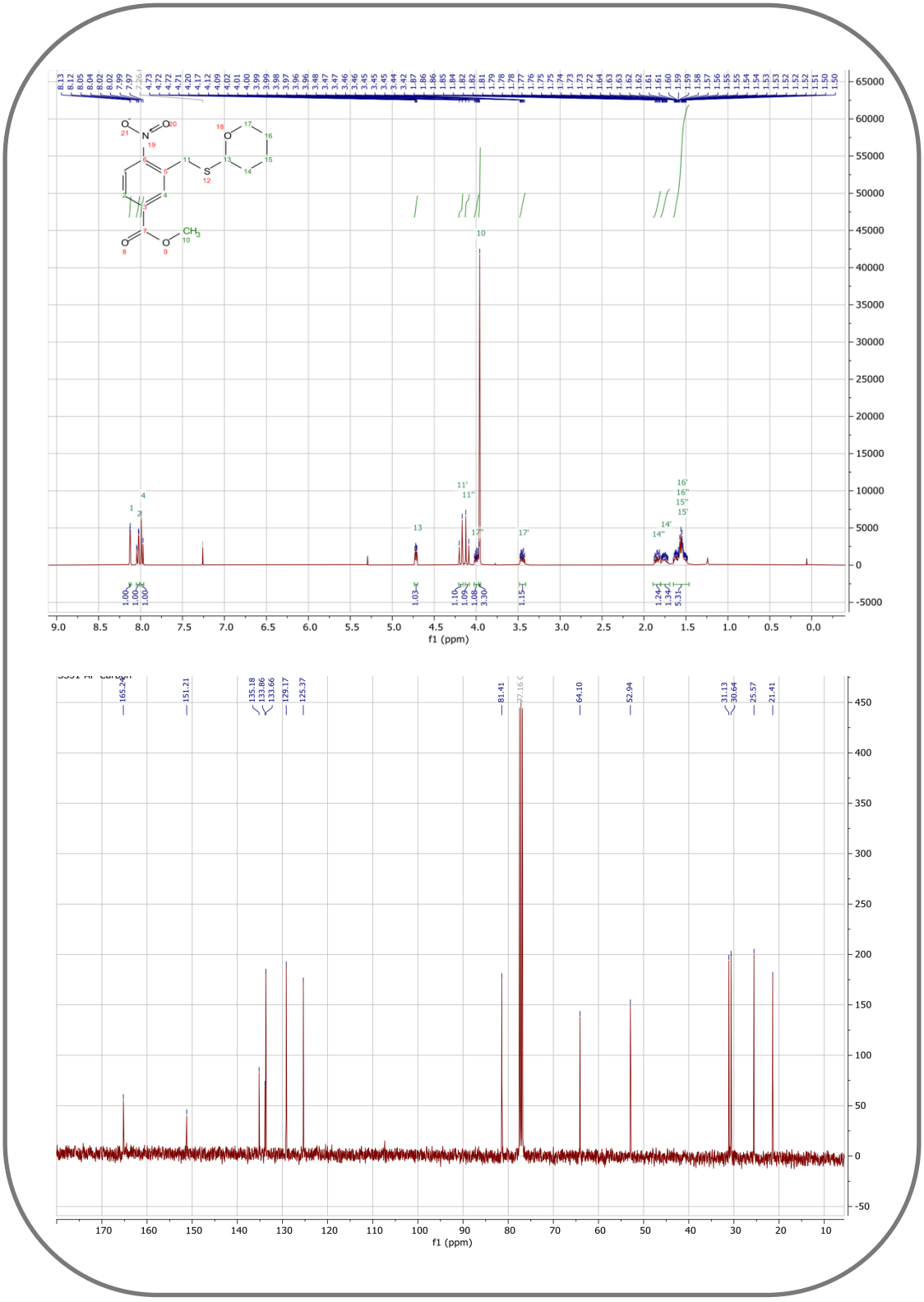
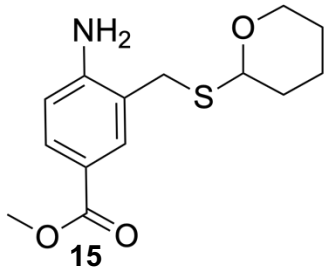


Figure 73: ^{1}H (top) and ^{13}C (bottom) NMR of **14**.

Methyl 4-amino-3-(((tetrahydro-2H-pyran-2-yl)thio)methyl)benzoate (15)



15

To a solution of methyl 4-nitro-3-(((tetrahydro-2H-pyran-2-yl)thio)methyl)benzoate (633 mg, 2.03 mmol, 1 eq.) in THF (26 mL), $Na_2S_2O_4$ (4.00 g, 19.5 mmol, 9.61 eq.) in H_2O (13 mL) was added and the reaction mixture was stirred at 50 °C for 25 h. The reaction mixture was cooled to r.t and subsequently extracted with EtOAc. The organic layers were washed with brine, dried over anhydrous $MgSO_4$, filtered and concentrated *in vacuo* to afford the target product **15** (540 mg, 94%) as a white solid. The purity of the product was sufficient at this stage to take forward without requiring additional purification.^{1}H NMR (400 MHz, $CDCl_3$) δ 7.80 – 7.76 (m, 2H), 6.65 (d, *J* = 8.9 Hz, 1H), 4.71 – 4.66 (m, 1H), 4.56 (s, 2H), 4.15 – 4.08 (m, 1H), 3.93 (d, *J* = 13.3 Hz, 1H), 3.85 (s, 3H), 3.65 (d, *J* = 13.3 Hz, 1H), 3.57 – 3.49 (m, 1H), 1.90 – 1.76 (m, 2H), 1.69 – 1.50 (m, 4H) ppm. ^{13}C NMR (101 MHz, $CDCl_3$) δ 167.3, 149.7, 132.7, 130.7, 120.9, 119.6, 115.3, 81.4, 65.6, 51.8, 31.0, 30.9, 25.6, 22.2 ppm.

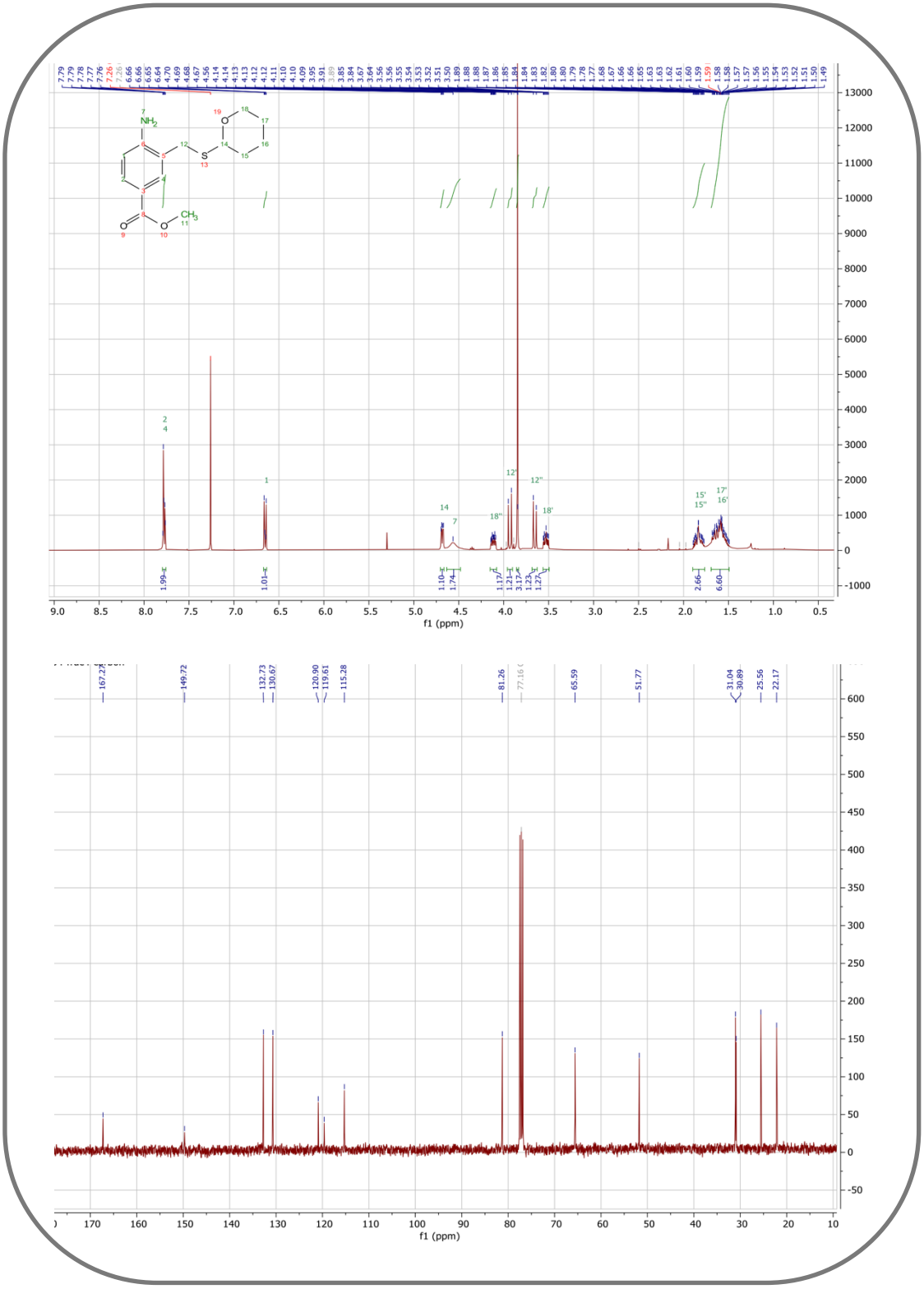
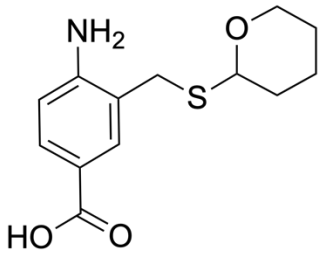


Figure 74: ^{1}H (top) and ^{13}C (bottom) NMR of **15**.

4-amino-3-(((tetrahydro-2H-pyran-2-yl)thio)methyl)benzoic acid (17)



17

To a solution of methyl 4-amino-3-(((tetrahydro-2H-pyran-2-yl)thio)methyl)benzoate (365 mg, 1.30 mmol, 1 eq.) in MeOH/THF (1:1, 4:4 mL), NaOH (10% w/v, 4 mL) was added. The reaction mixture was stirred at r.t for 17 h. Additional NaOH (1.5 mL) was added and the reaction mixture was stirred for 28 h. The organic solvents were removed *in vacuo* and the residue was dissolved in H_2O and acidified to PH 4 using 1 M HCl. The precipitate was then extracted with EtOAc and subsequently dried over anhydrous $MgSO_4$. It was then filtered and concentrated *in vacuo* to afford the target product **17** (328 mg, 95%) as a white solid, which was used without further purification. ^{1}H NMR (400 MHz, DMSO) δ 12.05 (s, 1H), 7.56 – 7.53 (m, 2H), 6.62 (d, *J* = 8.2 Hz, 1H), 5.81 (s, 2H), 4.69 (m, 1H), 4.01 – 3.96 (m, 1H), 3.72 (d, *J* = 13.5 Hz, 1H), 3.62 (d, *J* = 13.5 Hz, 1H), 3.50 – 3.42 (m, 1H), 1.82 – 1.73 (m, 1H), 1.71 – 1.63 (m, 1H), 1.55 – 1.44 (m, 4H) ppm. ^{13}C NMR (101 MHz, DMSO) δ 167.5, 150.7, 132.1, 129.9, 119.2, 116.9, 113.8, 80.1, 63.7, 30.5, 29.4, 25.2, 21.3 ppm.

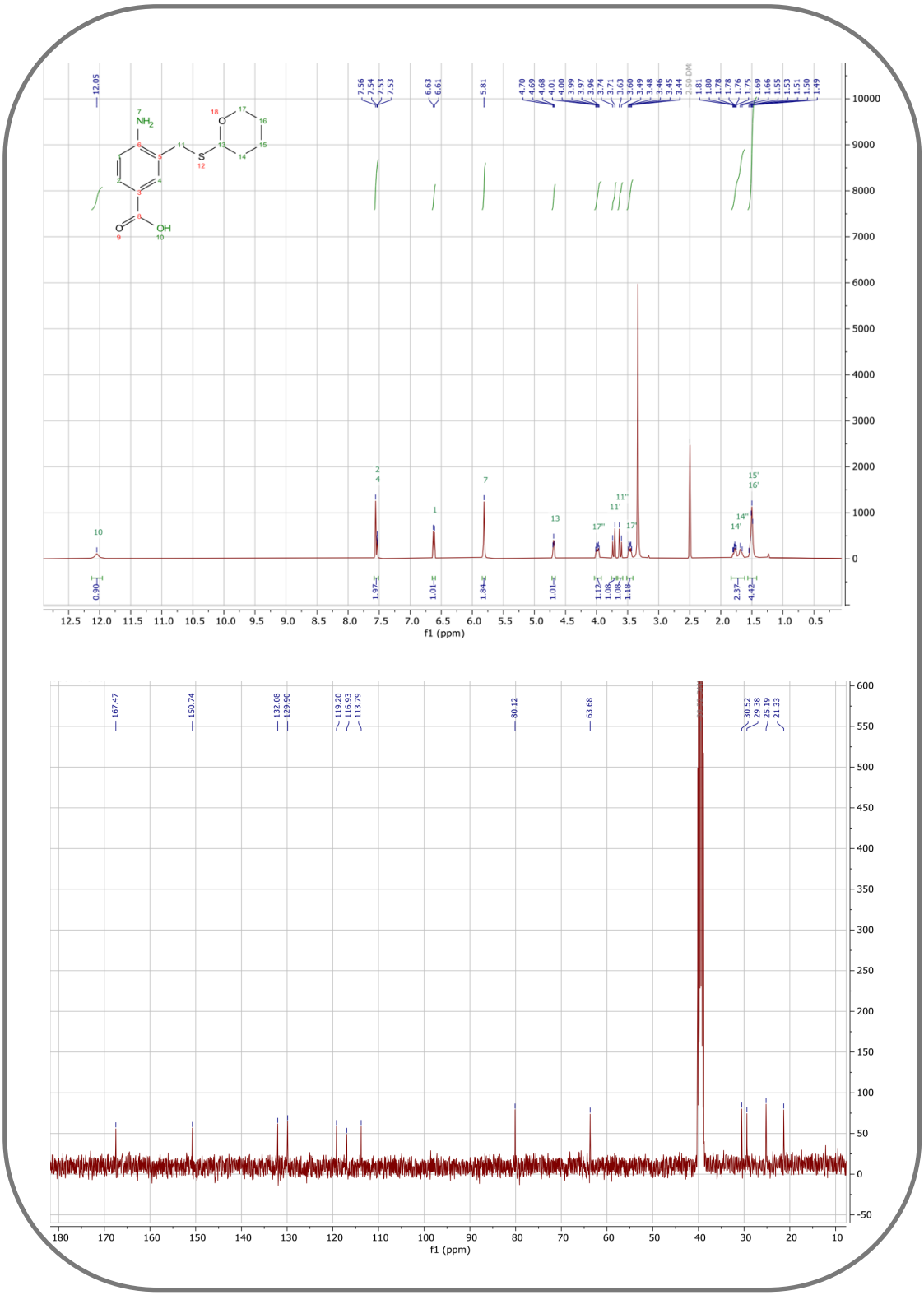
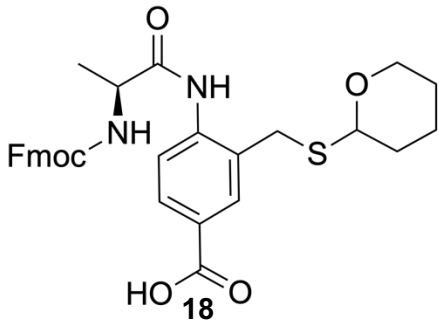


Figure 75: ^{1}H (top) and ^{13}C (bottom) NMR of **17**.

4-(2-((((9H-fluoren-9-yl)methoxy)carbonyl)amino)propanamido)-3-(((tetrahydro-2H-pyran-2-yl)thio)methyl)benzoic acid (18)



18

To a solution of Fmoc-Ala-OH (294 mg, 0.94 mmol, 4.9 eq.) in anhydrous $CHCl_3$ (1.5 mL) and anhydrous DMF (500 μL), Ghosez reagent (119 μL, 0.90 mmol, 4.7 eq.) was added and the reaction mixture was incubated at r.t for 1 h. The reaction mixture was subsequently added to a solution of 4-amino-3-(((tetrahydro-2H-pyran-2-yl)thio)methyl)benzoic acid (51 mg, 0.19 mmol, 1 eq.) in anhydrous $CHCl_3$ (1.0 mL) and microwaved at 60 ^oC for 30 min. The reaction mixture was then concentrated in vacuo. The crude mixture was purified by reverse phase chromatography to afford the target product **18** (16.3 mg, 15%) as a white solid.^{1}H NMR (400 MHz, DMSO) δ 7.88 (d, *J* = 7.6 Hz, 2H), 7.81 (d, *J* = 7.3 Hz, 1H), 7.70 (t, *J* = 7.1 Hz, 2H), 7.58 (s, 1H), 7.54 (d, *J* = 8.8 Hz, 1H), 7.41 (t, *J* = 7.5 Hz, 2H), 7.36 – 7.28 (m, 2H), 7.07 – 7.02 (m, 1H), 6.65 (d, *J* = 8.5 Hz, 1H), 4.48 – 4.40 (m, 1H), 4.33 – 4.26 (m, 2H), 4.26 – 4.19 (m, 1H), 4.13 – 4.00 (m, 3H), 3.97 – 3.89 (m, 1H), 3.84 – 3.77 (m, 1H), 1.92 – 1.81 (m, 1H), 1.80 – 1.68 (m, 1H), 1.63 (m, 2H), 1.56 – 1.46 (m, 2H), 1.29 (d, *J* = 7.3 Hz, 3H) ppm.^{13}C NMR (101 MHz, DMSO) δ 172.9, 167.5, 155.9, 147.6, 143.8, 140.7, 130.3, 128.9, 127.6, 127.1, 125.2, 120.1, 117.2, 116.6, 114.7, 65.6, 64.2, 57.3, 49.4, 46.6, 34.2, 29.7, 27.9, 22.0, 16.9 ppm.

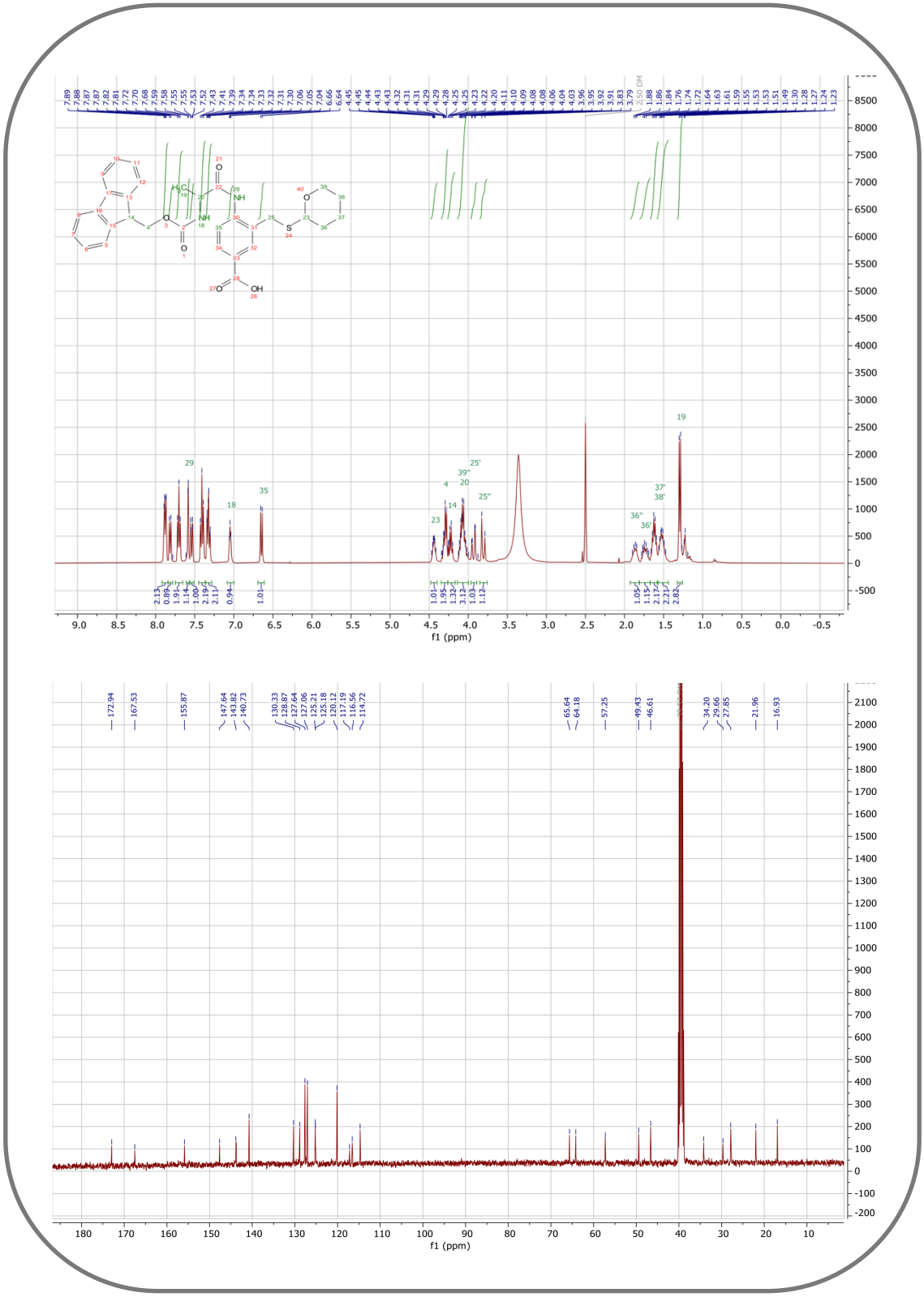


Figure 76: ^{1}H (top) and ^{13}C (bottom) NMR of **18.**

5.3 Protein Expression and Purification

5.3.1 General Protocols

5.3.1.1 SDS-PAGE

The protein samples to be analysed were transferred to microcentrifuge tubes, to which 4X SDS loading buffer (180 μL Laemmli, 20 μL 2-Mercaptoethanol, 600 μL Phosphate Buffered Saline) was added to give a final ratio of 1X. The microcentrifuge tubes were subsequently heated at 95 °C for 10 minutes. These samples, as well as the Precision Plus Protein™ All Blue ladder, were loaded onto a 12% Mini-PROTEAN® TGX™ Precast Protein Gel. This was used in conjunction with the Tris-Glycine-SDS Buffer from Sigma-Aldrich. The gel was run at a constant voltage of 160 V for 45 minutes, after which it was stained with InstantBlue Coomassie Protein Stain for 15 minutes. The gel was washed with distilled water for a further 30 minutes before it was imaged using the ImageQuant LAS 4000.

5.3.2 Site-Directed Mutagenesis

The template plasmid used to generate the BCL-X_L (Δ45-84, domain 1-209, C111S) construct was previously synthesised by Fiona Rowan. BCL-X_L (Δ45-84, domain 1-209) had been cloned into a pET24a vector to generate the [BCL-X_L]-LEHHHHHH construct. Site-directed mutagenesis was performed using the KOD Hot Start DNA Polymerase kit from Sigma-Aldrich. The complementary forward and reverse oligonucleotide primers were ordered from ThermoFisher Scientific.

For a 50 μL scale the components were as follows: 5 μL KOD buffer, 5 μL dNTPs, 1 μL KOD Hot Start DNA Polymerase, 0.5 μL forward primer, 0.5 μL reverse primer, 0.35 μL template plasmid, 3 μL $MgSO_4$, 35.15 μL dd H_2O. The PCR cycle conditions consisted of activation at 95 °C for 2 minutes; this was followed by 25 cycles of 95 °C for 30 seconds, 61 °C for 30 seconds and 72 °C for 4 minutes. The final elongation was at 72 °C for 10 minutes, after which the reaction was digested with 1 μL of DpnI for 1 hour at 37 °C.

This was then used to transform NEB® Competent *E. coli* DH5α cells, which were spread over a Lysogeny broth (LB) agar plate containing kanamycin (50 μg/mL). This was incubated overnight at 37 °C, to produce colonies of the transformed cells. Individual colonies were picked and used

to inoculate 30 mL cultures of LB medium containing kanamycin (50 μg/mL) overnight at 37 °C. The desired plasmids were extracted using the Qiagen QIAprep Spin Miniprep Kit according to the supplied protocol. The plasmids were sent for sequencing (Genewiz) to confirm the correct mutation and verify that the BCL-X_L (Δ45-84, domain 1-209, C111S) construct was generated.

5.3.3 Protein Expression

Invitrogen™ One Shot™ BL21(DE3) Chemically Competent E. coli cells (50 μL) were thawed on ice for 15 minutes. This was followed by the addition of the BCL-X_L plasmid (Δ45-84, C111S) to the chemically competent cells (2 μL at 27 ng/μL), after which the cells were placed back on ice for a further 15 minutes. The microcentrifuge tube containing the cells was then placed in a 42 °C water bath for 45 seconds, before being put back on ice for 5 minutes. The cells were subsequently removed from ice and in a sterile environment, SOC medium (450 μL) from ThermoFisher Scientific was added. This suspension was then incubated at 37 °C for 60 minutes. The cell culture (150 μL) was spread over a LB agar plate containing kanamycin (50 μg/mL) and was incubated overnight at 37 °C, to produce colonies of the transformed cells.

A colony was selected to inoculate LB medium (10 mL) containing kanamycin (50 μg/mL) and was left to incubate overnight at 37 °C whilst shaking. Following this, the bacterial culture was used to inoculate additional LB medium (1 L containing kanamycin (50 μg/mL)) and evenly split between 2 x 2 L conical flasks. The flasks were shaken at 37 °C until the optical density at 600 nM (OD_{600}) of the bacterial culture reached approximately 0.6, where isopropyl β-d-1-thiogalactopyranoside (IPTG) was then added to give a final concentration of 1 mM. The flasks were shaken overnight at 18 °C and the culture was subsequently centrifuged (4 °C, 30 min, 8000 rpm) using the ThermoFisher Scientific Sorvall LYNX 4000 centrifuge to produce the desired cell pellets. Expression of the target protein was monitored by SDS-Page as previously described, using samples of the culture from before and after IPTG induction.

5.3.4 Protein Purification

5.3.4.1 General Conditions

The purification of BCL-X_L was performed at 4 °C using the ÄKTA pure™ chromatography system. The immobilized metal affinity chromatography (IMAC) column used was the HiTrap TALON® crude 5 mL column packed with cobalt-based resins. The anion exchange chromatography column (AEC) used for purification was the HiTrap Q HP 5 mL column. For size exclusion

chromatography (SEC) the HiLoad 16/600 Superdex 75 pg column was used. The ÄKTA purification system, as well as all columns used, were purchased from Cytiva.

5.3.4.2 Buffers

All buffers were filtered through a 0.2 μM filter and subsequently degassed.

IMAC binding buffer: 50 mM K_2HPO_4, 300 mM NaCl, 5% glycerol, pH 8.0

IMAC elution buffer: 50 mM K_2HPO_4, 300 mM NaCl, 500 mM imidazole, 5% glycerol, pH 8.0

AEC binding buffer: 20 mM TRIS, 2 mM TCEP, 5% glycerol, pH 8.0

AEC elution buffer: 20 mM TRIS, 2 mM TCEP, 1 M NaCl, 5% glycerol, pH 8.0

SEC buffer: 50 mM TRIS, 200 mM NaCl, 2 mM TCEP, 5% glycerol, pH 8.0

5.3.4.3 Purification

The cell pellets from the previous step were resuspended in the IMAC binding buffer (5 mL per gram), after which 1 tablet of cOmplete protease inhibitor cocktail was added. This was followed by the addition of DNAse (1 μL per 50 mL) and $MgCl_2$ (5 mM final concentration) and subsequently stirred for 35 minutes. The Constant Systems CF1 Cell Disrupter was used to lyse the cells according to the manufactures instructions at 25 KPSI (2 cycles). The lysed cells were centrifuged (4 °C, 35 min, 18,000 rpm) using the ThermoFisher Scientific Sorvall LYNX 4000 centrifuge and the desired supernatant was isolated.

To begin purification, the HiTrap TALON® crude 5 mL column was equilibrated with the IMAC binding buffer. The supernatant was then injected onto the column, and it was subsequently washed with 100% IMAC binding buffer for 7 column volumes (CV). The bound protein was then eluted using the IMAC elution buffer at a gradient of 0-100% over 10 CV.

Fractions containing BCL-X_L were identified using SDS - PAGE as described previously. These fractions were combined and dialysed overnight using the ThermoFisher Scientific SnakeSkin™ Dialysis Tubing (3.5K MWCO) in a beaker containing AEC binding buffer (1.5 L).

Following this, the sample was filtered (0.2 μm) and loaded onto the HiTrap Q HP column (2 x 5 mL columns joined together). This column had been equilibrated with the AEC binding buffer prior to the injection of the sample. The column was then washed with 12 CV of the AEC binding buffer,

before the bound protein was eluted with the AEC elution buffer, with a gradient of 0-50% over 15 CV. Fractions containing BCL-X_L were subsequently verified using SDS- PAGE and combined. A Vivaspin™ ultrafiltration spin column (10 kDa MWCO) was used to concentrate the sample to 2 mL, after which the sample was once again filtered (0.2 μm).

The concentrated sample was loaded onto the HiLoad 16/600 Superdex 75 pg column that had previously been equilibrated with the SEC buffer. BCL-X_L was eluted through an isocratic elution method over 1 CV. The fractions were analysed for size and purity though SDS-PAGE before being combined. BCL-X_L was then concentrated using a Vivaspin™ ultrafiltration spin column (10 kDa MWCO) and subsequently aliquoted before being flash frozen with liquid N_2 and stored at –80 °C. The final concentration of BCL-X_L (Δ45-84, domain 1-209, C111S) was 165 μM or 3 mg/mL.

5.4 Biochemical Assays

5.4.1 Fluorescence Anisotropy

5.4.1.1 General Information

Fluorescence anisotropy (FA) was performed using the CLARIOstar® Plus multi-mode plate reader, with excitation at 482 nM (16 nM bandwidth), dichroic mirror at 504 nM and emission at 530 nM (40 nM bandwidth). The Fluorescence anisotropy assays were performed in 384 well plates at 25 °C. Assay plates used were either the Corning® 384-well (black polystyrene nonbinding) plates or the Greiner Bio-One 384-well (black nonbinding) plates. The fluorescein-labelled BAK peptide (FAM-BAK$^{72\text{-}87}$) used for all assays was synthesised and purified by Dennis Worm. Data analysis was performed using GraphPad.

FA buffer: 50 mM TRIS, 150 mM NaCl, 5% glycerol, pH 8.0

5.4.1.2 Saturation Assay

For FA saturation assays, both WT BCL-X_L (Δ45-84, domain 1-209) and mutant BCL-X_L (Δ45-84, domain 1-209, C111S) were titrated against a fixed concentration of FAM-BAK$^{72\text{-}87}$. A dilution series (final concentration 1 μM to 0.015 nM) for each construct of BCL-X_L was prepared using FA buffer in a 384-well plate. To each well a solution of FAM-BAK$^{72\text{-}87}$ in FA assay buffer was added (final concentration of 1 nM). The assay plate was covered in foil and incubated for 20 minutes at 25 °C whilst gently rocking, after which the FA measurements were taken. All measurements were blank corrected (wells without the addition of FAM-BAK$^{72\text{-}87}$) and repeated in triplicate.

5.4.1.3 Competition Assay

For FA competition assays, unlabelled peptides **SS1-4** were titrated against a fixed concentration of mutant BCL-X_L (Δ45-84, domain 1-209, C111S) and FAM-BAK$^{72\text{-}87}$. A dilution series was prepared for each unlabelled peptide (final concentration 40 μM to 1.2 nM) using FA buffer in a 384-well plate. To each well a solution of BCL-X_L (100 nM final concentration) and a solution of FAM-BAK$^{72\text{-}87}$ (1 nM final concentration) was added. The competition assay plate was covered in foil and incubated for 20 minutes at 25 °C whilst gently rocking, after which the FA measurements were taken. All measurements were blank corrected (wells without the addition of FAM-BAK$^{72\text{-}87}$) and repeated in triplicate.

5.4.2 Quantitative Irreversible Tethering (qIT)

5.4.2.1 General Information

Quantitative Irreversible Tethering (qIT) was performed using the CLARIOstar® Plus multi-mode plate reader, with excitation at 360 nM (20 nM bandwidth) and emission at 482 nM (16 nM bandwidth). The qIT assays were performed in 384 well plates at r.t. Assay plates used were the Corning® 384-well (black polystyrene nonbinding) plates. The semi-automatic pipetting device used was the analytikjena CyBio SELMA liquid handler. This protocol was adapted from Brad Hocking. Data analysis was performed using GraphPad.

Reaction Buffer: 25 mM HEPES, 150 mM NaCl, pH 8.0

Quench Buffer: 25 mM HEPES, 150 mM NaCl, pH 7.5

5.4.2.2 Compound Preparation

- **TCEP –** 600 μL of TCEP slurry (50% TCEP w/v TCEP-agarose beads) was washed 5 times with reaction buffer through stepwise resuspension, centrifugation (1 min, 2400 rpm) and removal of supernatant. The final suspension was made up to 10 mL in reaction buffer and resuspended, ready for plating (3% TCEP bead suspension).
- **Acrylamide dilution stock –** From 50 mM acrylamide library stock plates, 1.8 μL was taken and diluted into 58.2 μL reaction buffer to form a 1.5 mM stock plate.
- **Peptide stock** -To make a 9 mL stock at 45 μM (3X), 405 μL of a 1 mM peptide stock was taken and made up to 9 mL with reaction buffer.
- **CPM stock** – To make up a 15 mL stock at 4.17 μM, 125.1 μL of a 500 μM stock was taken and make up to 15 mL with quench buffer (500 μM CPM stock was in DMSO).

5.4.2.3 Reaction Plate

The 384 well reaction plate was set up such that columns 1 & 2 served as the negative control and columns 23 & 24 served as the positive control. The reaction plate was charged with 20 μL of TCEP beads, with an additional 20 μL of reaction buffer added to columns 1 & 2. Columns 3-24 were charged with 20 μL of the appropriate cysteine containing peptide, following which the

reaction plate was incubated for 1 h at r.t. to reduce said cysteine residue. The assay was formally started when 20 μL of 1.5 mM acrylamide was added to the reaction plate; DMSO was added to the control columns in place of this. Final reaction plate concentrations - 1% DMSO, 1% TCEP bead suspension, 500 μM acrylamide, 15 μM peptide.

5.4.2.4 Quench Plate

The reaction was quenched at regular time intervals (t = 7, 15, 30, 60, 120, 240, 300, 1380, 1500 min), where a 3 μL aliquot was taken from the reaction plate and quenched in a 384 well quench plate containing 27 μL of 4.17 μM CPM. The quench plate was covered and incubated for 1 h at r.t before the fluorescence intensity was measured.

5.4.3 qIT to FA

5.4.3.1 General Information

qIT to FA assays were performed in 384 well plates. Assay plates used were the Corning® 384-well (black polystyrene nonbinding) plates. Fluorescence intensity was measured using the CLARIOstar® Plus multi-mode plate reader with excitation at 482 nM (16 nM bandwidth) and emission at 530 nM (40 nM bandwidth). The semi-automatic pipetting device used was the analytikjena CyBio SELMA liquid handler. Data analysis was performed using GraphPad.

5.4.3.2 Compound Preparation

- BCL-X_L (Δ45-84, domain 1-209, C111S) – For 18 mL at 300 nM, 32.7 μL was taken from a 165 μM stock and made up to 18 mL with qIT reaction buffer.
- FAM-$BAK^{72\text{-}87}$ – For 20 mL at 9 nM, 120.8 μL was taken from a 1490 nM stock and made up to 20 mL with qIT reaction buffer.

5.4.3.3 Dilution Plates

To prepare a dilution plate series, a 10 μL aliquot was taken from the qIT reaction plate (**5.4.2.3**) and added into a 384 well dilution plate charged with 10 μL qIT reaction buffer, to afford the first dilution plate (DIL 1). 10 μL from this plate was taken and added into dilution plate 2 (DIL 2) which had been charged with 10 μL qIT reaction buffer. This process was repeated until the required number of dilution plates were prepared.

5.4.3.4 Reaction Plates

The 384 well reaction plates were set up such that columns 1 & 2 served as the negative control and columns 23 & 24 served as the positive control. 5 μL qIT reaction buffer was added into columns 1 & 2, whereas columns 3-24 were charged with 5 μL BCL-X_L. 5 μL FAM-BAK^{72-87} was added into all columns. The assay was formally started when 5 μL from the previously prepared dilution plate was added to the reaction plate. This was repeated for all dilution plates, producing a series of reaction plates with varying concentrations of compound (peptide + acrylamide). The reaction plates were covered and incubated for 20 min at r.t before the fluorescence intensity was measured. Final assay concentrations – 3 nM FAM, 100 nM BCL-X_L .

References

1. V. S. Rao, K. Srinivas, G. N. Sujini and G. N. S. Kumar, *Int. J. Proteomics*, 2014, **2014**, 1-12.
2. H. Lu, Q. Zhou, J. He, Z. Jiang, C. Peng, R. Tong and J. Shi, *Signal Transduct Target Ther.*, 2020, **5**, 213.
3. M. P. H. Stumpf, T. Thorne, E. De Silva, R. Stewart, H. J. An, M. Lappe and C. Wiuf, *PNAS*, 2008, **105**, 6959-6964.
4. M. K. Jayatunga, S. Thompson and A. D. Hamilton, *Bioorg. Med. Chem. Lett.*, 2014, **24**, 717-724.
5. V. Azzarito, K. Long, N. S. Murphy and A. J. Wilson, *Nat. Chem.*, 2013, **5**, 161-173.
6. S. Algar, M. Martín-Martínez and R. González-Muñiz, *Eur. J. Med. Chem.*, 2021, **211**, 113015.
7. J. A. Wells and C. L. McClendon, *Nature*, 2007, **450**, 1001-1009.
8. S. Jones and J. M. Thornton, *PNAS*, 1996, **93**, 13-20.
9. S. E. Acuner Ozbabacan, H. B. Engin, A. Gursoy and O. Keskin, *PEDS*, 2011, **24**, 635-648.
10. T. L. Blundell, B. L. Sibanda, R. W. Montalvão, S. Brewerton, V. Chelliah, C. L. Worth, N. J. Harmer, O. Davies and D. Burke, *Philos. Trans. R. Soc. B. Biol. Sci.*, 2006, **361**, 413-423.
11. D. E. Scott, A. R. Bayly, C. Abell and J. Skidmore, *Nat. Rev. Drug Discov.*, 2016, **15**, 533-550.
12. D. Bojadzic and P. Buchwald, *Curr. Top. Med. Chem.*, 2018, **18**, 674-699.
13. T. Clackson and J. A. Wells, *Science*, 1995, **267**, 383-386.
14. O. Keskin, B. Ma and R. Nussinov, *J. Mol. Biol.*, 2005, **345**, 1281-1294.
15. B. C. Cunningham and J. A. Wells, *J. Mol. Biol.*, 1993, **234**, 554-563.
16. A. A. Bogan and K. S. Thorn, *J. Mol. Biol.*, 1998, **280**, 1-9.
17. B. N. Bullock, A. L. Jochim and P. S. Arora, *J. Am. Chem. Soc.*, 2011, **133**, 14220-14223.
18. P. H. Kussie, S. Gorina, V. Marechal, B. Elenbaas, J. Moreau, A. J. Levine and N. P. Pavletich, *Science*, 1996, **274**, 948-953.
19. C. L. Day, C. Smits, F. C. Fan, E. F. Lee, W. D. Fairlie and M. G. Hinds, *J. Mol. Biol.*, 2008, **380**, 958-971.
20. M. Simonovic, Z. Zhang, C. D. Cianci, T. A. Steitz and J. S. Morrow, *J. Biol. Chem.*, 2006, **281**, 34333-34340.
21. S. Qian, Z. Wei, W. Yang, J. Huang, Y. Yang and J. Wang, *Front. Oncol.*, 2022, **12**, 985363.

22. A. Shamas-Din, H. Brahmbhatt, B. Leber and D. W. Andrews, *Biochim. Biophys. Acta.*, 2011, **1813**, 508-520.
23. K. J. Campbell and S. W. G. Tait, *Open Biol.*, 2018, **8**, 180002.
24. Y. Tsujimoto, *Genes to Cells*, 1998, **3**, 697-707.
25. R. Singh, A. Letai and K. Sarosiek, *Nat. Rev. Mol. Cell Biol.*, 2019, **20**, 175-193.
26. J. M. Hardwick and L. Soane, *Cold Spring Harb Perspect Biol.*, 2013, **5**, a008722-a008722.
27. J. Kale, E. J. Osterlund and D. W. Andrews, *Cell Death and Differentiation*, 2018, **25**, 65-80.
28. A. Shamas-Din, J. Kale, B. Leber and D. W. Andrews, *Cold Spring Harb Perspect Biol.*, 2013, **5**, a008714-a008714.
29. S. W. G. Tait and D. R. Green, *Cold Spring Harb Perspect Biol.*, 2013, **5**, a008706-a008706.
30. I. S. Park, H. R. Seo, K. Kim, H. Lee, D. Shum, I. Choi and J. Kim, *Biochem. Biophys. Res. Commun.*, 2020, **527**, 709-715.
31. Z. Dou, D. Zhao, X. Chen, C. Xu, X. Jin, X. Zhang, Y. Wang, X. Xie, Q. Li, C. Di and H. Zhang, *J. Exp. Clin. Cancer Res.*, 2021, **40**.
32. H.-D. Um, *Oncotarget*, 2016, **7**, 5193-5203.
33. B. C. Koehler, A.-L. Scherr, S. Lorenz, T. Urbanik, N. Kautz, C. Elssner, S. Welte, J. L. Bermejo, D. Jäger and H. Schulze-Bergkamen, *PLoS ONE*, 2013, **8**, e76446.
34. M. Li, D. Wang, J. He, L. Chen and H. Li, *Pharmacol. Res.*, 2020, **151**, 104547.
35. C. Tse, A. R. Shoemaker, J. Adickes, M. G. Anderson, J. Chen, S. Jin, E. F. Johnson, K. C. Marsh, M. J. Mitten, P. Nimmer, L. Roberts, S. K. Tahir, Y. Xiao, X. Yang, H. Zhang, S. Fesik, S. H. Rosenberg and S. W. Elmore, *Cancer Res.*, 2008, **68**, 3421-3428.
36. E. F. Lee and W. D. Fairlie, *Int. J. Mol. Sci.*, 2019, **20**, 2234.
37. M. Sattler, H. Liang, D. Nettesheim, R. P. Meadows, J. E. Harlan, M. Eberstadt, H. S. Yoon, S. B. Shuker, B. S. Chang, A. J. Minn, C. B. Thompson and S. W. Fesik, *Science*, 1997, **275**, 983-986.
38. I. Petta, S. Lievens, C. Libert, J. Tavernier and K. De Bosscher, *Mol. Ther.*, 2016, **24**, 707-718.
39. S. D'Aguanno and D. Del Bufalo, *Cells*, 2020, **9**, 1287.
40. M. P. Kline, S. V. Rajkumar, M. M. Timm, T. K. Kimlinger, J. L. Haug, J. A. Lust, P. R. Greipp and S. Kumar, *Leukemia*, 2007, **21**, 1549-1560.

41. I. Ploumaki, E. Triantafyllou, I.-A. Koumprentziotis, K. Karampinos, K. Drougkas, I. Karavolias, I. Trontzas and E. A. Kotteas, *Clinical and Translational Oncology*, 2023, **25**, 1554-1578.
42. A. J. Souers, J. D. Leverson, E. R. Boghaert, S. L. Ackler, N. D. Catron, J. Chen, B. D. Dayton, H. Ding, S. H. Enschede, W. J. Fairbrother, D. C. S. Huang, S. G. Hymowitz, S. Jin, S. L. Khaw, P. J. Kovar, L. T. Lam, J. Lee, H. L. Maecker, K. C. Marsh, K. D. Mason, M. J. Mitten, P. M. Nimmer, A. Oleksijew, C. H. Park, C.-M. Park, D. C. Phillips, A. W. Roberts, D. Sampath, J. F. Seymour, M. L. Smith, G. M. Sullivan, S. K. Tahir, C. Tse, M. D. Wendt, Y. Xiao, J. C. Xue, H. Zhang, R. A. Humerickhouse, S. H. Rosenberg and S. W. Elmore, *Nat. Med.*, 2013, **19**, 202-208.
43. J. Liu, Y. Chen, L. Yu and L. Yang, *Front. Oncol.*, 2022, **12**.
44. E. Curran, J. Byrd, W. Stock, M. Foster, F. Tan, Y. Chen, S. P. Anthony and A. Chen, *Ann. Oncol.*, 2022, **33**, S837-S838.
45. D. J. Craik, D. P. Fairlie, S. Liras and D. Price, *Chem. Biol. Drug. Des.*, 2013, **81**, 136-147.
46. L. Di, *The AAPS Journal*, 2015, **17**, 134-143.
47. P. Wójcik and Ł. Berlicki, *Bioorg. Med. Chem. Lett.*, 2016, **26**, 707-713.
48. J. L. Lau and M. K. Dunn, *Bioorg. Med. Chem*, 2018, **26**, 2700-2707.
49. A. C.-L. Lee, J. L. Harris, K. K. Khanna and J.-H. Hong, *Int. J. Mol. Sci.*, 2019, **20**, 2383.
50. L. Wang, N. Wang, W. Zhang, X. Cheng, Z. Yan, G. Shao, X. Wang, R. Wang and C. Fu, *Signal Transduct Target Ther.*, 2022, **7**.
51. A. Patgiri, A. L. Jochim and P. S. Arora, *Acc. Chem. Res.*, 2008, **41**, 1289-1300.
52. R. N. Chapman, G. Dimartino and P. S. Arora, *J. Am. Chem. Soc.*, 2004, **126**, 12252-12253.
53. Y. H. Lau, P. de Andrade, Y. Wu and D. R. Spring, *Chem. Soc. Rev.*, 2015, **44**, 91-102.
54. M. N. Saleh, M. R. Patel, T. M. Bauer, S. Goel, G. S. Falchook, G. I. Shapiro, K. Y. Chung, J. R. Infante, R. M. Conry, G. Rabinowits, D. S. Hong, J. S. Wang, U. Steidl, L. D. Walensky, G. Naik, V. Guerlavais, V. Vukovic, D. A. Annis, M. Aivado and F. Meric-Bernstam, *Clinical Cancer Research*, 2021, **27**, 5236-5247.
55. R. Fasan, R. L. A. Dias, K. Moehle, O. Zerbe, J. W. Vrijbloed, D. Obrecht and J. A. Robinson, *Angew. Chem. Int. Ed.*, 2004, **43**, 2109-2112.
56. X. Wang, D. Ni, Y. Liu and S. Lu, *Front. Chem.*, 2021, **9**.
57. S. Pallerla, H. Naik, S. Singh, T. Gauthier, R. Sable and S. D. Jois, *J. Pept. Sci.*, 2018, **24**, e3066.

58. T. Hara, S. R. Durell, M. C. Myers and D. H. Appella, *J. Am. Chem. Soc.*, 2006, **128**, 1995-2004.
59. C. Cabrele, T. A. Martinek, O. Reiser and Ł. Berlicki, *J. Med. Chem.*, 2014, **57**, 9718-9739.
60. E. P. English, R. S. Chumanov, S. H. Gellman and T. Compton, *J. Biol. Chem.*, 2006, **281**, 2661-2667.
61. J. W. Checco, E. F. Lee, M. Evangelista, N. J. Sleebs, K. Rogers, A. Pettikiriarachchi, N. J. Kershaw, G. A. Eddinger, D. G. Belair, J. L. Wilson, C. H. Eller, R. T. Raines, W. L. Murphy, B. J. Smith, S. H. Gellman and W. D. Fairlie, *J. Am. Chem. Soc.*, 2015, **137**, 11365-11375.
62. A. Barnard, K. Long, H. L. Martin, J. A. Miles, T. A. Edwards, D. C. Tomlinson, A. Macdonald and A. J. Wilson, *Angew. Chem. Int. Ed.*, 2015, **54**, 2960-2965.
63. T. Flack, C. Romain, A. J. P. White, P. R. Haycock and A. Barnard, *Org. Lett.*, 2019, **21**, 4433-4438.
64. B. P. Orner, J. T. Ernst and A. D. Hamilton, *J. Am. Chem. Soc.*, 2001, **123**, 5382-5383.
65. O. Kutzki, H. S. Park, J. T. Ernst, B. P. Orner, H. Yin and A. D. Hamilton, *J. Am. Chem. Soc.*, 2002, **124**, 11838-11839.
66. H. Yin, G. I. Lee, K. A. Sedey, J. M. Rodriguez, H. G. Wang, S. M. Sebti and A. D. Hamilton, *J. Am. Chem. Soc.*, 2005, **127**, 5463-5468.
67. C. G. Cummings, N. T. Ross, W. P. Katt and A. D. Hamilton, *Org. Lett.*, 2009, **11**, 25-28.
68. J. M. Rodriguez, L. Nevola, N. T. Ross, G. I. Lee and A. D. Hamilton, *Chembiochem*, 2009, **10**, 829-833.
69. I. C. Kim and A. D. Hamilton, *Org. Lett.*, 2006, **8**, 1751-1754.
70. C. G. Cummings and A. D. Hamilton, *Curr. Opin. Chem. Biol.*, 2010, **14**, 341-346.
71. J. T. Ernst, J. Becerril, H. S. Park, H. Yin and A. D. Hamilton, *Angew. Chem. Int. Ed.*, 2003, **42**, 535-539.
72. J.-M. Ahn and S.-Y. Han, *Tetrahedron Lett.*, 2007, **48**, 3543-3547.
73. J. Plante, F. Campbell, B. Malkova, C. Kilner, S. L. Warriner and A. J. Wilson, *Org. Biomol. Chem.*, 2008, **6**, 138-146.
74. J. P. Plante, T. Burnley, B. Malkova, M. E. Webb, S. L. Warriner, T. A. Edwards and A. J. Wilson, *Chem. Commun.*, 2009, **34**, 5091-5093.
75. V. Azzarito, P. Prabhakaran, A. I. Bartlett, N. S. Murphy, M. J. Hardie, C. A. Kilner, T. A. Edwards, S. L. Warriner and A. J. Wilson, *Org. Biomol. Chem.*, 2012, **10**, 6469-6472.
76. F. Campbell, J. P. Plante, T. A. Edwards, S. L. Warriner and A. J. Wilson, *Org. Biomol. Chem.*, 2010, **8**, 2344-2351.

77. A. Barnard, K. Long, D. J. Yeo, J. A. Miles, V. Azzarito, G. M. Burslem, P. Prabhakaran, T. A. Edwards and A. J. Wilson, *Org. Biomol. Chem.*, 2014, **12**, 6794-6799.
78. V. Blay, B. Tolani, S. P. Ho and M. R. Arkin, *Drug Discov. Today*, 2020, **25**, 1807-1821.
79. L. M. Mayr and D. Bojanic, *Curr. Opin. Pharmacol.*, 2009, **9**, 580-588.
80. L. T. Vassilev, B. T. Vu, B. Graves, D. Carvajal, F. Podlaski, Z. Filipovic, N. Kong, U. Kammlott, C. Lukacs, C. Klein, N. Fotouhi and E. A. Liu, *Science*, 2004, **303**, 844-848.
81. G. Karageorgis, S. Warriner and A. Nelson, *Nat. Chem.*, 2014, **6**, 872-876.
82. G. Karageorgis, S. Liver and A. Nelson, *ChemMedChem*, 2020, **15**, 1776-1782.
83. A. I. Green, F. Hobor, C. P. Tinworth, S. Warriner, A. J. Wilson and A. Nelson, *Chem. Eur. J.*, 2020, **26**, 10682-10689.
84. E. Oueis, C. Sabot and P.-Y. Renard, *Chem. Commun.*, 2015, **51**, 12158-12169.
85. D. Bosc, J. Jakhlal, B. Deprez and R. Deprez-Poulain, *Future Med. Chem.*, 2016, **8**, 381-404.
86. S. H. Hewitt and A. J. Wilson, *Eur. J. Org. Chem.*, 2018, **2018**, 1872-1879.
87. M. Jaegle, E. L. Wong, C. Tauber, E. Nawrotzky, C. Arkona and J. Rademann, *Angew. Chem. Int. Ed.*, 2017, **56**, 7358-7378.
88. A. Bhardwaj, J. Kaur, M. Wuest and F. Wuest, *Nat. Commun.*, 2017, **8**.
89. W. G. Lewis, L. G. Green, F. Grynszpan, Z. Radić, P. R. Carlier, P. Taylor, M. G. Finn and K. B. Sharpless, *Angew. Chem. Int. Ed.*, 2002, **41**, 1053-1057.
90. R. Huisgen, *Angew. Chem. Int. Ed.*, 1963, **2**, 633-645.
91. M. Whiting, J. Muldoon, Y. C. Lin, S. M. Silverman, W. Lindstrom, A. J. Olson, H. C. Kolb, M. G. Finn, K. B. Sharpless, J. H. Elder and V. V. Fokin, *Angew. Chem. Int. Ed.* , 2006, **45**, 1435-1439.
92. F. E. Kwarcinski, M. E. Steffey, C. C. Fox and M. B. Soellner, *ACS Med. Chem. Lett.*, 2015, **6**, 898-901.
93. K. Nacheva, S. S. Kulkarni, M. Kassu, D. Flanigan, A. Monastyrskyi, I. D. Iyamu, K. Doi, M. Barber, N. Namelikonda, J. D. Tipton, P. Parvatkar, H.-G. Wang and R. Manetsch, *J. Med. Chem.*, 2023, **66**, 5196-5207.
94. G. M. Burslem, H. F. Kyle, A. L. Breeze, T. A. Edwards, A. Nelson, S. L. Warriner and A. J. Wilson, *Chem. Commun.*, 2016, **52**, 5421-5424.
95. Z. Hegedüs, F. Hóbor, D. K. Shoemark, S. Celis, L.-Y. Lian, C. H. Trinh, R. B. Sessions, T. A. Edwards and A. J. Wilson, *Chem. Sci.*, 2021, **12**, 2286-2293.
96. G. B. Craven, D. P. Affron, C. E. Allen, S. Matthies, J. G. Greener, R. M. L. Morgan, E. W. Tate, A. Armstrong and D. J. Mann, *Angew. Chem. Int. Ed.*, 2018, **57**, 5257-5261.

97. X. Chen, Y. Zhou, X. Peng and J. Yoon, *Chem. Soc. Rev.*, 2010, **39**, 2120-2135.
98. A. Keeley, L. Petri, P. Ábrányi-Balogh and G. M. Keserű, *Drug Discov. Today*, 2020, **25**, 983-996.
99. F. Huang, X. Han, X. Xiao and J. Zhou, *Molecules*, 2022, **27**, 7728.
100. M. Proj, M. Hrast, D. Knez, K. Bozovičar, K. Grabrijan, A. Meden, S. Gobec and R. Frlan, *ACS Med. Chem. Lett.*, 2022, **13**, 1905-1910.
101. L. Boike, N. J. Henning and D. K. Nomura, *Nat. Rev. Drug Discov.*, 2022, **21**, 881-898.
102. G. B. Craven, D. P. Affron, T. Kösel, T. L. M. Wong, Z. H. Jukes, C. T. Liu, R. M. L. Morgan, A. Armstrong and D. J. Mann, *ChemBioChem*, 2020, **21**, 3417-3422.
103. S. Gul and K. Hadian, *Expert Opin. Drug Discov.*, 2014, **9**, 1393-1404.
104. I. R. Taylor, B. M. Dunyak, T. Komiyama, H. Shao, X. Ran, V. A. Assimon, C. Kalyanaraman, J. N. Rauch, M. P. Jacobson, E. R. P. Zuiderweg and J. E. Gestwicki, *J. Biol. Chem.*, 2018, **293**, 4014-4025.
105. K. Zhang, X. Yin, K. Shi, S. Zhang, J. Wang, S. Zhao, H. Deng, C. Zhang, Z. Wu, Y. Li, X. Zhou and W. Deng, *Sci. Rep.*, 2021, **11**.
106. O. Edelheit, A. Hanukoglu and I. Hanukoglu, *BMC Biotechnol.*, 2009, **9**, 61.
107. G. N. L. Rosano and E. A. Ceccarelli, *Front. Microbiol.*, 2014, **5**.
108. F. Perrin, *J. Phys. Radium*, 1926, **7**, 390-401.
109. N. J. Moerke, *Curr. Protoc. Chem. Biol.*, 2009, **1**, 1-15.
110. M. D. Hall, A. Yasgar, T. Peryea, J. C. Braisted, A. Jadhav, A. Simeonov and N. P. Coussens, *Methods Appl. Fluoresc.*, 2016, **4**, 022001.
111. R. B. Merrifield, *J. Am. Chem. Soc.*, 1963, **85**, 2149-2154.
112. J. M. Collins, K. A. Porter, S. K. Singh and G. S. Vanier, *Org. Lett.*, 2014, **16**, 940-943.
113. L. Gui, C. S. Adjiman, A. Galindo, F. B. Sayyed, S. P. Kolis and A. Armstrong, *Ind. Eng. Chem. Res.*, 2023, **62**, 874-880.
114. R. Subirós-Funosas, R. Prohens, R. Barbas, A. El-Faham and F. Albericio, *Chem. Eur. J.*, 2009, **15**, 9394-9403.
115. A. El-Faham, Z. Al Marhoon, A. Abdel-Megeed and F. Albericio, *Molecules*, 2013, **18**, 14747-14759.
116. K. Chandra, T. K. Roy, J. N. Naoum, C. Gilon, R. B. Gerber and A. Friedler, *Org. Biomol. Chem.*, 2014, **12**, 1879-1884.
117. W. A. Lea and A. Simeonov, *Expert Opin. Drug Discov.*, 2011, **6**, 17-32.
118. J. H. Zhang, T. D. Chung and K. R. Oldenburg, *J. Biomol. Screen.*, 1999, **4**, 67-73.

119. A. Barnard, J. A. Miles, G. M. Burslem, A. M. Barker and A. J. Wilson, *Org. Biomol. Chem.*, 2015, **13**, 258-264.
120. P. Prabhakaran, A. Barnard, N. S. Murphy, C. A. Kilner, T. A. Edwards and A. J. Wilson, *Eur. J. Med. Chem.*, 2013, **2013**, 3504-3512.
121. J. M. Davis, A. Truong and A. D. Hamilton, *Org. Lett.*, 2005, **7**, 5405-5408.
122. J. M. Rodriguez, N. T. Ross, W. P. Katt, D. Dhar, G.-i. Lee and A. D. Hamilton, *ChemMedChem*, 2009, **4**, 649-656.
123. W. Lu, P. Li, Y. Shan, P. Su, J. Wang, Y. Shi and J. Zhang, *Bioorg. Med. Chem.*, 2015, **23**, 1044-1054.
124. F. Albericio, *Biopolymers*, 2000, **55**, 123-139.
125. A. Toutchkine, V. Kraynov and K. Hahn, *J. Am. Chem. Soc.*, 2003, **125**, 4132-4145.
126. N. S. Murphy, P. Prabhakaran, V. Azzarito, J. P. Plante, M. J. Hardie, C. A. Kilner, S. L. Warriner and A. J. Wilson, *Chem. Eur. J.*, 2013, **19**, 5546-5550.
127. J. Qiu, B. Xu, Z. Huang, W. Pan, P. Cao, C. Liu, X. Hao, B. Song and G. Liang, *Bioorg .Med. Chem.*, 2011, **19**, 5352-5360.
128. J. R. Pliego and K. L. Lopes, *Comput. Theor. Chem.*, 2023, **1227**, 114261.
129. J. H. Incremona and J. C. Martin, *J. Am. Chem. Soc.*, 1970, **92**, 627-634.
130. G. F. Bloomfield, *J. Chem. Soc.*, 1944, DOI: 10.1039/jr9440000114, 114.
131. S. M. Kelly and B. H. Lipshutz, *Org. Lett.*, 2014, **16**, 98-101.
132. R. Das and M. Kapur, *J. Org. Chem.*, 2017, **82**, 1114-1126.
133. Y. Li, A. Silamkoti, G. Kolavi, L. Mou, S. Gulati, G. M. Air and W. J. Brouillette, *Bioorg. Med. Chem.*, 2012, **20**, 4582-4589.
134. K. S. Eccles, C. J. Elcoate, S. E. Lawrence and A. R. Maguire, *Arkivoc*, 2010, **2010**, 216-228.
135. D. Plano, Y. Baquedano, E. Ibáñez, I. Jiménez, J. A. Palop, J. E. Spallholz and C. Sanmartín, *Molecules*, 2010, **15**, 7292-7312.
136. N. Zhu, G. Xu, R. Wang, T. Zhu, J. Tan, X. Gu and C. Zhao, *Chem. Commun.*, 2020, **56**, 7761-7764.
137. M. J. Van Haren, R. Taig, J. Kuppens, J. Sastre Toraño, E. E. Moret, R. B. Parsons, D. Sartini, M. Emanuelli and N. I. Martin, *Org. Biomol. Chem.*, 2017, **15**, 6656-6667.
138. L. Zervas and I. Photaki, *J. Am. Chem. Soc.*, 1962, **84**, 3887-3897.
139. D. M. Whitehead, P. A. Helliwell, S. C. McKeown and A. Routledge, *React. Funct. Polym.*, 2009, **69**, 884-890.
140. M. J. Petersson, I. D. Jenkins and W. A. Loughlin, *Org. Biomol. Chem.*, 2009, **7**, 739-746.

141. I. Ramos-Tomillero, H. Rodríguez and F. Albericio, *Org. Lett.*, 2015, **17**, 1680-1683.
142. A. Sharma, I. Ramos-Tomillero, A. El-Faham, E. Nicolas, H. Rodriguez, B. G. De La Torre and F. Albericio, *ChemistryOpen*, 2017, **6**, 168-177.
143. J. Popovici-Muller, R. M. Lemieux, E. Artin, J. O. Saunders, F. G. Salituro, J. Travins, G. Cianchetta, Z. Cai, D. Zhou, D. Cui, P. Chen, K. Straley, E. Tobin, F. Wang, M. D. David, V. Penard-Lacronique, C. Quivoron, V. Saada, S. De Botton, S. Gross, L. Dang, H. Yang, L. Utley, Y. Chen, H. Kim, S. Jin, Z. Gu, G. Yao, Z. Luo, X. Lv, C. Fang, L. Yan, A. Olaharski, L. Silverman, S. Biller, S.-S. M. Su and K. Yen, *ACS Med. Chem. Lett.*, 2018, **9**, 300-305.
144. J. R. Rostrup-Nielsen, Dordrecht, 1982.
145. R. Xiong, W. Ren, Z. Wang and M. Zhang, *ChemCatChem*, 2021, **13**, 548-552.
146. M. Orlandi, D. Brenna, R. Harms, S. Jost and M. Benaglia, *Org. Process. Res. Dev.*, 2018, **22**, 430-445.
147. M. Orlandi, F. Tosi, M. Bonsignore and M. Benaglia, *Org. Lett.*, 2015, **17**, 3941-3943.
148. S. Y. Jabri and L. E. Overman, *J. Org. Chem.*, 2013, **78**, 8766-8788.
149. D. A. Hay, O. Fedorov, S. Martin, D. C. Singleton, C. Tallant, C. Wells, S. Picaud, M. Philpott, O. P. Monteiro, C. M. Rogers, S. J. Conway, T. P. C. Rooney, A. Tumber, C. Yapp, P. Filippakopoulos, M. E. Bunnage, S. Müller, S. Knapp, C. J. Schofield and P. E. Brennan, *J. Am. Chem. Soc.*, 2014, **136**, 9308-9319.
150. Z. Wang, X. Shi, H. Zhang, L. Yu, Y. Cheng, H. Zhang, H. Zhang, J. Zhou, J. Chen, X. Shen and W. Duan, *Eur. J. Med. Chem.*, 2017, **139**, 128-152.
151. C. Li, X. Yang, Y. Luo, H. Liu, X. Zhong, X. Zhou, T. Zeng, L. Tao, Y. Zhou, K. Gou, X. Yang, X. Liu, Q. Chen, Y. Zhao and Y. Luo, *J. Med. Chem.*, 2021, **64**, 18175-18192.
152. C. Ché, G. Yang, C. Thiot, M. C. Lacoste, J. C. Currie, M. Demeule, A. Régina, R. Béliveau and J. P. Castaigne, *J. Med. Chem.*, 2010, **53**, 2814-2824.
153. A. Devos, J. Remion, A.-M. Frisque-Hesbain, A. Colens and L. Ghosez, *J. C. S. Chem. Comm.*, 1979, DOI: 10.1039/C39790001180, 1180-1181.
154. A. Isidro-Llobet, J. Guasch-Camell, M. Álvarez and F. Albericio, *Eur. J. Org. Chem.*, 2005, **2005**, 3031-3039.
155. N. D. Ca, E. Motti, A. Mega and M. Catellani, *Adv. Synth. Catal.*, 2010, **352**, 1451-1454.
156. M. Zhao, L. Xiong, S. Li, J. Chang, H. Ning and C. Qi, *Z. Anorg. Allg. Chem.*, 2014, **640**, 159-167.
157. J. Im, *Bull. Korean. Chem. Soc.*, 2016, **37**, 7-12.

Appendix

A.1 SS1 High-Throughput Screen

A.1.1 Screen E

A.1.1.1 qIT Data

	1	2	3	4	5	6	7	8	9	10	11	12	13	14	15	16	17	18	19	20	21	22	23	24
A	12630	12610	189124	191674	200684	189081	186023	190825	199396	178865	178414	192683	198914	189938	192279	196454	212022	190135	197276	197385	204189	186318	198519	185340
B	14056	14137	189936	175123	187368	169985	182858	190690	189677	187379	193906	187889	158487	194075	193956	183197	155139	203656	250230	192363	186979	199652	203185	190882
C	13047	12476	180284	172121	192473	184245	225036	183694	114461	194778	117014	190326	195995	197110	142332	190608	172633	193634	201784	197948	187957	197558	179392	183410
D	10306		178847	165211	164887	169916	195207	167356	26834	173561	192281	156709	186289	173643	174532	158257	158325	177223	144371	194463	171508	76934	196878	177583
E	12942	12272	170493	169764	194769	180964	174730	178388	191891	173736	193897	173454	195379	178048	195193	192447	191551	179879	192622	181670	192307	186007	196782	172043
F	14228	13398	185262	187680	174106	189406	168725	195765	198373	181588	203055	182988	187236	195929	175073	226698	193076	192617	181876	189494	193959	181737	185079	169870
G	12591	13655	190356	185503	194153	178827	194207	196697	202218	190271	193908	153096	186852	181324	191522	133921	200155	25325	194729	188053	199674	182298	198276	185023
H	12917	10584	184951	171184	175327	177697	183800	55421	183920	172406	191432	180248	167527	183235	174591	169312	153343	189561	168448	132362	192346	179961	198605	182691
I	12558	11546	190843	193300	187174	180921	212557	177957	194023	187086	193183	181032	193243	206820	189637	203414	174327	193452	193887	188538	171024	200704	194970	184310
J	14110	12662	178006	176864	191957	188771	185194	188171	185230	193875	199894	173897	181150	185333	180913	175728	180737	187614	198694	201428	185818	182055	196565	175908
K	14043	11906	141420	192549	195618	122392	179659	154830	195962	197478	191056	175897	177878	200269	179933	192728	193516	190892	189046	186476	195760	188522	191456	179420
L	13169	11531	173610	180410	188113	167049	192994	176957	193097	173117	169363	183258	175386	179305	172880	182590	195693	169660	187391	179683	191598	185417	190800	177312
M	13148	13381	186459	172798	196429	188012	197858	186481	187704	188343	189635	193063	192301	192747	196214	181324	178508	194152	182443	187740	199821	166147	204462	181839
N	14186	14049	192203	186784	187921	186176	183059	162906	188518	192509	186878	187968	192868	151517	161131	188081	174774	165270	189820	190705	187811	192098	162754	191051
O	14807	13152	178535	173463	184328	175831	174490	167390	178082	182320	184191	163249	189130	186379	180913	186584	182094	188413	187088	184810	184444	187858	189097	178614
P	14151	11220	169877	139841	180213	183299	182235	175679	185923	177396	164342	176855	180414	181597	190716	181303	170019	172431	183529	191907	180528	176346	178813	192286

Appendix Table 1: Fluorescence data for the 7-minute timepoint (outliers removed as highlighted).

	1	2	3	4	5	6	7	8	9	10	11	12	13	14	15	16	17	18	19	20	21	22	23	24
A	13668	10858	211800	215434	220581	201428	198448	217806	215113	188026	207491	213445	214377	212554	211030	201392	219619	202056	206857	218427	214814	202757	217522	201887
B	15285	12983	202105	183580	203345	175248	197538	198249	203413	201595	207159	206290	174115	209512	210653	184084	170792	207667		195550	187908	216615	211559	196427
C	14225	10808	197668	190036	206006	202066	260000	199022	106700	200699	107993	205340	213569	207947	134876	200516	194776	209391	212218	200162	204047	221615	206295	205923
D	12947	12122	202904	197687	187321	193091	203286	188319	26150	177205	218156	184238	187355	197423	193050	169393	179125	181376	151260	213393	195376	65424	214402	192943
E	13848	12257	196417	175886	217024	197230	185436	207648	217857	191435	209754	190100	215704	192068	214012	213489	209710	206014	194216	209164	212978	212967	218693	196130
F	14280	12422	215493	213845	228257	213501	178156	219590	207181	211160	230878	208351	196865	222861	188396	237387	218639	212350	195475	208316	216910	205101	213383	207330
G	13777	12685	211975	202738	208505	198632	219736	222182	220510	215264	219347	148127	197491	190652	209211	118627	205006	23824	211189	200424	211904	195000	207735	195540
H	11362	13046	195207	183658	197501	198445	202700	44313	193635	179011	189412	196978	179429	194135	186274	193956	149985	187073	183029	192251	210463	194502	207429	193734
I	13027	13482	211241	212749	194875	198020	252929	197499	202740	201955	206945	188333	205331	219574	214560	212186	174459	212336	202383	198559	181396	208227	208872	199983
J	12437	13102	191814	199989	222346	201355	208228	203314	196167	211507	223286	180605	198739	186954	183967	189410	187763	196817	208562	219004	208029	184677	206699	199472
K	12923	12124	146057	207067	212402	118953	193251	158390	218684	217436	216543	190328	191694	214069	196620	215415	208891	211560	197683	196847	205471	198202	212701	192871
L	13527	11205	184158	175177	205061	178663	212225	187272	198887	179931	187118	185971	199840	196050	185633	203570	213529	179051	189650	197143	202223	119625	202658	196904
M	13034	15407	206543	191712	216582	197662	219074	209048	213356	201087	208684	198829	208369	211074	208835	193305	203292	210668	213512	214332	203349	209641	200140	203735
N	13559	15191	214212	204316	197636	207261	193288	166478	210223	196533	211769	197809	198474	165544	176531	208558	180934	175945	209296	212639	209130	189635	206090	207098
O	15727	13108	194701	196676	206595	198093	199523	179486	204798	211795	207459	192467	213409	204383	203464	206700	201892	209396	204363	198395	198962	199347	215810	201960
P	14006	12264	204127	187178	213995	196603	212568	196504	210241	199728	187835	212952	208582	199918	206936	198628	188951	185867	193410	215440	202243	185099	189763	213170

Appendix Table 2: Fluorescence data for the 15-minute timepoint (outliers removed as highlighted).

	1	2	3	4	5	6	7	8	9	10	11	12	13	14	15	16	17	18	19	20	21	22	23	24
A	12830	10680	204920	202823	216082	210378	205757	198982	217138	188496	211139	205657	202011	209647	212970	209025	219970	194392	205076	210831	208134	191580	211561	198491
B	15805	13367	208661	177656	202218	167460	218117		210500	205308	202935	197047	172699	209203	197999	175751	167195	206033	234762	200136	181105	205037	201741	192651
C	14019	10858	197822	188097	210772	182491	236971	173876	87330	199334	90056	185888	178794	206718	94130	205671	178666	204183	199613	177983	184813	200085	199250	198981
D	12273	9346	175139	171632	161988	176413	189200	187783	18041	165834	189010	162343	177754	179257	149487	152995	123694	175349	115400	1901	160730	47043		178690
E	13287	12783	189612	168548	202630	200883	185761	196007	209477	185161	206561	183336	207118	187972	206649	208057	206625	190511	202388	208719	199516	193055	204095	188923
F	11274	14676	199287	211128	212336	214149	157462	211855	206254	208639	206916	195988	195242	208294	181488	205431	201543	209987	189149	205357	204935	195110	198416	194782
G	13859	11960	200492	200595	207480	186190	213172	199170	215585	199829	209834	116462	193541	198820	199479	89540	208114	20135	179268	152159	211277	178640	201632	183767
H	12028	11684	180789	168150	182540	169976	182326	28624	192518	165444	185467	179593	165091	177048	167603	108194	147934	170858	2923	220937	185514	163318	184790	169317
I	11705	13657	210488	208694	197796	200493	250692	184041	205697	192947	209458	174772	221131	214784	216515	216508	160680	214914	202601	204772	172340	209186	206750	193963
J	12387	14062	190604	191791	211924	198263	202120	199745	192177	202804	213557	173672	192966	182877	195849	178676	183724	206004	217697	211214	201146	179074	195056	186790
K	12377	12788	132908	198127	203450	111776	186762	176957	215644	207586	211718	188348	179568	206345	182783	195870	204576	197876	180010	165586	203930	187873	198733	190259
L	12397	11940	168245	168248	194409	160870	194884	171540	184115	171491	174164	170466	178889	172298	171053	122641	191015	149641	128105	205991	180067	161871	178928	171204
M	10614	10657	211489	207437	213886	222406	211580	212439	219591	206670	209181	209181	219422	210495	212222	183624	210281	216567	209060	213011	202456	210560	192898	200758
N	10520	10968	215858	214730	207624	215460	203342	172176	213005	196586	215563	185323	202416	146233	173418	212587	144754	183674	202616	211497	206460	189325	196513	204857
O	10787	10294	196289	193469	215437	205820	208390	178105	216662	208835	221767	206133	211432	207739	207410	198610	204527	210968	210460	205688	199667	208040	206875	195443
P	9469	8792	200348	192996	215194	202403	216911	189115	217515	203682	185131	210451	207440	203530	211587	199272	189370	186190	199701	207999	198020	190168	190282	209677

Appendix Table 3: Fluorescence data for the 30-minute timepoint (outliers removed as highlighted).

	1	2	3	4	5	6	7	8	9	10	11	12	13	14	15	16	17	18	19	20	21	22	23	24
A	9926	7392	203820	201444	221929	204927	178448	211732	206023	185941	207485	211640	212635	202771	206992	209841	213933	194310	203746	216733	216592	197297	203870	211024
B	10582	8804	212511	199438	207607	146034	205282	199790	219478	190306	194165	177036	175948	182988	188667	135483	186432	193421	229454	179879	191360	206948	209401	198869
C	9814	9859	203605	187974	199816	215561	233608	201319	82256	195442	65706	181936	207103	211614	64558	205598	202422	203066	221299	209042	210787	208223	209605	202425
D	8764	6199	215659	194164	207383	199416	211417	188728	12237	184234	213572	178559	204859	188440	176119	131646	166049	163172	167918	209731	206833	33476	208304	196981
E	8403	7015	201880	163514	199381	213763	171679	205831	221862	180902	213375	178634	201487	196312	181031	213770	217942	178583	213945	196008	211478	206148	216838	196059
F	8657	9651	197394	202971	233263	222913	136911	193639	211222	210400	213786	174585	195421	219612	194412	224123	219118	221134	201168	225142	214932	206423	218185	202412
G	9149	8724	201984	207330	221492	160844	201209	217690	224236	211553	225064	80447	201154	217884	200226	52470	212604	20521	217832	205515	195774	165502	219620	201791
H	8612	6309	194159	183908	219883	182085	222155	14250	196165	155929	180829	187226	172621	188040	171431	187610	134826	188284	161567	214511	193609	199708	209691	200241
I	7373	7749	203162	225223	181742	215634	242531	166031	217405	204688	216043	168713	216739	216445	208259	223832	120156	219170	195366	189358	148623	194981	192769	193320
J	8502	7826	197613	205737	219230	200695	207038	216640	205659	208798	221184	171718	194741	162350	203862	159231	182384	214485	209112	213422	203171	180420	216033	201969
K	9614	8278	100567	213037	205988	94421	142901	162869	226111	198897	213695	174909	150886	226373	161068	216769	185470	203092	213403	215728	208173	206739	204716	197157
L	8323	6588	171207	206206	213152	203048	209178	160210	213884	197848	197126	208991	211543		193722	215988	217649	141227	207850	203489	210163	207634		198592
M	7886	6352	202671	212578	210555	212839	189862	204051	207492	196468	205861	186210	214631	207567	214804	176065	201574	209603	209188	212527	201350	204185	210186	199253
N	7819	7763	205941	201579	217561	193300	186770	178341	185130	190271	196253	169006	198988	111784	184099	190556	137069	144471	192388	203002	204702	195182	199377	193682
O	8424	7724	182022	181121	206328	205666	180670	153516	210743	183383	176507	166419	188703	211087	197505	205975	199064	164509	205688	196851	195107	197866	198010	183228
P	8493	6161	191977	184650	207052	180582	209731	175094	210414	196861	177509	208503	205525	199427	208309	171526	190487	167415	197100	203513	192899	180669		200679

Appendix Table 4: Fluorescence data for the 60-minute timepoint (outliers removed as highlighted).

	1	2	3	4	5	6	7	8	9	10	11	12	13	14	15	16	17	18	19	20	21	22	23	24
A	9102	8091	199222	205925	210992	210517	170047	212827	204690	169952	184188	212202	207546	199568	194945	203919	205411	189793	214548	213696	216405	184869	207188	200257
B	8886	10613	207632	194862	180685	130324	193109	192494	221255	180548	180603	210391	129029	187183	180740	116456	171457	181097	200295	179429	174635	198038	197704	215001
C	8619	7632	215968	182199	198638	206680	219454	200663	74435	198466	59645	166506	209875	207365	33400	198076	212383	194545	215789	206638	206600	203056	205495	209630
D	7398	7309	202126	187537	207181	187460	199035	191143	8809	175352	202944	191943	197723	189393	188046	94869	163854	176459	148025	206907	189895	30348	206174	194345
E	8811	8368	185202	135817	181046	219071	157689	196606	214640	166630	201742	180692	190692	187658	156927	217277	213679	180444	207687	204330	209392	190124	215806	199666
F	9142	9234	221381	193278	237829	222578	106528	188907	203032	220974	215927	165945	189598	215376	193090	226147	199263	220671	196454	227216	206970	196682	216278	204944
G	7542	6379	200629	194831	218020	133261	208132	215233	221009	196615	227179	48224	187334	223051	185056	29448	212946	9503	201883	196202	209531	153303	207915	210043
H	6039	5806	176994	183592	218184	188661	204428	8858	191626	151756	184774	173840	171089	201543	150863	170276	136142	178914	162896	209732	207456	195209	212564	195974
I	7960	7899	201446	227603	161225	216453	227827	154616	215154	198374	219738	143172	217706	207596	198773	221165	89232	212219	205225	164754	127960	199644	188924	193529
J	7972	8205	168719	199413	206726	192618	201718	209217	197691	205433	218262	169882	193789	148555	205016	125983	182661	207952	219295	222305	187888	165701	210409	210197
K	8635	8411	83734	198189	193943	71884	119540	160116	220075	201551	211138	165749	127893	225469	132611	216990	167701	197752	208801	206301	205159	199544	203620	202285
L	7486	7172	149398	207766	220689	183594	199866	163432	213709	200314	195127	208052	204391	212042	186152	213991	215303	100058	203973	195447	206983	197906		209270
M	6357	5932	189589	210174	197327	202876	189990	199469	194872	187964	207962	174709	203123	196978	206318	150724	184380	202929	202385	205759	194945	194013	203338	200126
N	5806	6000	180069	202151	203085	199289	185147	157648	187622	179860	182482	153077	196008	83105	166337	175187	98220	132484	189797	196049	192419	183677	186128	195796
O	5815	5854	164678	173268	190517	200241	166938	134201	203442	178843	169920	158342	187622	200714	188306	197041		158962	199086	185449	177939	186716	182485	181449
P	6524	5867	197575	191090	211004	184281	202526	174992	208193	204477	166682	209584	199466	200422	202592	178427	184902	161648	190306	203239	189242	181752		183655

Appendix Table 5: Fluorescence data for the 120-minute timepoint (outliers removed as highlighted).

	1	2	3	4	5	6	7	8	9	10	11	12	13	14	15	16	17	18	19	20	21	22	23	24
A		6727	216545	224301	219767	226496	174319	216595	218485	151086	203318	222465	214134	210663	188774	214029	212052	188808	230967	214427	220856	181806	205879	214331
B	6918	8236	218080	177095	206276	113149	205598	212413	211786	197145	151344	206640	169550	217726	195924	76945	166887	198090	232102	203875	160633	182884	212601	201876
C	7913	8836	195650	176991	191573	220655	231904	211311	84955	203849	65761	146350	197708	212528	15712	207409	184782	225622	210295	214538	209448	204552	214926	193643
D	6471	6645	209032	189307	207804	177899	186660	190556	8243	149473	214706	207123	192347	206527	171665	54566	155785	156193	166946	205417	185643	26892	206903	192484
E	6762	7530	149116	90606	155051	219502	126427	181130	208244	143705	201255	192450	184887	172773	183416	214862	227210	163090	204990	202013	194497	198468	216406	193407
F	8095	8630	216891	204510	239548	218255	60120	220148	207577	223155	237652	162997	206909	205917	200995	233289	215311	226435	190542	231162	198641	184688	219767	201898
G	7280	7963	205278	216549	219788	124089	232607	222815	231537	198951	241930	21926	188102	236141	179410	15469	205815	6797	247049	201882	220745	165108	214646	200423
H	6959	6464	175349	196451	219669	185217	228221	6256	211752	151161	222371	202119	175251	228928	172783	146912	139444	187400	169833	226129	209811	210590	216592	203729
I	7987	7580	180614	227597	128057	206823	228303	117290	211057	181083	226064	100859	228110	169779	180679	224087	45390	221006	215349	145630	115879	206388	210701	188894
J	7042	7913	188387	185282	227414	169345	211446	219869	201175	199608	237424	167427	206003	136352	184691	96455	176798	205440	220943	221286	175570	152327	214268	192743
K	7491	8335	38572	209063	187957	33072	110558	165085	235481	220261	236856	154127	111631	217525	105849	228272	154614	197453	191883	219465	202893	185777	210751	191275
L	7173	6762	114721	195475	226463	152531	207706	151059	230177	183485	187091	209278	199175	220616	175363	215500	223482	67015	202973	186959	188435	187340	205693	196392
M	7118	8165	184433	173806	197014	200219	223225	212742	212457	172964	227852	193129	210056	195102	202694	116692	194925	221887	208430	213676	192546	197534	211444	187083
N	7387	8236	209064	205429	217569	185899	183294	143018	196662	185342	218478	184624	210236	52985	158410	219114	50700	149607	209391	202736	192553	185560	198199	183131
O	7816	7031	139866	148744	188234	205323	174269	140525	212289	203530	205472	143314	216017	214351	190843	204544	173582	204473	200040	185723	174357	187364	194063	181183
P	7667	6085	179451	159596	199724	145390	209800	144346	212184	191702	144880	206322	206312	188231	207987	164089	171269	121407	171772	192378	183558	172648	182597	194279

Appendix Table 6: Fluorescence data for the 240-minute timepoint (outliers removed as highlighted).

	1	2	3	4	5	6	7	8	9	10	11	12	13	14	15	16	17	18	19	20	21	22	23	24
A	9043	8136	213365	223367	214753	220292	169738	208855	213209	142965	197224	221595	212097	214008	181398	207143	207930	181854	228766	210844	221359	176062	221863	215992
B	7217	7418	202330	170155	212868	105193	208325	208472	221616	191231	147225	196081	164061	217239	194617	63660	154918	193508	222489	206015	152869	186354	213424	196352
C	7105	6620	222576	167393	205465	217149	228403	209166	84879	198052	63686	136233	209251	205376	12381	208224	180207	217168	219518	212404	209894	196946	215326	193086
D	6119	6553	176083	179927	201644	167423	182917	180284	8446	136765	210280	199116	183368	199416	166982	40862	147749	142261	153246	203601	171331	28389	203774	192414
E	7506	8161	148327	80213	141505	216127	114470	172602	210318	130793	200155	174239	172922	163366	170389	208824	222867	151304	204737	195945	184002	195940	217286	192242
F	8016	8241	209852	196554	236806	219967	31373	205099	194639	227793	225706	177571	198268	194981	193992	225336	210801	218666	183191	227919	190319	181943	216742	203722
G	7632	8392	185817	219929	207787	110553	226976	214393	229999	192152	222209	15951	184685	232009	166322	13666	198568	7040	244173	190939	223917	158524	227995	200357
H	7094	6658	178820	182908	214321	177379	214734	6436	203375	137924	207736	193157	162531	203009	161995	137903	129180	180325	161693	216064	204141	206302	194016	202318
I	7064	6653	172931	224720	110033	201588	229430	97781	206183	177240	219346	85038	221139	192791	166911	219754	33445	217072	209625	131394	107756	210463	210607	198240
J	6944	8085	186721	178075	219940	159919	208110	213706	195714	192404	229873	161503	201469	113495	187257	83242	172842	199104	220593	219391	171900	152239	212078	194648
K	7502	7821	25491	207963	178729	21507	102020	154341	231083	218704	229259	139722	97906	215369	88253	215630	156890	188206	192673	213259	201908	180630	210650	194264
L	7220	6433	101553	194828	205593	159190	202696	134525	219162	166311	195569	188316	195489	213507	167758	196046	214486	53374	198757	179067	187147	188225	208311	192645
M	7707	7630	179764	184187	188874	194581	218330	211642	207552	171978	212600	183209	209272	182438	216476	98767	191735	220433	214736	201921	199191	195207	210960	190211
N	6878	7451	207341	203671	215959	195101	170151	144937	187422	176733	214611	186907	195837	48632	145844	213826	42612	135650	207931	198734	190127	185685	198311	185227
O	7648	7219	123352	141690	179894	202456	167095	122252	208333	202700	207248	146610	213421	210128	190869	199146	165293	204230	200962	178780	184433	178048	194786	180705
P	7305	6897	175694	162212	191973	139748	205310	154243	206778	188065	131075	207412	201704	187976	205389	160528	163596	111566	165016	188044	181375	175285	185077	193310

Appendix Table 7: Fluorescence data for the 300-minute timepoint.

	1	2	3	4	5	6	7	8	9	10	11	12	13	14	15	16	17	18	19	20	21	22	23	24
A	10219	8744	196697	200263	188823	203455	159361	178433	164050	87366	139284	194322	174590	205965	82470	171793	175264	105744	205848	186114	212494	146135	217785	218492
B	10336	9291	178031	101562	185591	91508	179840	177503	181704	144810	65917	152749	7525	183261	130154	14397	7474	140148	203959	197929	6227	169891	212104	199130
C	9648	8379	184967	95859	152399	180843	192765	184153	98437	135178	75013	68029	163975	162726	7500	168017	132915	181724	182404	186230	170374	177902	214086	200234
D	8702	8950	180602	140617	121706	127211	104772	162272	12226	52141	179155	141099	135247	148761	70396	8375	6298	53650	154998	169765	149400	38723	206846	197291
E	8337	8563	79042	20099	75254	187159	27278	111679	163662	46216	154795	98189	83529	51909	88265	159562	202959	66104	191294	154924	134026	186879	213520	199004
F	9437	10077	155357	172164	200359	178174	8377	129090	173649	181878	186785	141600	171383	134163	171085	183274	183796	180868	6930	195806	163168	135001	209129	203726
G	9095	9642	144740	187581	180270	50168	193991	170257	190903	129051	197002	6863	127001	189569	101487	12073	132080	71827	208032	176203	182557	88467	205135	205610
H	10934	8744	112679	172832	180818	114590	189972	7490	158653	59913	180690	163456	63173	186539	73107	53118	6336	119804	6534	191593	184406	185143	199718	207743
I	9763	7463	130077	191111	33141	175004	202790	16718	172817	153388	185258	6392	182144	92195	104424	185366	7598	157510	173837	46465	47294	178411	211987	203229
J	9479	9165	181870	89137	185491	77777	166187	178871	149584	130477	189584	116864	45272	42512	144589	26440	7318	150848	182262	191693	125232	132060	205139	196035
K	9005	9284	7710	173868	110914	8981	88684	112381	189395	185463	192463	49512	32899	193036	14972	185025	68207	141821	164830	187336	172918	138946	212218	203893
L	9865	8116	37694	164437	166129	108371	152137	45928	193010	104938	139671	148757	117058	190136	6340	179159	191962	13117	138776	128667	172023	184704	201765	201974
M	9127	9362	140227	156808	131613	132013	185785	180683	174713	98018	181003	110819	171318	110231	169305	33053	171362	191733	195942	167739	179880	188981	211407	197466
N	9148	9819	196510	187101	187957	167288	120172	102377	128166	130127	193283	176498	162191	16418	6626	194172	8933	99650	188993	183829	167496	175441	209425	195877
O	10622	9578	51815	93201	120432	183788	103778	6958	182180	179192	181610	140866	190089	194948	147838	184498	98276	186239	194046	165470	162431	181449	211608	191170
P	9769	7880	156444	132665	161752	74832	192504	113204	184178	166656	50417	197618	184613	156241	184756	115926	82676	50270	110434	192186	190469	180072	207919	209619

Appendix Table 8: Fluorescence data for the 1380-minute timepoint.

	1	2	3	4	5	6	7	8	9	10	11	12	13	14	15	16	17	18	19	20	21	22	23	24
A	10343	9742	201539	214586	204807	218893	161668	183938	166084	85899	136823	212801	174591	230357	73815	178213	176480	98914	200952	191680	220069	145724	242927	237910
B	10827	10224	183672	94554	197849	90775	184967	179882	208383	145386	61202	150969	6681	203824	128897	13491	6187	140789	225430	210567	5580	165921	227275	210213
C	9151	7978	209596	92688	169012	182327	218105	203277	100265	134048	76883	64665	168457	162541	6253	178924	123392	192129	204555	196571	173031	188983	229978	218022
D	7236	6608	189599	114998	115306	128241	97958	163106	11760	47894	181364	150206	135577	136942	5468	5720	5259	49818	159413	159323	169795	35085	209740	188247
E	7581	7425	76491	18769	70158	198419	22691	110462	161748	36487	159376	94071	77803	44888	77466	162926	210627	62776	190872	174499	131317	193878	219367	210885
F	9497	8860	152114	174245	215452	182459	6731	123807	177265	189642	197655	148990	175759	136226	175261	203342	194233	185920	5481	214121	164871	134693	226310	219900
G	9767	9648	139280	195307	181139	46608	204711	163610	210189	124758	217354	5396	123620	212464	96352	10952	129612	75163	212882	182751	185858	84640	226635	221451
H		7094	118860	176993	181388	110045	169051	5637	156311	55309	185055	177107	56844	191209	70381	50121	5527	116134	5295	194066	197555	176711	193999	208475
I	9459	7212	126264	198490	29745	183765	222535	14099	178371	164433	178248	5157	186682	84666	101700	198806	6526	155598	175456	42732	48398	175027	224278	228143
J	12135	8751	188186	86964	205083	73293	169960	179081	151660	127253	209619	120719	5773	37097	153432	24178	6947	149265	178913	203098	122492	132850	227416	217767
K	9127	8569	6235	177769	106505	7404	88588	107447	210652	190313	205104	46950	30176	200013	13005	188986	66193	136598	156148	193443	185480	137788	229293	219673
L	8390	7423	34503	153799	193945	94283	149937	39686	203832	102733	142898	136958	124128	184279	5199	170923	199949	11531	154919	126050	170880	188253	197025	200964
M	8084	8589	141357	164014	131864	128352	193474	198453	184578	92078	197725	107626	172933	104454	181125	31154	172488	207731	204161	172305	192898	198311	223157	218801
N	9384		205055	198272	202742	162243	120546	103574	126793	135415	211951	186718	186521	13800	5632	203706	7625	99458	185626	183666	174342	183030	226354	217005
O	10142	9440	50361	85868	118068	196717	99880	5944	194875	182491	185982	144456	204513	204345	149751	194541	104456	189648	191663	170155	166155	183851	225808	208992
P	8663	6165	164793	131438	175141	70482	199493	108439	190950	170917	46547	204480	194051	153486	188397	113673	80289	47282	105692	180540	195008	180938	208159	206876

Appendix Table 9: Fluorescence data for the 1500-minute timepoint (outliers removed as highlighted).

A.1.1.2 FA data

	1	2	3	4	5	6	7	8	9	10	11	12	13	14	15	16	17	18	19	20	21	22	23	24
A	24.8	26	77.2	73.2	97.5	95.6	27	58.4	84.8	37.5	90.5	77.7	27.7	80.2	75	78.3	89.2	43.9	68.3	68.2	74.1	58.8	82.2	84.3
B	22.9	24	63.5	68.2	89.4	27.3	36.9	28.8	93.5	35	64.7	34.6	94.2	84.6	52.5	109.8	119.1	26.4	85.7	81.7	122.3	32.3	79.6	85.8
C	25.8	24.2	89.7	41.2	67.8	28.5	101.2	81.3	123.4	68.6	66.6	40	74.2	38.8	75.4	75.6	42.8	83	85.7	71.5	81.5	47	81.4	85.3
D	26.7	26.3	43.8	102.6	73.2	50.7	53.1	91.4	111.2	46.2	91	63.7	81	69.8	75.4	74	54.6	70.2	80	73.4	76.5	30.4	81.9	82.8
E	26.1	26.1	62.2	48.4	49.5	73.9	61.3	107.7	80.5	36.7	85.1	77.1	85.3	53.1	51.6	35.6	85.8	82.9	92.4	90.3	48.5	70.5	81.9	85
F	26.3	25.9	93.8	39.8	75.3	32.4	78.9	69.9	82.2	89.8	83.7	92.9	78.4	63.5	95.2	57.9	68.5	85.6	96.9	76.6	82.9	44	86.1	79.1
G	26.3	30.9	80.5	85.1	38.9	69.5	85.3	87	70.1	78.3	71.4	73.6	64.4	81.4	56.4	26.3	27.7	140.7	78.7	81.1	79	78.1	79.9	81.9
H	27.6	25.8	67.4	87.1	77.8	32	84.1	44.4	45	122.1	67.8	37.6	95.2	43.3	30.5	59.3	33.1	60.2	43.8	75.2	86	88.3	87.4	80.8
I		25.2	84.8	80.6	26.2	88.2	84.3	108.9	79.4	87.3	82	59.1	56.1	29.7	28.5	79.1	54.3	61.2	62.4	103.1	109	42.5	91.7	84.7
J	25.9	26.4	78.1	52.9	76	66.7	90.1	36	53.5	46.9	65.7	47.7	116	75.2	47.2	32.5	129.2	34.2	79.9	72.1	48.3	99.9	86	81.6
K	25.6	27	56.1	64.6	71.8	69.7	64.1	33.8	89.9	70.3	92.7	38.5	45.6	78.9	104.7	80.7	49.6	35.1	85.6	34.2	49.4	93.9	80.8	80.8
L	23.2	23.8	118.5	40	45.7	54.6	73.2	59.6	79.4	52.1	89.7	68.9	72.3	78.2	69.5	63	84	84.1	50.9	24.1	90.5	89	84.1	81.6
M	25.1	26.9	60.4	56.6	52.2	30.3	78.6	49.6	88	74.7	88.1	68	70.7	83.1	87.2	54.8	59.2	84.4	47.6	89.2	63.6	81.1	85.3	80
N	29.1	27.2	80.7	87.2	72.4	75.7	64	87.8	92.2	57.1	58.7	74.1	81.8	24.1	130.3	83.5	55.5	72.5	65.8	85.8	77.3	92.7	85.3	85.4
O	29.3	25.4	110.7	34.6	37.9	50.1	59.3	66.6	65.3	73.3	63.4	91.3	42.7	82.8	70.8	70	45.8	85.1	82.1	37.2	91.5	84.3	84.8	85
P	24.1	24.8	75.3	90	90.4	83.8	59.1	60.8	28.4	71.2	29.6	63.3	65.2	75.9	35.1	56.1	108	27.2	54.1	75.5	79.6	86.3	79.7	89.1

Appendix Table 10: Fluorescence data from dilution 1 (2.5 μM) plate (outliers removed as highlighted).

	1	2	3	4	5	6	7	8	9	10	11	12	13	14	15	16	17	18	19	20	21	22	23	24
A	29	27.9	105.7	96	118.6	109.8	39.3	88.2	109.4	50.4	111.6	101.8	32.7	110.3	103	104.6	117.2	64.9	94.1	95	100.4	76	110.9	112.2
B	25.1	24.4	77.3	105.8	119.8	32.5	52.8	56.7	116.8	41.9	80.4	46.4	126.9	108.7	66.4	141.3	149.9	33.1	111.4	111.6	147.4	41.6	105.8	112
C	20.5	27.7	120.1	62	91.3	34.1	114.5	108.7	116.4	98.3	97.2	55.6	112.8	50.1	102.1	101.2	62	117.2	110.7	99.6	113.3	75.3	109.4	108.8
D	22.8	26.5	55.1	124.9	106.1	66	57.1	122.4	138.1	71.2	121.8	94.6	105.3	100.4	105.2	99.2	87.5	92.5	110.5	111	102.6	32.1	109.8	110.1
E	24.8	26	96.2	62.3	65.7	101.4	79.6	135.6	110.8	49.1	107.5	109.2	112.9	75.2	70.4	49.3	119.8	111.1	119.9	118.6	68.4	93.6	107.8	112.1
F	25.5	27.8	116	50.5	98.4	40.4	106.3	97.3	112.8	110	112.6	117.3	107.7	84	113.6	81.3	95.8	115	130.1	103.6	114	60.8	108.5	109.7
G	24.7	29.3	106.3	116.6	55.4	90.8	109.9	113.1	106.3	110.4	93	98.3	91.2	111.6	71.1	28.6	30	157.1	106.9	109.1	100.2	102.3		111.7
H	24.2	27.5	91.5	111.3	104.1	36.3	112.4	51.8	64.6	145.1	95.2	49.9	119.9	63.3	34.1	86.1	45.4	80.5	68.3	101.7	111.2	113.9	112	107.2
I	26.3	23.8	113.5	106	33.6	111.8	113	130.8	108.9	113.5	106.6	83	72.2	40.5	35.6	108.7	82.3	83.3	85.2	130.4	130.3	51.5	108.9	108.7
J	26.7	25.9	112.6	76.1	102.9	89.7	116.7	53.4	74.8	66.9	90.4	68	137.9	103.5	67.1	38.2	154	41.3	105.6	100.6	66.6	117.3	111	105.6
K	23.6	26.8	77.5	91	94.5	91.9	86.4	45.2	115.3	100.5	117.2	58.3	63.6	106.4	126.3	104.3	67.6	43.5	111.1	51.3	74.2	118.4		110.3
L	27.6	26.9	136.2	56	65.9	76.5	93.3	83	116.5	78	118.3	94.7	94.3	108.5	103.9	88.5	106.2	117.6	69.5	31.4	117.8	106.5	111.1	110.7
M	24.3	25.9	85.2	82.5	70.7	35.9	98.6	65.7	114.1	100.7	112.9	93.5	91.6	109.7	112.6	80.4	88.2	111.1	72.2	117.5	96	103.4	113.8	111.5
N	28.6	27.4	108.8	113.8	97.1	107.9	89.8	110.6	118	79.3	81.7	108.8	113.5	27	152	108.7	78	91.3	95.8	109.7	109.2	114.8	109.2	112.1
O	27.4	24.9	138.7	46	48.9	70.5	83.5	88.5	89.4	95.3	84.5	114.2	67.7	108	91.6	94.2	62	108.5	105.9	49.1	119.2	115.3	109.4	115.9
P	27.7	27	101.6	124.9	118	108.5	89.4	80.6	33.4	101.1	41.3	91.3	88	102.4	48.5	78.9	142.1	24.2	79.4	102.3	109.8	113	112.7	110.8

Appendix Table 11: Fluorescence data from dilution 2 (1.25 μM) plate (outliers removed as highlighted).

	1	2	3	4	5	6	7	8	9	10	11	12	13	14	15	16	17	18	19	20	21	22	23	24
A	29.8	33	143.4	131.2	148.7	149.6	45.5	127.4	146.4	79.9	141.9	134	48	146.6	130.7	137.3	133.5	100.5	161.1	123.2	123.9	104.4	139.1	142.8
B	31.9	28.5	115.2	124.1	148.2	36.2	121.4	132	141.6	70.9	108.5	55.5	165.5	139.9	88.4	160.9	167.8	39	136.4	157	168.3	78.6	139.6	140.2
C	28.1	33.3	150.2	79.5	117.2	59.4	143.1	136.8	147.6	129	131.9	71.3	139	78.2	130.3	135.1	76.9	141.1	132.2	125.5	137.5	97.9	138.9	137.2
D	28.8	30.4	96	143.1	140.3	95.1	80.6	155	160.9	87.6	145.7	116	130.4	121	133.9	128.4	134.7	122.7	140.4	133.2	131	38	136.2	137.7
E	32.8	29.3	132.3	80.4	88.3	130.5	113.1	164	139.5	64.1	140.7	127.6	136.6	102.5	100.4	74	137.7	136.4	140.9	144.5	93	124	138.1	132.7
F	30.3	29.4	141.4	74.9	124.4	61.6	131.5	123.2	137.6	133	131	139.5	138.5	108.2	136.8	107.6	125.3	140.6	155.8	134.1	137.3	100.2	132.7	131.2
G	28.5	28.4	131.8	133.9	79.4	117.5	136.9	138.2	118.2	130	121.5	124.5	115.2	126.7	91.6	33.4	40.5	174.2	138.3	138.6	126.4	127.8	132.8	131.4
H	27.9	27.3	116.4	138.5	127.4	52.7	139.8	76.7	90	165.4	118.1	68	143.4	92	47.2	104.8	64.1	106.7	79.5	124.1	137.4	138.8	139.9	130.4
I	32.4	28	141.4	131.5	46.1	134.7	133.9	156.5	135.4	133.1	132.1	97.4	100.5	56	50.7	133.9	102.8	110.5	107.8	150.2	155.2	75.9	130.4	135.5
J	29.8	29.7	136.2	100.1	122.6	118.2	146	85.8	102	87.7	118.4	98.8	162.4	122.6	106	43.4	167.6	55	126.3	125.7	90.1	147.6	134.1	132.6
K	27.3	29.3	104.2	117.3	117.4	120.9	108.3	68	138.3	129.3	147	75.2	86.7	134.5	148.4	140.2	98	69.8	137.7	91.9	107.5	144.8	146.3	135.2
L	29.9	28	158.9	70.9	98.9	106.3	113.5	110.4	134.9	96.1	139.2	120.6	124.9	136.8	145.9	113	142.1	135.5	95.6	43	137.3	140.6	138.3	132.9
M	31.6		108.8	115.5	92.9	44.9	125.2	99.7	134.8	128.8	141.4	120.2	121	135.3	142.1	109.9	120.8	142.2	108.1	143.9	126.3	135.5	143.3	138.9
N	28.1	29.7	133.3	137	126.3	132.3	112.7	143.1	140.5	103.3	120.5	136.3	139.7	27.3	170.3	133.4	95.8	116.9	123.4	137	131.8	137	132.7	138.1
O	29.8	30.4	154.6	66.9	69	103.2	108.8	116.6	122.2	132.4	118.7	142.3	98.1	135.2	122.8	121.9	86.2	133.8	129	72.1	145.1	134.8	135.3	138.3
P	26.9	27.2	133.2	145.4	139.1	130.2	118.6	111.2	55	133.8	56.6	118.1	122.5	136.2	69.9	100.8	161.5	30.1	98.5	130	134.5	142.3	134.1	142.1

Appendix Table 12: Fluorescence data from dilution 3 (0.63 μM) plate (outliers removed as highlighted).

	1	2	3	4	5	6	7	8	9	10	11	12	13	14	15	16	17	18	19	20	21	22	23	24
A	28.5	29.1	154	152	161.7	165.6	84.3	145.5	153.6	106.7	157.7	163.9	74.2	162	152.2	156.7	161.4	137.9	160.9	147.4	146.4	138.5	161	159.5
B	24.6	27.8	143.2	158.4	163.7	42.6	137.6	157	154.2	108.3	130.9	102.2	173.7	157.7	118.8	173.9	175.7	56.5	152.5	168.7	179.6	127.7	161.5	161
C	26.7	27.3	166.4	109.7	144.8	124.2	159.3	155.2	170.1	144	136.7	84.4	158.4	104.7	147.4	150.5	104.3	160.8	154.1	149.6	160.4	140.7	159	156.7
D	23	26.7	134.8	170	168.2	121.6	107.8	167.8	180.9	131	171.7	149.7	162.4	149.7	164.2	143.6	164.6	141.7	156.8	152.4	153.9	46.8	164.5	160.5
E	26	28.4	157.1	98.2	103.3	148	140.7	173.9	162.9	124.3	165.7	154.4	161	125.1	124.7	102.3	155.8	156.1	156.8	159	116.7	150.6	162.4	157.7
F	26.2	25.5	159.3	104.3	156.3	101.9	159.5	146.3	159.5	164.2	150.9	158.7	158.1	136.8	162.1	133	152.5	157.2	172.9	155.8	155.7	137.4	157.9	156.8
G	30.3	27.1	152.4	161.4	112.8	138.9	154.6	160.2	141.2	156.8	153	145.1	141.1	154.5	116.4	43.4	48.7	179.5	158.2	155.8	148.4	153.3	155.3	154.8
H	27.2	27.7	134.8	159.7	150.3	70.8	154.5	97.3	119.4	173.7	148.6	104.8	157.6	126.1	56.6	128.7	96.6	132.4	121.9	149	159.8	155.4	160	153.1
I	26.7	27.3	160.2	152.6	58.9	160.7	156.8	169.3	155.4	153.9	157.5	126.2	131.8	77.6	64	160	131.3	135.6	138.9	162.1	172.8	120.2	152.2	151.8
J	24.5	28	156.9	131.4	150.8	138.5	163.1	120.8	130.7	115	150.4	126.8	174.5	139.4	128.7	57.9	179.2	80.4	149.8	154.2	110.9	167.7	159.1	153.7
K	28.3	26.1	133.8	144.9	144.4	149.9	135.6	107	162.2	150.1	165.7	101.6	110.9	147.9	171.2	155	121.3	91.1	158.3	132.5	138.9	162.7	161.7	156.6
L	25.6	25	174.2	110.2	126.5	132.9	146.7	134.4	152.5	129.1	162.7	138.1	149.7	149.3	166.5	140.9	155.9	156.9	134.5	53.8	160.1	159.6	154.2	162
M	29.1	26.5	138.3	144.8	121.3	62	148.5	125	157.1	149.9	157.3	138	146.9	153.8	162.6	136.2	145.8	154.4	142.9	162.1	151.6	152.1	153.3	153.9
N	25.4	27.1	158.3	160.6	149.6	158.5	148.3	160.9	165.2	135.9	145.4	150.5	157.7	31.6	177.2	133	123.7	144.5	149.1	160.2	153.6	158.1	153.6	157.3
O	24.6	28.3	174.7	97.4	97.5	139.6	139.9	141.2	147.4	148.6	145.3	163.1	138.9	153.2	145.8	144.9	116.3	151.6	157.6	112.7	165.4	158.6	157.4	153.7
P	28.2	27.3	149.9	163.3	159.8	153.1	141.2	137.7	85	149.5	80.4	144.6	147.3	148.7	107.2	126.5	168.7	34.8	130.1	153.1	153.8	161.3	160.1	158.9

Appendix Table 13: Fluorescence data from dilution 4 (0.31 μM) plate.

	1	2	3	4	5	6	7	8	9	10	11	12	13	14	15	16	17	18	19	20	21	22	23	24
A	31	34.7	175.6	169.7	173.1	176.2	139.6	175.2	177.2	137.6	172.1	173.8	138.2	178.5	169.2	173.8	173.3	168.4	171.3	168.7	169	159.4	175	175.1
B	31.5	29.5	174.1	183	181.9	59.4	159.2	173.3	169.8	131.7	161.7	142.8	190.8	180.3	146.8	185.9	184.2	105.2	174	177.7	189.3	157.9	179.8	173.6
C	30.6	29.7	181.6	145.4	169.2	161.5	175.1	172.8	181.7	170.2	174.8	114.7	175	142.5	172.1	169.9	144.9	172.8	175.3	167.6	174.6	160.7	175.9	172
D	28.2	31.3	163.9	182.2	184.4	165.1	146.6	178.6	183.7	141.9	180.4	173.5	170.8	162.4	175.8	163.7	183.7	165.2	172.3	173.6	171.8	74.6	171.9	173
E	25.7	27.5	173.3	143.3	139.9	168.6	165.9	181.9	175.2	123.4	172.1	164	172.6	153	150.5	136.1	171.3	171.9	176.8	177.4	152.4	161	175.7	172.2
F	26.6	28.5	175.1	146.4	163.6	137.5	169.4	164.4	172.6	169.2	170.6	171.8	170.3	158.4	171.7	159.2	164	175	182.6	169.3	171	167.9	171.7	170.7
G	27.2	28.3	166.9	164.8	151.4	165.5	166.2	172.7	161.1	169.1	168.5	160.9	160.3	168.3	145.9	55.1	70.5	185.6	170.4	170	169	168.9	173.4	174.5
H	28.1	25.8	151.4	175.1	169.5	102.9	167.4	125.3	146.3	184	165.6	144.4	173.5	152.4	97.6	148	141.5	154.6	166.6	168.4	173.9	172.8	172.9	169.3
I	24.7	29.6	171.5	169.4	85.3	172.4	170.8	181.4	166.9	168.2	175.6	148.5	158.8	117.5	105.5	175.2	163	158.6	165.1	175.4	181.5	147.7	168.9	169.7
J	26.1	26.8	174.1	161.3	166.5	162.9	172.7	156.7	163.7	143.1	163.7	156.2	185.4	161.6	159.8	89	183.7	129.5	168	170.6	147.8	168.6	172.8	173.7
K	28	27.9	159.7	165.5	163.7	168.8	160.3	147.4	176.4	169	176	136.4	148	168.5	178.9	170.3	144.6	129.3	175.1	162.3	164.2	176.6	172.9	168.9
L	30.3	27.7	183.1	140.5	157.6	156.9	167.3	151.1	166.7	157.6	169.8	169.1	167.7	170.4	180.5	159.8	172.9	174.1	161.5	93.3	177.3	171	172.2	169
M	28.5	29.6	164.1	161	156	96.7	168.5	163.4	176.3	165.5	173.2	166.2	169	172	175.8	156.8	162.1	173.6	164.6	174.8	171.1	167	173.6	171.5
N	32.5	26.4	173.9	175.6	170.6	168.6	162.1	178.6	175.5	164.3	175.6	174.2	177.1	38.8	188.9	147.6	156.2	159.2	166	175	172.7	175.1	170	169.5
O	26.9	28.5	179.1	128.5	136.8	164	161.7	170.6	163.7	174.7	167.8	173.8	169.7	173.5	167.2	165.6	144.4	168.6	172.3	152.4	176.9	173.3	170.3	169.7
P	30.1	30.7	167.1	172.1	174.7	169.8	164.2	159.8	159.6	173.4	123.6	168.9	169.8	171.7	147.5	155.8	178.4	44.3	154.5	171.6	169.2	170.4	170.9	174.5

Appendix Table 14: Fluorescence data from dilution 5 (0.16 μM) plate.

	1	2	3	4	5	6	7	8	9	10	11	12	13	14	15	16	17	18	19	20	21	22	23	24
A	22.8	24.7	188.1	183.5	183.2	182.3	169.4	179.9	178.6	163.7	178	181.6	165.8	182.9	179.1	180.6	182.3	178.8	182.1	167.4	174.6	170.5	183.4	178.8
B	25.8	26.2	178.5	184.3	185.2	95.5	174.2	182.3	179.3	178	167.4	155.9	189.1	173.3	165.7	184	183.7	148.4	177.8	178.2	188.9	176.1	180.1	180.4
C	26.9	25.7	185.5	162.4	173.3	166.5	180.9	178.3	177.9	171.1	177.5	124.6	178.1	165.5	175.7	177.4	169	182.7	177.1	177.1	176.2	177.7	179.5	177.7
D	25.3	26.4	172.5	184.7	181.6	166	154.1	183.9	185.8	157.3	180.5	179.1	176.1	174.5	181.1	173.8	181.9	175.2	179.3	177.3	176.7	118	182	178.3
E	26.1	23.7	181.1	155	156.2	179.5	175.7	184	175.9	144.1	181.2	177	176.8	167.5	168.7	166.5	182	178.3	185.1	182.2	165.7	175.4	185.2	178.9
F	24.4	23.9	179	169.4	173.9	168.3	179.6	176.3	177.6	180.2	173.8	177	176.3	172.2	177.4	169.3	173.9	183.3	184	176.2	177	179.3	180	178.3
G	22.6	23.4	179.4	180.4	168.6	173.5	177.9	176.8	175.5	176.4	181.7	177	175.6	180.3	165.3	77.4	115	185.8	176	178.5	179.6	178.4	176	176.4
H	22.3	26.1	173	174.9	176.5	149.2	176.6	141.6	167.3	182.9	182.8	169.7	184.2	169.2	140.3	165.9	167.3	165.1	177.7	172.4	183.4	178.8	177.6	177.6
I	23.1	22.7	177.7	178.3	124.4	182.1	177.3	183.6	175	180.7	181.1	168.2	174.5	153.4	143.3	181.8	166.4	169.4	171.2	180.4	185.7	169	176.9	174.8
J	22.7	23.2	179.2	170.3	176	174.2	181.8	171.5	174.7	161.9	177.8	175.8	185.1	174.2	173.7	117.6	183.1	155.5	175.5	174.1	169.5	178.7	178.2	174.8
K	21.5	23.6	170.9	176.3	175	179	174.4	173.4	181.8	181.5	179.9	159.1	158.5	178.1	182.1	177.7	163.9	165.8	181.7	174.2	176.1	181.4	184.7	180.2
L	24.3	25.1	185.8	169	174.5	169.2	172.7	172	177.3	166.4	181.9	172.8	177.2	181.6	186.7	175.8	176.5	183.3	174.2	140.4	181.4	179.2	176.8	177.1
M	22.7	26.2	174.3	177.4	172.7	154	179.8	175.3	175.3	175.5	181.2	170.7	178	180.4	179.7	172.1	175.2	178.9	176.4	179.3	178.5	175.7	181.6	179
N	22	24	175.5	180.6	175.8	179.6	173.9	184.3	179	175.1	176.2	178	182.8	45.8	185.1	178.9	164.5	172	174.6	177.8	182.6	175.6	180.8	178.1
O	23.9	25	181.7	157.6	161.3	175.9	175.8	169.4	168.5	176.2	176.8	180	179.6	179.1	175.1	171	164.3	181.6	177	170.2	184.8	178.7	181.1	176.6
P	23.6	24.7	178.5	184.7	180	176.3	176.1	167.4	160.7	179.2	144.7	174.6	172.6	171.2	163.2	165	179.1	66.2	171.8	173.2	171.9	181.6	177.3	175.4

Appendix Table 15: Fluorescence data from dilution 6 (0.08 μM) plate.

	1	2	3	4	5	6	7	8	9	10	11	12	13	14	15	16	17	18	19	20	21	22	23	24
A	28.3	30.3	186.4	187.1	191.6	191.2	184.7	183.5	187.5	178.3	187	188	182.9	188.3	184	190.5	185.8	182.9	185.9	184.9	179.7	180.4	189.1	184
B	21.7	26.5	190.3	191.3	190.8	151.1	189.7	190.1	185.6	181.8	182.1	179.1	192.1	188.7	181.9	186.7	190.3	172.9	191.2	187	194.7	186.8	185.3	187.3
C	28.2	28.3	187.9	183.4	186.5	184.9	187.8	191.3	193.6	182.1	192.6	169.8	189	179.6	188.1	183.3	176.7	189.2	186.5	182.6	186.9	184.4	182.6	188.2
D	26.6	24.5	182.9	192.5	190.8	184.8	182.6	188.5	188.9	176.6	191.8	185.5	183.5	184.6	190.5	185.4	187	185.3	185.1	186.7	188.1	165.3	189.1	185.5
E	27.3	27.3	186	177.3	175.7	185.7	184.2	189.4	185.5	170.3	186.1	190.9	184.8	180.2	177.7	179.9	186.7	186.1	190	189.3	181.7	183.9	185	185.9
F	25	24.5	185.8	184	180.3	182.8	188.5	180.6	188.5	184.7	185.2	189.1	187.3	182.3	185.3	184.5	181.9	187.1	190.2	184	182.5	184.9	187.3	183.5
G	25.8	25.2	183.4	190.3	185.1	182.4	181.2	185.4	185.7	187.6	182.1	182.8	182.7	185.7	177.7	131.2	168.2	188.8	188	184.4	182.7	185.7	184.9	183.6
H	28.4	28.4	182.3	189	182.2	169.1	187	168.4	180	190.3	185.3	181.6	182.6	181.7	164.8	179	181.3	185.3	182.4	184.9	188.4	184.5	188	183.7
I	25.4	27.3	185.9	183.4	164.7	185.6	183.9	189.5	185.5	185.2	186.9	176.2	187.6	165.7	173.4	184.6	180.5	183.1	184.4	185.7	188.1	179.5	184.7	184.4
J	26.5	30.1	186.8	184.6	184.8	177.6	187.5	183.3	184.1	178.7	187.2	184.4	188.8	178.7	179.4	156.7	192.5	175.1	184.6	186	180.4	181	186.6	186.6
K	24.4	27.8	182.1	185.7	184.6	183.3	182.3	183.7	186.9	183.8	185.8	171	173.5	184.9	187.7	182.9	180.3	178	192.2	181.5	186.7	187.9	188.5	185.8
L	28.5	23.9	188.1	181.3	180.4	179.1	182.7	183.4	185.9	183.5	188.4	181.6	185.6	186.7	186.2	184.3	187.2	183.8	183.7	172.2	186.6	182.5	186.2	182.7
M	24.5	27.8	181.5	182.2	183.8	172.6	183.1	181.2	186.8	184.5	188.3	177.6	186.8	183.6	185.3	182	185.9	187.4	187.7	187	185.3	184	184.4	183.6
N	24.9	28.7	185.6	187.3	183.2	182.5	179.7	184.4	183.4	181.9	183.8	184	180.5	128.2	187.8	186.7	176.3	185.9	183.3	183.7	188.1	187.2	181.8	184.1
O	27.5	22.8	190.2	172.7	176.4	184.8	182.5	178	182.6	182.4	186.7	186.6	183.1	181.5	182.5	187	177.3	188.1	182	181.8	183	186.4	179.6	186.3
P	23	27.4	185.5	184.2	183	182.5	181.5	176.6	176.4	181.6	172.3	184.2	180.3	178.7	172.4	175.7	183.2	147.9	181.1	179.3	183.5	182.3	182.8	182.6

Appendix Table 16: Fluorescence data from dilution 7 (0.04 μM) plate.

	1	2	3	4	5	6	7	8	9	10	11	12	13	14	15	16	17	18	19	20	21	22	23	24
A	26	31.6	192.3	193.2	192	197.8	189.8	191.1	191	195.3	196.3	191.9	199	196.4	196.9	194	193.5	188.9	191.6	187.2	188.4	189	187.7	188.9
B	29.3	31.1	194.2	196.4	192.2	189	198	195.7	188.7	196.6	191	188.2	198.6	192.7	194	195	194.5	181.7	190.5	196.2	194	192.6	192.3	192
C	27.3	27.7	195.5	189.8	191.9	196.5	195.6	194.8	196.6	196.5	192.5	186.8	194.4	187.7	193	190.7	187.9	190.6	193.9	189.1	191.7	188.5	192.6	186.4
D	29	26.9	196.3	194.3	199.7	193.9	188.9	196.9	193.1	186.4	194.3	192.6	191.3	189.1	194.3	193.3	195.4	186	190.7	194.4	193.3	180.1	187.6	193.3
E	30.3	27.1	195.4	184.3	187.1	189.7	193.3	192.1	197.1	185.2	191.4	193.6	191.1	191.7	188	188.4	195.5	192.5	193.1	194	190.2	192	193.7	190.1
F	27.7	31.3	193.5	190.1	189.3	192.1	191.1	189	190	192.8	187.8	190.6	190.9	190.2	190.6	189.3	192.1	191.5	194.6	189.8	190.5	196.6	188.8	189.8
G	27.5	25.1	194.9	193	185.8	192.2	193.1	191.8	190.8	189.4	196.7	189.9	190.2	187.3	187	165.7	182.5	195	189.2	191	190	193.2	187	188.9
H	27.3	29.1	191.8	194.5	190.3	183.7	189.2	183.1	190.3	192.5	189.9	183.8	189.5	190.2	177.4	188.8	189.5	193.2	189.1	191.6	190.2	191.2	193.1	184.1
I	31.3	28.1	195.3	192.4	178.5	193.2	188.5	191.8	189.8	190.7	189.7	183.3	187.4	180.8	187.6	186	185.8	186	187.5	187.7	193.5	186.4	189.2	189.9
J	27.9	27.8	193.4	187.8	194.3	191.5	189.8	185.7	191.3	182.9	190.7	188.2	195.3	187.7	190.1	176.8	194.4	189.2	190.9	191.8	187.1	190.7	190.7	185.6
K	27.4	31	189.5	187.9	189.6	192.4	188.1	188.4	194.5	190.8	190.7	186.1	186.2	186.8	190.3	188.5	188.1	183.8	190.3	189.7	190.3	188.5	190.4	189.7
L	29.1	27.1	196.4	187.8	185.8	186.6	188	189	188.7	184.9	191.3	187.7	188.6	190.2	192.9	186.7	189.4	190.4	184.4	177.1	188.5	192.1	188.2	188.7
M	29.9	32.2	193.4	189.1	191	184.7	190.8	188.3	192.1	188	189.7	187.4	187.5	190.1	189.9	184.8	189	190.1	189.3	189.7	190.5	189.7	190.6	186
N	28	28.3	191	191.8	188.2	188.5	185.6	196.1	190.4	189.1	201.5	190.7	188.5	162.4	192.5	188.6	188.4	189.2	187.6	189.1	188	190.4	187.9	189.3
O	27.3	27.6	192.6	180.9	186.2	189.6	189.6	191.1	185.2	190.6	192.5	198.3	196.4	190.5	187.8	188.3	185.7	186.7	189.7	189.6	187.4	189	187.4	187.8
P	27.1	29.4	188.2	189	190.1	187.5	187.1	181.2	183.1	189.8	186.7	197.2	185.5	182.7	181.5	181.7	190.2	173.2	185.6	184.6	185.8	191.8	189	187.3

Appendix Table 17: Fluorescence data from dilution 8 (0.02 μM) plate.

A.1.2 Screen F

A.1.2.1 qIT data

	1	2	3	4	5	6	7	8	9	10	11	12	13	14	15	16	17	18	19	20	21	22	23	24
A	9220	13091	204785	190182	187978	196168	183081	210707	170195	200401	161275	210652	214002	212759	196216	204602	206730	108451	210953	181187	196151	152252	174372	201699
B	10433	9303	189419	89290	171447	167612	184253	163991	175171	197214	196737	203255	35397	185678	162305	190917	16893	206582		181703	18989	145416	192977	175590
C	12065	12706	192460	174058	177848	147719	191143	220250	115690	193410	124697	187714	198034	191948	115563	165860	179674	182325	216956	192292	210372	181154	178969	194691
D	13598	11789	188071	147020	184485	174887	182762	197827	29564	196542	200721	110305	157704	171105	57311	130140	13831	167506	141764	193297	200928	49601	199958	196821
E	14764	9841	183032	150932	186533	185653	158824	170498	189332	197007	185514	136995	204603	101532	193139	212174	169469	193456	191892	195438	194810	210694		195762
F	13434	13513	212114	193297	179707	182465	115558	183686	192163	164051	156159	207405	185314	187847	121025		178822	170985	49795	197979	196748	174993	186939	201276
G	12494	11558	184611	173572	199983	158666	204365	189466	208821	181224	205151	97979	176331	189084	196087	133113	209905	17851	210067	88714	197057	161865	207506	190312
H	11297	9472	182358	158834	164751	112183	184764	84607	182828	169819	201923	193108	71932	194130	80709	151609	46427	193784	14495	193235	197284	194710	203825	196779
I	11521	11855	200043	165481	182127	91833	219167	138454	154739	163122	148002	69732	168110	210404	197421	198204	163228	212139	191702	196986	201064	179812	206056	212845
J	13294	9333	181899	46215	188140	156479	160492	159157	128060	188998	200942	144721	45297	173352	104903	188946	118191	103446	206923	197508	190142	180298	218376	197693
K	11039	10156	134043	171526	193124	90173	188147	112283	189299	196269	193255	109677	171083	204882	153806	170128	179784	181234	118495	154327	162874	192160	207148	207406
L	9334	11798	161687	172944	185522	139387	193591	188769	177850	32071	62321	154337	95485	188740	18345	184863	166352	161997	111414	174555	196359	196755	175050	207975
M	12397	9154	196732	182170	192299	196142	197251	191501	172564	172594	174498	210804	197844	196599	191049	183437	197197	173274	180115	172366	220622	204217	224675	210019
N	10722		197363	120788	184237	148794	161518	149312	187031	148588	218896	192364	182149	148033	73400	193966	146593	167355	181227	175792	154096	186725	214351	198037
O	11117	10726	191715	166320	149274	181855	183803	28720	146734	200694	162409	201554	204804	189944	187755	203985	201885	216731	184498	148477	179507	220639	218592	205276
P	9989	8945	147954	128537	151646	163589	166418	178125	177953	171339	89172	188151	176932	187446	193624	192127	29700	153398	184132	201222	185281	149578	206020	189819

Appendix Table 18: Fluorescence data for the 7-minute timepoint (outliers removed as highlighted).

	1	2	3	4	5	6	7	8	9	10	11	12	13	14	15	16	17	18	19	20	21	22	23	24
A	11534	10692	218656	225043	203898	208496	198530	224651	186636	218997	187099	217148	206689	212887	205990	212276	213441	118288	219424	189997	213032	184525	184904	207383
B	10381	11071	207330	104035	188140	166419	193761	176022	207558	199470	207710	198361	65990	218633	183255	192537	14920	224717		235871	56565	168264	202320	187417
C	10301	10313	209670	188036	210655	189534	203940	235734	104931	208875	106236	178821	210749	183298	98084	200144	199287	219763	220912	198452	213107	200901	208516	205857
D	10309	9398	209080	173761	201048	178172	191411	208483	28579	196863	215760	133214	170653	196259	84440	135476	12200	179618	145655	197830	212509	40489	216397	182154
E	11019	8903	191264	159997	201023	205416	153917	184487	203645	196949	199346	142494	215180	128638	205642	212580	193009	198341	205701	206777	215224	212836		220811
F	10563	9673	224809	186514	189800	197976	102696	210631	204763	188201	174350	216961	193093	197563	116852		188224	189016	73230	221337	183693	193231	209376	218885
G	11641	9385	203894	195518	207400	187195	208700	217640	225746	195144	214992	99878	203094	211171	198392	106900	203901	12023	221844	107467	224911	186263	220951	226144
H	9726	7576	202262	170717	181140	127927	190301	66790	202322	189980	217417	195954	109970	203332	103028	191821	64051	216476	12175	212592	225121	213276	216492	210429
I	11376	9526	212736	194632	191274	118754	246009	152883	178979	172495	174064	89332	181675	217669	214234	208047	162023	223003	200986	208768	197699	211745	233745	225677
J	9587	10694	189633	87568	204033	182505	153084	186827	152785	209204	219192	141175	69866	165885	124684	183466	138142	126408	218061	210304	201541	196150	218091	214256
K	10793	10293	138995	174476	211713	110021	176247	110556	215065	213981	211891	124609	185221	225334	158580	201302	175346	187461	137164	179800	178053	213059	230576	215755
L	9268	9000	173631	194982	206792	157525	205732	205269	209101	61377	81429	180051	123905	208045	41772	204487	176471	169507	134608	174349	213369	217882	213954	206292
M	11925	10162	218510	212186	207925	209263	216240	213268	188256	188180	205728	217101	221063	214737	207122	194934	222930	195296	201110	192362	237657	219246	235849	221467
N	11739	9822	219818	150360	204996	169959	191320	156967	207391	162440	228293	200637	198210	157891	102099	217807	168493	164880	230445	193241	181937	203802	229920	205545
O		9911	210885	193256	213354	200071	169714	51953	209337	213391	185045	180188	218282	207947	203812	218598	211797	231180	207541	171728	197146	230916	225961	214126
P	10819	10092	162787	153004	189919	185119	195775	198541	209788	190184	102136	188571	190623	199704	206734	195355	57881	168842	193225	214887	195432	164353	219389	196545

Appendix Table 19: Fluorescence data for the 15-minute timepoint (outliers removed as highlighted).

	1	2	3	4	5	6	7	8	9	10	11	12	13	14	15	16	17	18	19	20	21	22	23	24
A	11121	9309	187559	207616	179220	192256	170690	205726	170630	206106	162671	205025	197866	201911	188739	196360	206687	134024	202156	190149	194904	172931	170138	189673
B	10031	10748	191781	127220	180012	142001	177712	170953	164478	194486	175741	198743	42259	175607	178036	148139	13259	186720		198260	70840	170333	193366	174342
C	10460	9749	198010	169920	190693	161933	163198	220247	81437	183131	67262	172349	213137	191821	57279	183187	194121	192947	188805	197955	206843	179313	193944	187876
D	8756	8875	183836	164727	184083	154536	171192	161114	17174	171419	200699	115400	137019	176628	75995	113242	9701	170194	103515	171360	192910	23690	201182	197258
E	9118	10081	159871	137120	181436	195333	138658	176624	186693	183742	164767	144690	191971	124276	197617	209352	168380	188569	194695	215787	202366	209098		205682
F	8192	9521	206109	162521	184781	193071	82901	195675	188513	199455	163843	168252	172522	194155	120025		176715	181841	68808	207285	173793	179638	205278	203303
G	7149	9073	195006	178876	208957	155053	176588	203673	214489	180040	209242	72339	179449	202132	177855	67841	193542	11984	223656	120983	193834	158105	220564	207318
H	9509	7223	174498	161585	177836	126492	177884	42627	178725	151341	177383	153714	113283	181014	99919	143801	61945	173876	10123	197658	191345	174348	181807	194036
I	9865	8598	193838	186401	167217	127003	230500	130268	174521	155795	172975	87706	178792	177722	205628	196551	121250	185607	185172	174146	159868	139355	180594	193656
J	8619	9399	170176	99814	183893	176889	147254	179779	153005	182735	194538	113754	73458	156722	124221	150671	118502	127788	207812	199340	180905	165698	207721	200276
K	8298	10210	87226	183107	181718	96747	145677	95447	202119	194565	180282	119892	146364	210143	145017	181215	182043	191063	146739	179939	184487	200080	211374	202391
L	8925	8325	165251	177001	195008	151269	149849	166614	194637	65784	113268	164540	122400	193528	47754	176707	159099	102685	132503	172221	199155	203830		197552
M	10737	9042	198102	197305	191246	191041	156268	180462	185564	170857	180970	179593	171711	191483	183602	158681	191850	159292	185225	172352	176704	194259	206234	195714
N	9705	9075	189177	150305	205219	153526	175584	129662	164816	144452	181930	151486	181127	137930	112373	187919	130875	120246	187671	184865	166254	187327	197021	192824
O	10069	10490	184681	187337	194336	196161	156724	55097	197492	180024	164710	163339	166756	194452	193219	203210	189052	168913	188236	149335	180979	201294	198636	191641
P	7792	9664	149081	142768	173919	165287	177777	178718	196260	179200	82666	181999	173898	182081	188633	161053	48571	137983	174138	141387	167934	150180	181301	173355

Appendix Table 20: Fluorescence data for the 30-minute timepoint (outliers removed as highlighted).

	1	2	3	4	5	6	7	8	9	10	11	12	13	14	15	16	17	18	19	20	21	22	23	24
A	10185	11698	203184	224905	190275	200706	179305	219959	171773	212713	185935	217126	198688	202301	182363	205889	204419	144157	206421	190685	205209	180221	182205	180694
B	11325	10158	206319	149991	179339	126935	191828	188560	202354	197814	169786	192866	45135	206756	195735	131507	11774	201988	223676	215431	53081	174316	193453	176408
C	10653	9996	206722	166606	209531	186345	185939	199620	75399	193506	75124	165581	208790	194439	40904	188443	191125	192795	217714	192625	202919	180123	196127	174907
D	9625	8627	199795	161923	167133	178644	164131	176222	11979	166997	200216	135327	174000	167088	85661	89629	9421	164080	156868	160700	198545	16024	199975	186978
E	9081	9200	160454	126615	168527	203340	130963	180559	193079	168303	178238	151945	196872	143891	183470	196915	184902	172713	188356	199787	188600	194439		188724
F	9592	10178	211028	201510	194771	195088	65071	196707	184644	197327	185344	181258	178812	195527	130955		170416	181473	60267	203177	169486	175292	195837	203911
G	11399	11302	196154	195987	207395	160144	208788	209606	216084	185125	207735	46988	186979	204475	184301	41324	200013	10664	215579	109681	218422	174809	212921	201397
H	9684	9689	180447	180927	176463	147802	188789	29822	196350	172963	204427	199598	118870	218993	130308	162361	46108	202467	8902	195509	223074	199835	191528	194672
I	9137	8926	199803	193820	146040	141874	209994	132281	180991	139501	177637	78157	192086	185252	199065	208689	89853	202357	201312	173422	138719	200794	204053	191915
J	8673	9564	165966	116533	196818	155227	161735	199879	162402	190680	209021	112377	81839	144148	138814	127168	136829	135423	203885	197546	177428	149053	207286	199485
K	9465	10059	100883	193135	186055	89327	128664	114595	211578	214611	205862	135736	138222	209807	123961	183382	174716	177086	148928	185464	181751	191116	203783	200188
L	9272	8933	143275	180177	210881	150179	181136	177261	196920	84706	122080	179299	148521	179493	51985	189752	172041	106154	135781	167718	180050	190380	209467	188003
M	9719	8953	207020	199756	192508	194360	205147	195317	199257	165070	203578	189916	213066	203176	196261	136393	197596	193808	185266	183399	210069	203617	211446	186527
N	9854		212122	153477	200355	177796	174880	159499	200043	166162	215536	174814	194520	116175	121989	204158	100586	144591	214913	186453	175285	183572	206123	182216
O	9686	9262	177972	188822	194630	201257	152751	42180	204267	191134	173468	160501	206256	203697	196809	204748	185438	207785	193050	160857	176282	197703	199198	195145
P	9013	8556	154596	154786	176664	166825	180024	175712	203215	192760	113214	189534	173720	189204	192383	181500	41090	139005	173379	203288	166042	154981	208999	165465

Appendix Table 21: Fluorescence data for the 60-minute timepoint (outliers removed as highlighted).

	1	2	3	4	5	6	7	8	9	10	11	12	13	14	15	16	17	18	19	20	21	22	23	24
A	6017	6359	189353	207945	169715	196592	160524	203491	157534	194367	169641	208026	182423	187285	173611	192152	190041	134676	197133	178041	186705	161841	191485	167936
B	5098	5745	185565	130231	171805	90496	178554	177098	202010	171936	142987	183562	9449	202535	178040	87444	6298	187803	213409	195027	10042	160346	183948	168303
C	5858	6225	194520	154733	183486	171596	171579	188821	53081	183671	55557	128064	196266	183811	16010	173636	176015	176596	216626	175916	189765	162621	190422	167772
D	5252	4806	184359	144269	151336	159906	142500	171212	8345	135332	188883	110840	159563	156522	27722	54349	5044	134566	135568	149210	170914	7528	195483	180383
E		6579	128936	90307	147592	196707	101738	166081	178278	141430	171501	139619	176740	125256	166398	187288	175828	153687	173832	185605	173293	187352		179140
F	5953	6622	196774	187442	182427	193579	22768	175506	165338	190986	175844	155856	159150	191619	126705		165814	174759	13514	195854	152726	159189	192997	191724
G	6572	6219	175748	180417	196052	105959	200397	194985	197916	171988	205474	17544	163583	195569	163653	20700	186189	5750	202118	78675	199085	142832	203210	191104
H	5673	5385	155964	160168	162622	127228	176997	12875	176120	139372	183759	183815	102229	204975	109167	128300	7388	176208	5492	182993	200063	181855	176075	181362
I	5726	5808	166448	173142	109687	125374	191950	106137	163141	123814	162842	14357	177749	165019	178525	182255	43122	183159	183841	137926	99944	185423	192057	182250
J	5804	6105	150126	105625	191133	127382	153658	184849	151659	172405	200029	105691	14846	108236	133535	83066	118165	119943	190016	186733	150390	123166	197452	187358
K		5341	54803	182826	156427	51040	89287	110970	198778	199279	196840	104900	92108	193345	84468	165116	147576	160853	140213	172633	170055	168642	196789	183431
L	6085	5455	107843	158621	196990	122042	172925	142457	170304	35491	119537	162553	128655	158141	8516	172713	162277	59670	120617	143215	160129	172046	194292	172902
M	5818		184556	195996	173147	168954	191095	179909	189951	151140	180801	165526	202548	185889	181708	99169	170789	190121	164951	172865	204569	171080	193454	172809
N	5699	7284	193696	145835	180631	162965	151130	146914	179678	146295	198983	155518	180558	78628	110398	189123	59245	116888	198042	164818	157257	173856	193153	162102
O	6097	5570	148052	165723	171722	191315	130723	6660	190989	189302	159568	150032	199477	196868	181778	200151	163297	190376	181919	155892	165764	187181	186284	192981
P	5684	5441	129708	134042	156510	135041	164515	158295	186531	179452	92727	173464	159384	171277	176414	146989	5822	103142	149722	189198	144162	137809	191478	154256

Appendix Table 22: Fluorescence data for the 120-minute timepoint (outliers removed as highlighted).

	1	2	3	4	5	6	7	8	9	10	11	12	13	14	15	16	17	18	19	20	21	22	23	24
A	6652		178733	204313	155097	192033	151476	188325	147868	185884	161990	205504	177415	194327	150477	182557	182912	117264	193375	171854	190108	141179	181422	171466
B	6271	6872	182632	112346	160437	61898	174024	163018	201437	153154	107680	174980	8317	190564	149182	35721	6146	168046	223552	195406	5951	146799	195088	169539
C	6586	6263	182289	123156	167801	160559	151173	185853	45785	161894	46630	90226	182543	178837	6318	165126	154666	164636	211102	175541	185151	157850	189693	166487
D	5866	5634	178469	130316	143501	135717	120303	154281	8120	111096	187380	93997	144841	150069	5167	20492	4904	103850	135981	147760	162455	7292	198174	180402
E	6675	6868	104415	44539	106144	185708	66935	160447	170647	103773	173166	120367	152143	113966	130702	178689	175991	125461	162771	173046	157486	180416		175076
F	6348	6550	179447	168197	181596	181211	7798	145137	143663	189571	170136	122023	145663	178293	122881		171906	171586	5754	195284	136686	140068	191751	192491
G	6391	6709	152034	179293	186032	57578	184939	188205	200438	154487	212359	5895	153549	207804	144043	17614	175082	4877	199778	61324	192633	108611	198599	192996
H	6060	5714	132456	145719	164670	106286	171841	7453	157342	96411	171518	171907	69569	192784	79369	84006	5110	153662	5644	184237	188645	151528	201441	175377
I	6348	6128	145239	170878	59780	114610	199157	79718	159521	115366	165136	5644	171796	140232	170503	183080	12561	163067	172881	92188	69397	173086	180001	181602
J	6185	6010	136493	90768	187186	102345	134485	164489	150068	153876	185881	113771	5894	71663	134938	36628	100640	113862	193608	180933	128402	105512	194229	180544
K	6332	6089	13969	164617	126078	22392	62989	116980	189112	193222	188139	60980	42349	201122	39894	157822	107310	139781	145130	164622	168843	148438	192030	181571
L	6261	5530	81511	150711	185382	98704	153729	87573	179912	5123	115840	137216	113013	186706	5505	169075	150990	25790	119970	120068	150513	166215	197543	175473
M	6293	5756	153107	182164	146056	153583	174170	188298	172508	113274	172360	135586	188707	168349	169765	74162	174546	169595	164706	157982	190962	172655	193144	171164
N	6340	6359	177947	129937	174643	132774	124946	130054	151782	125915	189613	133746	168116	40300	98029	182496	21637	92743	182371	166294	148594	156642	188557	162571
O	6355	6074	103526	127262	141789	179310	118623	5690	136934	189472	146103	171017	188057	192349	164828	194380	126587	195581	166067	135806	150693	181472	179539	179336
P	5841	5490	99391	111280	130179	102156	155150	129750	178507	172479	55000	167787	144488	152670	162027	122229	5365	59770	121793	184834	120187	108684	193344	

Appendix Table 23: Fluorescence data for the 240-minute timepoint (outliers removed as highlighted).

	1	2	3	4	5	6	7	8	9	10	11	12	13	14	15	16	17	18	19	20	21	22	23	24
A	5017	5154	185052	211164	151182	194053	169445	189278	158142	190911	161821		178481	204908	146039	186718	184715	111328	205848	178020	196993	133700	187238	195342
B	4523	4745	185949	114620	162842	62707	180615	171171	201654	148614	93892	139967	6297	203120	151606	25822	4495	166092	228649	204844	4072	151136	195420	177674
C	4926	4673	197307	109676	180044	162412	149545	216863	41110	162208	44140	87503	182553	168734	4452	157602	136429	169641	216313	175509	175276	162455	196959	174285
D	4312	4223	181376	129997	139852	136478	115614	159972	6918	82289	201126	83894	143021	152885	4067	8275	3916	93337	121090	141594	176610	6579	203731	186661
E	4638	4857	95788	36999	103861	195441	53241	141904	173620	83222	172468	110724	145500	94627	130161	180115	172546	117478	166709	177385	151098	185614		184052
F	4701	4374	183820	180209	180574	181331	5897	146852	146355	187899	175428	122500	145461	103943	125869	225272	172859	159479	4365	197547	133817	137355	196173	194366
G	4593	4882	148156	177543	193179	48935	189744	180584	215959	149510	198632	3932	143077	196744	132477	16379	167421	3996	210819	66850	194924	105303	198764	190922
H	4334	4205	130425	148561	167830	101576	177774	5140	162103	85786	179607	174833	57644	192109	63331	70644	4098	148809	4383	177612	194779	172448	184453	184697
I	4451	4399	145207	181363	48346	101285	209556	57526	159913	101518	159213	4027	154990	140558	162428	175168	7506	169300	172368	79437	61903	174321	181460	180249
J	5029	4681	139307	78900	179619	99387	138401	168219	137042	154403	193640	101850	4281	48413	125081	26268	82668	98743	186009	190088	131163	100237	203958	175511
K	4196	4523	8917	159575	118720	12563	60492	115153	196094	199842	191554	44409	30150	192932	26342	143449	96346	139272	128783	160753	161385	137578	192313	182927
L	4290	4041	68026	143204	188979	95470	147326	76529	174986	3657	98791	128569	104106	156946	4394	162211	157517	15859	88687	109927	154920	162839	204702	181495
M	4465	4512	163797	180860	143503	146833	178576	187189	167964	111592	181606	135961	184809	150765	158776	57696	172460	190323	167446	150112	202062	162009	200439	180824
N	4471	4601	175620	145962	183569	141595	117549	118552	148642	119795	190278	133441	166280	31662	211289	181445	14084	84261	191830	161534	138709	155612	194425	167728
O	5273	4375	98660	120486	136398	174379	97466	3717	175037	178917	149673	141017	192894	188153	160385	189664	125275	190893	162049	131047	147504	179333	182562	186580
P	4622	4199	92486	108915	131543	95006	158824	124963	171945	175368	35631	171137	134896	145778	161397	114049	3807	27613	113459	186942	114240	100822	199062	

Appendix Table 24: Fluorescence data for the 300-minute timepoint (outliers removed as highlighted).

	1	2	3	4	5	6	7	8	9	10	11	12	13	14	15	16	17	18	19	20	21	22	23	24
A	15707	13967	141243	189425	97103	184456	146055	103766	59928	158196	82937	197818	127622	214205	39437	126317	126523	11352	182109	136133	189758	10685	195523	184516
B	12967	12479	173115	9675	108800	39007	148953	131147	202756	49755	21058	135422	11663	174373	67517	9530	11147	92475	210949	191600	9706	111863	207225	179606
C	12609	11939	174109	22723	110770	107355	99044	185502	62272	79863	63673	14333	125202	119629	9186	104482	52474	127093	207441	150585	132226	139271	208540	179977
D	10868	10102	166952	7660	85054	65172	42314	125645	12249	13886	172324	9036	78674	75141	8419	8960	8107	7828	113178	108466	129621	30133	206239	185197
E	14332	13578	21770	10268	25760	186644	11833	9795	121644	18194	105960	8866	58116	9474	38885	115503	156102	32912	142167	140949	87772	174339		191209
F	13831	13308	139600	156698	161652	178855	11898	62717	137757	161795	131083	62867	111144	44515	109661	181137	169955	128351	9873	193351	94727	34693	198554	199521
G	14156	12639	69324	160212	176935	10415	189635	139133	200643	64451	219257	8831	86634	186574	40226	18006	98525	8813	187532	53447	155198	10417	209120	196306
H	11120	9807	49133	130547	132449	8475	173975	9506	86551	15225	154861	128373	7953	185674	8850	9850	8490	44963	9062	156832	164445	135556	187699	194788
I	11175	11042	57114	162210	11443	12931	201276	8702	118260	78712	115003	8923	98426	46303	93900	155634	9749	105820	90116	12294	30457	124641	192244	192030
J	10248	11109	159049	9273	182798	27931	88713	131642	88425	67657	175653	56579	9653	9971	50754	10255	11548	18931	157173	169135	54617	47743	212678	189574
K	10553	10555	9888	125504	32346	11333	52986	47848	168902	179135	161056	9539	8639	190194	9276	80971	17051	68177	74777	129840	117359	58743	203822	196349
L	10118	9340	14450	101068	153065	7685	82398	12029	180908	7671	7789	63798	6844	155505	8577	125899	128891	7908	7418	11238	138570	168304	198649	185320
M	10122	10124	99293	173648	59241	68405	166019	184964	159016	9562	159848	43565	161094	78358	118747	15738	139578	176851	139464	107703	183644	144003	207270	186298
N	10679	10930	165488	115023	175366	65718	34848	73330	51481	9618	196617	101119	131394	9461	9079	172226	9680	28384	162284	135037	35620	117291	206210	179162
O	11099	11182	29146	31820	65086	181822	23366	7651	151147	165195	123376	117891	199454	187157	111818	174798	38140	161282	164973	8984	122604	177194	196923	188086
P	8965	9165	23439	8738	24559	21366	137031	37272	138433	140245	8199	165504	98745	83949	121203	10355	8348	8303	22140	177969	67105	8315	207030	

Appendix Table 25: Fluorescence data for the 1380-minute timepoint (outliers removed as highlighted).

	1	2	3	4	5	6	7	8	9	10	11	12	13	14	15	16	17	18	19	20	21	22	23	24
A	11473	9928	128425	175335	88124	182735	136801	94370	50024	149786	69763	188270	117312	199088	31093	116658	114919	7399	174183	122309	180471	7071	185724	174674
B	8676	10759	166443	7167	100103	35651	137614	124819	183724	41187	15201	129887	9299	164104	56502	6658	7713	82500	205546	180145	6888	95169	198506	173597
C	9570	7644	175235	17753	100808	99047	84897	208982	53095	68904	59150	8765	114819	105353	6475	91551	40921	115128	202086	135783	121143	129561	199805	174237
D	6482	7124	154938	6049	86093	55381	33803	123685	8938	9837	162613	5303	66015	68537	5339	5298	4985	4420	106391	98313	125716	28721	200821	177155
E	8568	5988	15119	7318	19040	175708	8342	7507	108706	12630	94090	6483	49220	6240	31405	108264	142687	23898	132893	128446	75937	161749		184149
F	7968	7328	128490	146212	164017	162256	9256	54847	131690	151263	123240	54487	110979	52861	103060	176849	161462	116884	7807	181561	86278	9089	192467	190520
G	10443	8975	60865	152989	170843	8020	179759	130151	193052	54221	187233	5744	77031	173904	34284	15000	87366	6926	174859	46589	140291	7958	204690	191332
H	8345	6892	41101	122026	130890	5322	167680	6094	73650	10982	149711	120555	5857	181361	6368	6084	6293	35950	6425	144450	149767	121781	178165	188154
I	7945	8142	51628	161053	7256	12206	196232	6658	107371	72952	104156	6219	89082	42275	82499	142845	5905	96760	76861	9728	27507	114795	188955	177549
J	7555	8754	147975	5781	171315	21529	75460	121137	76752	59549	168711	46633	7082	7223	7315	7257	7685	16499	148071	162601	43894	31847	204737	188046
K	7749	7107	6706	122502	24910	8065	46745	39443	160532	171929	150969	6278	7394	176175	6874	66462	12091	57138	63259	114289	105371	49711	194436	187152
L	9438	8477	10846	91151	145919	4895	69274	9713	172233	5540	5517	51888	6175	135425	6067	119547	124135	5443	6151	5262	133375	157955	197883	171503
M	6305	5129	88413	164607	51212	60041	160214	189688	154628	6690	149360	34904	141368	67436	117679	10314	129004	169403	131047	95152	173340	134552	201926	178411
N	5307	5350	160951	118239	166543	49153	28662	63669	44190	6878	190858	94247	122383	6440	5449	160620	5521	21219	154028	123679	6646	102910	197185	171395
O	6427	5397	22415	21190	57061	173364	17322	5975	143868	147867	117911	111517	195842	183969	101505	165269	28986	153281	146451	6860	109524	172011	189431	180390
P	5499	6320	8131	6542	6711	16067	128909	29906	130269	127427	5246	158230	89389	72381	110492	6701	5168	5021	7398	165925	57774	5537	198566	

Appendix Table 26 : Fluorescence data for the 1500-minute timepoint (outliers removed as highlighted).

A.1.2.1 FA data

	1	2	3	4	5	6	7	8	9	10	11	12	13	14	15	16	17	18	19	20	21	22	23	24
A	23.9	26.7	84.7	82.4	143.1	107.6	37.5	55.2	108.6	55.2	112	100.9	31.3	109.9	84.2	109.8	117.9	82	99.4	105.4	98.3	72.7	127.5	108.8
B	24.4	25	42.7	81.9	94.6	27.7	39.2	55.9	121.5	36.5	70.2	42.7	138.9	103.5	56.4	142.7	148.4	31.7	131.6	113.2	143.2	40.3	113.7	122.9
C	26.6	23	85.8	46.1	59.7	30.2	57.7	94.9	70.2	81	67.9	45.2	97.8	40.2	101.7	108.9	45.7	113.8	123.4	99.4	113.5	68.3	128.6	128.4
D	27.4	26	39.5	145.7	99.3	40.7	43.1	124.1	134.7	60.6	134.2	131.1	114.2	97.5	148	111.9	148.9	97	105.8	110.1	95.7	28.5	129.2	115.6
E	25.3	25.1	67.7	54.8	59	92.6	83.7	149.7	116.7	44.7	110	115.6	107.4	78.5	67.9	38.9	121.6	109.2	121.2	129.1	59.5	90.5	100.8	114.2
F	24.8	23.2	105.4	45	100.9	36.9	143.3	85.5	120.6	111.2	117.7	130.5	120	184.2	130.7	68.5	98.3	122.4	147.6	101.5	116.2	61.6	124	116.5
G	21.9	26	95.1	108.5	54.4	89	113.8	108.4	95.1	98.9	99.5	101.6	83.9	118.4	60.7	27.6	28.1	166.8	122.3	144.9	94.4	107.3	111.3	114.4
H	26.2	21.4	78.3	122	96.3	36.9	106.9	51.5	49.6	157	74.1	32.9	143	78.4	38.1	87.8	45.2	74.1	137.3	107.8	124.4	130.3	99.9	118
I	23.9	27	109.4	116.4	34	148.9	125.8	137.9	113.2	126.7	119.3	105	79.9	41.2	35.9	119.6	78.2	78.4	76.8	137	137.8	38.6	113.7	122.4
J	25.1	25.7	108.1	86.9	97.3	85	139.8	42	73.7	53.3	82.6	52.9	164	108.2	50.8	35.1	153.3	57.6	107.1	105.9	57.5	152.1	119.4	118
K	24.8	23.1	67	80.9	90.4	96	76.9	32.2	138.2	97.8	135.5	64.7	62.3	112.4	134.4	126	64.3	39.8	133.6	46.8	64.1	141.4	124.5	121.8
L	27.5	24.2	138.9	47.3	44.7	77	85	77.2	114.4	135.3	138	88.2	114.3	103.1	139.9	81.2	126.9	109.5	86.1	29.8	130	118.8	124.1	129.4
M	25.2	28.1	60.5	72.7	53.8	32.3	89.5	64.7	121.4	103.2	113.5	88.7	86	109.5	126.4	76.4	87	117.5	62.1	136.2	75.2	120.6	118.3	124
N	24.4	25.4	110.8	121.5	93	122.9	85.2	112.8	127.1	75.7	93.4	123.5	125.2	25.8	153.4	114.9	79.4	76.8	85.4	125.4	128.3	137	130.4	131.1
O	27.6	24.3	133.3	45.2	43.4	63.7	73.1	135.7	88.6	100.3	87.2	129.1	79.4	112.6	86	89.2	52.4	104.2	122.4	46.7	127.5	122.6	122.7	118.7
P	24	24.6	135.9	136.3	149	124	89.7	89.7	31.9	102.9	54.9	113	102.3	121.6	44.2	92.8	156.6	25.1	72.5	119.1	126.9	154.4	119.8	133.6

Appendix Table 27: Fluorescence data from dilution 1 (2.5 μM) plate.

	1	2	3	4	5	6	7	8	9	10	11	12	13	14	15	16	17	18	19	20	21	22	23	24
A	29.8	29.7	116.6	118.5	149.5	138.2	40	80.6	124.6	61.6	113.4	96.8	35.2	139.3	118.9	129.9	140.6	128.8	117.8	118.6	127	92.2	147.6	143.9
B	23.7	26	72.3	134	128	30.3	48.9	66.7	118.9	31.7	79.6	65.1	168.4	121.5	68.9	164.5	157.9	36.3	150.4	140.1	172.1	41.4	139.1	145.1
C	25.8	24.9	129	54.9	86.4	28	74.9	127.3	73.5	81.2	96.3	59.9	114.4	53.1	129.3	119	55.5	148.5	142.6	128.5	134.2	78.5	141.2	151.3
D	26	28.7	47.4	167	105.3	59	62.2	150.7	153.3	77.3	136	161.6	141.5	116.3	163.3	132.7	165.2	125.3	133.7	132.5	122.7	38.7	140	146.3
E	30.4	26.8	90.8	57.1	60.9	113.4	120.7	168.9	132.5	65.8	134.6	135.4	130.1	103.1	80.6	53.4	149.8	133.7	142.8	157.4	82.8	124.5		140.9
F	26.5	28.4	155.7	73.3	134.1	68.1	180.8	123.8	147.8	142.6	140.1	144.3	146.3	191.5	160.5	85.2	113.2	143.9	165.5	134.1	137.8	81.3	136.5	143.5
G	25.8	29	116.8	145.9	81.7	126.7	156.8	143.2	124.6	129.8	142.1	123.8	104.2	149.3	77.7	37.2	32.8	186.6	143.6	157.1	123.8	128.7	137.1	145.9
H	24.7	29.2	96.3	157.3	128.3	55.8	140	72.7	67.3	172.1	131.4	45.9	142.1	104.5	52.9	106.4	73.7	104.5	157.3	130	152.2	149.8	126.3	145.3
I	24.5	26.1	154.8	145.4	43.6	176.9	138.7	157.6	140.3	152.4	141.1	137.3	102.9	49.9	51	142.1	107.2	95.2	107	153.1	156.9	52.1	143.4	144
J	23.1	30	138.5	133.5	123.4	105.2	161.8	78.7	118	68.6	117.8	81.2	175.2	127.3	78.8	43.8	162	69.5	118.7	138.8	66.4	170	151.6	148.3
K	26.4	25.1	105.9	128.8	113.9	127.3	95.4	36.8	153.2	129.3	158.7	96.6	86.9	129	156.1	141.4	77.7	51	147.2	52.8	84.7	161.4	150.1	149.1
L	27.1	25.7	164.7	58.2	76	106.8	116.8	110.9	150.6	163.6	161.3	110.5	143.2	129.8	165	95.6	150.3	133.4	115.6	36.6	158.4	145	147.2	146.6
M	26	22.9	90.2	105	74.4	32.9	119	85.2	144.5	128.1	143.8	103.5	100.6	135	141.3	103.3	98.8	143.3	78.5	162.1	101.3	148.4	147.1	149.8
N	23	26.1	151.2	157.1	136.6	154.2	118.2	140.6	126.3	108.8	97.6	141.2	158.5	27.7	167.4	146.5	93.1	93.7	113.1	152.6	152.1	151	152.1	143.8
O	26.7	26.1	166.5	59.8	75.9	93.6	102	134.4	85.9	97.7	87.3	141.4	120.6	125.7	115.6	114.8	72.2	141.8	135.6	64.8	153.3	146.5	146.8	147.2
P	28.8	22.7	156.3	165.9	171.9	138.4	117.7	103.3	35.5	130.6	75.5	157	134.9	146.7	63.2	112.6	166.8	30.1	86.6	132.7	159.9	166.5	141.3	152

Appendix Table 28: Fluorescence data from dilution 2 (1.25 μM) plate (outliers removed as highlighted).

	1	2	3	4	5	6	7	8	9	10	11	12	13	14	15	16	17	18	19	20	21	22	23	24
A	27.5	29.2	129.3	146.4	183.9	139.9	56.2	95.7	135.7	96.8	141.4	145.8	51.2	152.5	146.2	151.5	157.3	121.6	129.5	143.9	146.1	102.6	164	158.5
B	27.1	27.5	107.5	164.5	153.7	38.1	99.6	126	161.4	42.4	85.4	55.1	183.3	145.9	87.2	168.4	179.2	39.2	141.3	149.3	176	56.7	155.1	159.8
C	29.7	26.9	162.8	68.3	112.2	34.1	136	164	108.6	112.5	122	66.2	157.5	68.7	144.3	144.7	81.8	162.2	153.4	135.4	155.3	116.9	164.7	161.3
D	29.1	28.9	65.9	185.9	171.7	93.7	84.7	152.7	177.4	94.2	170.1	170.5	151.5	140.7	182	145	179.3	142.3	148.8	150.8	124	41.6	170.5	161.5
E	27.5	27.2	140.2	109.3	118.9	161	135.9	175.8	154.5	77.2	146.5	142.2	150.8	113.3	105.5	59.2	159.7	148.4	155.5	172	90.9	130.9	153.1	160.9
F	29.9	29	153.5	62.4	139.9	72.1	186.6	185.8	164.8	160.9	174.8	165.2	152	207.3	161.2	106.2	142.2	166.1	176.6	148.4	156.3	125.6	166	160.4
G	27.3	27.4	140.4	165.7	117.7	131.6	167.5	168	152.5	143.1	157.9	145.7	125.8	157.1	102.2	37.5	42.3	183.7	154.5	167.3	128	134.5	167.6	167.9
H	29.6	30	119.6	170.2	147.7	52.9	163.8	94.5	98.2	176.4	161.4	61.7	172	125	61.9	106.9	117.3	121.2	172.4	159.5	159.6	170.4		157.6
I	27.8	28.5	160.7	157.7	49.3	186.7	170.2	167.3	174.6	172.4	161.2	149.2	123.6	56.4	52.8	166.6	132.2	116.3	128.3	159.4	173.9	67	159.2	151.5
J	25.9		149.5	155.2	154.1	117.7	187.1	78.7	119	95.1	138.1	95.5	178.1	154.5	92.9	53.1	173.6	115.7	146.7	145	88.7	173.5	156.3	163.3
K	29.6	27.5	124.1	154.6	131.6	148.3	125.2	53.3	172.2	144.5	176	109.5	98.2	161.6	171.3	156.7	110.1	63	158.6	108.9	93.3	169.1	156.8	167.8
L	28.9	26.2	171.7	78.2	82.2	134.1	135.9	126.5	165.9	174.8	172.7	132.8	156.1	149.3	175.7	121.6	163.5	148.6	140	43.9	167.1	159.2	166.7	153.4
M	30.2	29.4	106	122.2	76.4	44.9	155.2	129.5	160.4	138.8	170.1	129.1	126.6	151.4	163.5	116.4	118.8	159.8	115.8	164.2	130.7	153.8	163	159.6
N	29.2	26.4	168.2	174.1	162.1	168.1	133.6	161	164.2	110.2	171.7	168.8	168.6	31.7	177.4	148.9	113.1	122.1	133.7	149.9	158.2	166.8	161.3	167.3
O	27.9	28.8	168.8	62.3	65.9	135.1	128.8	180.9	152.8	154.5	140.3	175	112.4	166.6	133.8	135.4	77.8	155.1	160.5	77.7	169.6	163.1	163.1	158.8
P	27.8	26.6	174.8	180.8	174.5	163.2	147.4	124.6	43.7	144.6	88.8	155.8	145.5	157.9	76.4	123.2	179.3	34	109.7	150.3	163.8	175.9	154.3	171.8

Appendix Table 29: Fluorescence data from dilution 3 (0.63 μM) plate (outliers removed as highlighted).

	1	2	3	4	5	6	7	8	9	10	11	12	13	14	15	16	17	18	19	20	21	22	23	24
A	31.9	29.8	157.8	125.4	187.4	179.2	74.8	93.6	178	136.8	167	173.4	184.1	167.9	139.4	160.3	171.9	162.3	151.4	164.4	156.4	145.5	179.4	180.3
B	32.3	30	162.5	186.3	177	51.5	188.4	188.4	180.6	83.1	140.3	93.6	184.4	164.4	113.5	179.5	184.6	49.1	176	177	185.2	67.6	174.2	182.1
C	29.5	32.1	179.2	119.2	150.3	147.9	175.8	194.7	188.8	165.7	150.9	103.1	165.8	78.5	160.1	156.8	99.1	174.2	176.9	158.7	154.2	133	175	173.4
D	30.1	33	162.7	192.5	177.8	153.8	104.6	177.8	187.1	122.4	186.1	183.1	175.5	152.9	186.3	159.7	179.7	150.4	161	160.5	146.3	40.4	176.7	173.5
E	31.5	29.8	177.9	108.3	136.5	168.7	152.9	192	174.2	97.2	165.4	164.8	176.7	151.6	142.1	88	177.5	146	177.4	175	120	144.5	178.2	181
F	32.6	28.9	174	109.3	174.9	134.6	192	151.8	180.9	177	178.4	180.6	174.5	204.9	181.5	119.6	175	179.5	177.2	166.6	171.7	137	167.3	175.2
G	30.1	31	160.8	178.1	142.2	146.5	179.2	174	177.2	163.8	168.9	162.3	154.3	164.4	119.7	48.1	49.7	189.8	166.5	180.6	145.7	156.6	177.3	173.9
H	31.8	30.6	144.5	173.8	162.3	78.3	169.6	97.6	122.8	185.8	156.3	105.8	181	152.8	70.6	141	139.8	135.9	181.3	166.1	172.7	178.3		171.1
I	33.1	28.9	169.8	171.6	55.5	188.3	179.7	182.5	179.3	183.8	184.9	167.6	148.8	64	72.9	180.1	134.3	136.6	144.8	171.3	177.6	71.6	177	173.5
J	29.7	30.2	180.6	166.4	161.4	149.5	184	136.1	133.7	110.5	136.2	117.1	190.2	164.3	131.9	66.4	183.4	116.3	152.9	172.2	105.8	180.6	178.1	174.5
K	31.5	27.7	129	162.9	152.7	158.6	149.4	76.8	181.5	164.4	184.7	129.7	117.7	174	176.1	174.1	127.4	93.6	178	143.7	136.1	178.9	174.1	175.4
L	28.7	29.6	184.1	96.7	123.1	147.9	157	144.2	176	184.7	189.4	155.6	174.9	165.2	186.8	153.6	178.9	166.7	159.3	56.7	178.7	176.7	177.4	174.9
M	27.1	30	135.4	146.4	122.1	63.4	152.8	159.2	185.1	158.1	183.3	150.9	159.9	156.4	171.4	146.8	159.8	175.4	151.4	183.9	162.6	173.6	182.4	176.5
N	30.2	29.2	170.1	181.2	155.3	180.9	149	183	175.6	166.8	176.2	173.8	178.1	33.7	192.3	179.3	137.7	135.9	155.2	176.8	181.6	183.3	174.7	181
O	29.2	30.2	176.8	90	101.6	156.2	134.1	185.4	168.2	168.8	170.6	193.2	167.5	170.3	152.5	144.8	101.2	169.2	178.4	114.7	172.2	174.2	173.1	179.1
P	27.1	29.9	184.6	185.6	184.2	160.4	158.6	151.4	75.2	157.8	118.6	177.8	168	163.9	95.3	135.1	186.8	36.7	130	168.8	171.8	185.7	169.8	180.5

Appendix Table 30: Fluorescence data from dilution 4 (0.31 μM) plate (outliers removed as highlighted).

	1	2	3	4	5	6	7	8	9	10	11	12	13	14	15	16	17	18	19	20	21	22	23	24
A	29.4	28.9	151.3	155	180.3	175.4	66.4	103.4	151	148.3	176.5	172.6	178.6	175.6	152.1	161.3	171	163.6	169.4	157.4	172.7	149.9	185.1	180.7
B	25.5	27.8	175.2	192	181.2	68.2	185.6	176.5	191	67.5	120.4	126.2	186.2	172.3	129.9	177.3	186.8	49.9	173.1	182.5	191.1	124.4	180.9	183.7
C	25.8	26.1	187.2	139.6	167.2	125.3	163.9	182.7	164.7	155.6	172.4	109	168.5	98.5	164.8	177.9	90	180.4	179	165.2	168.9	147.1	184	178.3
D	27.7	27.3	151.6	195.9	184	121.2	101.1	188	184.2	135.8	185.8	185.9	165.3	159.7	188.6	168.9	183.6	160.8	173.3	174.8	161.5	63.2	180.1	173.8
E	27.3	30.3	162.6	130.4	137.1	173.3	155.3	188.3	178.3	111.7	179.4	169.8	172.2	147.1	135.6	103.4	173.9	165.3	181.3	181.4	134.4	166.3	176.1	179.5
F	27.8	26.5	175.7	137	175.3	157.2	191.4	160.2	185.4	177.4	174.1	183.4	176.8	206.6	176.6	143.9	185	183.6	187.9	178.7	178.6	143.2	177.7	176.6
G	28.1	27.1	160.2	181.2	157.2	162.5	175.9	174.5	179.3	157.2	167.2	169.3	163.7	179.3	126.3	47.5	58.7	193.2	181.3	184.1	157.3	172.3	175.8	177
H	24.5	27.3	151.1	179.5	175.2	79.4	166.3	82.5	123.2	183.2	168.1	139.4	182	146	107.6	149.1	166.9	135.9	187	172.9	172.1	180.2	169.5	176.8
I	24.9	25.6	172.8	184.1	60.5	187	174.3	188.3	184.4	183.1	186.1	171.9	154.3	75.3	90.8	183.2	141.4	155.1	152.3	181.1	178.9	91.7	182	178
J	25.7	24.4	185.3	174.3	177.6	157.5	184.7	149.8	161.6	112.8	169.8	143.5	191	156.6	156.2	80	185.8	151.2	163	169.1	118.9	182.8	177.8	176.6
K	27	26.2	155.2	168.1	137.3	180.1	131.4	101.3	183.5	175.8	182.2	141.7	134	177.3	178.5	180.8	133.7	78.5	176.4	150.3	159.2	181.5	178.4	171.6
L	23.7	22.8	181.1	138.8	152.3	166	166.9	141.5	180.5	189	187.1	166.4	180.1	174.2	184	153.3	185.4	172.8	159	60.6	179	179	178.7	176
M	28	26.1	119.1	165.4	139.4	75.4	155.9	155.7	178.8	174.1	182.9	152.8	163.3	165.5	181.3	134.1	163.7	178.8	165.4	186.1	173.6	173.1	181.4	176.2
N	25.9	25.7	172.8	179.3	174.6	181.2	159.4	178.4	177.2	163.5	176.4	183.1	176.1	38.1	189.2	174.8	141.8	158.5	159.1	173.7	178.3	183	178.8	176.9
O	25.9	26.7	179.6	129.4	98.9	153.7	153.1	187	177.1	174.6	176.1	179.8	184.5	175.7	158.8	165.9	112.4	177.7	176.4	101.4	182.4	171.4	184.6	174.8
P	27.8	26.9	179.1	186	185.9	164.5	161.2	149.8	87.3	164.6	130.6	184.7	159.5	169.4	120.8	143.3	183.6	46.8	144.9	171.4	177.2	187.2	176.6	175.5

Appendix Table 31: Fluorescence data from dilution 5 (0.16 μM) plate.

	1	2	3	4	5	6	7	8	9	10	11	12	13	14	15	16	17	18	19	20	21	22	23	24
A	28.5	29.1	159.9	167.9	182.5	187.2	140.5	122	191.9	174.9	187.3	186.4	197.8	183.2	167.7	163.9	177.6	171.6	173.8	172.7	176.9	148.3	181.5	177.2
B	27.3	27.1	189	191.5	190.9	107.4	195.8	194	196.9	127.3	165.7	162.5	188.9	177	120.6	185.3	189.8	60.1	179.8	184.9	192.1	129.4	180.1	180.4
C	30.6	28.6	190.1	152.7	179.9	176.3	164.1	190.1	170.8	159.7	170.6	109.9	174.4	110.3	168.9	174.5	95.2	178.3	174.9	174.4	172.7	165.5	183.1	186.3
D	29.2	25.9	173.3	182.2	168.6	160.3	125.6	184.7	191.5	148.6	196.2	193.5	181	163.5	189.5	167.8	190.3	178.6	177.5	180	175.7	57.6	177.3	186.7
E	27.1	28.8	167	113.5	108.9	160.5	152	194.8	180	142	186.1	181.9	178.2	154.8	147.6	126	186.8	168.4	188	187.3	134.8	175.3	184.8	184
F	25.4	28.5	177.5	135.6	182.9	159.6	192.3	160.6	184.8	185.5	181.7	182.4	179.6	208.3	183.7	141.2	189	181.1	191.4	180.6	181.7	169.3	179.7	181
G	27.8	26.3	165.1	183.7	159.2	158	187.7	173.6	181.7	172.5	186.7	156.5	165.4	184.9	146.6	63.4	89.7	194	189.2	187.7	172.4	168.5	177.2	181.7
H	28.5	24.1	156.2	180.6	173.1	136.4	179.2	114.4	127.2	193.2	167.3	122	187.2	170.8	99.8	159.4	179.1	153.8	186.3	183.1	181.2	189.5	180.3	184.9
I	27.1	27.7	170.9	186.3	86.1	191.2	189.8	181.4	181.2	177.2	186.4	169.5	163	102.1	101.2	183.3	158.9	156.8	155.8	181.7	184.1	131.7	180	181.2
J	29.7	25.8	174.9	161	176.5	154.7	190.5	157.2	160.4	126.2	171.5	139.3	188.5	167.1	167.1	71	187.1	170.9	171.1	178.8	148	189	181.4	181.7
K	29.8	28.1	162.1	170.8	166.6	165.9	146.6	93	181.6	179.4	186.5	144	142.7	176.1	186.4	176.8	141.1	87.4	184.2	165	161.7	184.9	181.5	175.7
L	33	26.7	184.6	141.9	151.2	159.6	166.2	146.3	183.3	187.6	186.8	165.5	177.8	176.4	183.1	155.3	185.5	169.6	169.7	72.4	186.4	184.4	178.5	181.5
M	30.3	28.7	133.4	155.9	111.8	71.7	148.8	175	183.1	176.3	183.5	157.4	176.8	169.2	181.7	148.6	157.4	186.5	159	182.9	155.6	174	176.7	181.9
N	29.4	31.1	179.3	187.3	175.8	177.1	173.2	184.5	175.8	181.3	169.1	184.7	179.4	33.1	190.2	175	141.3	144	164.8	179.4	171.5	173	176.2	176.1
O	31.1	25.3	184.4	115.4	126	166.9	167.2	182.8	158	173	165.3	190.5	181.4	178.3	158.3	162.1	128.3	173.7	184.5	144.4	184.1	180.9	175.5	178.5
P	31.5	23.7	189.2	183.9	185.7	177.9	172.5	146.2	140.5	178.8	139.5	193	171	171.5	150.7	162.5	188.6	56.4	159.4	183.2	184.7	190	178.6	183.8

Appendix Table 32: Fluorescence data from dilution 6 (0.08 μM) plate.

	1	2	3	4	5	6	7	8	9	10	11	12	13	14	15	16	17	18	19	20	21	22	23	24
A	31.3	32.4	174.5	173.9	188.6	190.1	158.8	165.4	189.2	189.6	191.4	193.3	184.3	187.8	181.7	175.7	179.8	179.7	172.3	182.8	181.6	141.8	184.6	
B	34.6	27	196.9	193	193.2	164.9	194.1	197	196.7	187.3	169.6	155.7	190.5	184.4	147.8	189.9	193	70	183.6	186.2	187.5	155.1	185.3	185.6
C	29.9	29.9	188.4	179.2	187.6	187.8	179.7	196.5	189.6	187.4	186.1	142.1	177.9	118.3	176.6	171.2	113	186.3	182.8	180.8	174.6	165	181.5	185.8
D	31.4	27.4	184.6	192.3	185.8	178.1	143.9	189.2	185.5	147.2	195.2	188	173.4	178.3	190.2	176.1	195	171.8	185.4	178.8	176.4	55.6	182.7	185.8
E	33.9	25.9	180.9	141.5	143.6	181.2	177.4	193.6	185.2	114	183.3	179.7	184.2	167.4	160.8	144.3	192.1	177.4	184.2	188.4	147.9	174.7	186	184.9
F	25.4	32.9	179.1	156.9	181.6	165.1	191.6	171.9	185.8	187.1	184.9	186.8	175.1	211.4	192	175.1	187.7	190.4	192.3	184.6	187.4	171.8	183.4	182.3
G	28.4	29.2	169.4	183.6	178.7	169.4	185.1	185.3	183.7	174.4	178.7	168	167.5	189.6	150.5	72.4	96.4	196.4	184.4	186.8	176	172.5		178.3
H	26.9	29.6	167	188.3	181.7	137.2	186.8	132	128.3	188.6	172.1	124.9	185.8	175.2	114.3	162.3	165.1	155.3	187.7	184.5	184.6	188.5	189.6	185.1
I	31.3	26	177.7	180.9	112.5	193.7	189.8	188.1	190	191.1	191.5	180.1	172	125	135.3	188.2	158.2	162.9	171.5	189.6	190	160.4	182.5	186
J	24.2	26.1	177.9	180.7	178.5	164.7	192.2	158.7	166.2	134.9	170.7	155	192.1	174.5	166.7	93	192.3	170.7	171.9	187.1	132.4	190.9	182.2	181.3
K	28.8	29.4	156.5	171.2	163.6	182.7	161.6	95.2	189.8	181.7	186.8	152.5	145.3	182.9	188.2	181.2	131	106	181.9	178.3	166	185.2		186
L	31.1	28.2	188.3	137.9	164.5	150.2	171.3	158.7	182.8	189.9	187.2	168.4	183.5	180.4	186.7	171.9	185.1	171.1	168.1	80.7	188	188.2	182.3	182.9
M	29.3	27.6	154.7	180.5	139.1	72.9	170.9	184.3	187.2	181.3	188.5	167.1	169.9	179.7	181.6	154.4	170.8	188	169.8	185.3	171.8	181.5	185.1	183.4
N	29.7	31.5	184.6	189	172.5	184.9	173	184.9	184.1	186.9	182.3	186.1	189.6	34.9	186.2	176.2	156.3	155.4	171.5	182.4	179	180.8	182.5	179.2
O	25.9	27.8	187.7	124.7	111.7	167.2	165.7	191.7	183.7	188.1	179.4	192.7	185.6	186.3	171.9	169.1	140.9	175	187	151.2	186.9	174.4	186.4	185.5
P	28.3	28.3	191.6	187	186.9	182.5	172.3	159.4	149.5	171.2	158.3	180.5	180.2	179.7	138.3	150.3	189.1	63.2	169.2	179.1	187	186.4	189.8	182.5

Appendix Table 33: Fluorescence data from dilution 7 (0.04 μM) plate (outliers removed as highlighted).

A.2 SS4 High-Throughput Screen

A.2.1 qIT data

	1	2	3	4	5	6	7	8	9	10	11	12	13	14	15	16	17	18	19	20	21	22	23	24
A	6286	7206	179571	168171	181743	191523	157013	192482	185229	193333	184605	190122	181116	188693	177396	185816	177932	170563	184360	177938	185316	184422	184886	181076
B	6240	7731	155065	136008	162258	170972	173075	180027	185337	194884	196622	181756	166916	179802	192754	173307	124571	178216	203952	177547	148569	165633	170488	190477
C	6738	7690	190403	175296	190353	184180	172007	195544	103689	184950	131801	170981	182472	193478	164937	178014	165783	193513	187357	195756	193448	182255	196075	180066
D	6672	6325	181230	186167	172296	173706	164533	181052	21757	198003	224226	159062	173704	184492	141669	150583	123264	175058	119709	192834	157198	126700	183968	178144
E	4781	7299	154762	170214	155161	181926	150216	174870	180722	185755	170234	175612	176601	168956	169610	188533	153878	192396	174108	172159	164485	180295	183123	186297
F	7642	9335	177309	171541	191188	181474	151975	187352	187620	181160	185937	182374	180178	179718	163125	259843	157942	187023	149126	187673	189063	174131	191136	183265
G	8416	8524	195774	185319	191138	182301	186169	187936	183901	185961	199651	176448	192443	195162	181114	173944	167461	9572	183787	157830	185249	172620	186845	172995
H	7905	7251	177434	170040	177217	166660	174176	107163	182125	176912	193232	168194	165844	186222	168410	175377	131605	178240	124500	185441	183088	183232	191738	187060
I	8440	7334	185517	189923	187497	179881	175020	176432	181886	180014	175659	174714	177776	183095	182023	192807	162261	185422	178869	187790	177011	199118		181191
J	6821	7777	182541	147923	176842	181307	144984	173839	171240	170807	201085	153226	155324	163595	173896	166427	143460	163013	187005	182523	192099	171565	176048	175561
K	9088	5995	139362	165382	189288	122422	171735	169097	183504	170557	183589	162223	182464	201276	181162	192578	159866	176887	170920	175730	174387	182205	201513	176974
L	6237	7385	169098	180279	193249	157183	177431	188954	187891	158748	182813	163380	158234	190612	154354	182129	171269	179656	165196	187993	177102	183604	188324	188375
M	8416	7852	179791	157590	186845	191670	160316	185514	159729	186260	174356	194172	179857	193563	164675	182105	160384	180735	180944	183384	172403	181086	193827	181969
N	6572	7013	188355	181830	174801	188448	158068	146464	174383	155655	182629	159018	185022	166097	146949	169020	144167	181311	182468	180284	180470	182301	190196	181519
O	6615	6695	191136	174619	192690	180425	172367	163993	187810	188432	190592	206376	183125	191166	188394	184006	171207	182571	186191	159998	192994	190081	199133	176797
P	6455	6229	176590	167856	186109	186189	179808	178926	194427	184831	168750	193999	187658	195501	201652	179000	140457	179467	181585	198382	184469	172464	191272	192355

Appendix Table 34: Fluorescence data for the 7-minute timepoint (outliers removed as highlighted).

	1	2	3	4	5	6	7	8	9	10	11	12	13	14	15	16	17	18	19	20	21	22	23	24
A	8763	8432	197304	199904	188610	199722	170461	197633	193033	194914	185795	199082	185304	192683	180443	193348	177054	150720	189467	173031	188351	164234	202957	203512
B	8734		177684	158778	189578	172941	171171	181461	191382	199916	195001	182281	167389	189006	193849	174261	109692	174170	217263	191622	155376	191759	196780	176676
C	7553	5813	190490	198955	185288	195429	174659	191968	116958	199248	121032	168178	194565	201025	145517	191312	164163	202987	206364	201231	199320	190833	209027	188912
D	6828	6699	192155	201608	203750	175415	178278	178197	23887	182926	196456	179153	193213	192703	156070	154689	118653	173105	121169	193044	185460	112022	192873	187413
E	7376	7765	166238	167328	170266	196556	161704	185178	176277	185051	172990	181517	179685	177623	148152	186838	164177	190298	172580	192574	159111	192783	184227	189658
F	6794	8311	181985	185912	205274	192917	144955	194877	194286	176118	191543	188300	187458	180448	165246		162441	167355	159505	194108	196890	177495	197050	191139
G	6311	7037	202577	200628	195936	192770	196271	190802	175144	174370	203138	177229	193900	200344	188794	168286	175843	9535	201947	172672	180684	182478	200583	198249
H	7767	6341	155016	148670	189670	177683	182641	84945	171630	166644	203416	167406	166269	196653	178030	182250	127207	190825	138634	199062	200900	199427	210104	195092
I	6963	5220	170250	186786	198474	187706	208921	181366	161555	152949	186947	177227	182685	171709	171222	190615	150792	199604	176587	168937	174001	167547	191922	180295
J	6069	6838	187417	164200	182986	193694	164543	185350	155073	159083	206744	161995	151752	176843	173212	175483	137801	174227	194319	190064	184859	188536	190791	183706
K	7160	6537	157407	182575	202659	127267	177768	150542	169364	156597	193801	176044	181197	201851	182050	197156	157256	173772	179656	188702	188542	196412	212835	194056
L	8989	8129	186463	167428	210422	159084	180965	199735	177387	134584	186960	173388	170631	196082	153891	188217	167623	183428	164452	181371	187360	194781	199332	198425
M	7461	6813	164709	150054	194455	176396	176433	198613	160941	166269	174231	195766	183047	196332	168388	181744	163411	187252	185939	187647	150632	177726	204673	194923
N	6408	5313	186973	182619	193511	190116	170838	144695	162161	151185	189137	177380	193669	177005	149409	183812	145802	180276	188144	187584	190512	186349	200625	197358
O	6578	7565	194933	164814	201827	185450	190311	166547	182867	179546	201351	157066	185556	199165	190348	190555	174748	196440	191740	179042	193937	189843	211631	196841
P	5186	5741	186506	184122	189034	186055	181234	175149	196950	185158	182277	195847	187605	209327	213279	180773	150483	183332	193458	211845	170939	182628	204942	202806

Appendix Table 35: Fluorescence data for the 15-minute timepoint (outliers removed as highlighted).

	1	2	3	4	5	6	7	8	9	10	11	12	13	14	15	16	17	18	19	20	21	22	23	24
A		6145	204232	169039	193625	171373	180045	195002	203352	188851	196765	201724	196806	194346	190470	196056	181894	174336	201928	195794	202180	186857	208377	192752
B	6005	5136	157256	153310	185539	175897	166049	188850	181765	199319	193839	168450	164825	197823	194702	171585	136085	187095	255446	187407	169331	179256	204083	197274
C	7630	5910	184879	164220	193976	180911	177482	193588	72933	177020	67209	148830	191292	192053	125635	189709	153502	204801	184214	188354	195814	186351	209365	194802
D	5025	3671	169925	185694	187764	179728	165329	179192	13714	168390	191226	176049	181053	187129	145181	143194	135139	169289	123764	196104	167023	87113	200007	191776
E	7337	5870	171113	181687	163683	199024	160087	182831	193484	144832	192740	165829	184912	181743	180966	193700	172654	173457	182295	191561	170294	200672	204546	183889
F	5033	5392	195065	186708	203248	210831	134073	194359	192158	183416	187163	177215	187511	186400	165763	247739	163358	195255	158092	190895	196484	186032	199661	
G	6521	4648	197180	189325	195921	169107	178367	191270	162715	172645	201085	151661	194664	200731	189739	142915	167561	11188	172064	176139	196827	183587	203716	200750
H	6508	3944	191923	176365	190769	169683	171441	57788	176711	175360	197899	177377	176345	174762	167835	173938	129431	177324	142116	198744	193678	186350	183601	201665
I	6893	5554	193412	189363	186117	187495	232483	181165	186662	180727	183416	164124	181456	194251	187539	194028	152971	198424	190103	190142	147341	206120	220669	207156
J	6287	8098	182764	163684	191073	193257	169985	191257	183080	188352	203597	167295	165391	178057	169497	169867	150695	176615	199283	190616	187000	187041	194874	189451
K	7150	6886	150102	186624	205052	121990	169381	160677	200047	187724	192060	170041	182403	192693	177914	197741	176779	193364	186338	182014	189017	192114	218428	199711
L	6476	6198	192358	176302	200246	163850	182138	184829	197011	155498	183498	176627	156342	197971	162620	177305	171794	167968	182009	196401	148738	159028	199997	203039
M	8534	6914	168918	160492	194410	203541	164692	194857	189003	164397	182812	199963	196053	194019	156234	169972	169194	199838	189847	180275	194069	194259	208984	198351
N	6425	7770	189406	188234	203514	192505	172878	165570	194547	171403	196649	173674	198992	159504	153010	186181	149675	167445	197712	192532	196251	197390	204805	203663
O	9374	7142	195184	170376	208488	194442	186601	151113	197274	180822	206875	168087	199732	197343	198973	187843	175330	200814	198595	195986	189399	201039	217071	194274
P	6989	5687	187210	184567	200737	193366	186501	196861	190016	193885	185237	202929	192819	201209	212680	181672	157854	187425	199540	211967	190790	174046	197104	207959

Appendix Table 36: Fluorescence data for the 30-minute timepoint (outliers removed as highlighted).

	1	2	3	4	5	6	7	8	9	10	11	12	13	14	15	16	17	18	19	20	21	22	23	24
A	5128	5540	211485	210959	180057	206511	180632	209453	202887	200124	199174	206754	192283	198142	188207	203078	184925	184033	199240	193722	201430	201035	209252	187437
B	5182	4366	191602	161064	196905	168150	168297	193721	201396	208145	187536	170582	160029	193702	196024	155153	138471	187725	215667	184591	163986	177200	202325	197523
C	3836	3576	203197	184403	191875	190245	176873	197511	75888	195362	62651	167195	194457	194272	100662	191223	162549	201583	196643	180681	187419	189534	212555	196636
D	3845	3949	191641	189054	201359	174169	166306	186041	7602	191264	180313	181746	177853	173573	158956	131868	139328	180672	128536	173237	172870	63594	202384	181521
E	4511	4006	181570	172161	161950	201982	157143	172424	194392	173357	183693	176539	182312	182265	188777	198241	175655	195979	184069	186788	186068	195338	207190	198990
F	3939	5097	200642	186388	202022	190894	115101	188885	193895	194604	188806	175489	188579	193326	149565	203700	161517	199521	159275	195367	195554	186856	200210	194647
G	4724	4911	183419	181897	198273	181310	186559	190953	201423	188192	194442	120483	194627	203934	185757	105880	181596	8179	205369	178640	200093	181294	198158	199414
H	4822	5001	188187	162765	192725	174288	179532	38868	192723	188206	183960	181240	164933	185791	155719	168608	126885	192691	143629	196016	199838	179879	204118	199228
I	5758	5805	200980	198988	182343	182793	208228	175091	185468	179748	179876	160005	189064	191845	180345	185027	134001	201215	196177	188523	162879	203621	209000	195685
J	5345	6355	180847	175125	191358	187970	173636	184316	191151	186411	208774	161456	169166	172146	166927	165947	150928	181228	198936	187240	199794	181397	185079	189891
K	6147	5766	145585	194270	199705	118578	156232	158405	197690	186551	199776	172740	176892	192016	174537	200546	166203	197571	183620	182085	192681	195240	219744	181818
L	6575	4838	188666	183725	189968	169451	179616	186827	204259	165029	179233	175242	178687	180262	161090	184319	178825	163693	173642	192207	181717	200529	190679	198866
M	5037	5690	197471	165903	197509	194771	171128	196873	175075	190583	183598	199298	184183	196438	171325	161811	172300	202365	182817	191178	194114	199133	205026	197787
N	5424	5250	197807	192063	200736	196579	155552	168380	173658	189036	190070	178940	185865	161414	157873	184129	152431	155979	196782	194655	192873	194746	206108	199798
O	4839	5128	200711	195058	206638	196616	190178	170501	211164	199625	209956	156066	204813	199209	201119	191662	181545	200300	190089	194381	188544	203433	217487	192572
P	4693	4675	193602	191562	203288	192230	185513	194566	205505	201579	179615	203228	192418	199513	207859	182764	160026	185455	195741	202837	203609	192763	205362	201267

Appendix Table 37: Fluorescence data for the 60-minute timepoint.

	1	2	3	4	5	6	7	8	9	10	11	12	13	14	15	16	17	18	19	20	21	22	23	24
A	4201	4242	206656	216776	190375	217578	194196	209202	217283	212091	213151	224431	216517	212849	206645	217638	202830	197887	208842	205098	219908	214759	228881	231227
B	3837	3918	208314	164256	200183	174557	197118	204612	205562	215827	203307	162812	168945	210318	207165	152580	150369	208001	217028	207220	182412	188760	218572	221169
C	4006	3929	193249	191154	202872	179975	197622	186300	59054	200706	56575	199777	216241	191304	79051	203695	166715	214967	198470	207651	211579	197747	226402	207798
D	3578	3747	196325	188202	202016	188033	176790	187047	4896	178327	202631	172542	197639	163881	175632	128433	145686	184126	130052	188788	174393	53323	205579	191793
E	3505	3354	185069	171474	166784	213179	165574	188785	205100	188609	205061	188666	197361	191982	191562	207829	187073	202554	196729	207043	192119	208234	220403	214507
F	3739	3821	209641	191393	211073	198414	101677	205572	196249	213562	202559	182860	200556	201940	183714	234890	182865	213553	167062	205286	201039	196274	215008	205157
G	3790	3745	200054	201430	212677	176590	197597	205611	216518	192309	219735	99242	206057	212227	198839	81634	191633	3478	215701	187132	209318	184260	215482	206460
H	3318	3527	185526	175155	192221	178664	179957	20155	195451	184291	200619	182770	178745	175933	172052	169128	131359	189391	152527	198296	192614	188986	183910	198186
I	4080	3848	202707	203704	176532	185128	201488	181300	195621	174863	204177	149159	202230	207594	206870	198545	131842	199655	202964	180849	165080	201413	225840	210162
J	3932	3965	189805	182325	191623	194429	183737	204518	202751	196802	217469	179071	178259	179601	175777	162380	158178	197950	211296	197105	205038	187342	215145	198257
K	4109	3816	133604	198121	200934	108984	149471	177668	209385	202750	204083	173573	182361	202435	169054	190029	181595	202887	194988	201033	194956	198040	223447	202054
L	3484	3421	179756	180055	197032	165125	176920	171926	203541	162606	185216	181344	170701	196949	169742	188527	184828	143990	180326	184603	173868	192081	186707	199487
M	3806	4051	200318	168745	196212	204433	187194	197593	182449	198184	194224	206208	193874	197014	189347	156596	175840	197447	197958	198287	205185	204657	219196	202523
N	3810	3985	205145	194771	204580	198938	154034	166581	177057	192748	199754	184746	202061	162283	162967	193077	147278	169211	208895	203089	190509	191151	213094	209497
O	3613	3781	200126	195321	206983	201263	188259	160600	208260	207268	207535	148595	210341	200960	206690	195804	186352	200046	201960	197929	206351	200344	219265	197551
P	3728	3432	192373	186553	195974	185376	185707	191168	202150	193452	177732	199903	195598	190699	201962	179565	163392	178817	192412	196388	193492	189862	204539	208904

Appendix Table 38: Fluorescence data for the 120-minute timepoint .

	1	2	3	4	5	6	7	8	9	10	11	12	13	14	15	16	17	18	19	20	21	22	23	24
A	4851	5400	206975	205988	190636	198927	189034	194928	193813	199066	206667	215360	210716	208518	196891	205386	198655	186031	190338	195754	209016	195552	217417	196467
B	4690	4933	201033	157283	200333	160711	187193	199020	206908	205461	180624	173229	154610	201296	200236	117942	127658	201091	208122	201600	149763	185729	210043	201089
C	5075	4821	201042	174116	188373	179463	174139	193386	59336	203313	59791	176713	204892	183533	38704	203823	162182	204669	215382	169444	195018	198759	219490	202085
D	4587	4960	187601	184834	187457	167148	174390	177365	5510	180715	190381	181741	167536	180021	149463	104586	116973	173442	132174	172275	180543	32754	198499	185056
E	5122	5028	176886	143533	147496	209868	157376	185669	200113	185433	207293	175343	201973	175751	176524	203694	186883	192017	198278	198295	188341	194987	213507	200959
F	4903	4800	203000	190713	197471	192187	53152	189791	185677	206769	191800	181924	187424	196899	185108	228401	171524	206891	151016	201265	188898	184854	203541	197300
G	4648	4792	196846	206541	189522	155218	188680	202282	209620	191544	219071	47176	205758	206209	185123	36899	182311	4062	206545	178934	200006	164137	202599	198226
H	4714	4532	172318	174339	173198	176660	181319	9836	193937	171360	202011	187944	159578	171962	158825	161767	108757	177966	123418	186749	188354	185129	188969	192373
I	4550	4333	196305	198295	157150	185945	195650	169716	192059	168573	194077	133000	199537	194180	197768	199819	85639	195753	196570	184946	146205	202524	215017	200761
J	4818	4704	183687	161341	202776	180419	171886	187894	189771	184305	209095	169364	169952	147295	170401	133226	140014	176698	197813	179763	187827	172710	203774	199712
K	5062	4527	99415	184603	185740	75113	137324	150750	204914	196644	192855	150254	152119	196824	135769	187427	157999	186044	194410	188601	185378	181484	215213	196200
L	4408	4401	163549	160399	189584	150998	171401	167662	192282	158897	162133	171586	161423	184681	147886	173869	174595	111800	160458	170194	165747	170105	185079	181081
M	4722	4763	185641	182595	192756	192892	184936	196361	179640	183982	196042	194426	188897	188985	182549	138643	171858	203286	200767	189167	187987	192301	199605	192584
N	4806	4928	198018	181633	206281	182098	171085	163454	172330	186158	193875	173586	185032	149746	147766	198836	110457	149726	190671	192331	171225	189356	200300	199980
O	4707	4409	184594	179311	200520	193635	147475	152588	211373	196100	196597	152345	207937	195025	197641	187005	173785	197921	184510	181796	174283	191219	208280	191398
P	4342	4522	187718	175877	194680	177457	185208	182464	198505	192382	164650	198164	189977	184655	196612	173190	148460	164801	178173	189368	184068	182057	188784	190704

Appendix Table 39: Fluorescence data for the 240-minute timepoint.

	1	2	3	4	5	6	7	8	9	10	11	12	13	14	15	16	17	18	19	20	21	22	23	24
A		4810	199846	192954	173590	194534	171844	206575	177942	185195	191824	211276	194886	202033	183013	197549	187124	170777	195509	167611	197123	178985	213228	185868
B	4344	4024	165988	141164	182792	141422	157647	185309	207497	195204	167794	159154	137959	193794	187334	92426	118831	189055	199697	180894	136507	169089	191256	189551
C	4382	3926	186072	177205	173613	192040	170932	202809	59051	187473	55469	154575	187033	194831	25318	188764	146912	189567	208965	195602	195329	184321	195548	194830
D	4421	4445	195701	171823	189553	176380	153168	171246	6765	165079	200921	155735	163960	191133	134317	87473	101653	163493	144442	186031	165847	31399	200205	179786
E	4264	3270	161679	113540	145809	200246	129377	168135	189382	160908	182510	174401	177483	161417	165980	190649	174285	173057	180744	178213	169686	178062	207713	194108
F	4589	5065	194059	184940	194621	193123	35081	185121	182856	195376	187615	150411	177786	190948	164731	228642	163807	193876	127008	200648	179533	169191	197376	187761
G	5059	4905	188728	198229	197485	131258	185416	191853	210858	177605	207986	27303	185443	202677	172467	25294	169161	5159	202381	163742	193134	146948	202110	193481
H	5596	4063	174839	158693	186405	161945	182058	8923	184555	159699	197127	193561	145945	181454	147537	150409	95917	179985	109385	191345	196351	179767	172411	195219
I	4280	5997	167809	173146	123837	176522	186177	150475	177995	168354	176055	118268	186238	189966	162728	185760	67008	192886	189416	157820	127760	179409	212181	193764
J	5351	5009	169696	152004	198189	160998	168505	189366	180734	172196	207806	157415	147440	133135	162168	104708	139848	176878	196017	187191	184179	158620	205232	187794
K	5639	4884	71694	179717	171254	55011	123587	160551	201904	182189	202120	129492	134453	189974	109997	186928	135252	181050	173382	184726	178951	177008	214144	199970
L	3859	4776	143640	153788	193571	149916	165100	155470	177080	158731	168836	159065	163198	197798	134344	177287	172288	92771	142364	167369	172400	180527	192804	188832
M	4496	4243	185630	158238	180493	178261	173535	193067	175002	180739	185051	189913	182226	188097	169469	121864	169922	202605	190855	178392	189628	195858	205537	183998
N	4239	4268	198866	190426	192589	183407	157027	155933	175781	172944	193851	162918	171159	142895	135759	186865	119249	137974	196227	190652	183042	180196	193881	189443
O	6065	5184	169871	169769	190130	194836	168754	134867	203291	199421	190529	140116	203958	195459	196186	185921	169135	193619	197329	157496	188386	187214	209463	184515
P	5062	5228	183367	173187	191581	170862	183335	188066	196125	190937	146894	193365	188812	186951	203287	167693	137611	160175	176242	195854	194976	185034	195822	188842

Appendix Table 40: Fluorescence data for the 300-minute timepoint (outliers removed as highlighted).

	1	2	3	4	5	6	7	8	9	10	11	12	13	14	15	16	17	18	19	20	21	22	23	24
A	7327	7851	200014	202837	160120	203468	182692	168918	154807	149577	157291	209759	172228	207291	125968	165183	160746	111074	195030	157132	210819	146619	228117	214114
B	7467	7038	173305	65622	163111	134599	169352	155707	217730	154308	94129	151984	78381	169650	157213	15327	33519	154856	215465	178668	27147	160769	222802	212107
C	7103	6959	189210	121265	168776	158356	140516	187470	81833	144449	74764	86731	167343	179567	5575	181526	123814	194335	202051	165943	181432	174612	221191	207680
D	6410	8396	189465	137254	153090	139603	122226	169185	8617	106038	167503	129632	133199	146039	77171	17699	31143	108513	140958	150614	160936	31358	208336	192266
E	6999	7155	127028	24338	98281	185875	65649	133111	189332	84641	155002	116697	144740	88738	127563	176258	160142	115943	168765	150564	153879	204734	223417	211786
F	7687	7760	176121	158612	176389	201595	6546	143027	176334	181481	181355	114785	152592	160465	162376	197713	163976	175491	37021	190486	160270	141482	212862	205987
G	7750	7560	154901	175057	184384	35947	202510	182357	197690	139696	188294	4842	173390	194901	119175	12334	149106	12950	198852	131912	194396	77622	207465	201012
H	7416	7142	130025	155814	172720	112845	177641	4693	145058	89486	194334	174606	61855	158160	56916	74421	9700	134123	6044	162789	175775	172429	185853	194927
I	7440	6278	162142	185854	34309	152246	215849	74773	169180	143700	186154	14330	179072	154440	160680	174629	7421	172344	167827	86798	40062	202030	227787	218705
J	7610	8172	194807	103661	187579	119408	150036	197552	180383	147847	221760	144525	110072	60743	154105	24676	89411	162514	197042	191934	162199	135684	219139	196339
K	7586	7310	7818	180860	126600	7716	116254	141121	196441	201696	187620	33774	40617	190136	16700	176250	85112	164680	154194	186926	175349	149515	228350	215914
L	6746	7931	75652	154526	159092	90869	150486	78966	194734	107233	139086	133508	106855	192247	57196	162877	173264	18256	106774	131514	157244	162440	174471	194530
M	7787	8850	175920	165732	136600	167315	196578	191681	176406	135351	193934	150359	183181	155620	172552	68508	169378	191406	193104	176486	177719	167715	224840	204430
N	9696	9555	203861	174259	216750	171414	138529	119486	150949	137430	213884	174802	184225	121987	93924	200472	17540	119954	196658	198725	164822	176814	200568	205708
O	8537	8593	139841	131619	172946	197909	115162	30686	207590	200927	199713	141399	227229	201496	190930	190002	140793	196749	210235	159211	174298	191178	212905	197543
P	8353	8199	163431	136445	175317	133128	173614	161642	183362	177824	63115	196266	175736	163316	193431	132585	59582	91833	130016	185834	186168	161477	192714	193606

Appendix Table 41: Fluorescence data for the 1380-minute timepoint.

	1	2	3	4	5	6	7	8	9	10	11	12	13	14	15	16	17	18	19	20	21	22	23	24
A	6935		175836	203600	148481	200175	150662	167719	128132	130845	138417	186568	150526	187107	112221	160094	162141	91598	191355	150499	180156	119309	209097	200878
B	6577	6642	160744	54998	147395	123709	156807	150640	201329	143261	81411	163518	65135	164609	134955	11599	22539	164725	202034	174011	14412	151116	202376	204236
C	6829	6565	184020	112454	172619	150988	138404	179984	76658	135211	70523	80632	158932	155751	4597	144795	126342	160650	195829	152900	154356	156124	215816	174331
D	6177	6993	185115	116181	115958	139116	117193	159168	8577	99377	167511	118806	139880	149147	65727	15037	20448	105202	134075	141336	148034	29079	188281	179917
E	6822	7682	113641	17865	95986	196615	54587	120993	151964	71872	148609	99832	134710	72775	112303	156107	145368	99757	168460	161328	157016	174803	214182	196277
F	6510	6680	162930	175322	170319	186050	5740	133831	152027	164740	155026	102680	140577	158781	150020	169362	154621	167760	26391	187425	146749	123041	193768	191842
G	6669	5552	137639	169571	176541	28277	173939	149333	202604	124412	187615	4442	141126	176550	107570	11340	130867	11648	198791	128798	169770	62506	196709	176333
H	6748	6225	117561	154267	158679	107066	153494	4163	136821	81707	164659	155090	51946	182767	45342	63936	4428	130031	4341	169791	179173	153472	168923	167163
I	6924	6453	144295	170417	26153	147484	187092	60890	156098	133734	162949	9549	148759	128627	128991	160397	5484	172941	143459	74603	28895	164873	205571	180999
J	6752	6811	170341	88686	189812	94706	155534	173737	147168	148674	194314	120562	89943	48615	132129	18852	71689	137321	182233	171461	135029	121209	180365	195823
K	6731	7226	6179	159241	118782	6664	107875	114394	188950	185840	166915	23413	31177	187526	10961	147167	73083	136982	141915	152940	163242	131876	202810	180848
L	5518	6660	60014	131244	155313	74067	137442	59313	163268	95723	108642	125454	92072	153786	39576	144206	145923	14417	82558	107943	165055	161507	180982	169563
M	5402	6161	148658	191103	134907	140992	160650	176421	172728	112289	165818	122076	157536	139096	163313	56720	158970	161963	156108	157787	171051	151872	204599	184885
N	6931	6384	179550	174397	186771	151334	122379	112021	142407	117781	187291	150131	155068	114651	81356	180144	13916	107255	181038	174532	146047	153811	190215	184456
O	6451	5576	95492	106225	142834	161961	118787	17314	171596	164368	152431	133474	199605	181913	174364	172276	123358	160302	187864	135552	154961	179196	204280	186534
P	6122	6279	145456	125164	154373	116062	165869	152447	156363	170381	49704	182976	143659	150847	182838	118264	46619	77408	115879	175550	170224	152531	171872	183921

Appendix Table 42: Fluorescence data for the 1500-minute timepoint (outliers removed as highlighted).

A.2.2 FA data

	1	2	3	4	5	6	7	8	9	10	11	12	13	14	15	16	17	18	19	20	21	22	23	24
A	31.7	30.6	82.1	84.2	98.5	80.3	74.7	85.4	86.5	90	83.5	79.6	83.9	75.5	89.7	91.7	79.9	70.2	80.4	69.9	86.5	75.6	81.7	79.8
B	29.4	30.9	80.5	68.9	87.7	75.5	78.8	80.8	80.2	84.1	105.3	80	63.2	80.9	80.6	158.6	53.6	69.4	79.2	87.8	188.4	84	77.8	69.3
C	28.7	29.3	79.1	87.6	75	73.6	86.1	81.4	98.6	83.1	102.2	90.1	82.5	85	95.2	77.2	85	78.9	78.8	79.1	81.8	77	74.2	73.8
D	29.6	29	81.7	75.9	83	87.2	90.3	85	138	95.9	78.3	73.8	87.7	81	60.8	136.5	56	80.2	95.6	77.9	82.9	52	76.3	76.6
E	31.7	31.1	85.3	122.7	94.4	75.4	98.1	75.5	80.2	68.5	82.4	75.6	94.3	72.4	96.9	82	77.3	91.2	79.3	80.5	93.9	78.6	78.9	72.9
F	31.3	30.1	82.1	83	79.1	73.3	119.5	88.8	83.6	76.9	77.9	77.2	80.8	82.2	81.6	97.1	84.4	78.2	60.5	72.8	83	80.1	78.8	75.7
G	28.2	30.3	87	77.7	73.1	89.9	83.8	82.4	79.1	84.9	80.6	102.5	92	72.6	68.2	86.9	84.8	158.7	74.6	84.5	81.8	192.7	80.6	75.7
H	32.1	31.8	88.3	80.5	70.8	77	84.8	101.6	78.2	99.6	78.9	76.5	67.8	80.1	71.2	98.3	78	76.5	82.8	77.4	81	73.1	76.3	77.2
I	29.4	28.3	83.8	78.3	87.8	78.8	85.9	106.3	72.7	78.9	73.7	77.7	75.5	85.3	77.3	75.6	145.3	80.1	78.8	103.1	192.2	81.3	68.7	73.6
J	31.8	32.5	79	67.7	74.2	100.5	73.6	72.5	77.8	86.1	77.8	81.7	57.4	120.6	71.6	122.4	69.2	80.8	81.8	75.9	78.6	82.5	73.4	75.2
K	32.5	34.2	123.6	77.7	89.7	121.8	98.6	77.3	78.9	76.6	78.2	70.2	77.5	73.5	113.4	76.3	91.7	77.4	78.3	194.4	193.6	84.9	71.8	74
L	32.5	32.7	112.9	79	72.8	85.7	85.6	99.6	79.9	66.4	68.7	83.9	65.1	77.1	57.3	78.1	78.4	122.7	77.4	77.7	79.3	80		75.5
M	30.1	29.1	82.8	80	83.2	84.5	84.8	76.1	87	77.3	69.8	85.5	80.6	82	80.1	111	87.2	72.7	71.9	73.7	77.6	83.5	72.7	72.6
N	32.3	31.4	72.9	74.1	76	72.3	89.5	100.4	87.7	78.3	78.2	91.3	77.7	76.1	59.3	81.2	125.4	82.1	73	75.2	66.3	73.2	72.1	74.1
O	30.7	30.8	101.5	94.1	92.6	82.1	86.8	66	80.8	86	84.4	196.1	81.7	78.6	77.4	78.8	74	76.2	75.7	73.2	75.9	80.2		76.2
P	30.8	33.9	80.2	75.4	78.8	95.6	82.8	87.5	79.6	79.8	75.4	85.5	74.6	82.8	74.6	84.6	59.4	82.7	80.5	73.4	75.4	66.4	69.7	

Appendix Table 43: Fluorescence data from dilution 1 (2.5 μM) plate (outliers removed as highlighted).

	1	2	3	4	5	6	7	8	9	10	11	12	13	14	15	16	17	18	19	20	21	22	23	24
A	23.8	22.8	96.8	89.6	107.4	95	92.1	92.1	107.9	91	96.9	94.6	89	78.2	115.6	91.2	95	75.3	89.1	79	90.3	85.5	93.7	84.6
B	23.9	25.8	82.9	83.6	95.2	84.6	94.8	82.5	86.4	93.5	120.2	79.7	79.1	86.6	97.5	156.1	67.8	74	87.5	90.4	79.4	87.4	87.9	91.5
C	23.8	25.9	87.6	92.9	93.8	83.9	98	93.4	107.3	98.1	105.3	105.3	93.1	94.9	98.6	90.3	96	85	82	83.7	85.6	91.2	81.7	84.8
D	24.6	24.5	83.5	92.5	88.4	87.4	105.8	88.5	150	109.3	95.4	79.7	92.5	88.4	67.2	147.8	62.2	88.1	94.9	93.3	95.9	49.2	81.1	95.7
E	22.9	23.1	101.1	138.3	102.3	84.7	106.3	81.3	95.1	72.3	93.8	79.9	100.4	85	97.7	91.4	89.1	99.4	90.1	92	93	83.3	84.5	85.5
F	23.5	23.4	90.5	87.5	79.2	86.9	129.5	112.5	92.1	86.9	81.2	84.8	89.8	89.1	90.5	114.7	89.4	90.7	65	85	92.3	87.3	88.7	90.7
G	23.2	24.2	85.4	87.5	75.5	93.8	80.7	88.6	84.9	92.1	81.4	109.6	94.5	84.5	65.8	100.1	92.5	165.7	76.5	94.2	96	111.9	77.5	84.7
H	23.8	24.4	94.9	85.2	80.9	86.6	85.3	106.8	89.2	129.4	88.7	86.4	75.7	79.4	86.4	111.8	87	83.8	94.4	81.4	87.9	86.1	83.5	83
I	26.4	27.1	92.8	84.7	92.8	86.7	90.9	117.4	79.1	82.9	75.9	85.8	80.5	96.6	84.8	82.2	151.6	83.8	82.7	114	139.8	89.1	78.5	81.2
J	25.8	24.8	86	77.9	83.9	105.5	81.7	79	80	90.1	84.5	88	60.8	129.1	73.7	136.2	80.9	87.1	86.5	81.6	96.8	85.7	83.9	85.3
K	26	27.2	143.9	83.5	101.8	132.2	108.7	86	84	84.7	83.3	77.5	90	80.9	130	83.7	104.6	90.5	86.5	78.6	83.1	93	82.1	85.2
L	24.4	24.5	127.3	91.5	83.1	107.7	97.5	113.5	86.6	74.5	74	88.4	73.3	85.4	61.6	81.7	85.8	138.7	89.9	91.6	87.1	87.4	86.8	82.7
M	25.1	27.1	88.8	86.8	82.6	96.1	98.5	84.7	85.3	92.3	87	96.2	89.7	101.4	88	117.1	90.2	80.8	84.9	85.4	87	98.6	92.4	87.9
N	24	25.7	85.1	86	85.4	88.2	99.2	117.1	90.9	86.4	79.5	94.4	84.2	80.5	63.7	84.3	125.5	97.1	79.8	89.1	70.5	95.2	80.2	84.8
O	23.6	23.8	103.2	106.5	92.7	82.9	102.3	80.2	101	91.8	87.5	84.5	81.9	86.5	178.2	81.4	80.8	89.5	85.5	88.1	86.6	89	83.1	88.8
P	23.5	26.6	87	85.1	82.7	106.6	86.3	92.3	83	93.9	81.5	86.4	79.5	90.9	84.6	92.9	70.9	98.6	100.2	83.5	88.6	76.4	83.9	79.5

Appendix Table 44: Fluorescence data from dilution 2 (1.25 μM) plate.

	1	2	3	4	5	6	7	8	9	10	11	12	13	14	15	16	17	18	19	20	21	22	23	24
A	23.4	26.3	124.1	116.2	131.6	115.3	116	120.5	129	119.8	136	116.4	134.9	118.1	130.9	116.6	118.4	90.1	114.8	97.7	106.9	96.5	98.3	100.6
B	25.8	24.3	123.9	122.7	122.6	118.1	135.3	139.7	126.7	129	148.1	121.7	103.7	111.7	124.3	177.2	85.2	106.7	103.9	104.7	96.3	102.9	100.5	113.8
C	23.6	22	111.7	129.3	119.6	114.9	126.3	121.9	143.9	124.4	136.2	128.7	117.2	115.6	126.7	105.7	116.3	111.4	105.1	103.6	109.2	104.5	100.8	111
D	25.1	23.4	110.3	113.9	119.8	122.8	128.7	119.6	162.5	136.3	112.5	104.3	116.4	111.1	81.6	159.4	81.3	108.2	117.7	108.9	105.4	55.2	108.8	108.2
E	22.1	25.8	124.2	157.4	130.6	103.3	136.7	108.1	110	94.5	109.3	102.7	123.4	106	124.9	104.3	114.3	130.3	105.5	109.7	134.7	100.5	101.8	113.9
F	24.7	24.3	117.9	115.5	107.6	111.2	157.1	119.6	115	108	108.9	108.8	117.5	112.1	106.8	126	108.7	108.4	95.9	103.5	110.1	118.3	106.9	113.7
G	22.4	23	114.4	111.2	107.9	122.9	110.2	113.2	105.6	116.7	106.8	131.1	109.4	107.5	84.6	130	119.7	166.9	101.2	118.2	107.2	124.4	97.7	105.8
H	25.7	23.1	124.9	112.3	109.2	113.5	115.9	123.3	114.8	145.1	111.9	110.8	100.6	111.7	106	132.4	111.8	108.1	118.3	105.6	106.9	118.5	96.7	106.4
I	22.6	23.4	113.7	113.1	119.2	111.4	116.9	138.1	116.7	109.6	110.8	115.5	110.2	122.8	111.2	112.7	169.9	117	113.6	139.1	166.7	115.7	107	109.9
J	27.9	25.2	115.7	109.4	108.5	130.8	101.1	109.3	111.4	116.1	102.5	116	83.2	151	103.5	152.5	120.6	116.7	108.8	103.8	104.9	118.5	104.5	108.3
K	26	24.6	158.9	110	120.2	154.6	136.7	112.3	112.7	118	108	119.2	100.7	116.7	144.5	105.1	127.1	111.7	112.2	106.1	108	118.7	100.1	106
L	24.6	27.6	143.9	119.8	111.5	123.3	125.7	132.5	113.2	99.6	103.3	115.2	109.2	107.5	85.5	111.2	113	152.4	117.2	108.6	107.4	113.3	108.1	106.6
M	24.4	26.3	108.3	109.7	115.4	119.7	116.3	107.1	112.7	112.3	110	120.4	113.3	123.5	113.3	141.1	116.2	98.9	107.7	110.5	105.4	114.1	102.2	105.4
N	26.1	25.4	109.1	114.4	102.2	117.5	122	146.7	115.5	115	107.9	121.1	101.6	110.8	84.8	115.9	144.1	107.7	103	112.4	93.1	118.1	103.8	110.8
O	23.6	22.9	129.7	128.2	116.4	106.8	127.3	101.6	110.4	118.6	129.7	117.2	105.5	112.6	192	115.1	101.2	99.1	114.3	107.6	103.2	110.4	101.3	106.6
P	26.8	22	118.2	113.1	110.8	132.5	112.2	117.2	105.1	109.6	110.7	111	106.3	112.9	109.6	119.3	98.8	122.8	116	105.1	108.1	103.5	103	111.5

Appendix Table 45: Fluorescence data from dilution 3 (0.63 μM) plate.

	1	2	3	4	5	6	7	8	9	10	11	12	13	14	15	16	17	18	19	20	21	22	23	24
A	25.8	24.7	139.9	134.2	148.1	126.7	139.9	147.8	152.3	144.3	159.3	137.8	147.8	142.5	154.1	143.3	138.6	115.3	129.5	127.1	138	127.9	141.6	130
B	28.6	25.6	144.2	161.4	146.2	146.6	167.2	159.7	150.1	162.1	165.7	125.8	127.2	136.5	150.3	179	115.6	115.7	117.2	130.5	108.6	131.4	141.6	130.2
C	28.2	26.6	150.1	156	152.6	153.4	153.2	154.7	163.6	149.8	154	147.5	139.6	133.1	156.6	137.9	138.1	127.3	131.9	133.6	133	129.4	124.2	137.6
D	25.7	25.2	126	140	152.6	149.7	154.5	133.8	170.6	149.7	135.2	130.4	143.7	124.7	103.2	171	98.5	135.6	140.6	135.1	134.7	80.6	130.6	131.5
E	26	25	151.8	176.5	150	126.7	162.3	145.1	137.4	126.9	128.4	117	141.6	141.4	146.2	194.2	135.9	156.3	129	142.8	134.9	123.5	123.8	135.2
F	24	25.1	141.8	135.3	135.4	128.2	171.2	149.7	147.6	106.2	123.9	138.7	137.8	141.3	131.4	150.4	127.6	134.3	114	126.4	132.7	139.1	127.4	136.5
G	27.7	24	135.4	137.7	131.6	144.4	133.6	134.9	127.1	146.7	134.2	148.2	133.8	123.6	122.5	142.4	151.6	184.6	127.4	149.1	132.7	138	126	122.7
H	24.4	26.6	141.5	148.6	135.4	139	136.7	151.8	141.4	163.4	131.4	135.3	123.5	136.9	119.5	169.8	137.5	131.9	135.4	131.2	132.4	129.5	129.3	132.8
I	26.7	25.8	138.9	126.9	142.2	136.2	121.6	163.3	137.9	142.5	127.6	124.7	143.8	168.5	132.6	135.7	176.1	136.4	132.7	160.3	178.5	131.5	119.4	126.6
J	27.3	27.5	130.6	144.8	138.2	140	131	126.4	131.3	149.6	125.2	134.3	135.6	165.7	121.3	169	136.6	142.4	135.6	137	148.3	138.7	128.5	140.4
K	27.7	22.2	165.9	132.2	148.4	163.1	160.1	137.3	131.5	127.7	130.6	134.9	128	126.3	165.7	139.8	149	131.7	137.6	127.3	128.1	144.8	129.2	124
L	26.8	24.7	170.4	132.9	132.8	143.4	150.6	155.4	140.7	120.5	125.6	134.2	121.8	127.3	112.6	131.5	136.4	163	140.1	142.6	128.5	129.5	126.1	133.9
M	24.9	30.1	133.9	124.7	128.1	142.9	149	131.9	123.9	141.9	126.7	150.5	140.7	137.8	125.5	163.7	133.9	122.7	132.2	121.7	131.6	115.9	128.3	132.4
N	26.2	24.9	126.9	138.2	127.5	133.7	144.3	150.2	126.4	143.6	118.1	137.2	131.4	128.4	114.8	126.1	164.5	131.8	132.6	127.6	123.4	135.2	126.8	137.6
O	27.6	22.9	150.3	147.9	146.7	134.1	146.9	142.5	132.1	135.1	137.7	129.3	121.5	123.9	202.6	125.6	117.2	119.7	125.3	123.3	126.2	142.7	128.4	129.3
P	25.9	22.6	143.9	137.1	133.6	144	144.3	142.9	126.7	129.6	145.3	127	129.7	134.3	134.8	147.6	130.7	141.1	140.6	130.2	139.1	127.3	129.7	132.8

Appendix Table 46: Fluorescence data from dilution 4 (0.31 μM) plate.

	1	2	3	4	5	6	7	8	9	10	11	12	13	14	15	16	17	18	19	20	21	22	23	24
A	27.1		155	161.7	165.7	160.2	153.6	161.6	170.3	166.8	161.6	155.9	165.7	160.5	169.2	152.9	147.5	154.4	150	158.2	159.5	151.7	139	144.2
B	27	24.5	168.6	170.7	155.9	150.9	166.2	161	157.5	172	176.9	155.1	130	149	153.7	187.1	143.1	136.1	129.1	158.2	159.7	155	153.5	152.7
C	23.5	25.8	147.2	161.6	155.3	157.2	164.3	151.7	164.8	169.4	164.4	172.3	148.5	160.5	155.2	153.8	145.9	161.5	148.9	153.3	153.3	147.7	141.5	139.9
D	26.3	23.3	143.6	148.9	161.2	157.8	162.2	160	173.4	173.8	153.8	149.2	153.8	159.4	131.6	179.4	134.1	152.4	157.5	148	156.2	94	146.4	140.3
E	24.4	24.6	162.6	186.8	167.2	148.1	170.4	155.4	154.2	145.3	167.9	145.1	157.3	151.4	163.8	148.6	149.4	163.6	154	160.8	163	146.5	134.9	139.9
F	23.5	26.2	150.8	153.8	158.5	143.9	180.9	192	152	149.6	150.3	162.6	154.3	153.6	148.3	169.9	151.2	163.6	148.8	158.8	155.4	160.3	141.7	150.4
G	26.5	25.5	151.1	160.2	141.4	161.6	154.7	155	145.3	155.3	160.4	163.4	151.6	161.3	142.4	156.9	162.2	186.2	156.8	163.4	153.1	163.4	147.4	147.7
H	27.6	27	157.7	145.5	153.5	158.9	148.4	164	160.3	171	155.6	151.2	155.7	150.4	155.5	170.3	167.8	151.8	172.4	155.3	148.3	150.7	146.2	150.8
I	25.7	26.4	157.7	148.4	152.4	156.2	154.9	176.2	146.5	158	145.9	161.7	159.4	161.3	153.4	143	182.7	158.1	152.8	172.6	183.3	154.9	150.8	151.6
J	23.5	26.3	153.6	149.2	143.2	173.7	150.1	144.2	149.3	161.3	144.5	147.6	149.1	175.6	142.5	177.3	153	160.5	139.8	151.9	146.4	167.7	151.9	145.9
K	26.9	24.6	178.8	157.2	161.9	180.3	165.6	155.3	147	149	154.1	166.3	144.8	150.5	175.1	154.9	159.5	157.7	154.1	143.6	157.1	168.1	149.1	146.9
L	28.7	23.2	175.2	165.2	148.2	168.5	161.4	161.5	155.2	154.3	141.4	154	149.5	155	146.2	149.8	148.4	177	164.2	152.8	156	153.6	146.4	153.4
M	26.4	26	153.2	144.6	155.5	150.3	153.3	157.4	161.9	151.6	152.7	164.7	151.8	156.5	150.7	171.2	153.7	146.7	158.7	144.5	155	144.6	152	144.1
N	26	25.7	153.3	142.5	148.8	154.6	158	172.5	160	150.8	161.6	157.7	151	151.4	138.2	152.2	177.1	159.6	150.3	156.4	160.6	152.6	145.2	151.9
O	27.8	27.4	164.3	158	159.5	152.3	160.1	148.2	152.9	148.6	151	165	149	137.5	193	141.4	140.5	144.3	158.2	155.6	149.3	155.5	149.6	147.6
P	26.1	25.8	158.6	154.6	155	166.5	159.1	157.3	155.2	151.2	165.4	150.1	151	149.4	150.2	149.4	146.5	159.7	165.3	148.7	146.3	164.8	153.5	

Appendix Table 47: Fluorescence data from dilution 5 (0.16 μM) plate (outliers removed as highlighted).

	1	2	3	4	5	6	7	8	9	10	11	12	13	14	15	16	17	18	19	20	21	22	23	24
A	29.4	31.7	171.7	166	180.3	175.8	173.4	168.4	177.1	166.7	182.8	167.9	168.4	164.3	173.4	166.7	165.9	162.4	168.2	162.9	162.7	165.2	161.3	166.9
B	30.8	30.7	183.3	181	175.6	161.2	177.8	164.9	171.1	169.4	186.4	165	165.2	166.9	168.2	191.2	143.2	162.1	153.3	164.5	173.2	165.7	163.8	160.8
C	29.3	28	165.5	176.4	173.9	175	174.7	162.4	181.7	174.2	179.9	176	177.4	171.8	174.1	167.2	175.7	167.9	160.2	160.9	158.6	168.8	171.3	160.2
D	32.7	28.9	167.1	178.3	179.2	174.1	172.8	175.3	186.8	181.5	180.3	159.9	168.2	173.6	155.4	188.3	159.2	171.1	170.3	164.1	162.7	135.2	162.5	154.8
E	28.6	27.9	178	185.4	170.2	167.8	183.1	173.6	168.8	159.5	178.7	182.6	173.6	164.1	170.3	164.9	170.1	178.3	167.4	169	171.7	170.2	160.6	161.6
F	29.3	28.3	170	170.2	168.8	174.5	184.8	174.4	170.3	170.2	174.3	170.2	173.2	170.9	168.7	184.8	173.2	162.4	162.3	166.4	168	171.6	164.1	166.6
G	27.1	30.7	171	167	166.3	176.4	171.7	174.4	163.2	175.5	158.2	177.3	171.7	163.9	154.2	179.9	174.4	192.3	166.1	172.8	166.3	180.9	167.2	157.5
H	31.3	28.2	180.4	172	172.6	172.2	171	173.5	168.1	181.4	167.8	159.2	171	163.2	170.1	185.6	175.2	176.3	181	161.9	163.5	171.7	162.6	164.8
I	30.7	30.2	170.9	165.7	169.2	172.1	164.6	183.9	146.3	169.5	166.6	174.7	167.9	170.4	165.9	162.1	188.4	166	167.1	184.9	182.6	164.9	160.5	165.5
J	31	27.1	168.9	171.1	163.6	184.7	173.1	168.2	171.2	162.5	164.1	170.8	149.8	185.2	164.2	184	176.9	173.1	163	163.6	170.1	174.8	160.7	163
K	27.5	29.2	187.4	165.9	178.2	186.1	179	170.8	167.3	167.6	169.2	181.7	169.9	166.3	187.5	159.9	174.7	177.3	169.9	161.3	164.6	176	165.3	167.5
L	29.2	30.7	184.7	174.9	168.1	180.4	174.6	179.1	161.2	175.8	164.4	175	169.8	169.1	172.5	168.9	171.7	186.1	175.3	170.2	162.5	160	158.5	163
M	30.4	26	158.3	172.5	155.6	171.2	164.6	166.4	161.4	163.7	171.9	174	161.4	171.6	164.7	184.1	170.2	158.5	171	166.6	171.7	172.6	160.9	163
N	30.8	28.7	170.1	169.8	164	165.4	170.1	180.5	173.1	162.1	159.6	169	151.7	165.1	157.4	169.8	182.7	171	170.4	164.7	167.9	173.1	167.5	169.8
O	28.5	30.2	170.9	174.7	172.8	170.8	168.8	176.6	163	165.3	170.5	175.9	165.4	152.1	198.3	164.2	171.9	162.8	162.1	166.5	161.3	164.1	154.8	165.1
P	26.3	31.1	167.3	175	176.4	176.7	169.7	169.1	165.1	158.3	169	160.8	171.4	166.4	167.2	177.1	168.2	175.6	170.3	169.6	164.5	166.6	163	162.3

Appendix Table 48: Fluorescence data from dilution 6 (0.08 μM) plate.

	1	2	3	4	5	6	7	8	9	10	11	12	13	14	15	16	17	18	19	20	21	22	23	24
A	26	27.4	144.6	133.3	161.5	155	161.8	143.9	157.6	146.8	163.3	151.1	160.6	147.1	161.7	152.6	163.1	156.7	158.1	154	166	169.5	147.6	163.3
B	26	26.3	145.9	155.7	136.9	137.4	152.9	140.1	152.6	147.3	173	150.7	141.1	143.5	147.2	190	142.4	150.5	153.2	160.2	162.3	158.4	161.3	156
C	22.4	28.7	135.9	147	141.1	158.3	155.2	132.6	160.9	158.1	170	162.5	149.4	150.3	169.2	164	168.8	157.4	152.6	153.4	168.2	162.3	159.4	156.3
D	23.9	24.9	137.7	144.3	152.3	146.2	158.5	159.6	179.1	168.4	155.2	141.3	151.6	157.7	158.1	181.2	141.6	160.8	161.4	155.2	154.5	119	159.2	147.4
E	24	23.4	139.6	177.3	153.8	142.8	173	151.4	149.4	135.8	153.4	161.7	163.8	145.7	158.1	162.9	158.8	173.7	162	160.1	165.2	160	160.1	161.2
F	21.8	24.5	135	136.2	140.4	148.9	175.5	159	150.5	145.6	156.4	157.3	157.4	155.4	161.9	170.7	161.3	160.5	166.9	155.5	166.8	166	151.9	166.3
G	26	24.3	138.1	142.7	140	148.6	154.7	156.3	146.6	157.3	139.7	173.4	163	154.9	140.9	168.7	166.9	189.2	163.6	167.7	169.2	177.1	153.7	152.4
H	24.6	25.4	157.8	146.5	153	149.3	153	163.5	152.8	174.2	160.2	140.3	156.8	153.6	157.7	177.9	169.4	163.8	179.8	150.4	161.3	170.5	150.6	167.2
I	25.6	22.5	151.7	137.7	152.1	148.7	142	179.4	141.8	159.9	156.6	163.9	152.5	165.4	153.5	153.9	186	167.3	159.8	177.8	183.6	161.3	157.8	157
J	27.6	25	137.6	144.4	144.6	165.5	155.2	155.8	160.7	151.9	158.6	163.2	139.6	179.6	161.1	177.5	173.5	173	153.8	151.9	173.1	169.8	158	167.2
K	26.6	23.5	171.9	148.7	166.4	174.5	170.6	145.6	160	148.5	163.5	164.3	154.2	149.5	182.9	150.3	171.6	163.6	169.4	149.2	162.8	170.4	162.6	167.4
L	24.8	24.6	162.3	153.2	143.1	160.8	156.3	167	140.9	149.6	142.2	165.1	158.8	159.8	163.9	157.8	162.1	182.8	174.1	159.6	158.7	154.5	158.3	158.5
M	25	25.6	128.1	142.3	145.7	151.1	154.3	144.6	138.5	140.5	154.5	163.6	146.1	163.6	164.9	171.9	163	158.9	165.8	159.6	167.5	158.3	153.5	160.5
N	23.7	24.1	145.9	142.3	140.6	146	159.4	168.4	149.8	158.4	145.3	158.3	142	155.3	142.2	165.4	172.9	163.9	159.7	160.7	169.1	172.5	162.9	163.3
O	25.5	21.7	144.4	155.6	143.9	149.2	150.4	145.5	143.4	155.7	148.2	154.1	151.3	151.2	194.1	158.2	158.6	156	151.3	155.7	158.9	162.8	151.1	160.6
P	23.2	25.4	147.3	152.2	153.1	160.5	161.9	154.5	153.5	148.7	156.5	146.2	158.7	160.9	158.4	164.4	165.6	163.5	163.2	160.1	163.1	162.5	151.7	165.7

Appendix Table 49: Fluorescence data from dilution 7 (0.04 μM) plate.